frontiers | Research Topics

# Micro/nano materials for energy storage and conversion

**Edited by**
Jinlin Lu, Shiyong Zhao, Hailong Wang, Andreas Ruediger, Feng Gu and Dongliang Yan

**Published in**
Frontiers in Chemistry

ISSN 1664-8714
ISBN 978-2-83251-971-4
DOI 10.3389/978-2-83251-971-4

## About Frontiers

Frontiers is more than just an open access publisher of scholarly articles: it is a pioneering approach to the world of academia, radically improving the way scholarly research is managed. The grand vision of Frontiers is a world where all people have an equal opportunity to seek, share and generate knowledge. Frontiers provides immediate and permanent online open access to all its publications, but this alone is not enough to realize our grand goals.

## Frontiers journal series

The Frontiers journal series is a multi-tier and interdisciplinary set of open-access, online journals, promising a paradigm shift from the current review, selection and dissemination processes in academic publishing. All Frontiers journals are driven by researchers for researchers; therefore, they constitute a service to the scholarly community. At the same time, the *Frontiers journal series* operates on a revolutionary invention, the tiered publishing system, initially addressing specific communities of scholars, and gradually climbing up to broader public understanding, thus serving the interests of the lay society, too.

## Dedication to quality

Each Frontiers article is a landmark of the highest quality, thanks to genuinely collaborative interactions between authors and review editors, who include some of the world's best academicians. Research must be certified by peers before entering a stream of knowledge that may eventually reach the public - and shape society; therefore, Frontiers only applies the most rigorous and unbiased reviews. Frontiers revolutionizes research publishing by freely delivering the most outstanding research, evaluated with no bias from both the academic and social point of view. By applying the most advanced information technologies, Frontiers is catapulting scholarly publishing into a new generation.

## What are Frontiers Research Topics?

Frontiers Research Topics are very popular trademarks of the *Frontiers journals series*: they are collections of at least ten articles, all centered on a particular subject. With their unique mix of varied contributions from Original Research to Review Articles, Frontiers Research Topics unify the most influential researchers, the latest key findings and historical advances in a hot research area.

Find out more on how to host your own Frontiers Research Topic or contribute to one as an author by contacting the Frontiers editorial office: frontiersin.org/about/contact

# Micro/nano materials for energy storage and conversion

**Topic editors**

Jinlin Lu — Guangzhou Maritime College, China
Shiyong Zhao — University of New South Wales, Australia
Hailong Wang — Ningxia University, China
Andreas Ruediger — Université du Québec, Canada
Feng Gu — Jiangxi University of Science and Technology, China
Dongliang Yan — Guangxi University for Nationalities, China

**Citation**

Lu, J., Zhao, S., Wang, H., Ruediger, A., Gu, F., Yan, D., eds. (2023). *Micro/nano materials for energy storage and conversion*. Lausanne: Frontiers Media SA. doi: 10.3389/978-2-83251-971-4

# Table of contents

frontiers | Frontiers in Chemistry

TYPE Editorial
PUBLISHED 07 March 2023
DOI 10.3389/fchem.2023.1150885



OPEN ACCESS

EDITED BY
Edison Huixiang Ang,
Nanyang Technological University,
Singapore

REVIEWED BY
Jun Yang,
Jiangsu University of Science and Technology, China

*CORRESPONDENCE
Jinlin Lu,
jinlinlu@hotmail.com

SPECIALTY SECTION
This article was submitted to Nanoscience, a section of the journal Frontiers in Chemistry

RECEIVED 25 January 2023
ACCEPTED 27 February 2023
PUBLISHED 07 March 2023

CITATION
Zhao S, Wang H, Ruediger A, Gu F, Yan D and Lu J (2023), Editorial: Micro/nano materials for energy storage and conversion.
*Front. Chem.* 11:1150885.
doi: 10.3389/fchem.2023.1150885



# Editorial: Micro/nano materials for energy storage and conversion

Shiyong Zhao[1], Hailong Wang[2], Andreas Ruediger[3], Feng Gu[4], Dongliang Yan[5] and Jinlin Lu[6]*

[1]Australian Carbon Materials Centre (A-CMC), School of Chemical Engineering, University of New South Wales, Kensington, NSW, Australia, [2]School of Materials and New Energy, Ningxia University, Yinchuan, China, [3]Nanoelectronics-Nanophotonics INRS-EMT, Université Du Québec, Québec, QC, Canada, [4]Laboratory of Advanced Materials and Manufacturing, Nanchang Key Laboratory for Advanced Manufacturing of Electronic Information Materials and Devices, International Institute for Innovation, Jiangxi University of Science and Technology, Nanchang, Jiangxi, China, [5]School of Materials and Environment, Guangxi Minzu University, Nanning, China, [6]Research Center for Corrosion and Erosion Process Control of Equipment and Material in Marine Harsh Environment, Guangzhou Maritime University, Guangzhou, Guangdong, China

KEYWORDS

**nanotechnology, micro/nano materials, energy conversion, catalysis, battery**

Editorial on the Research Topic
Micro/nano materials for energy storage and conversion

The demand for energy is increasing dramatically at an alarming rate, resulting from rapid economic development and the ever-increasing requirements of energy-based appliances. With energy usage increasing, concerns about environmental Research Topic and the social problems associated with the consumption of conventional fossil fuels are becoming serious (Yu D. et al., 2014; Fang R. et al., 2017). As a cutting-edge approach, nanotechnology has opened new frontiers in the field of materials science and engineering to meet the challenge by designing novel materials, especially micronanometer, subnano, and even atomic scale materials, for efficient energy storage and conversion. Recently, the applications of micro/nano materials in energy storage and conversion fields, including lithium batteries, metal-ion batteries, water splitting, photocatalytic reactions, and electrochemical catalysis, have been widely investigated (Dai L. et al., 2015; Hao J. et al., 2020; Zhang S. et al., 2022). However, the practical application of micro/nano materials is still far from being satisfactory, as it is mainly impeded by costs and efficiency. Therefore, the design of cost-saving and highly efficient micro/nano materials in the field of energy storage and conversion is still very significant. Numerous papers have been reported in this Research Topic, and herein we introduce the representative advances in the collected papers that discuss how micro/nano materials work in the area of energy conversion and storage.

Currently, the highest energy density of lithium-ion batteries (LIBs) is approaching its limitation but is still unable to satisfy the growing requirements of electric vehicles. Furthermore, the high cost and safety Research Topic severely limit their large-scale practical application for renewable energy storage systems. It is urgent to develop an innovative and highly efficient battery system to meet the ever-increasing demands for energy. Cao et al. reported one electrospinning approach to synthesize a novel nanocompound, namely, the $FeS_2$ nanoparticles encapsulated in S/N co-doped three-dimensional multi-channel structural carbon nanofibers ($FeS_2$@ CNFs). The $FeS_2$@ CNFs electrode exhibited an excellent rate property and cyclic stability as cathode materials for LIBs. The electrode also showed a high initial capacity of 1,336.7 mAh $g^{-1}$,

and it still had a capacity of 856.5 mAh $g^{-1}$ remaining at 0.02A $g^{-1}$ after 100 cycling tests. Li et al. fabricated a new ZnO@CZIF-8 nanocompound comprising the hierarchical ZnO nanospheres coated with inherently derived ZIF-8 porous carbon shells, which could provide sufficient active sites, facilitate rapid electronic migration, and effectively restrain the volume expansion of electrode materials. Finally, the ZnO@CZIF-8 nanospheres electrode exhibited a high capacity of 316 mAh $g^{-1}$ at a current density of 1 A $g^{-1}$ after 50 cycles and a satisfactory rate capacity used as the anode material for the Ni-Zn secondary battery using a commercial $Ni(OH)_2$ cathode. Iron–chromium redox flow batteries (ICRFBs) possessed the advantages of long cycling performance, flexible design, and high safety, as well as affordable maintenance costs. Su et al. reported one method to prepare an indium ions composite electrode by introducing the indium ions into graphite felt surfaces, which exhibited dramatically enhanced electrochemical properties after $In^{3+}$ modification.

It is worth noting that the aqueous metal-ion batteries with high safety and economical costs show promising opportunity for the development of an efficient large-scale energy storage system. Gan et al. summarized the main factors of the cyclic stability attenuation of cathode materials and the strategies of how to optimize the stability of cathode materials for aqueous zinc-ion batteries, including introducing vacancy, doping, combination engineering, and object modification. Besides these, the applicable material system and corresponding mechanisms of the relevant optimization strategies were provided, and finally, perspectives of further research directions and development prospects were proposed for practical industrial application. Sodium-ion batteries (SIBs) have attracted much attention as potential alternatives to LIBs owing to their high abundance, environmental friendliness, and low cost. Wang et al. reviewed the significant research progress on $Sb_2S_3$-based nanomaterials for SIB, mainly focusing on $Sb_2S_3$, $Sb_2S_3$/carbon composites, $Sb_2S_3$/graphene composites, and the $Sb_2S_3$/$M_xS_y$ composites structure. $Sb_2S_3$-based micro/nano materials displayed promising potential for developing high-performance SIBs.

Besides the batteries energy system, supercapacitors are a significant device because of their many advantages, such as high power density, good charge/discharge rate performance, and long cycling stability. Liu et al. synthesized a flower-like $MnO_2$/G microsphere by optimizing the TE-G/$KMnO_4$ ratio of carbon and $KMnO_4$ in the redox reaction. The $MnO_2$/G electrode demonstrated a superior rate performance with a specific capacitance of 500 F $g^{-1}$ at the current density of 1 A $g^{-1}$, and the capacitance retention was kept at 85.3% after 5,000 cycles tests, which was much better than the optimized $MnO_2$/rGO electrode. Wu et al. reported a hybrid $Ti_3C_2Tx$/C nanosphere microsupercapacitor structure through aerosol jet printing technology. The planar devices were manufactured by the hybrid spherical nanostructures, which showed excellent areal capacitance performance. This design provided a straightforward and effective technique on how to build up a 3D-structured MXene with suppressed self-stacking in order to achieve microenergy storage devices with high electrochemical performances.

Moreover, photocatalysis technology has attracted wide attention recently due to its good performance in degrading series of toxic compounds. It can provide an efficient approach to solve environmental problems. Lu et al. synthesized a ZnO-reduced graphene oxide (rGO) solid catalyst through a one-step electrodeposition method, with lithium perchlorate ($LiClO_4$) as the supporting electrolyte on the FTO substrate. Thanks to the cooperative effect between rGO and ZnO, the as-obtained ZnO-rGO structure showed a much-enhanced photocatalytic degradation performance. The degradation rate of methylene blue could reach up to 99.1% in 2 h through optimizing the ZnO-rGO composite structure by adjusting the electrodeposition process, which confirmed the effectiveness of the hierarchical approach. Yin et al. fabricated periodic epitaxial junctions utilizing $Sb_2Te_3$ nanoblades serialized by Te nanowires ($Sb_2Te_3$/Te) through a one-step hydrothermal epitaxial growth method. The as-obtained product possessed a good crystal shape and heterojunction construction, resulting in a very fast photo response owing to the efficient separation of photogenerated carriers. The responsivity and detectivity were $9.5 \times 10^{11}$ $\mu AW^{-1}$ and $1.22 \times 10^{11}$ Jones at 50 K, respectively, thus exhibiting a better detection ability than other Te-based photodetector devices.

Micro/nano materials also play a significant role in the field of electrocatalysis. Zhang et al. reported one facile organic–inorganic hybridization approach to synthesize Co-N-$C_X$ catalysts, which showed excellent hydrogen evolution reaction (HER) performances, achieving a low overpotential of 145 mV to reach 10 mA $cm^{-2}$ in 0.5 M sulfuric acid. This Co-N-C catalyst greatly facilitated the charge transfer to enhance the HER kinetics, and it also improved the durability during the long cycling tests. Cao et al. reported a feasible molecular self-assembly method to fabricate Pt/Mo carbide/multi-walled carbon nanotubes (Pt/MoCx/MWCNTs) as an active electrode for ethanol electrooxidation reaction (EOR) in acid media. The composite catalyst demonstrated high catalytic activity and a prominent anti-CO poisoning ability. As described in the paper, the abundant exposure of the active sites and the synergistic effect between Pt and MoC contributed to the superior EOR performance.

Besides experimental methods, simulation and numerical analysis are very powerful tools to design and develop a novel energy storage and conversion system. Fahim et al. reported a numerical analysis that was performed to enhance the heat transmission in the receiver of a parabolic solar collector by introducing perforated barriers. In this work, the flow and thermal characteristics of a solar collector were investigated. Moreover, it also analyzed the beneficial effects of using perforated baffles to improve the heat transfer. The position and perforation number were optimized to achieve the best heat transfer. How to achieve efficient heat transfer and energy storage is still a key problem for engineers and industrialists. Adnan et al. studied the energy storage efficiency between $(Al_2O_3\text{-}CuO\text{-}Cu/H_2O)_{mhnf}$ and $(Al_2O_3\text{-}CuO/H_2O)_{hnf}$ under the condition of novel viscous dissipation effects. The results confirmed that the third generation of heat transfer fluids $(Al_2O_3\text{-}CuO\text{-}Cu/H_2O)_{mhnf}$ possessed a much higher thermal energy storage efficiency than that of the traditional nano and hybrid nanofluids. Overall, the new insights in heat transfer are promising and could help deal with the requirements of energy storage that must be met in the modern technological world.

We sincerely hope that this Research Topic will inspire and provide new ideas for the design and fabrication of novel micro/nano materials for energy storage and conversion. All the collected works have

contributed significantly to novel micro/nano materials design and synthesis. Furthermore, all the manuscripts have innovatively provided new approaches for the field of energy storage and conversion, covering experimental and theoretical calculations. Moreover, some suggestions have been provided with respect to the development of the field of energy conversion and storage. The realization of a heterostructure is a significant and promising means to improve the performance of micronanostructures in energy storage and conversion; this deserves more research efforts. This heterogeneous structure can achieve a good synergistic effect, combining different performance advantages so as to enhance the overall performance and open up different applications in different fields. Finally, we sincerely thank all the authors, reviewers, and editors who have highly contributed to this Research Topic.

## Author contributions

SZ: Writing—original draft. HW: Review and Editing. AR: Review and Editing. FG: Review and Editing. DY: Review and Editing. JL: Supervision, Review and Editing.

## Funding

This work was supported by the National Natural Science Foundation of China (52274296).

## Conflict of interest

The authors declare that the research was conducted in the absence of any commercial or financial relationships that could be construed as a potential conflict of interest.

## Publisher's note



## References

Dai, L., Xue, Y., Qu, L., Choi, H.-J., and Baek, J. (2015). Metal-free catalysts for oxygen reduction reaction. *Chem. Rev.* 115 (11), 4823–4892. doi:10.1021/cr5003563

Fang, R., Zhao, S., Sun, Z., Wang, D., Cheng, H., Li, F., et al. (2017). More reliable lithium-sulfur batteries: Status, solutions and prospects. *Adv. Mater.* 29 (48), 1606823. doi:10.1002/adma.201606823

Hao, J., Li, B., Li, X., Zeng, X., Zhang, S., Yang, F., et al. (2020). An in-depth study of Zn metal surface Chemistry for advanced aqueous Zn-ion batteries. *Adv. Mater.* 32 (34), 2003021. doi:10.1002/adma.202003021

Yu, D., Goh, K., Wang, H., Wei, L., Jiang, W., Zhang, Q., et al. (2014). Scalable synthesis of hierarchically structured carbon nanotube–graphene fibres for capacitive energy storage. *Nat. Nanotechnol.* 9 (7), 555–562. doi:10.1038/NNANO.2014.93

Zhang, S., Hao, J., Li, H., Zhang, P., Yin, Z., Li, Y., et al. (2022). Polyiodide confinement by starch enables shuttle-free Zn–iodine batteries. *Adv. Mater.* 34 (23), 2201716. doi:10.1002/adma.202201716

frontiers in Chemistry

MINI REVIEW
published: 20 January 2022
doi: 10.3389/fchem.2021.828119

# Stability Optimization Strategies of Cathode Materials for Aqueous Zinc Ion Batteries: A Mini Review

*Yi Gan[1,2], Cong Wang[1,2], Jingying Li[1,2], Junjie Zheng[1,2], Ziang Wu[1,2], Lin Lv[1,2], Pei Liang[3], Houzhao Wan[1,2]*, Jun Zhang[1,2]* and Hao Wang[1,2]*

[1]School of Microelectronics, Hubei University, Wuhan, China, [2]Hubei Yangtze Memory Laboratories, Wuhan, China, [3]College of Optical and Electronic Technology, China Jiliang University, Hangzhou, China

Among the new energy storage devices, aqueous zinc ion batteries (AZIBs) have become the current research hot spot with significant advantages of low cost, high safety, and environmental protection. However, the cycle stability of cathode materials is unsatisfactory, which leads to great obstacles in the practical application of AZIBs. In recent years, a large number of studies have been carried out systematically and deeply around the optimization strategy of cathode material stability of AZIBs. In this review, the factors of cyclic stability attenuation of cathode materials and the strategies of optimizing the stability of cathode materials for AZIBs by vacancy, doping, object modification, and combination engineering were summarized. In addition, the mechanism and applicable material system of relevant optimization strategies were put forward, and finally, the future research direction was proposed in this article.

**Keywords: aqueous zinc ion battery, cathode materials, cyclic stability, stability attenuation, optimization**

OPEN ACCESS

***Edited by:***
*Hailong Wang,*
*Ningxia University, China*

***Reviewed by:***
*Hai-Chao Chen,*
*Qingdao University, China*
*Yunjun Ruan,*
*Guizhou University, China*

****Correspondence:***
*Houzhao Wan*
*houzhaow@hubu.edu.cn*
*Jun Zhang*
*gwen_zhang@126.com*

***Specialty section:***
*This article was submitted to Nanoscience, a section of the journal Frontiers in Chemistry*

***Received:*** *03 December 2021*
***Accepted:*** *27 December 2021*
***Published:*** *20 January 2022*

***Citation:***
*Gan Y, Wang C, Li J, Zheng J, Wu Z, Lv L, Liang P, Wan H, Zhang J and Wang H (2022) Stability Optimization Strategies of Cathode Materials for Aqueous Zinc Ion Batteries: A Mini Review. Front. Chem. 9:828119. doi: 10.3389/fchem.2021.828119*

## INTRODUCTION

In response to the global climate crisis, the research of new energy storage devices has been widely focused on expanding the application of renewable energy to replace fossil energy (Tan et al., 2020a; Wang et al., 2020a; Gan et al., 2020; Cai et al., 2021a; Liu et al., 2021a; Cai et al., 2021b; Deng et al., 2021; Zhao et al., 2021). In the field of new energy storage, lithium-ion batteries have been widely used because of their high energy density and wide working voltage (Park et al., 2021; Xia et al., 2021; Feng et al., 2022). However, the scarcity of lithium resources increases the cost of lithium batteries, and the majority of the organic electrolyte used are poisonous or flammable, reducing the safety of lithium batteries (Li et al., 2021a; Du et al., 2021; Hou et al., 2021). Comparatively, zinc metal has the advantages of non-toxic, low cost, and redox potential, which is more suitable for aqueous electrolytes (Yao et al., 2021). Moreover, the high density and multi-charge of zinc render aqueous zinc ion batteries (AZIBs) with excellent energy density, which makes it have great application prospects (Gao et al., 2021). However, the low cycle stability of AZIBs is an inevitable problem. As one of the most core components, cathode materials for the improvement of AZIB performance critically depend on the optimization of stability. The storage mechanism and capacity attenuation of zinc ions in AZIBs system have not been fully clarified. Thus, the latest research progress is necessary to be summarized, which is conducive to providing the following research direction.

Herein, the primary factors causing the performance degradation of cathode materials for AZIBs are summarized, and optimization strategies for the stability of cathode materials are introduced. Finally, according to the optimization strategy introduced in the summary, some problems to be

further studied will be put forward, and the subsequent optimization research of stability will be prospected.

## PERFORMANCE DEGRADATION OF CATHODE MATERIALS

The strong electrostatic interaction and large steric effect between divalent $Zn^{2+}$ and the main structure of cathode materials in AZIBs lead to poor cyclicity and very slow intercalation kinetics. Meanwhile, the pH, additives, types, and concentrations of zinc salts in the electrolyte will also affect the energy storage characteristics of cathode materials. The attenuation of cathode material performance is mainly divided into the following situations:

Irreversible phase transition: During the charge–discharge process of the battery, $Zn^{2+}$ intercalation, ion/molecule co-intercalation, and conversion reaction are likely to cause irreversible damage to the structure of cathode materials (Chen et al., 2020). For instance, $Zn_xMnO_2$ will be formed when $Zn^{2+}$ is inserted into the space of $MnO_2$ with a layered structure, while MnOOH with a tunnel structure will be formed when $H^+$ is inserted into the material in solution (Liu et al., 2021b; Ma et al., 2021). This phase transition in varying degrees will destroy part of the original structure, resulting in the attenuation of performance. Moreover, the $H^+$ insertion process is usually accompanied by-products [such as $Zn_4SO_4(OH)_6{\cdot}5H_2O$] with the change of pH, which will cause the adhesion of insulation corrosion on the cathode surface and also continuously reduce the electrochemical activity of the cathode (Li et al., 2019).

Cathodic dissolution: The dissolution and diffusion of cathode materials in electrolytes are irreversible to a certain extent, which will cause the instability of the material structure. For example, the Jahn–Teller effect in high-valence manganese-based oxides induces the irreversible transformation of some $Mn^{3+}$ to $Mn^{2+}$ in the process of cathode discharge and then will destroy the main structure of materials (Heo et al., 2021). In addition, for most material systems such as vanadium-based compounds, Prussian blue and analogs, and their structures are not stable in electrolytes, and irreversible dissolution will occur when the cathode is discharged for a long time (Wan and Niu, 2019; Li et al., 2021b).

In conclusion, the performance degradation of cathode materials is not only due to the influence of the electrolyte environment but also related to its own structural characteristics and reaction mechanism. Moreover, according to the research reported at present, the cycle stability of cathode materials can be optimized from four aspects: introduction of vacancy, substitution/gap doping, object modification, and combination engineering.

## STABILITY OPTIMIZATIONS FOR CATHODE MATERIALS

### Introduction of Vacancy

The introduction of an appropriate amount of vacancy engineering (oxygen vacancy, metal vacancy, etc.) has been confirmed that it not only can reduce the bandgap, improve the conductivity, and promote the diffusion kinetics of $H^+/Zn^{2+}$ to improve the capacity but also enhance the structural stability to inhibit its dissolution, so as to improve the cycle stability (Wang et al., 2020b; Luo et al., 2020; Tan et al., 2020b; Cao et al., 2021; Tong et al., 2021; Cui et al., 2022). Zhang et al. achieved the doping of $Cu^{2+}$ substituting $Mn^{3+}$ by solvothermal and annealing and synthesized oxygen-containing vacancy $Mn_2O_3$ ($O_{Cu}$-$Mn_2O_3$) (Liu et al., 2020a). The uniform distribution of oxygen vacancies can adjust the internal electric field and crystal structure by compensating the non-zero dipole moment (in **Figure 1A**), thereby promoting the reaction kinetics and improving the stability of the crystal structure. Unlike the rapid decline in the capacity of Zn||$Mn_2O_3$ battery (capacity retention less than 50%), the capacity of Zn||$O_{Cu}$-$Mn_2O_3$ battery still retains 88% of the initial capacity after 600 cycles at 1 $Ag^{-1}$. In addition, Peng et al. prepared pristine $V_6O_{13}$ (p-VO) *via* electrodeposition and the self-assembly process, and then, oxygen-deficient $V_6O_{13}$ cathode ($O_d$-VO) was obtained by annealing (Liao et al., 2020). Simulated results indicated that the introduced oxygen vacancy can reduce the Gibbs desorption free energy of $O_d$-VO, which is more conducive to the desorption of $Zn^{2+}$ than p-VO (shown in **Figure 1B**). The prepared $O_d$-VO cathode has displayed roughly a capacity retention rate of 95% after 200 cycles at 0.2 $Ag^{-1}$, which is significantly higher than p-VO cathode (collapsed within 180 cycles). Moreover, Kim et al. synthesized *in situ* growth of $ZnMn_2O_4$@C with Mn deficiency (Mn-d-ZMO@C) from the ZnO-MnO@C nanocomposite by solvent dry process and annealing methods (Islam et al., 2021). As shown in **Figure 1C**, ZnO-MnO@C transformed into Mn-d-ZMO@C *via* an aging process in electrolytes, which was along with the formation of $Zn_4(OH)_6SO_4{\cdot}5H_2O$ (ZBS) on the surface. Furthermore, Mn-d-ZMO@C and by-products realized reversible conversion by reacting with $Zn^{2+}$ and $Mn^{2+}$, respectively. The Zn/Mn-d-ZMO@C cell still maintained 84% of the highest capacity (98 mAh $g^{-1}$) after 2000 cycles at 3 $Ag^{-1}$. Thus, it can be seen that some vacancy optimization strategies reported recently have provided detailed analyses of the concentration and location distribution of introduced vacancies. However, more material systems need to be further studied to verify the universality of the optimization mechanism of this strategy.

### Substitution/Gap Doping

As reported earlier, the vacancy defects caused by doping modification have been confirmed stabilizing the crystal structure of cathode materials. Besides, the substitution doping of multivalent metal ions can effectively reduce the formation energy of cathode materials, which can effectively inhibit the collapse of crystal structure (Kim et al., 2021; Li et al., 2020). Ni et al. synthesized Mn-substituted zinc hexacyanoferrate materials (MZHCFs) using a simple precipitation method (Ni et al., 2021). The substitution of Mn ions in the N-bonded sites can restrain the cubic-rhombohedral phase transition and the dissolution of active materials in electrolytes, resulting in improving the structural stability. As shown in **Figure 1D**, the MZHCF (MZHCF-7) with Mn content of 7% retained 94% of the

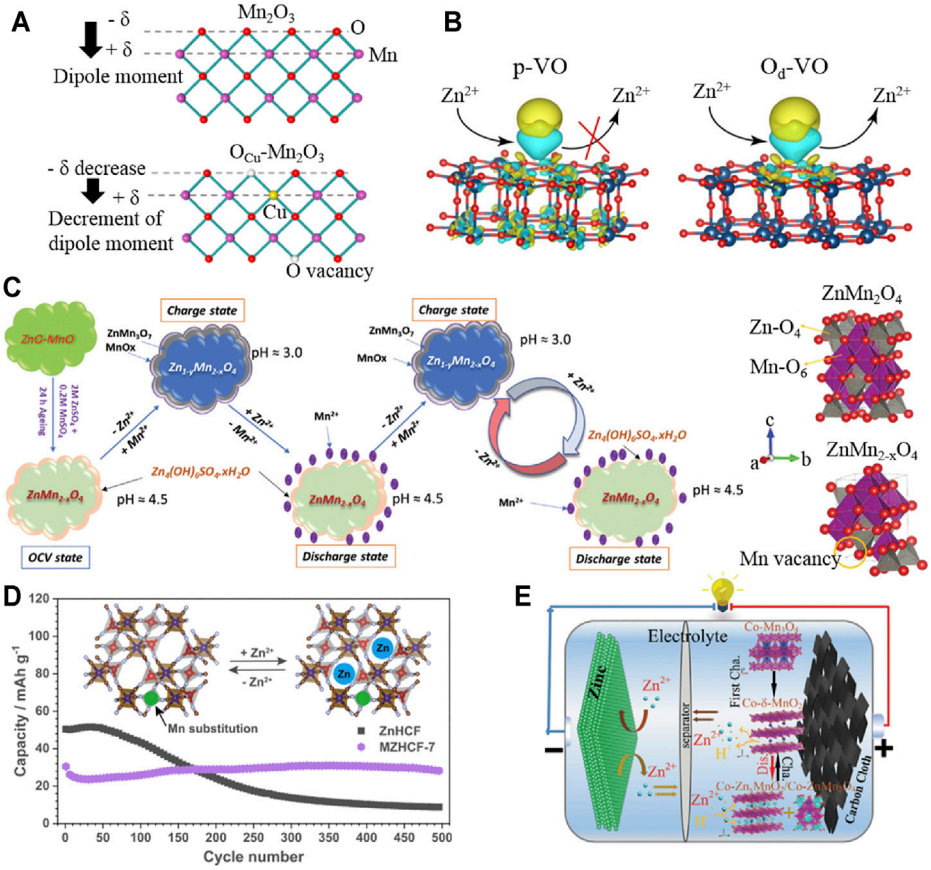


**FIGURE 1 |** Vacancies and doping modification of cathode materials. **(A)** Atomic structure models of a single layer height in $Mn_2O_3$ and $O_{cu}$-$Mn_2O_3$, respectively; **(B)** illustrations of the $Zn^{2+}$ storage/release for p-VO and $O_d$-VO; **(C)** schematic illustration for the reaction mechanism of the *in situ* formed Zn/Mn-d-ZMO@C; **(D)** schematic diagram of the reaction mechanism of MZHCFs; **(E)** schematic illustration of Zn|| Co-$Mn_3O_4$/CAN battery. Reproduced with permission (Liu et al., 2020a; Liao et al., 2020; Islam et al., 2021; Ji et al., 2021; Ni et al., 2021).

initial capacity (far more than 17% of ZnHCF) after 500 cycles at 0.25 $Ag^{-1}$, displaying a significant synergistic optimization effect. In addition, the gap doping of heteroatoms (especially metals with similar ion radius) has been proved to effectively stabilize the phase transition structure and inhibit the dissolution of materials, which contributes to improving the reversibility of cathodic electrochemical reaction (Xu et al., 2021a; Chen et al., 2021). Moreover, Wang et al. obtained multivalent cobalt ($Co^{2+}$, $Co^{3+}$)-doped $Mn_3O_4$ nanosheets (Co-$Mn_3O_4$/CNA) based on carbon nanosheets array by electrodeposition on the basis of Co-MOF precursors prepared in water bath and annealing (Ji et al., 2021). Doped $Co^{2+}$ in the interlayer of initial phase change products δ-$MnO_2$ can play a supporting role due to strong adsorption energy (in **Figure 1E**). Meanwhile, doped $Co^{4+}$ in the [$MnO_6$] octahedral structure can improve the conductivity of $Mn^{4+}$ and maintain a high specific capacity, which is owing to its low energy bandgap. In the subsequent charge–discharge process, cobalt with different valence states not only plays a supporting role in the phase change products but also can effectively inhibit the Jahn–Teller effect and promote the diffusion of ions. The prepared Co-$Mn_3O_4$/CNA cathode can still maintain 80% of the initial capacity after 1,100 cycles at 2 $Ag^{-1}$. Nevertheless, the current research on doping modification has not further analyzed the influence of doping position and the proportion of different doping components on the stability of optimized materials. Furthermore, the similarities and differences of optimization mechanisms from different doping elements still need to be further discussed.

## Object Modification

The stability optimization strategy of cathode materials also includes object modification methods such as intercalation and surface coating. Moreover, object modification has been proved to effectively promote the reversibility of the reaction process and inhibit the dissolution of structures (Zhang et al., 2021). For layered cathode materials, the insertion of highly stable objects can promote the interlayer reversible transfer of $Zn^{2+}$ (Liu et al., 2020b; He et al., 2021a; He et al., 2021b; Li et al., 2021c). Li et al. synthesized $MoS_2$/graphene nanomaterials with a sandwich interlayer structure by solution stirring in an argon atmosphere at room temperature (Li et al., 2021d). **Figures 2A–C** show that reduced graphene oxide (rGO) was inserted between $MoS_2$ layers, resulting in the significant expansion of the $MoS_2$ layer spacing and the sharp decrease in the $Zn^{2+}$ migration barrier. In addition, the stable flow structure alleviates the

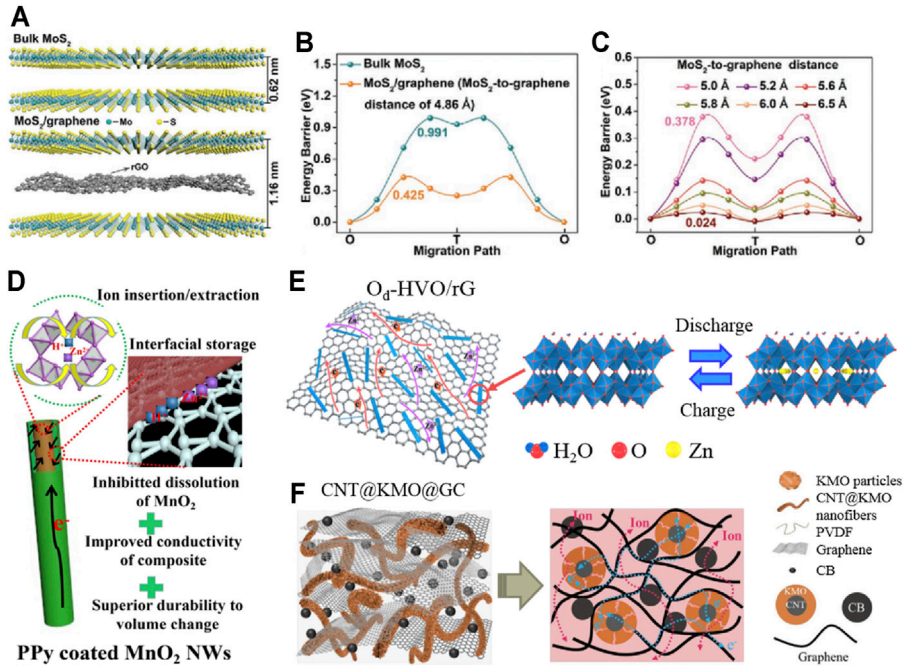


**FIGURE 2 |** Structural modification and composite of cathode materials: **(A)** Crystal structures of bulk $MoS_2$ and $MoS_2$/graphene; **(B,C)** the corresponding migration energy barriers with the variation of the $MoS_2$-to-graphene distance; **(D)** schematic illustration of freestanding CNT/$MnO_2$-PPy; **(E)** schematic diagram of $Zn^{2+}$ (de)intercalating mechanism in $O_d$-HVO/rG; **(F)** illustration of electron/ion transport and ion diffusions across the electrodes of CNT@KMO@GC. Reproduced with permission (Zhang et al., 2020a; Li et al., 2021d; Huang et al., 2021; Wang et al., 2021).

instability caused by interlayer stacking. The prepared cathode has a capacity retention rate of 88.2% after 1,800 cycles at 1 $Ag^{-1}$, and its optimization effect is significantly outstanding compared with the previously reported transition metal sulfide cathode.

In addition, the surface coating belongs to the modification of the electrode/electrolyte interface, which is an effective strategy to inhibit dissolution and phase transformation of cathode materials (Gao et al., 2020). It has been confirmed that coating materials with high stability and conductivity can effectively improve the specific capacity and cycle stability of the cathode (Bin et al., 2021; Xu et al., 2021b; Ren et al., 2021; Xing et al., 2021). Yang et al. prepared an independent flexible membrane (CNT/$MnO_2$-PPy) composed of carbon nanotubes and polypyrrole (PPy)-coated $MnO_2$ nanowires through typical *in situ* reaction self-assembly and vacuum filtration (Zhang et al., 2020a). $MnO_2$ nanowires coated with PPy (about 5 nm in thickness) are uniformly dispersed in highly conductive and interconnected carbon nanotube networks, improving the reaction kinetics and structural stability of the cathode (in **Figure 2D**). After 1,000 cycles at 1 $Ag^{-1}$, the optimized electrode still maintained 87.4% of the initial capacity. Nevertheless, the range of structural modification materials used at present is limited, and the related synthesis processes still do not meet the needs of economic efficiency. Then, there are still some challenges in practical application.

## Combination Engineering

The adjunction of materials with a high stability structure for combination is also an exploration direction to improve the stability of cathode (Zhang et al., 2020b; Shan et al., 2021). The optimization strategy of combination engineering usually includes carbon-based materials, which can improve the electron transmission efficiency and structural stability of materials (Yang et al., 2021; Zeng et al., 2021). Hou et al. synthesized a 3D reticular graphene-based hydrated vanadium dioxide composite ($O_d$-HVO/rG) with abundant oxygen vacancies using the solvothermal method (Huang et al., 2021). The research confirmed that oxygen vacancy defects can provide more active sites and promote the reversibility of the reaction, while the highly conductive and robust rG sponge can promote electron migration and reduce the accumulation of $O_d$-HVO to improve the conductivity and structural stability, as shown in **Figure 2E**. Compared with HVO (capacity retention of 86.5%) and Od-HVO (capacity retention of 93.6%), the $O_d$-HVO/rG cathode expressed scarcely any attenuation after 750 cycles at 5 $Ag^{-1}$. Moreover, Li et al. obtained a cathode material (CNT@KMO@GC) composed of graphene (G), carbon black (CB), and K-sodium manganite ($K_xMnO_2{\cdot}yH_2O$, KMO) based on core–shell carbon nanotube (CNT) by hydrothermal and solution treatment (Wang et al., 2021). In **Figure 2F**, KMO provides the main charge storage due to the interlayer intercalation of $K^+$ and $H_2O$; CNT provides a conductive framework for the loaded KMO owing to high conductivity and structural stability; G and CB provide the conductive network to reduce the accumulation of active substances. The prepared cathode has a capacity retention rate of 65.2% after 10,000 cycles at 5 $Ag^{-1}$, which is significantly higher than KMO (39.1% of the initial capacity) and CNT@

KMO (51.5% of initial capacity). However, the influence of the composite ratio on stability optimization has not been deeply analyzed, and the composite research of non-carbon matrix materials needs to be further explored. Chen et al. revealed the performance attenuation mechanism of $MnO_2$-based AZIBs by contrasting with different polymorphs and found that the low manganese dissolution of R-$MnO_2$ inhibits the degradation of performance (Liao et al., 2022). Therefore, the reasonable composite design of $MnO_2$ polymorphs with high initial capacity and R-$MnO_2$ may have certain advantages in capacity and stability compared with single crystal form, which provides a direction for the next optimization.

## SUMMARY AND PERSPECTIVES

In summary, the progress of cathode stability optimization for aqueous zinc ion batteries has been reviewed; the main of which can be divided into four aspects, including the introduction of vacancy, substitution/gap doping, object modification, and combination engineering. Thus, cathode stability optimization strategies can be designed from three aspects: inhibiting material dissolution, improving reaction reversibility, and enhancing structural stability.

However, there are several aspects to be further researched in the aforementioned optimization schemes of cathode materials. For quantitative analysis, most of the doping and composite research studies lack exploring the relationship between concentration/location and the optimization degree of stability. For universality analysis, material systems introduced into optimization research are still limited. For practical application, some synthetic processes, such as surface coating, still need to meet the demands of the economy, efficiency, and safety. In addition, the realization of the most stable cathode performance needs to eliminate the factors that reduce the reversibility according to the reaction mechanism of materials, such as inhibiting the irreversible dissolution of materials and the formation of inert by-products. Therefore, these fields to be explored can be the focuses of stability optimization in the future.

## AUTHOR CONTRIBUTIONS

YG was responsible for text editing and article composing. JL and JjZ were responsible for the review. HW and JnZ were responsible for article review and revision.

## FUNDING

This work was financially supported by the National Natural Science Foundation of China (No. 52002122), the Science and Technology Department of Hubei Province (No. 2019AAA038), the application Fundamental Research Project of Wuhan Science and Technology Bureau (No. 2019010701011396), and the Project funded by China Postdoctoral Science Foundation (No. 2021M690947).

## REFERENCES

Bin, D., Wang, Y., Tamirat, A. G., Zhu, P., Yang, B., Wang, J., et al. (2021). Stable High-Voltage Aqueous Zinc Battery Based on Carbon-Coated NaVPO4F Cathode. *ACS Sustain. Chem. Eng.* 9, 3223–3231. doi:10.1021/acssuschemeng.0c08651

Cai, P., Momen, R., Li, M., Tian, Y., Yang, L., Zou, K., et al. (2021). Functional Carbon Materials Processed by NH3 Plasma for Advanced Full-Carbon Sodium-Ion Capacitors. *Chem. Eng. J.* 420, 129647. doi:10.1016/j.cej.2021.129647

Cai, P., Zou, K., Deng, X., Wang, B., Zheng, M., Li, L., et al. (2021). Comprehensive Understanding of Sodium-Ion Capacitors: Definition, Mechanisms, Configurations, Materials, Key Technologies, and Future Developments. *Adv. Energ. Mater.* 11, 2003804. doi:10.1002/aenm.202003804

Cao, J., Zhang, D., Yue, Y., Wang, X., Pakornchote, T., Bovornratanaraks, T., et al. (2021). Oxygen Defect Enriched (NH4)2V10O25·8H2O Nanosheets for superior Aqueous Zinc-ion Batteries. *Nano Energy* 84, 105876. doi:10.1016/j.nanoen.2021.105876

Chen, C., Shi, M., Zhao, Y., Yang, C., Zhao, L., and Yan, C. (2021). Al-intercalated MnO2 Cathode with Reversible Phase Transition for Aqueous Zn-Ion Batteries. *Chem. Eng. J.* 422, 130375. doi:10.1016/j.cej.2021.130375

Chen, Q., Jin, J., Kou, Z., Liao, C., Liu, Z., Zhou, L., et al. (2020). Zn 2+ Pre-Intercalation Stabilizes the Tunnel Structure of MnO 2 Nanowires and Enables Zinc-Ion Hybrid Supercapacitor of Battery-Level Energy Density. *Small* 16, 2000091. doi:10.1002/smll.202000091

Cui, F., Wang, D., Hu, F., Yu, X., Guan, C., Song, G., et al. (2022). Deficiency and Surface Engineering Boosting Electronic and Ionic Kinetics in NH4V4O10 for High-Performance Aqueous Zinc-Ion Battery. *Energ. Storage Mater.* 44, 197–205. doi:10.1016/j.ensm.2021.10.001

Deng, X., Zou, K., Momen, R., Cai, P., Chen, J., Hou, H., et al. (2021). High Content Anion (S/Se/P) Doping Assisted by Defect Engineering with Fast Charge Transfer Kinetics for High-Performance Sodium Ion Capacitors. *Sci. Bull.* 66, 1858–1868. doi:10.1016/j.scib.2021.04.042

Du, K. D., Ang, E. H., Wu, X. L., and Liu, Y. (2021). Progresses in Sustainable Recycling Technology of Spent Lithium-Ion Batteries. *Energ. Environ. Mater.* doi:10.1002/eem2.12271

Feng, X. Y., Wu, H. H., Gao, B., Świętosławski, M., He, X., and Zhang, Q. B. (2022). Lithiophilic N-Doped Carbon Bowls Induced Li Deposition in Layered Graphene Film for Advanced Lithium Metal Batteries. *Nano Res.* 15, 352–360.

Gan, Y., Wang, C., Chen, X., Liang, P., Wan, H., Liu, X., et al. (2020). High Conductivity Ni12P5 Nanowires as High-Rate Electrode Material for Battery-Supercapacitor Hybrid Devices. *Chem. Eng. J.* 392, 123661. doi:10.1016/j.cej.2019.123661

Gao, J., Xie, X., Liang, S., Lu, B., and Zhou, J. (2021). Inorganic Colloidal Electrolyte for Highly Robust Zinc-Ion Batteries. *Nano-micro Lett.* 13, 1–12. doi:10.1007/s40820-021-00595-6

Gao, Q.-L., Li, D.-S., Liu, X.-M., Wang, Y.-F., Liu, W.-L., Ren, M.-M., et al. (2020). Biomass-derived Mesoporous Carbons Materials Coated by α-Mn3O4 with Ultrafast Zinc-Ion Diffusion Ability as Cathode for Aqueous Zinc Ion Batteries. *Electrochimica Acta* 335, 135642. doi:10.1016/j.electacta.2020.135642

He, D., Peng, Y., Ding, Y., Xu, X., Huang, Y., Li, Z., et al. (2021). Suppressing the Skeleton Decomposition in Ti-Doped NH4V4O10 for Durable Aqueous Zinc Ion Battery. *J. Power Sourc.* 484, 229284. doi:10.1016/j.jpowsour.2020.229284

He, T., Weng, S., Ye, Y., Cheng, J., Wang, X., Wang, X., et al. (2021). Cation-Deficient Zn0.3(NH4)0.3V4O100.91H2O for Rechargeable Aqueous Zinc Battery with superior Low- Temperature Performance. *Energ. Storage Mater.* 38, 389–396. doi:10.1016/j.ensm.2021.03.025

Heo, J., Chong, S., Kim, S., Kim, R., Shin, K., Kim, J., et al. (2021). Suppressing Charge Disproportionation of MnO 2 Cathodes in Rechargeable Zinc Ion

Batteries via Cooperative Jahn-Teller Distortion. *Batteries & Supercaps* 4, 1881–1888. doi:10.1002/batt.202100181

Hou, J., Wang, L., Feng, X., Terada, J., Lu, L., Yamazaki, S., et al. (2021). Thermal Runaway of Lithium-ion Batteries Employing Flame-retardant Fluorinated Electrolytes. *Energy Environ. Mater.* doi:10.1002/eem2.12297

Huang, S., He, S., Qin, H., and Hou, X. (2021). Oxygen Defect Hydrated Vanadium Dioxide/graphene as a superior Cathode for Aqueous Zn Batteries. *ACS Appl. Mater. Inter.* 13, 44379–44388. doi:10.1021/acsami.1c12653

Islam, S., Alfaruqi, M. H., Putro, D. Y., Park, S., Kim, S., Lee, S., et al. (2021). *In Situ* Oriented Mn Deficient ZnMn 2 O 4 @C Nanoarchitecture for Durable Rechargeable Aqueous Zinc-Ion Batteries. *Adv. Sci.* 8, 2002636. doi:10.1002/advs.202002636

Ji, J., Wan, H., Zhang, B., Wang, C., Gan, Y., Tan, Q., et al. (2021). Co 2+/3+/4+ -Regulated Electron State of Mn-O for Superb Aqueous Zinc-Manganese Oxide Batteries. *Adv. Energ. Mater.* 11, 2003203. doi:10.1002/aenm.202003203

Kim, S., Koo, B.-R., Jo, Y.-R., An, H.-R., Lee, Y.-G., Huang, C., et al. (2021). Defect Engineering via the F-Doping of β-MnO2 Cathode to Design Hierarchical Spheres of Interlaced Nanosheets for superior High-Rate Aqueous Zinc Ion Batteries. *J. Mater. Chem. A.* 9, 17211–17222. doi:10.1039/d1ta04051k

Li, B., Parekh, M. H., Pol, V. G., Adams, T. E., Fleetwood, J., Jones, C. M., et al. (2021). Operando Monitoring of Electrode Temperatures during Overcharge-Caused Thermal Runaway. *Energy Technol.* 9, 2100497. doi:10.1002/ente.202100497

Li, M., Mou, J., Zhong, L., Liu, T., Xu, Y., Pan, W., et al. (2021). Porous Ultrathin W-Doped VO2 Nanosheets Enable Boosted Zn2+ (De)Intercalation Kinetics in VO2 for High-Performance Aqueous Zn-Ion Batteries. *ACS Sustain. Chem. Eng.* 9, 14193–14201. doi:10.1021/acssuschemeng.1c04675

Li, Q. L., Zhang, Q. C., Zhou, Z. Y., Gong, W. B., Liu, C. L., Feng, Y. B., et al. (2020). Boosting Zn-Ion Storage Capability of Self-Standing Zn-Doped $Co_3O_4$ Nanowire Array as Advanced Cathodes for High-Performance Wearable Aqueous Rechargeable Co//Zn Batteries. *Nano Res.* 14, 1–9. doi:10.1007/s12274-020-3046-8

Li, S., Liu, Y., Zhao, X., Shen, Q., Zhao, W., Tan, Q., et al. (2021). Sandwich-Like Heterostructures of MoS 2 /Graphene with Enlarged Interlayer Spacing and Enhanced Hydrophilicity as High-Performance Cathodes for Aqueous Zinc-Ion Batteries. *Adv. Mater.* 33, 2007480. doi:10.1002/adma.202007480

Li, Z., Ganapathy, S., Xu, Y., Zhou, Z., Sarilar, M., and Wagemaker, M. (2019). Mechanistic Insight into the Electrochemical Performance of Zn/VO 2 Batteries with an Aqueous ZnSO 4 Electrolyte. *Adv. Energ. Mater.* 9, 1900237. doi:10.1002/aenm.201900237

Li, Z., Liu, T., Meng, R., Gao, L., Zou, Y., Peng, P., et al. (2021). Insights into the Structure Stability of Prussian Blue for Aqueous Zinc Ion Batteries. *Energ. Environ. Mater.* 4, 111–116. doi:10.1002/eem2.12108

Liao, M., Wang, J., Ye, L., Sun, H., Wen, Y., Wang, C., et al. (2020). A Deep-Cycle Aqueous Zinc-Ion Battery Containing an Oxygen-Deficient Vanadium Oxide Cathode. *Angew. Chem.* 132, 2293–2298. doi:10.1002/ange.201912203

Liao, Y., Chen, H.-C., Yang, C., Liu, R., Peng, Z., Cao, H., et al. (2022). Unveiling Performance Evolution Mechanisms of MnO2 Polymorphs for Durable Aqueous Zinc-Ion Batteries. *Energ. Storage Mater.* 44, 508–516. doi:10.1016/j.ensm.2021.10.039

Liu, N., Wu, X., Yin, Y., Chen, A., Zhao, C., Guo, Z., et al. (2020). Constructing the Efficient Ion Diffusion Pathway by Introducing Oxygen Defects in Mn2O3 for High-Performance Aqueous Zinc-Ion Batteries. *ACS Appl. Mater. Inter.* 12, 28199–28205. doi:10.1021/acsami.0c05968

Liu, S., Zhu, H., Zhang, B., Li, G., Zhu, H., Ren, Y., et al. (2020). Tuning the Kinetics of Zinc-Ion Insertion/Extraction in V 2 O 5 by *In Situ* Polyaniline Intercalation Enables Improved Aqueous Zinc-Ion Storage Performance. *Adv. Mater.* 32, 2001113. doi:10.1002/adma.202001113

Liu, W., Zhang, X., Huang, Y., Jiang, B., Chang, Z., Xu, C., et al. (2021). β-MnO2 with Proton Conversion Mechanism in Rechargeable Zinc Ion Battery. *J. Energ. Chem.* 56, 365–373. doi:10.1016/j.jechem.2020.07.027

Liu, X., Ji, T., Guo, H., Wang, H., Li, J., Liu, H., et al. (2021). Effects of Crystallinity and Defects of Layered Carbon Materials on Potassium Storage: a Review and Prediction. *Electrochem. Energ. Rev.* doi:10.1007/s41918-021-00114-6

Luo, H., Wang, B., Wang, C., Wu, F., Jin, F., Cong, B., et al. (2020). Synergistic Deficiency and Heterojunction Engineering Boosted VO2 Redox Kinetics for Aqueous Zinc-Ion Batteries with superior Comprehensive Performance. *Energ. Storage Mater.* 33, 390–398. doi:10.1016/j.ensm.2020.08.011

Ma, Y., Ma, Y., Diemant, T., Cao, K., Liu, X., Kaiser, U., et al. (2021). Unveiling the Intricate Intercalation Mechanism in Manganese Sesquioxide as Positive Electrode in Aqueous Zn-Metal Battery. *Adv. Energ. Mater.* 11, 2100962. doi:10.1002/aenm.202100962

Ni, G., Xu, X., Hao, Z., Wang, W., Li, C., Yang, Y., et al. (2021). Tuning the Electrochemical Stability of Zinc Hexacyanoferrate through Manganese Substitution for Aqueous Zinc-Ion Batteries. *ACS Appl. Energ. Mater.* 4, 602–610. doi:10.1021/acsaem.0c02496

Park, K. Y., Zhu, Y., Torres-Castanedo, C. G., Jung, H. J., Luu, N. S., Kahvecioglu, O., et al. (2021). Elucidating and Mitigating High-Voltage Degradation Cascades in Cobalt-Free LiNiO 2 Lithium-Ion Battery Cathodes. *Adv. Mater.* 2021, 2106402. doi:10.1002/adma.202106402

Ren, L., Yu, G., Xu, H., Wang, W., Jiang, Y., Ji, M., et al. (2021). Doping-Induced Static Activation of MnO2 Cathodes for Aqueous Zn-Ion Batteries. *ACS Sustain. Chem. Eng.* 9, 12223–12232. doi:10.1021/acssuschemeng.1c03767

Shan, L., Wang, Y., Liang, S., Tang, B., Yang, Y., Wang, Z., et al. (2021). Interfacial Adsorption-Insertion Mechanism Induced by Phase Boundary toward Better Aqueous Zn-ion Battery. *InfoMat* 3, 1028–1036. doi:10.1002/inf2.12223

Tan, Q., Chen, X., Wan, H., Zhang, B., Liu, X., Li, L., et al. (2020). Metal-organic Framework-Derived High Conductivity Fe3C with Porous Carbon on Graphene as Advanced Anode Materials for Aqueous Battery-Supercapacitor Hybrid Devices. *J. Power Sourc.* 448, 227403. doi:10.1016/j.jpowsour.2019.227403

Tan, Q., Li, X., Zhang, B., Chen, X., Tian, Y., Wan, H., et al. (2020). Valence Engineering via *In Situ* Carbon Reduction on Octahedron Sites Mn 3 O 4 for Ultra-Long Cycle Life Aqueous Zn-Ion Battery. *Adv. Energ. Mater.* 10, 2001050. doi:10.1002/aenm.202001050

Tong, H., Li, T., Liu, J., Gong, D., Xiao, J., Shen, L., et al. (2021). Fabrication of the Oxygen Vacancy Amorphous MnO 2 /Carbon Nanotube as Cathode for Advanced Aqueous Zinc-Ion Batteries. *Energ. Technol.* 9, 2000769. doi:10.1002/ente.202000769

Wan, F., and Niu, Z. (2019). Design Strategies for Vanadium-based Aqueous Zinc-Ion Batteries. *Angew. Chem.* 131, 16508–16517. doi:10.1002/ange.201903941

Wang, C., Song, Z., Wan, H., Chen, X., Tan, Q., Gan, Y., et al. (2020). Ni-Co Selenide Nanowires Supported on Conductive Wearable Textile as Cathode for Flexible Battery-Supercapacitor Hybrid Devices. *Chem. Eng. J.* 400, 125955. doi:10.1016/j.cej.2020.125955

Wang, G., Wang, Y., Guan, B., Liu, J., Zhang, Y., Shi, X., et al. (2021). Hierarchical K-Birnessite-MnO 2 Carbon Framework for High-Energy-Density and Durable Aqueous Zinc-Ion Battery. *Small* 17, 2104557. doi:10.1002/smll.202104557

Wang, J., Wang, J.-G., Qin, X., Wang, Y., You, Z., Liu, H., et al. (2020). Superfine MnO2 Nanowires with Rich Defects toward Boosted Zinc Ion Storage Performance. *ACS Appl. Mater. Inter.* 12, 34949–34958. doi:10.1021/acsami.0c08812

Xia, R., Zhao, K., Kuo, L. Y., Zhang, L., Cunha, D. M., Wang, Y., et al. (2021). Nickel Niobate Anodes for High Rate Lithium-Ion Batteries. *Adv. Energ. Mater.* 2021, 2102972. doi:10.1002/aenm.202102972

Xing, F., Shen, X., Chen, Y., Liu, X., Chen, T., and Xu, Q. (2021). A Carbon-Coated Spinel Zinc Cobaltate Doped with Manganese and Nickel as a Cathode Material for Aqueous Zinc-Ion Batteries. *Dalton Trans.* 50, 5795–5806. doi:10.1039/d1dt00686j

Xu, J.-W., Gao, Q.-L., Xia, Y.-M., Lin, X.-S., Liu, W.-L., Ren, M.-M., et al. (2021). High-performance Reversible Aqueous Zinc-Ion Battery Based on Iron-Doped Alpha-Manganese Dioxide Coated by Polypyrrole. *J. Colloid Interf. Sci.* 598, 419–429. doi:10.1016/j.jcis.2021.04.057

Xu, J., Hu, X., Alam, M. A., Muhammad, G., Lv, Y., Wang, M., et al. (2021). Al-doped α-MnO2 Coated by Lignin for High-Performance Rechargeable Aqueous Zinc-Ion Batteries. *RSC Adv.* 11, 35280–35286. doi:10.1039/d1ra06808c

Yang, F., Shen, Y., Cen, Z., Wan, J., Li, S., He, G., et al. (2021). *In Situ* construction of Heterostructured Bimetallic Sulfide/phosphide with Rich Interfaces for High-Performance Aqueous Zn-Ion Batteries. *Sci. China Mater.* doi:10.1007/s40843-021-1739-0

Yao, J., Wan, H., Chen, C., Ji, J., Wang, N., Zheng, Z., et al. (2021). Oxygen-defect Enhanced Anion Adsorption Energy toward Super-rate and Durable Cathode for Ni-Zn Batteries. *Nano-Micro Lett.* 13, 1–14. doi:10.1007/s40820-021-00699-z

Zeng, Y. X., Wang, Y., Jin, Q., Pei, Z. H., Luan, D. Y., Zhang, X. T., et al. (2021). Rationally Designed $Mn_2O_3$-$ZnMn_2O_4$ Hollow Heterostructures from Metal-

Organic Frameworks for Stable Zn-Ion Storage. *Angew. Chem. Int. Edition* 60, 1–7. doi:10.1002/anie.202113487

Zhang, L., Hu, J., Zhang, B., Liu, J., Wan, H., Miao, L., et al. (2021). Suppressing Cathode Dissolution via Guest Engineering for Durable Aqueous Zinc-Ion Batteries. *J. Mater. Chem. A.* 9, 7631–7639. doi:10.1039/d1ta00263e

Zhang, L., Miao, L., Zhang, B., Wang, J., Liu, J., Tan, Q., et al. (2020). A Durable VO2(M)/Zn Battery with Ultrahigh Rate Capability Enabled by Pseudocapacitive Proton Insertion†. *J. Mater. Chem. A.* 8, 1731–1740. doi:10.1039/c9ta11031c

Zhang, Y., Xu, G., Liu, X., Wei, X., Cao, J., and Yang, L. (2020). Scalable *In Situ* Reactive Assembly of Polypyrrole-Coated MnO 2 Nanowire and Carbon Nanotube Composite as Freestanding Cathodes for High Performance Aqueous Zn-Ion Batteries. *ChemElectroChem* 7, 2762–2770. doi:10.1002/celc.202000253

Zhao, X., Wan, H., Liang, P., Wang, N., Wang, C., Gan, Y., et al. (2021). Favorable Anion Adsorption/desorption of High Rate NiSe2 Nanosheets/hollow Mesoporous Carbon for Battery-Supercapacitor Hybrid Devices. *Nano Res.* 14, 2574–2583. doi:10.1007/s12274-020-3257-z

**Conflict of Interest:** The authors declare that the research was conducted in the absence of any commercial or financial relationships that could be construed as a potential conflict of interest.

**Publisher's Note:** All claims expressed in this article are solely those of the authors and do not necessarily represent those of their affiliated organizations, or those of the publisher, the editors, and the reviewers. Any product that may be evaluated in this article, or claim that may be made by its manufacturer, is not guaranteed or endorsed by the publisher.

frontiers in Chemistry

ORIGINAL RESEARCH
published: 01 February 2022
doi: 10.3389/fchem.2021.828964

# Impacts of Metal–Support Interaction on Hydrogen Evolution Reaction of Cobalt-Nitride-Carbide Catalyst

*Xuan Zhang†, Yu-An Li†, Yaozhen Huang, Haiqiang Mu, Xiaofeng Gu, Feng Li*, Zheng Wang* and Jing Li**

*State Key Laboratory of High-Efficiency Utilization of Coal and Green Chemical Engineering, School of Chemistry and Chemical Engineering, Ningxia University, Yinchuan, China*

Cobalt-nitride-carbide (Co-N-C) catalysts are promising cost-efficient transition metal catalysts for electrocatalytic hydrogen evolution, but few works investigate the metal–support interaction (MSI) effect on hydrogen evolution reaction (HER) performance. Herein, efficient Co-N-$C_X$ catalysts with controllable MSI between encapsulated Co nanoparticles and nitrogen-doped graphitic carbon nanosheets were synthesized via a facile organic–inorganic hybridization method. Results demonstrate that the Co-N-$C_{0.025M}$ catalyst with the coexistence of single-atom Co sites and Co nanoparticles prepared by 0.025 M cobalt nitrate shows excellent HER performance, achieving a low overpotential of 145 mV to reach 10 mA $cm^{-2}$ in 0.5 M sulfuric acid, which is mainly because the optimal MSI, which leads to a moderate hydrogen adsorption energy and improved electroactive sites, not only facilitates the charge transfer to improve the HER kinetics, but also improves the durability of the catalyst by Co-N bond anchoring and encapsulation of active Co species. This work provides guidance to further reveal the influence of MSI on their catalytic activity.

**Keywords: cobalt nanoparticles, green hydrogen, energy conversion, metal–support interaction, adsorption energy**

OPEN ACCESS

***Edited by:***
*Jinlin Lu,*
*Guangzhou Maritime College, China*

***Reviewed by:***
*Xing Zhong,*
*Zhejiang University of Technology, China*
*Yu Long,*
*Lanzhou University, China*
*Haidong Yang,*
*Northwest Normal University, China*

****Correspondence:***
*Feng Li*
*fengli@nxu.edu.cn*
*Zheng Wang*
*wzheng@nxu.edu.cn*
*Jing Li*
*jingli18@nxu.edu.cn*

*†These authors have contributed equally to this work and share first authorship*

***Specialty section:***
*This article was submitted to Nanoscience, a section of the journal Frontiers in Chemistry*

***Received:*** *04 December 2021*
***Accepted:*** *27 December 2021*
***Published:*** *01 February 2022*

***Citation:***
*Zhang X, Li Y-A, Huang Y, Mu H, Gu X, Li F, Wang Z and Li J (2022) Impacts of Metal–Support Interaction on Hydrogen Evolution Reaction of Cobalt-Nitride-Carbide Catalyst. Front. Chem. 9:828964. doi: 10.3389/fchem.2021.828964*

## INTRODUCTION

Hydrogen energy is believed to be an ideal energy source to counter climate-related environmental degradation and mitigate energy crisis thanks to its renewability, high energy density, and the absence of greenhouse gas emissions (Zhu et al., 2020). Additionally, hydrogen evolution reaction (HER) through electrolytic water splitting has been considered as an efficient approach to transfer intermittent energy sources such as solar or wind power to stable hydrogen energy (Li et al., 2020a). The Pt-based catalysts are well known as the most ideal electrocatalytic materials for HER, but Pt resources are scarce and expensive, which hinder its large-scale industrialization (Liu et al., 2019). Therefore, it is indispensable to find non-precious metal alternatives with abundant resources and outstanding catalytic activity for HER.

Transition metal compounds, such as metal oxides ($CoO_x$, $FeO_x$, and $CuO_x$) (Ling et al., 2017; Suryanto et al., 2019; Zhang et al., 2021), sulfides ($MoS_x$ and $CuS_x$) (Guo et al., 2019a; Aslan et al., 2019; Yang et al., 2021), phosphides ($CoP_x$ and $WP_x$) (Du et al., 2018; Liu et al., 2021; Zhao et al., 2021), nitrides ($MoN_x$ and $CoN_x$) (Jin et al., 2018; Peng et al., 2019; Shu et al., 2020), carbides ($Ni_3C$ and $Mo_2C$) (Li et al., 2016; Gao et al., 2019; Lu et al., 2019; Ma et al., 2020), and metal-nitride-carbide (M-N-C, M = Fe, Co, Ni, etc.) (Liu et al., 2017; Roy et al., 2018; Jin et al., 2019; Shi et al., 2020), have gradually attracted attention in electrocatalytic hydrogen production applications (Dinh et al., 2019).

Among these transition metal electrocatalysts, the Co-based electrocatalysts have been proposed as the ideal alternatives for cost-efficient and highly active HER owing to their extensive availability, high catalytic performance, and being environmental friendly (Zhang et al., 2020).

In recent years, Co-N-C has attracted growing interest as a highly efficient catalyst for HER (Deng et al., 2019; Sa et al., 2019). Usually, single-atom Co sites are regarded as the most active sites (Sun et al., 2018), and when the Co-N-C electrocatalysts are synthesized, strong acid etching is used to remove Co nanoparticles (NPs) agglomerated during thermal polymerization. For example, Sun et al. (2018) compared the HER performance of as-prepared cobalt based catalyst with single-atom Co sites encapsulated in hierarchically ordered porous nitrogen-doped carbon (Co-SAS/HOPNC) with the acid-treated Co-NPs/HOPNC electrocatalyst to confirm that atomically dispersed Co sites contribute to the enhanced HER activity, and the overpotential of Co-SAS/HOPNC catalyst was 137 mV in 0.5 M sulfuric acid at the current density of 10 mA $cm^{-2}$. However, numerous studies demonstrate that hydrogen evolution activity not only depended on single-atom Co sites, but also was affected by the interaction between embedded metallic cobalt particles and nitrogen-doped carbon supports (Wang et al., 2014; Guo et al., 2019b; Jia et al., 2019; van Deelen et al., 2019; Zhang et al., 2019; Yang et al., 2020). Benefiting from the strong synergy between Co NPs and carbon supports, the hybrid Co-N-C catalysts showed excellent HER activity. For instance, Chen et al. (2018) fabricated an efficient electrocatalyst with ultrafine Co NPs embedded in nitrogen-doped carbon nanotube grafted graphene nanosheets, and the as-prepared composite catalyst exhibited remarkable HER performance to reach 10 mA $cm^{-2}$ at a low overpotential of 87 mV in 0.5 M $H_2SO_4$. Additionally, Lyu et al. (2019) prepared efficient Co-N-C catalysts with a hybrid structure comprising Co-N species and Co NPs embedded in nitrogen-doped carbon shell, which could achieve an overpotential of 180 mV to reach 10 mA $cm^{-2}$ in 1.0 M KOH. Furthermore, Du et al. (2020a) synthesized a uniform Co NP (about 7 nm in diameter) embedded in nitrogen-doped carbon that exhibited high HER activity with a stabilized overpotential of 180 mV at the current density of 10 mA $cm^{-2}$ in sulfuric acid medium. However, the synthesis procedures of these Co NPs-based Co-N-C catalysts are usually complex and involve expensive modulator or template agents, which is not appropriate for the extensive commercial application.

Metal–support interaction (MSI) is of great importance for heterogeneous catalysis, which is widely exploited as a strategy to improve the catalytic activity, due to the synergy effect on chemical bonding and electron transition, where the chemical bonding at the interfacial provides a bridge for the electron transition between the metal and support, leading to a change of the charge distribution on the metal surface and further on the adsorption energy. but a full investigation of the nature of MSI has not been achieved on the HER electrocatalysts.

Herein, a facile one-pot organic–inorganic hybridization method was employed to synthesize Co-N-C hybrid catalysts with single-atom Co sites and encapsulated Co NPs for HER, which act as a model catalyst to investigate the influence of MSI on the HER activity. The cobalt nitrate was employed as the metal precursor, and glucose and dicyandiamide were applied as the carbon and nitrogen precursors, respectively. The concentration of cobalt nitrate was regulated to control the diameter of the Co NPs, so as to adjust the interaction between encapsulated Co NPs and nitrogen-doped carbon supports to obtain optimized hydrogen evolution activity in acid medium. Finally, the Co-N-$C_{0.025M}$ catalyst demonstrated the best HER performance, which could achieve a low overpotential of 145 mV to reach 10 mA $cm^{-2}$ in 0.5 M $H_2SO_4$. The remarkable hydrogen evolution activity and good durability were attributable to the strong synergistic effects between single-atom Co sites and embedded Co NPs that had the suitable interaction with surrounding nitrogen-doped carbon supports.

# EXPERIMENTAL SECTION

## Materials

Glucose (14431-43-7, 98%), dicyandiamide (461-58-5, 99%), Co $(NO_3)_2{\cdot}6H_2O$ (10026-22-9, 99.99% metals basis), $Fe(NO_3)_3{\cdot}9H_2O$ (7782-61-8, 99.999% metals basis), Cu $(NO_3)_2{\cdot}3H_2O$ (10031-43-3, 99.99% metals basis), and $(NH_4)_6H_2W_{12}O_{40}{\cdot}xH_2O$ (12333-11-8, 99.5% metals basis) were purchased from Aladdin Chemical Reagent Co., Ltd. $H_2SO_4$ (7664-93-9, AR 95.0%–98.0%), HCl (7647-01-0, AR 36.0%–38.0%), and $C_2H_5OH$ (64-17-5, AR ≥ 99.5%) were purchased from Sinopharm Chemical Reagent Co., Ltd. All aqueous solutions were prepared with a Milli Q water purification system (18.2 MΩ cm), and all the reagents and solvents employed were commercially available and used as received without further purification.

## Synthesis of Co-N-CX

In general, 0.25 g glucose (14431-43-7, 98%) and 5 g dicyandiamide (461-58-5, 99%) were dissolved in 200 ml of deionized water, and 2 ml of Co $(NO_3)_2{\cdot}6H_2O$ (10026-22-9, 99.99% metals basis) solution of certain concentration was added dropwise to the above solution with vigorous stirring. After stirring for 2 h, the solvent was evaporated under reduced pressure, and the obtained solid was carbonized at 900°C for 2 h under an Argon atmosphere (ramp rate = 3°C $min^{-1}$). The products were abbreviated as Co-N-$C_X$, where X was the concentration of Co $(NO_3)_2{\cdot}6H_2O$ solutions. Additionally, N-C was prepared for comparison, using the same route as for Co-N-$C_X$, except for the addition of Co $(NO_3)_2{\cdot}6H_2O$ solution.

## Synthesis of Acid-Treated Co-N-$C_X$

Twenty-five milligrams of each Co-N-$C_X$ catalyst was treated by 250 ml of 1 M HCl for 8 h at 80°C with reflux, respectively. Then, the samples were vacuum-dried at 60°C overnight after washing with deionized water, and the final products were abbreviated as H-Co-N-$C_X$.

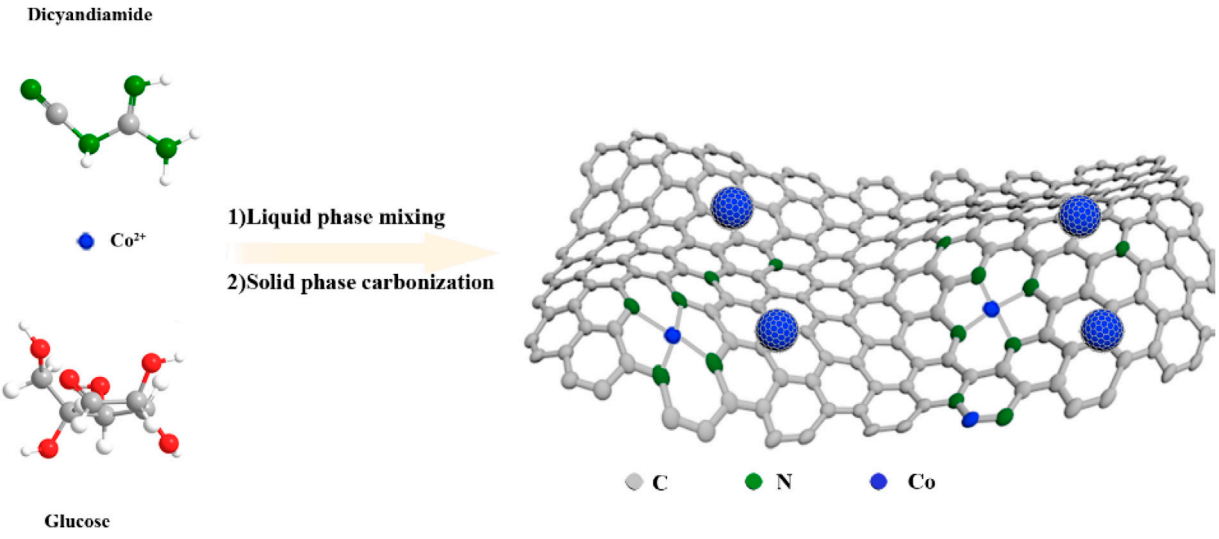


**SCHEME 1 |** The schematic illustration for the preparation of Co-N-$C_X$.

## Synthesis of M-N-$C_X$

M-N-$C_X$ samples were synthesized using the same method as for Co-N-$C_X$, where M was Mo, Fe, W, Ni, and Cu rather than Co.

## Electrochemical Measurements

The electrochemical measurements were conducted on a CHI 760E electrochemical workstation (Shanghai Chenhua Co., Ltd., Shanghai, China) with a standard three-electrode system. A graphite electrode was used as the counter electrode, and an Ag/AgCl electrode (KCl-saturated) was employed as the reference electrode. A glassy carbon rotating disk electrode (RDE) (Model 636A, Princeton Applied Research, Ametek Advanced Measurement Technology Inc.) with coated electrocatalysts was used as the working electrode, which was prepared as follows: 2 mg of catalyst and 500 μl of 0.5% Nafion solution were homogenously dispersed under ultrasound conditions in 1.5 ml of ethanol–water solution at room temperature (the volume ratio between ethanol and deionized water was 2:1). Then, 30 μl of catalyst ink was dropped onto the polished glassy carbon surface (4 mm in diameter), leading to a catalyst loading of 0.24 mg $cm^{-2}$. The HER tests were carried out with RDE at a rotation rate of 2,000 rpm, and linear sweep voltammetry (LSV) measurements were recorded at a scan rate of 10 mV $s^{-1}$ in 0.5 M $H_2SO_4$ solution. Electrochemical impedance spectroscopy (EIS) was performed over a frequency range from 0.1 MHz to 0.1 Hz with an amplitude of 5 mV. All the potentials in this study were iR corrected and converted to the reversible hydrogen electrode (RHE). The Ag/AgCl electrode was calibrated with respect to RHE, using Pt as working and counter electrodes, purged with high pure hydrogen gas during the measurement (**Supplementary Figure S1**) (Mukherjee et al., 2016). The calibration value was: $E_{vs.\ RHE} = E_{vs.\ Ag/AgCl} + 0.059pH + 0.285$ V.

# RESULTS AND DISCUSSION

The Co-N-$C_X$ catalysts were synthesized as follows (as shown in **Scheme 1**): (1) The precursor solution was synthesized via a one-pot reaction by just mixing dicyandiamide, glucose, and cobalt nitrate solution with concentration X. (2) The precursor solution was dried well under reduced pressure and the remaining powder was then carbonized at high temperature under an Argon atmosphere to obtain Co-N-$C_X$. In addition, the Co-N-$C_X$ catalysts were further heated under reflux in hydrochloric acid to gain H-Co-N-$C_X$ for comparison. This method was also used to prepare other M-N-$C_X$; however, the performance of the Co-N-$C_{0.025M}$ catalyst was significantly better than other M-N-$C_{0.025M}$ catalysts, and the Co-N-$C_{0.025M}$ prepared at 900°C was found to yield the best HER activity, eventually (as shown in **Supplementary Figures S2, S3**).

The morphologies of the Co-N-$C_X$ catalysts were characterized through transmission electron microscopy (TEM) linked to an x-ray energy dispersive spectrometer (EDS). The TEM images (**Figures 1A–D**) showed that all the Co-N-$C_X$ catalysts possessed transparent and wrinkled characteristics, regarded as the structural features of ultrathin graphene-like carbon nanosheets (Wang et al., 2019). Although it was not very obvious, there were few small Co NPs presented in Co-N-$C_{0.0125M}$ (**Figure 1A**). Aberration-corrected high-angle annular dark-field scanning transmission electron microscopy (HAADF-STEM) was applied to further investigate the structural details of Co-N-$C_{0.0125M}$, and single-atom Co sites, which were distinguished as brighter spots in **Figure 1E**, were noted homogeneously dispersed throughout the carbon supports in Co-N-$C_{0.0125M}$. In comparison with Co-N-$C_{0.0125M}$, spherical Co NPs were easily observed in Co-N-$C_{0.025M}$, Co-N-$C_{0.05M}$, and Co-N-$C_{0.075M}$, and the particle size gradually increased from about 30 to 70 nm (**Figures 1B–D**) with the increase of

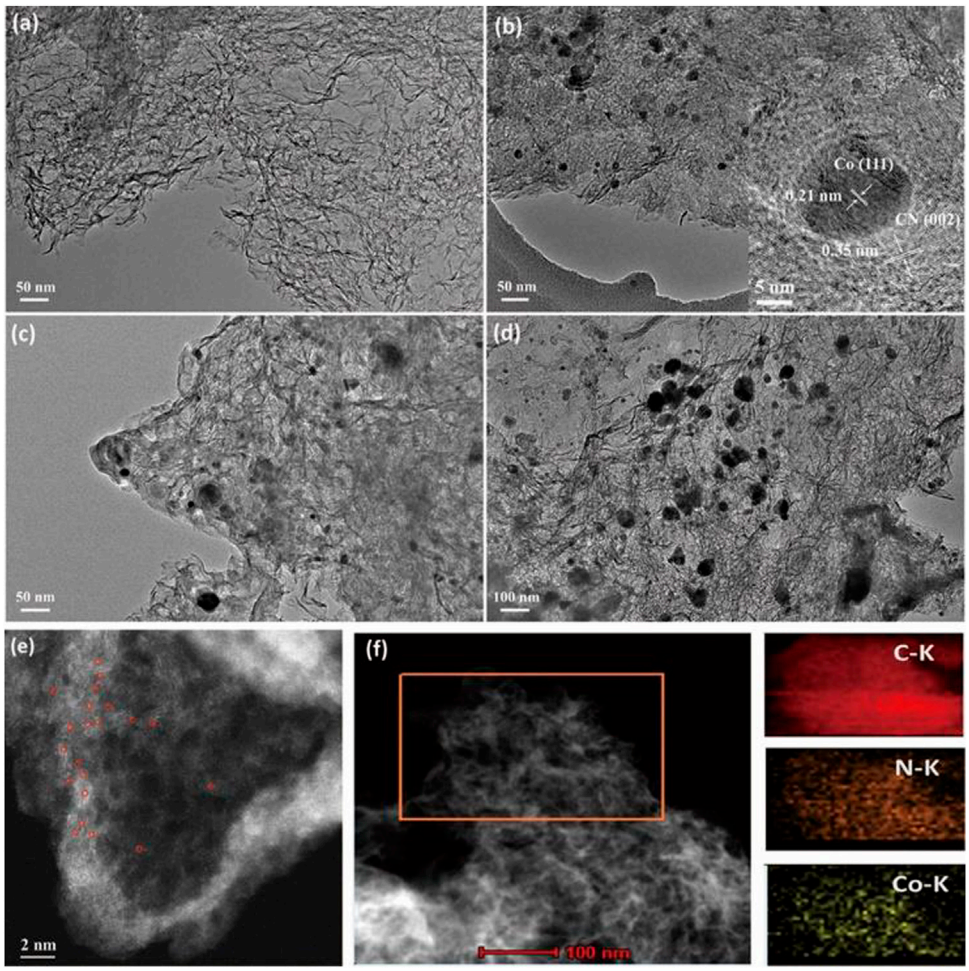


**FIGURE 1 |** TEM images of the Co-N-$C_X$ catalysts: **(A)** Co-N-$C_{0.0125M}$, **(B)** Co-N-$C_{0.025M}$ (Inset: HRTEM image of Co-N-$C_{0.025M}$). **(C)** Co-N-$C_{0.05M}$ and **(D)** Co-N-$C_{0.075M}$. **(E)** HAADF-STEM image of Co-N-$C_{0.0125M}$. **(F)** STEM image and corresponding element mapping of Co-N-$C_{0.025M}$.

the cobalt precursor concentration. This phenomenon revealed that the concentration of cobalt precursor used in the synthesis could be regulated to adjust the diameter of the Co NPs to obtain a hybrid catalyst with coexistence of single-atom Co sites and Co NPs. In addition, the HRTEM image (inset of **Figure 1B**) showed that Co nanoparticle was tightly encapsulated with several layers of carbon nanosheets, and the lattice fringe of Co nanoparticle was 0.21 nm, corresponding to the (111) crystal plane of β-Co phase. Moreover, the lattice fringe of surrounding carbon nanosheets was 0.35 nm, which was slightly larger than pure graphitic carbon, on account of the successful doping of nitrogen into the carbon matrix (Jia et al., 2019). Element mapping was performed to analyze the element distribution, and the elements Co, N, and C were found distributed uniformly on the carbon supports (**Figure 1F**). Corresponding to the TEM image, the nanosheet structure of the Co-N-$C_{0.025M}$ sample could also be observed in the AFM image (**Supplementary Figure S4**), and the thickness of the carbon nanosheet was about 3.42 nm. Thus, the as-prepared Co-N-$C_X$ catalysts had a hybrid structure comprising single-atom Co sites and embedded Co NPs, while Co NPs and the nitrogen-doped carbon supports were in intimate contact. The presence of encapsulated Co NPs would affect the features of the surrounding carbon supports by altering the electron density. This might boost the electron transfer from carbon supports to Co NPs during the HER processes and was helpful in promoting high catalytic performance.

The crystal phases of the as-prepared catalysts were analyzed by x-ray powder diffraction (XRD), and the XRD patterns of N-C, Co-N-$C_X$, and H-Co-N-$C_X$ are presented in **Figures 2A,B**. As shown in **Figure 2A**, the N-C sample displayed two broadening diffraction peaks around 26.5° and 43.3°, which corresponded to the (002) and (100) lattice planes of graphitic carbon, respectively (Chen et al., 2018). As expected, for the Co-N-$C_{0.0125M}$ and Co-N-$C_{0.025M}$, there were two diffraction planes corresponding to graphitic carbon, but no peaks related to the crystalline cobalt. However, for the Co-N-$C_{0.05M}$ and Co-N-$C_{0.075M}$, besides the broadened peaks of graphitic carbon, additional sharp peaks located at 44.2° [Co (111)] and 51.5° [Co (200)], which were related to the β-Co phase (JCPDS No. 15-0806), were observed. Interestingly, a broadening diffraction peak around 13.3°

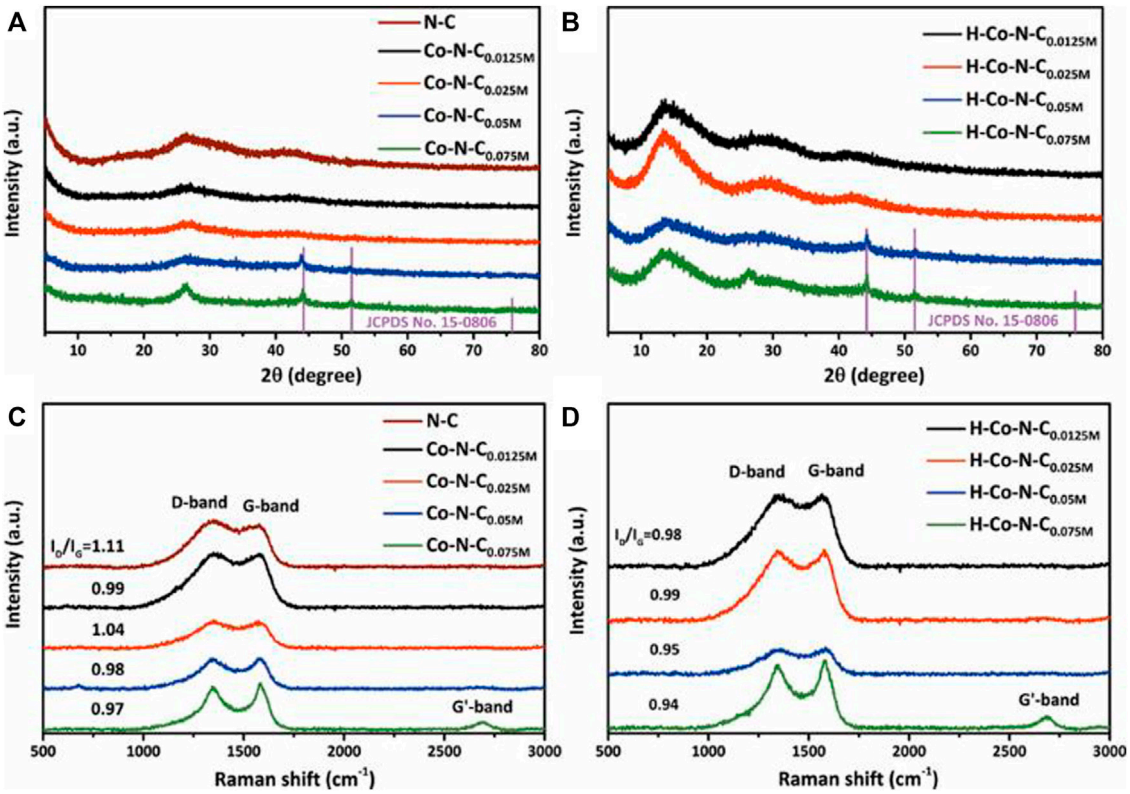


**FIGURE 2 |** XRD patterns of **(A)** N-C, Co-N-$C_X$ and **(B)** H-Co-N-$C_X$, and Raman spectrum of **(C)** N-C, Co-N-$C_X$, and **(D)** H-Co-N-$C_X$.

appeared after acid treatment for each H-Co-N-$C_X$ sample, which corresponded to the typical interplanar structural packing of the graphitic-like carbon nitride and indicated that acid treatment could destroy the interlayer stacking of the graphite-like structure, making nitrogen-doped graphitic carbon become more like the planar graphene structure with much sp2 hybridized carbon (Tian et al., 2013; Wu et al., 2015). The structural changes of the nitrogen-doped carbon supports might lead to changes of the MSI, and the Co NPs that had weak interaction with the carbon supports might be etched off by acid, while the well-encapsulated Co NPs that had strong MSI were not affected, since the diffraction peaks of crystalline cobalt did not change significantly for both H-Co-N-$C_{0.05M}$ and H-Co-N-$C_{0.075M}$ (**Figure 2B**).

To analyze the structure of nitrogen-doped carbon nanosheets, Raman spectroscopy was employed. As shown in **Figure 2C**, the two strong peaks at about 1,349 and 1,590 $cm^{-1}$ corresponded to the D and G bands, respectively, where the D band was related to disordered carbon structure and the G band was representative features of in-plane vibrations of sp2 hybridized carbon (Wang et al., 2014; Guo et al., 2019b). The relative intensity ratios of D/G ($I_D/I_G$) calculated from the peak intensity indicated the defect level and degree of graphitization of carbon structure. **Figure 2C** demonstrates that the $I_D/I_G$ value for N-C was 1.11, and the $I_D/I_G$ value of Co-N-$C_{0.025M}$ was 1.04, which was higher than those of Co-N-$C_{0.0125M}$ (0.99), Co-N-$C_{0.05M}$ (0.98), and Co-N-$C_{0.075M}$ (0.97). It suggested that Co-N-$C_{0.075M}$ had a higher degree of graphitization, which was consistent with the XRD results in which Co-N-$C_{0.075M}$ exhibited a sharper diffraction peak of graphitic carbon (**Figure 2A**). Compared with N-C, the addition of Co species could affect the *in situ* nitrogen doping and carbonization process, gaining higher degree of graphitization accordingly (Jia et al., 2019). In addition, when the concentration of cobalt precursor increased, the cobalt NPs agglomerated to form large particles, which would change the interaction between Co species and graphitic carbon supports; thus, $I_D/I_G$ values of the corresponding Co-N-$C_X$ catalyst showed a decreased trend, except for Co-N-$C_{0.025M}$. This exception indicated that Co-N-$C_{0.025M}$ had the highest level of nitrogen-doped sites, which enabled optimal MSI among the Co-N-$C_X$ catalysts. This feature could have a great contribution to the HER performance. Furthermore, the $I_D/I_G$ values of the acid-treated H-Co-N-$C_X$ samples were lower than that of the corresponding Co-N-$C_X$ (**Figure 2D**), demonstrating again that acid treatment would destroy the graphite-like stacking and recover the in-planar structure (Wu et al., 2015).

The surface elemental composition and chemical states of the Co-N-$C_X$ and H-Co-N-$C_X$ samples were verified by x-ray photoelectron spectroscopy (XPS) (**Supplementary Figure S5**). The high-resolution N 1s spectrum (**Figure 3A**) of Co-N-$C_{0.0125M}$ indicated that pyridinic N, Co-$N_x$, pyrrolic N, graphitic N, and oxidized N were located respectively at 398.4, 399.2, 400.7, 401.8, and 405.5 eV. Compared with Co-N-$C_{0.075M}$, there were slight

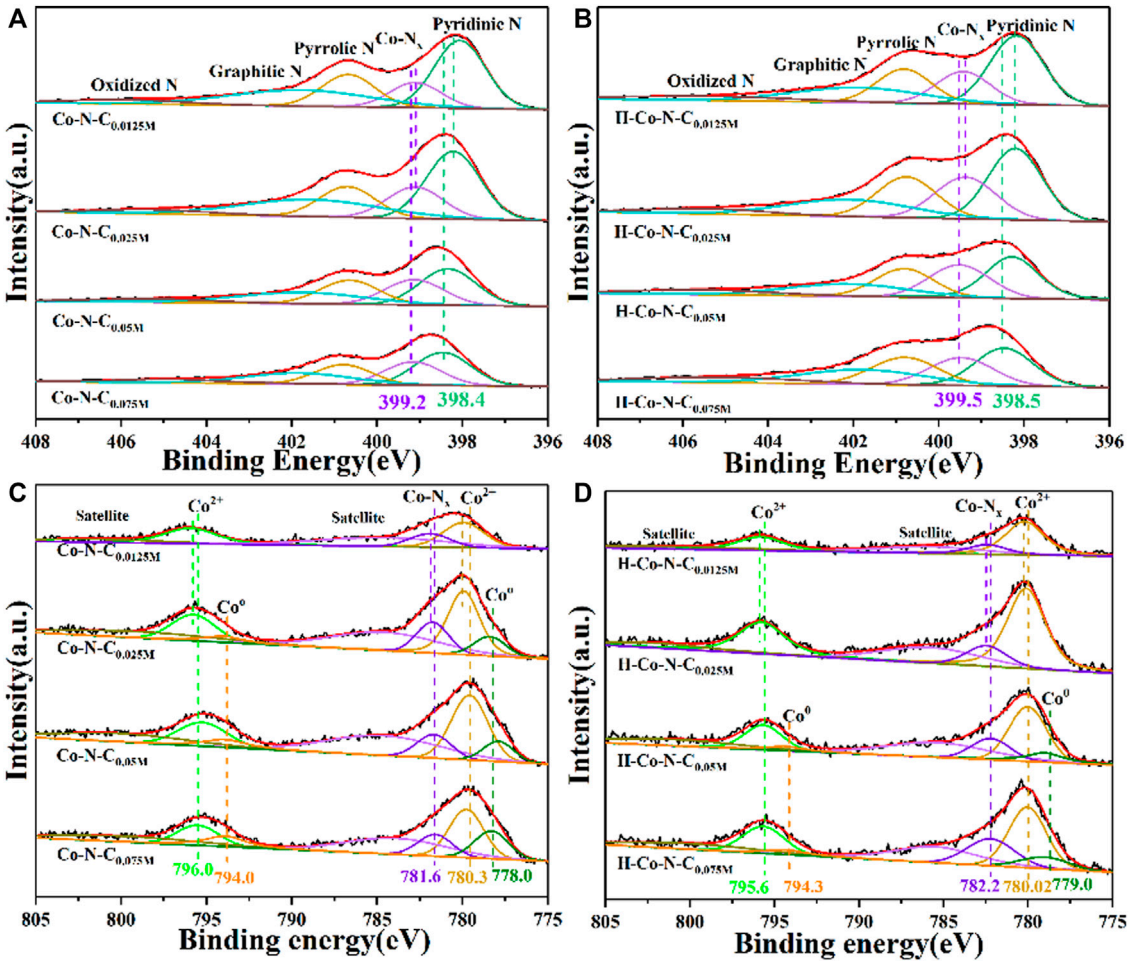


**FIGURE 3 |** High-resolution N 1s spectra of **(A)** Co-N-C$_X$ and **(B)** H-Co-N-C$_X$, and high-resolution Co 2 p spectra of **(C)** Co-N-C$_X$ and **(D)** H-Co-N-C$_X$.

negative displacements of Co-N$_x$ when the concentration of cobalt precursor decreased, and Co-N-C$_{0.0125M}$ showed the lowest binding energy of Co-N$_x$. This is mainly due to the different electronegativity causing an electron transfer from Co to N; thus the binding energy shift can be used as an indicator to the MSI, because the strong MSI always leads to an obviously electronic environment change of Co-N$_x$, and the same trend can be observed for all H-Co-N-C$_X$ after acid treatment (**Figure 3B**). Curve fitting of the high-resolution Co 2p peak spectrum of Co-N-C$_X$ and H-Co-N-C$_X$ are shown in **Figures 3C,D**, respectively. For Co-N-C$_{0.0125M}$, two main peaks appeared at 780.0 and 795.8 eV, demonstrating that Co was mainly in divalent Co state, which might be due to the strong interaction between the Co species and nitrogen-doped carbon nanosheets (Song et al., 2017; Guo et al., 2019b). Moreover, the peak at 781.7 eV was ascribed to Co-N$_x$ species. Low-intensity peak located at 778.0 eV could be attributed to metallic Co NPs. A minor positive shift of $Co^0$, $Co^{2+}$, and Co-N$_x$ would be observed when compared Co-N-C$_{0.075M}$ with other Co-N-C$_X$. When the concentration of cobalt precursor decreased, the binding energy of Co-N$_x$ gradually shifts to the positive direction and the fitting peak area of metallic Co decreases obviously, and declines in proportion, indicating that more metallic Co species are encapsulated to weaken the MSI. Offset with moderate binding energy of Co-N-C$_{0.025M}$ illustrated that there were electron transfer processes between Co species and the nitrogen-doped carbon supports, and the unique MSI of Co-N-C$_{0.025M}$ might lead to outstanding catalytic performance for HER (Hernandez Mejia et al., 2018). Compared with Co-N-C$_X$, there were obviously negative offset of $Co^0$ and little positive deviance of Co-N$_x$ for all H-Co-N-C$_X$; these changes demonstrated that the interaction between Co species and surrounding nitrogen-doped carbon supports might be changed by acid etching, causing a decrease in HER catalytic performance.

The electrocatalytic HER performance of the as-synthesized catalysts was investigated using linear sweep voltammetry (LSV) in 0.5 M $H_2SO_4$. The polarization curves of Co-N-C$_X$ and H-Co-N-C$_X$ were compared in **Figures 4A,B**, respectively. For the Co-N-C$_X$ catalysts, the overpotential of Co-N-C$_{0.0125M}$, Co-N-C$_{0.025M}$, Co-N-C$_{0.05M}$, and Co-N-C$_{0.075M}$ at a current density of 10 mA cm$^{-2}$ was 176,

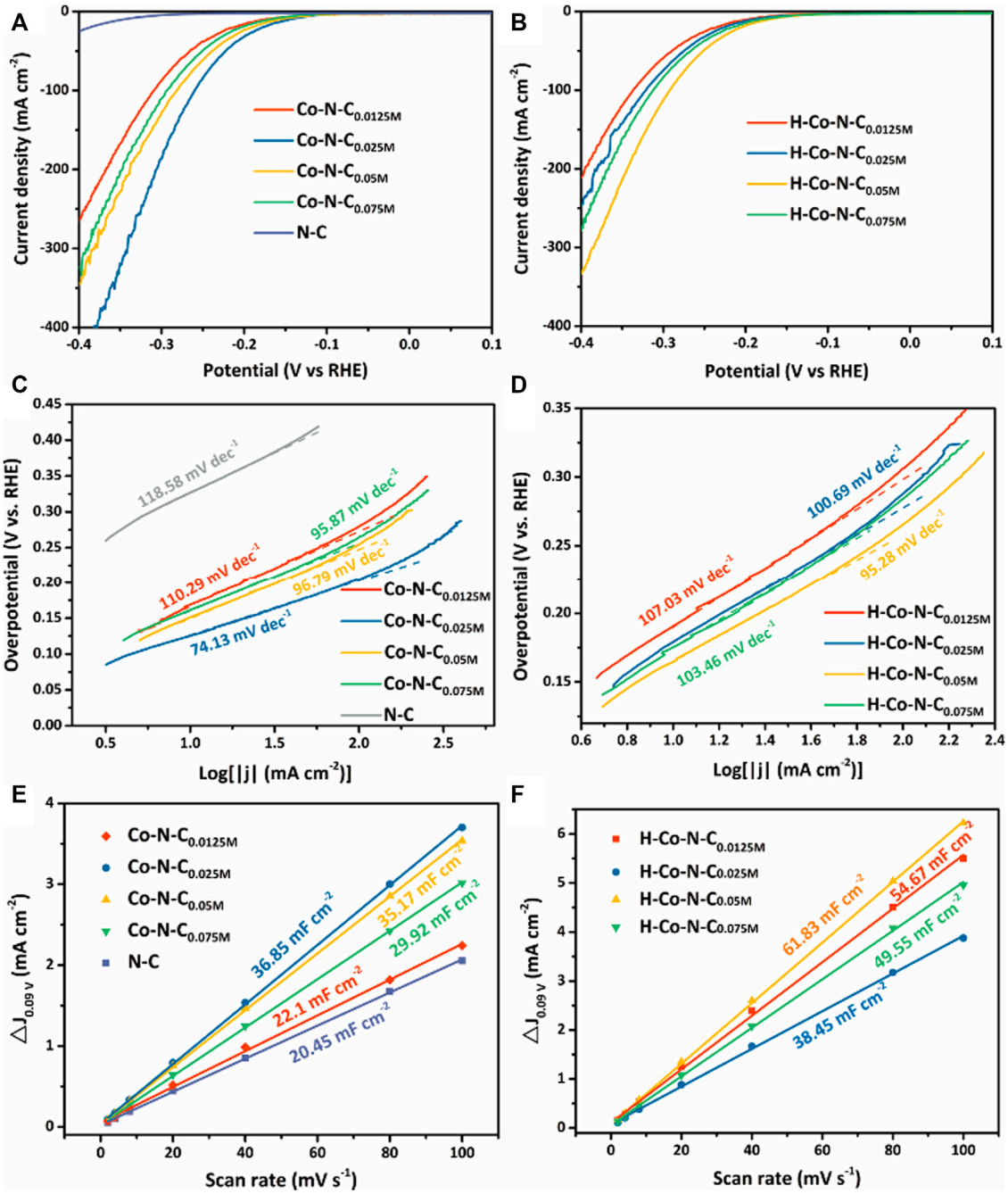


**FIGURE 4 |** LSV curves of **(A)** Co-N-$C_X$ and **(B)** H-Co-N-$C_X$ in 0.5 M $H_2SO_4$. Tafel plots of **(C)** Co-N-$C_X$ and **(D)** H-Co-N-$C_X$ in 0.5 M $H_2SO_4$. $C_{dl}$ values of **(E)** Co-N-$C_X$ and **(F)** H-Co-N-$C_X$.

145, 158, and 170 mV, respectively. In the series of H-Co-N-$C_X$ samples, H-Co-N-$C_{0.05M}$ possessed much lower overpotential (172 mV) than those of H-Co-N-$C_{0.0125M}$ (198 mV), H-Co-N-$C_{0.025M}$ (191 mV), and H-Co-N-$C_{0.075M}$ (182 mV). In addition, potassium thiocyanate (KSCN) poisoning tests (**Supplementary Figure S6A**) were carried out to confirm the important role of Co sites, and the results showed that obvious recession occurred when 0.1 M KSCN solution was added in the acid electrolyte. The significant increase of the overpotential after KSCN treatment confirmed that Co species were the catalytic active sites (Li et al., 2020b). The Co-N-$C_{0.025M}$ on glass carbon electrode had the same onset potential compared with RDE, which means an excellent intrinsic HER activity of Co-N-$C_{0.025M}$, but a

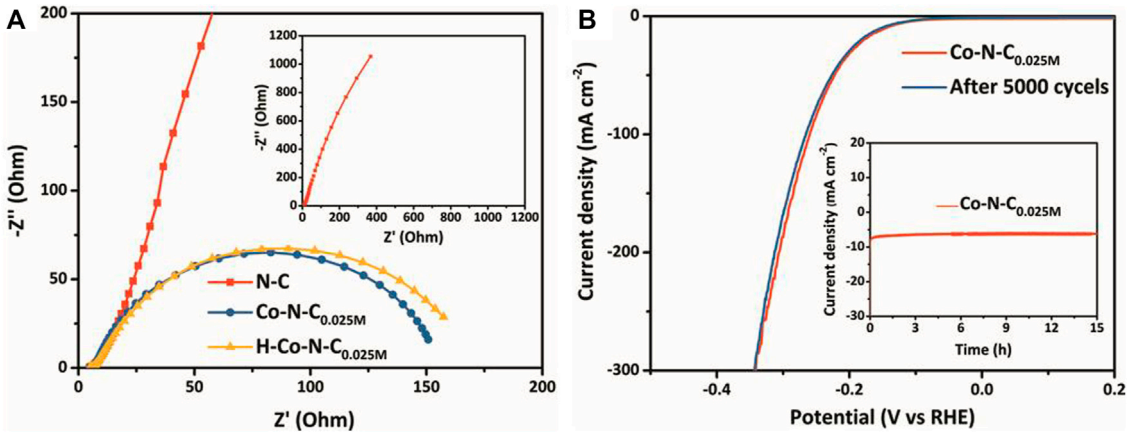


**FIGURE 5 | (A)** Nyquist plots of Co-N-$C_{0.025M}$, H-Co-N-$C_{0.025M}$, and N-C. **(B)** LSV curves of Co-N-$C_{0.025M}$ original and after 5,000 cycles; inset: time-dependent current density curve of Co-N-$C_{0.025M}$ in 0.5 M $H_2SO_4$ under an overpotential of 145 mV.

decreased current density was possibly caused by the mass transfer restriction (**Supplementary Figure S6B**). Moreover, Tafel slopes of these electrocatalysts were calculated (**Figures 4C,D**) so as to investigate the mechanism of HER activity. The lower Tafel slope of the Co-N-$C_X$ catalysts revealed that the catalysts without acid etching possessed faster HER catalytic kinetics. Interestingly, neither of the Co-N-$C_{0.0125M}$ catalyst mainly based on single-atom Co sites and the Co-N-$C_{0.075M}$ catalyst with the largest Co NPs yielded the best HER activity. Both of the overpotential and Tafel slope of Co-N-$C_{0.025M}$ were lowest among the Co-N-$C_X$ and H-Co-N-$C_X$ catalysts, representing the best HER catalytic activity. Meanwhile, the larger concentration of cobalt precursor catalysts possess recession HER performance, further confirming that the optimal MSI leads to a moderate hydrogen adsorption energy and improved electroactive sites (Du et al., 2020b). Furthermore, acid treatment could change the MSI, and the HER activity was suppressed. However, the catalytic performance of H-Co-N-$C_{0.05M}$ was even a little better after acid etching, which might be due to the fact that the acid treatment etched off some larger Co NPs and made the MSI more appropriable for HER; this viewpoint can be proved by the below electrochemical surface area measurement.

To further verify the HER catalytic performance of various samples, cyclic voltammetry (CV) measurements with varying scan rates (see **Supplementary Figure S7**) were performed to explore the electrochemical double-layer capacitance ($C_{dl}$) of as-prepared catalysts. The $C_{dl}$ values were calculated to make an estimate of the electrochemical surface area (ECSA) of the as-synthesized catalysts (**Figures 4E,F**). Compared to other Co-N-$C_X$ and N-C, Co-N-$C_{0.025M}$ exhibited the largest $C_{dl}$, suggesting that the Co-N-$C_{0.025M}$ had more electroactive species. In addition, corresponding H-Co-N-$C_X$ had larger ECSA but poorer performance than Co-N-$C_X$, attributed to the changes of carbon stacking structure and MSI. Therefore, compared with the ECSA, the MSI was the key factor in determining the catalytic performance. Thus, the best HER activity for Co-N-$C_{0.025M}$ is beneficial from the optimizing MSI due to the coexistence of single-atom Co sites and Co NPs.

The HER catalytic kinetics was further investigated by electrochemical impedance spectroscopy (EIS). The Nyquist and Bode (**Supplementary Figure S8**) plots of Co-N-$C_{0.025M}$, H-Co-N-$C_{0.025M}$, and N-C by applying an AC voltage with varying frequencies (range from 0.1 MHz to 0.1 Hz; amplitude 5 mV) were recorded at −0.215 V vs. RHE in 0.5 M $H_2SO_4$. As shown in **Figure 5A**, the H-Co-N-$C_{0.025M}$ exhibited larger charge transfer resistance because of the larger arc radius in the high-frequency region than Co-N-$C_{0.025M}$, which was attributed to the change in MSI caused by acid treatment. In addition, the similar diffusion resistance for the H-Co-N-$C_{0.025M}$ and Co-N-$C_{0.025M}$ in the low-frequency region confirms that the use of rotating disk electrode effectively reduces the resistance of mass transfer process. Both the resistances of Co-N-$C_{0.025M}$ and H-Co-N-$C_{0.025M}$ were much smaller than that of N-C, demonstrating that cobalt species acted as active sites and interacted with the nitrogen-doped carbon supports, which was beneficial to the adsorption of reactants and would speed up the kinetic process of HER; the Tafel slopes also proved this conclusion. Furthermore, a long-term hydrogen evolution test was performed to investigate the durability of Co-N-$C_{0.025M}$. There was neither obvious degradation in HER activity after 5,000 cycles (**Figure 5B**) nor a significant decrease in current density after 15 h continuously working at −145 mV vs. RHE (inset of **Figure 5B**), suggesting that the stability of the Co-N-$C_{0.025M}$ catalyst was remarkable.

## CONCLUSION

In summary, the Co-N-$C_X$ catalysts with Co NPs encapsulated in nitrogen-doped graphitic carbon nanosheets were successfully synthesized via an organic–inorganic hybridization method. The concentration of cobalt precursor

imposed a strong effect on the nanoparticle diameter and MSI of the Co-N-$C_X$ catalysts. Meanwhile, encapsulated Co NPs affected the features of the surrounding carbon supports by means of altering the electron density and promoting electron transfer from the carbon supports to embedded Co NPs, thus generating a great synergic effect between encapsulated Co NPs and single-atom Co sites to improve electrocatalytic HER activity. The Co-N-$C_{0.025M}$ catalyst without acid etching showed excellent catalytic performance for HER in acid medium, which was ascribed to its composite structure comprising single-atom Co sites and encapsulated Co NPs that optimally interact with surrounding carbon supports. This work may provide a potential approach for the design and preparation of high activity non-precious metal hybrid catalysts for electrocatalytic HER.

## DATA AVAILABILITY STATEMENT

The original contributions presented in the study are included in the article/**Supplementary Material**, further inquiries can be directed to the corresponding authors.

## AUTHOR CONTRIBUTIONS

All authors listed have made a substantial, direct, and intellectual contribution to the work and approved it for publication.

## FUNDING

This research was supported by the National Natural Science Foundation of China (21908115), the West Light Foundation of the Chinese Academy of Sciences (XAB2019AW06), the Natural Science Foundation of Ningxia Hui Autonomous Region (Grant No. 2020AAC03017), and the College Students' Innovative and Entrepreneurship Training Program of Ningxia University, China (Q2020107490044).

## SUPPLEMENTARY MATERIAL

The Supplementary Material for this article can be found online at: https://www.frontiersin.org/articles/10.3389/fchem.2021.828964/full#supplementary-material

## REFERENCES

Aslan, E., Sarilmaz, A., Ozel, F., Hatay Patir, I., and Girault, H. H. (2019). Catalytic Hydrogen Evolution by Molybdenum-Based Ternary Metal Sulfide Nanoparticles. *ACS Appl. Nano Mater.* 2 (11), 7204–7213. doi:10.1021/acsanm.9b01694

Chen, Z., Wu, R., Liu, Y., Ha, Y., Guo, Y., Sun, D., et al. (2018). Ultrafine Co Nanoparticles Encapsulated in Carbon-Nanotubes-Grafted Graphene Sheets as Advanced Electrocatalysts for the Hydrogen Evolution Reaction. *Adv. Mater.* 30 (30), 1802011. doi:10.1002/adma.201802011

Deng, C., Wu, K.-H., Scott, J., Zhu, S., Zheng, X., Amal, R., et al. (2019). Spherical Murray-Type Assembly of Co-N-C Nanoparticles as a High-Performance Trifunctional Electrocatalyst. *ACS Appl. Mater. Inter.* 11 (10), 9925–9933. doi:10.1021/acsami.8b20565

Dinh, K. N., Liang, Q., Du, C.-F., Zhao, J., Tok, A. I. Y., Mao, H., et al. (2019). Nanostructured Metallic Transition Metal Carbides, Nitrides, Phosphides, and Borides for Energy Storage and Conversion. *Nano Today* 25, 99–121. doi:10.1016/j.nantod.2019.02.008

Du, H., Kong, R.-M., Guo, X., Qu, F., and Li, J. (2018). Recent Progress in Transition Metal Phosphides with Enhanced Electrocatalysis for Hydrogen Evolution. *Nanoscale* 10 (46), 21617–21624. doi:10.1039/c8nr07891b

Du, Y., Chen, H., Huang, Z., He, X., Fang, W., Li, W., et al. (2020a). Unique Size of Co Nanoparticles Encapsulated in N-Rich Carbon Structure Derived from Electrochemical Etching for Enhanced Electrocatalytic Hydrogen Evolution. *ACS Appl. Energ. Mater.* 3 (1), 687–694. doi:10.1021/acsaem.9b01877

Du, X., Huang, Y., Pan, X., Han, B., Su, Y., Jiang, Q., et al. (2020b). Size-Dependent strong Metal-Support Interaction in $TiO_2$ Supported Au Nanocatalysts. *Nat. Commun.* 11 (1), 5811. doi:10.1038/s41467-020-19484-4

Gao, Q., Zhang, W., Shi, Z., Yang, L., and Tang, Y. (2019). Structural Design and Electronic Modulation of Transition-Metal-Carbide Electrocatalysts toward Efficient Hydrogen Evolution. *Adv. Mater.* 31 (2), 1802880. doi:10.1002/adma.201802880

Guo, Y., Park, T., Yi, J. W., Henzie, J., Kim, J., Wang, Z., et al. (2019a). Nanoarchitectonics for Transition-Metal-Sulfide-Based Electrocatalysts for Water Splitting. *Adv. Mater.* 31 (17), 1807134. doi:10.1002/adma.201807134

Guo, H., Feng, Q., Zhu, J., Xu, J., Li, Q., Liu, S., et al. (2019b). Cobalt Nanoparticle-Embedded Nitrogen-Doped Carbon/Carbon Nanotube Frameworks Derived from a Metal-Organic Framework for Tri-functional ORR, OER and HER Electrocatalysis. *J. Mater. Chem. A.* 7 (8), 3664–3672. doi:10.1039/c8ta11400e

Hernández Mejía, C., van Deelen, T. W., and de Jong, K. P. (2018). Activity Enhancement of Cobalt Catalysts by Tuning Metal-Support Interactions. *Nat. Commun.* 9 (1), 4459. doi:10.1038/s41467-018-06903-w

Jia, Q., Gao, Y., Li, Y., Fan, X., Zhang, F., Zhang, G., et al. (2019). Cobalt Nanoparticles Embedded in N-Doped Carbon on Carbon Cloth as Free-Standing Electrodes for Electrochemically-Assisted Catalytic Oxidation of Phenol and Overall Water Splitting. *Carbon* 155, 287–297. doi:10.1016/j.carbon.2019.08.031

Jin, H., Liu, X., Jiao, Y., Vasileff, A., Zheng, Y., and Qiao, S.-Z. (2018). Constructing Tunable Dual Active Sites on Two-Dimensional C3N4@MoN Hybrid for Electrocatalytic Hydrogen Evolution. *Nano Energy* 53, 690–697. doi:10.1016/j.nanoen.2018.09.046

Jin, J., Yin, J., Liu, H., Lu, M., Li, J., Tian, M., et al. (2019). Transition Metal (Fe, Co and Ni)–Carbide–Nitride (M–C–N) Nanocatalysts: Structure and Electrocatalytic Applications. *ChemCatChem* 11 (12), 2780–2792. doi:10.1002/cctc.201900570

Li, J.-S., Wang, Y., Liu, C.-H., Li, S.-L., Wang, Y.-G., Dong, L.-Z., et al. (2016). Coupled Molybdenum Carbide and Reduced Graphene Oxide Electrocatalysts for Efficient Hydrogen Evolution. *Nat. Commun.* 7, 11204. doi:10.1038/ncomms11204

Li, Y., Wei, X., Chen, L., and Shi, J. (2020a). Electrocatalytic Hydrogen Production Trilogy. *Angew. Chem. Int. Ed.* 60 (36), 19550–19571. doi:10.1002/anie.202009854

Li, S., Zhou, Q., Yu, G., Lei, Z., Liu, Z., Xu, Q., et al. (2020b). Ultra-Low Cobalt Loading on N-Doped Carbon Nanosheets by Polymer Pyrolysis Strategy for Efficient Electrocatalytic Hydrogen Evolution. *Appl. Surf. Sci.* 518, 146239. doi:10.1016/j.apsusc.2020.146239

Ling, T., Yan, D.-Y., Wang, H., Jiao, Y., Hu, Z., Zheng, Y., et al. (2017). Activating Cobalt(II) Oxide Nanorods for Efficient Electrocatalysis by Strain Engineering. *Nat. Commun.* 8 (1), 1509. doi:10.1038/s41467-017-01872-y

Liu, K., Zhong, H., Meng, F., Zhang, X., Yan, J., and Jiang, Q. (2017). Recent Advances in Metal-Nitrogen-Carbon Catalysts for Electrochemical Water Splitting. *Mater. Chem. Front.* 1 (11), 2155–2173. doi:10.1039/c7qm00119c

Liu, D., Li, X., Chen, S., Yan, H., Wang, C., Wu, C., et al. (2019). Atomically Dispersed Platinum Supported on Curved Carbon Supports for Efficient Electrocatalytic Hydrogen Evolution. *Nat. Energ.* 4 (6), 512–518. doi:10.1038/s41560-019-0402-6

Liu, W., Geng, P., Li, S., Liu, W., Fan, D., Lu, H., et al. (2021). Tuning Electronic Configuration of WP2 Nanosheet Arrays via Nickel Doping for High-Efficiency Hydrogen Evolution Reaction. *J. Energ. Chem.* 55, 17–24. doi:10.1016/j.jechem.2020.06.068

Lu, X. F., Yu, L., Zhang, J., and Lou, X. W. (2019). Ultrafine Dual-Phased Carbide Nanocrystals Confined in Porous Nitrogen-Doped Carbon Dodecahedrons for Efficient Hydrogen Evolution Reaction. *Adv. Mater.* 31 (30), 1900699. doi:10.1002/adma.201900699

Lyu, D., Du, Y., Huang, S., Mollamahale, B. Y., Zhang, X., Hasan, S. W., et al. (2019). Highly Efficient Multifunctional Co-N-C Electrocatalysts with Synergistic Effects of Co-N Moieties and Co Metallic Nanoparticles Encapsulated in a N-Doped Carbon Matrix for Water-Splitting and Oxygen Redox Reactions. *ACS Appl. Mater. Inter.* 11 (43), 39809–39819. doi:10.1021/acsami.9b11870

Ma, Y., Chen, M., Geng, H., Dong, H., Wu, P., Li, X., et al. (2020). Synergistically Tuning Electronic Structure of Porous β-Mo 2 C Spheres by Co Doping and Mo-Vacancies Defect Engineering for Optimizing Hydrogen Evolution Reaction Activity. *Adv. Funct. Mater.* 30 (19), 2000561. doi:10.1002/adfm.202000561

Mukherjee, D., Austeria, P. M., and Sampath, S. (2016). Two-Dimensional, Few-Layer Phosphochalcogenide, FePS3: A New Catalyst for Electrochemical Hydrogen Evolution over Wide pH Range. *ACS Energ. Lett.* 1 (2), 367–372. doi:10.1021/acsenergylett.6b00184

Peng, X., Pi, C., Zhang, X., Li, S., Huo, K., and Chu, P. K. (2019). Recent Progress of Transition Metal Nitrides for Efficient Electrocatalytic Water Splitting. *Sustain. Energ. Fuels* 3 (2), 366–381. doi:10.1039/C8SE00525G

Roy, A., Hursán, D., Artyushkova, K., Atanassov, P., Janáky, C., and Serov, A. (2018). Nanostructured Metal-N-C Electrocatalysts for CO2 Reduction and Hydrogen Evolution Reactions. *Appl. Catal. B: Environ.* 232, 512–520. doi:10.1016/j.apcatb.2018.03.093

Sa, Y. J., Park, S. O., Jung, G. Y., Shin, T. J., Jeong, H. Y., Kwak, S. K., et al. (2019). Heterogeneous Co-N/C Electrocatalysts with Controlled Cobalt Site Densities for the Hydrogen Evolution Reaction: Structure-Activity Correlations and Kinetic Insights. *ACS Catal.* 9 (1), 83–97. doi:10.1021/acscatal.8b03446

Shi, Z., Yang, W., Gu, Y., Liao, T., and Sun, Z. (2020). Metal-Nitrogen-Doped Carbon Materials as Highly Efficient Catalysts: Progress and Rational Design. *Adv. Sci.* 7 (15), 2001069. doi:10.1002/advs.202001069

Shu, X., Chen, S., Chen, S., Pan, W., and Zhang, J. (2020). Cobalt Nitride Embedded Holey N-Doped Graphene as Advanced Bifunctional Electrocatalysts for Zn-Air Batteries and Overall Water Splitting. *Carbon* 157, 234–243. doi:10.1016/j.carbon.2019.10.023

Song, A., Yang, W., Yang, W., Sun, G., Yin, X., Gao, L., et al. (2017). Facile Synthesis of Cobalt Nanoparticles Entirely Encapsulated in Slim Nitrogen-Doped Carbon Nanotubes as Oxygen Reduction Catalyst. *ACS Sustain. Chem. Eng.* 5 (5), 3973–3981. doi:10.1021/acssuschemeng.6b03173

Sun, T., Zhao, S., Chen, W., Zhai, D., Dong, J., Wang, Y., et al. (2018). Single-Atomic Cobalt Sites Embedded in Hierarchically Ordered Porous Nitrogen-Doped Carbon as a Superior Bifunctional Electrocatalyst. *Proc. Natl. Acad. Sci. USA* 115 (50), 12692–12697. doi:10.1073/pnas.1813605115

Suryanto, B. H. R., Wang, Y., Hocking, R. K., Adamson, W., and Zhao, C. (2019). Overall Electrochemical Splitting of Water at the Heterogeneous Interface of Nickel and Iron Oxide. *Nat. Commun.* 10 (1), 5599. doi:10.1038/s41467-019-13415-8

Tian, J., Liu, Q., Ge, C., Xing, Z., Asiri, A. M., Al-Youbi, A. O., et al. (2013). Ultrathin Graphitic Carbon Nitride Nanosheets: a Low-Cost, green, and Highly Efficient Electrocatalyst toward the Reduction of Hydrogen Peroxide and its Glucose Biosensing Application. *Nanoscale* 5 (19), 8921–8924. doi:10.1039/c3nr02031b

van Deelen, T. W., Hernández Mejía, C., and de Jong, K. P. (2019). Control of Metal-Support Interactions in Heterogeneous Catalysts to Enhance Activity and Selectivity. *Nat. Catal.* 2 (11), 955–970. doi:10.1038/s41929-019-0364-x

Wang, J., Gao, D., Wang, G., Miao, S., Wu, H., Li, J., et al. (2014). Cobalt Nanoparticles Encapsulated in Nitrogen-Doped Carbon as a Bifunctional Catalyst for Water Electrolysis. *J. Mater. Chem. A.* 2 (47), 20067–20074. doi:10.1039/c4ta04337e

Wang, Y., Chen, L., Mao, Z., Peng, L., Xiang, R., Tang, X., et al. (2019). Controlled Synthesis of Single Cobalt Atom Catalysts via a Facile One-Pot Pyrolysis for Efficient Oxygen Reduction and Hydrogen Evolution Reactions. *Sci. Bull.* 64 (15), 1095–1102. doi:10.1016/j.scib.2019.06.012

Wu, G., Hu, Y., Liu, Y., Zhao, J., Chen, X., Whoehling, V., et al. (2015). Graphitic Carbon Nitride Nanosheet Electrode-Based High-Performance Ionic Actuator. *Nat. Commun.* 6, 7258. doi:10.1038/ncomms8258

Yang, J., Li, W., Wang, D., and Li, Y. (2020). Electronic Metal-Support Interaction of Single-Atom Catalysts and Applications in Electrocatalysis. *Adv. Mater.* 32 (49), 2003300. doi:10.1002/adma.202003300

Yang, D., Cao, L., Huang, J., Liu, Q., Li, G., He, D., et al. (2021). Vanadium-doped Hierarchical Cu2S Nanowall Arrays Assembled by Nanowires on Copper Foam as an Efficient Electrocatalyst for Hydrogen Evolution Reaction. *Scr. Mater.* 196, 113756. doi:10.1016/j.scriptamat.2021.113756

Zhang, J., Zhang, Q., and Feng, X. (2019). Support and Interface Effects in Water-Splitting Electrocatalysts. *Adv. Mater.* 31 (31), 1808167. doi:10.1002/adma.201808167

Zhang, W., Cui, L., and Liu, J. (2020). Recent Advances in Cobalt-Based Electrocatalysts for Hydrogen and Oxygen Evolution Reactions. *J. Alloys Compd.* 821, 153542. doi:10.1016/j.jallcom.2019.153542

Zhang, Y., Yan, Z., Zhang, M., Tan, Y., Jia, S., and Liu, A. (2021). Green Electroless Plating of Cuprous Oxide Nanoparticles onto Carbon Nanotubes as Efficient Electrocatalysts for Hydrogen Evolution Reaction. *Appl. Surf. Sci.* 548, 149218. doi:10.1016/j.apsusc.2021.149218

Zhao, Z., Zhu, Z., Bao, X., Wang, F., Li, S., Liu, S., et al. (2021). Facile Construction of Metal Phosphides (MP, M = Co, Ni, Fe, and Cu) Wrapped in Three-Dimensional N,P-Codoped Carbon Skeleton toward Highly Efficient Hydrogen Evolution Catalysis and Lithium-Ion Storage. *ACS Appl. Mater. Inter.* 13 (8), 9820–9829. doi:10.1021/acsami.0c19914

Zhu, J., Hu, L., Zhao, P., Lee, L. Y. S., and Wong, K.-Y. (2020). Recent Advances in Electrocatalytic Hydrogen Evolution Using Nanoparticles. *Chem. Rev.* 120 (2), 851–918. doi:10.1021/acs.chemrev.9b00248

**Conflict of Interest:** The authors declare that the research was conducted in the absence of any commercial or financial relationships that could be construed as a potential conflict of interest.

**Publisher's Note:** All claims expressed in this article are solely those of the authors and do not necessarily represent those of their affiliated organizations, or those of the publisher, the editors, and the reviewers. Any product that may be evaluated in this article, or claim that may be made by its manufacturer, is not guaranteed or endorsed by the publisher.

frontiers | Frontiers in Chemistry

MINI REVIEW
published: 07 April 2022
doi: 10.3389/fchem.2022.870564

# Recent Advances in Antimony Sulfide-Based Nanomaterials for High-Performance Sodium-Ion Batteries: A Mini Review

*Guangxin Wang[1†], Mingyi Guo[1*†], Yunchao Zhao[1,2], Yibo Zhao[1], Kun Tang[1], Zhijun Chen[3], Heinz-Rolf Stock[1] and Yong Liu[1,2*]*

[1]Research Center for High Purity Materials, Henan University of Science and Technology, Luoyang, China, [2]Provincial and Ministerial Co-Construction of Collaborative Innovation Center for Non-Ferrous Metal New Materials and Advanced Processing Technology, Henan Key Laboratory of Non-Ferrous Materials Science and Processing Technology, School of Materials Science and Engineering, Henan University of Science and Technology, Luoyang, China, [3]Luoyang Bearing Research Institute Co., Ltd, Luoyang, China

Recently, sodium-ion batteries (SIBs) have attracted extensive attention as potential alternatives to lithium-ion batteries (LIBs) due to the abundance, even distribution, low cost, and environmentally friendly nature of sodium. However, sodium ions are larger than lithium ions so that the anode materials of LIBs are not suitable for SIBs. Therefore, many negative electrode materials have been investigated. Among them, $Sb_2S_3$-based nanomaterials have gradually become a research focus due to their high theoretical specific capacity, good thermal stability, simple preparation, and low price. In this review, the research progress of $Sb_2S_3$-based nanomaterials in the SIB field in recent years is summarized, including $Sb_2S_3$, $Sb_2S_3$/carbon composites, $Sb_2S_3$/graphene composites, and $Sb_2S_3/M_xS_y$ composites. Furthermore, the challenges and prospects for the development of $Sb_2S_3$-based nanomaterials are also put forward. We hope this review will contribute to the design and manufacture of high-performance SIBs and promote its practical application.

**Keywords: sodium-ion batteries, electrochemical performance, $Sb_2S_3$-based nanomaterials, anode materials, composites**

OPEN ACCESS

***Edited by:***
*Jinlin Lu,*
*Guangzhou Maritime College, China*

***Reviewed by:***
*Zhenyu Xing,*
*South China Normal University, China*
*Hongshuai Hou,*
*Central South University, China*

***Correspondence:**
*Mingyi Guo*
*gmy19910513@163.com*
*Yong Liu*
*liuyong209@haust.edu.cn*

*[†]These authors have contributed equally to this work*

***Specialty section:***
*This article was submitted to Nanoscience, a section of the journal Frontiers in Chemistry*

***Received:*** *07 February 2022*
***Accepted:*** *24 February 2022*
***Published:*** *07 April 2022*

***Citation:***
*Wang G, Guo M, Zhao Y, Zhao Y, Tang K, Chen Z, Stock H-R and Liu Y (2022) Recent Advances in Antimony Sulfide-Based Nanomaterials for High-Performance Sodium-Ion Batteries: A Mini Review. Front. Chem. 10:870564. doi: 10.3389/fchem.2022.870564*

## INTRODUCTION

Recently, lithium-ion batteries (LIBs) have developed rapidly and are extensively used in electronic devices such as notebook computers, electric vehicles, and mobile phones (Qin et al., 2017; Chong et al., 2018; Schmuch et al., 2018; Pang et al., 2019; Yuan et al., 2019; Wang et al., 2020; Tao et al., 2022). Nevertheless, the distribution of lithium on earth is uneven, and its reserves are limited. In addition, there are still some problems that need to be solved for LIBs, such as poor low-temperature performance, safety problems, and high cost (Liu G. et al., 2018; Xing et al., 2020; Sui D. et al., 2021; Wang et al., 2021c; Shi et al., 2021). As a potential substitute for LIBs in energy storage devices, SIBs have attracted extensive attention because sodium is much cheaper than lithium, environmentally friendly, and SIBs show the same energy storage mechanism as LIBs (Wang et al., 2018; Cao et al., 2020; Sui et al., 2020). However, the ionic radius of sodium ion ($Na^+$: 102 p.m.) is larger than that of lithium ion ($Li^+$: 76 p.m.), which will lead to difficulties in the sodiation/desodiation process combined with a greater volume change. Consequently, electrode materials matched with LIBs are

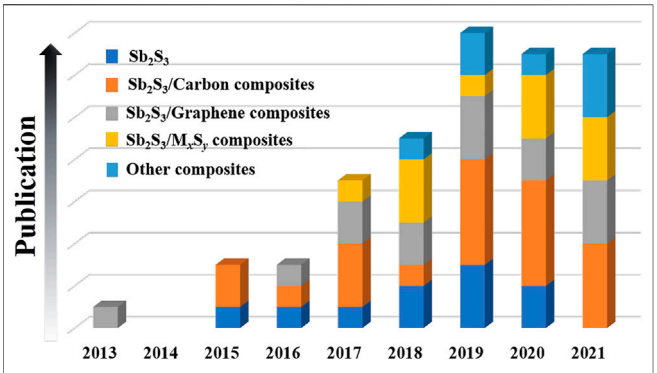


**FIGURE 1 |** Bar chart of $Sb_2S_3$-based nanomaterials as anodes for SIBs in recent years.

not suitable for SIBs (Zhao and Arumugam, 2015; Wang et al., 2017; Liu Q. et al., 2019; Liu Y. et al., 2019; Hao et al., 2019; Sui et al., 2020). Therefore, it is critical to investigate SIB electrode materials with high reversible capacity and excellent cycle stability.

As an important type of electrode material for SIBs, anode materials have been widely studied (Tao et al., 2021). Until now, considerable achievements have been made in the research of SIB anode materials, such as layered transition metal oxides (Xiong et al., 2011; Ma et al., 2020; Li Y. et al., 2020), polyanionic compounds (Li et al., 2015; Yu et al., 2018; Guo et al., 2020; Sui Y. et al., 2021), metal sulfide composites (Cui et al., 2018; Zhao et al., 2020), or alloy composites (Liu et al., 2016; Tao et al., 2021). Metal sulfide anodes have a higher sodium storage capacity, and generally have lower redox potential, better electrochemical reversibility, and longer cycle life than metal oxides in charge/discharge reaction (Xie et al., 2018; Liu G. et al., 2019; Xu et al., 2019; Yao et al., 2019; Shan et al., 2020). Among them, $Sb_2S_3$ has a high theoretical capacity of 946 mA h $g^{-1}$, and it is cheap and harmless to the environment (Zhu et al., 2015; Xie F. et al., 2019). Moreover, by combining the conversion reaction (**Eq. 1**) and alloying reaction (**Eq. 2**) between Na and S, $Sb_2S_3$ can produce a high-capacity anode and effectively play the role of S–Na and Sb–Na nanocomposites in SIBs (Yu et al., 2013; Liu et al., 2017). The following is the generally proposed electrochemical reaction mechanism between $Sb_2S_3$ and $Na^+$ (Liu et al., 2017; Xie F. et al., 2019):

$$\text{Conversion reaction}: Sb_2S_3 + 6Na^+ + 6e^- \rightarrow 2Sb + 3Na_2S. \quad (1)$$

$$\text{Alloying reaction}: 2Sb + 6Na^+ + 6e^- \rightarrow 2Na_3S. \quad (2)$$

$Sb_2S_3$-based anode materials, such as multi-shell hollow $Sb_2S_3$ (Xie F. et al., 2019), $Sb_2S_3$/graphene composites (Li C.-Y. et al., 2017; Zhao et al., 2021), $Sb_2S_3$@$FeS_2$/N-graphene (SFS/C) (Cao et al., 2020), and L-$Sb_2S_3$/$Ti_3C_2$ composites (He et al., 2021), have been reported in the application field of SIBs. For instance, Xiong et al. reported about $Sb_2S_3$ with nanostructure on S-doped graphene sheets for high-performance anode materials of SIBs (Xiong et al., 2016). Based on the interaction of heterogeneous interfaces between different components of metal sulfide, Cao et al. reported $Sb_2S_3$@$FeS_2$ with heteroatom-doped graphene as a superior SIB anode material (Cao et al., 2020). Xu et al. (2019) reviewed updated research on multiple phase transformation mechanisms and strategies to improve the performance of Sb- and Bi-based chalcogenides for SIBs. Liu et al. reviewed recent studies on Sb-based electrode materials for applications, storage mechanisms, and synthesis strategies in SIBs, LIBs, and LMBs (liquid metal batteries) (Liu Z. et al., 2018). However, so far as we know, critical reviews that focus on $Sb_2S_3$-based electrode nanomaterials specifically for SIBs have rarely been reported.

Herein, the research achievements and progresses of $Sb_2S_3$-based nanomaterials for SIBs in recent years are summarized (see **Figure 1**). In addition, some rational suggestions on the research and design of $Sb_2S_3$-based nanomaterials for SIBs in the future are also presented. Finally, we hope that this review can attract more attention and promote the practical applications of $Sb_2S_3$-based nanomaterials in the SIB field.

## RESEARCH PROGRESS OF $SB_2S_3$-BASED NANOMATERIALS IN HIGH-PERFORMANCE SIBS

$Sb_2S_3$ has advantages of low price, simple preparation, and good thermal stability (Xie F. et al., 2019; Cao et al., 2020). It is promising to be used as anode materials for high-capacity SIBs. A variety of $Sb_2S_3$-based anode materials have been reported. These are listed in **Table 1**.

### $Sb_2S_3$

To obtain $Sb_2S_3$ anodes with high energy density and capacity in SIBs, researchers prepared $Sb_2S_3$ with different morphologies, such as amorphous $Sb_2S_3$ (Hwang et al., 2016), flower-like $Sb_2S_3$ (Zhu et al., 2015), multi-shell $Sb_2S_3$ (Xie F. et al., 2019), or $Sb_2S_3$ hollow microspheres (Xie et al., 2018).

For example, Hwang et al. (2016) synthesized aspherical, amorphous α-$Sb_2S_3$ *via* a facile polyol route at room temperature, which is different from the previous routes of forming crystalline $Sb_2S_3$ at high temperature (mainly, hydrothermal method) (Zhu et al., 2015). As shown in **Supplementary Figure S1A**, α-$Sb_2S_3$ nanoparticles were composed of spherical aggregates of sub-component nanoparticles with diameters of 150–300 nm. When investigated as SIB anodes, the α-$Sb_2S_3$ nanoparticle electrode displayed a charge capacity of 512 mA h $g^{-1}$ after 100 cycles at a current density of 50 mA $g^{-1}$, and showed a better cycle performance and excellent rate performance, in contrast with the commercial crystal $Sb_2S_3$ electrode (**Supplementary Figure S1B**).

Moreover, two-dimensional (2D) nanomaterials with large surface area and ultrafine thickness have attracted more and more attention. For instance, Yao et al. (2019) designed 2D-$Sb_2S_3$ nanosheets by using a facile and scalable Li intercalation assisted stripping method. The 2D-$Sb_2S_3$ nanosheets (2D-SS) showed a good layered structure with a mean thickness of 3.8 nm (**Supplementary Figure S1C**). The large pore volume and

**TABLE 1 |** Electrochemical performances of $Sb_2S_3$-based nanomaterials as anodes for SIBs.

| Materials | Initial Coulomb Efficiency [%] | Capacity [mAh $g^{-1}$/ Cycles] | Rate capability [mAh $g^{-1}$] | Ref |
|---|---|---|---|---|
| $Sb_2S_3$ | | | | |
| $Sb_2S_3$ | 72.4 | 195 (200) at 0.1 A $g^{-1}$ | – | Fu et al. (2019) |
| Amorphous $Sb_2S_3$ | 65 | 512 (100) at 0.05 A $g^{-1}$ | 534 at 3 A $g^{-1}$ | Hwang et al. (2016) |
| $Sb_2S_3$ micro tubes | 37.1 | 201 (20) at 0.1 A $g^{-1}$ | 286 at 0.2 A $g^{-1}$ | Jin Pan et al. (2017) |
| Colloidal $Sb_2S_3$ | – | 580 (100) at 0.3 A $g^{-1}$ | 620 at 1.2 A $g^{-1}$ | Kravchyk et al. (2020) |
| Single crystal $Sb_2S_3$ | 50 | 579 (50) at 0.1 A $g^{-1}$ | 358 at 1 A $g^{-1}$ | Pan et al. (2018a) |
| $Sb_2S_3$ hollow microspheres | 62 | 384 (50) at 0.2 A $g^{-1}$ | 386 at 2 A $g^{-1}$, 314 at 3 A $g^{-1}$ | Xie et al. (2018) |
| Multi-shell $Sb_2S_3$ | 55 | 909 (50) at 0.1 A $g^{-1}$ | 725 at 1 A $g^{-1}$,604 at 2 A $g^{-1}$ | Xie et al. (2019a) |
| 2D-$Sb_2S_3$ | - | 500 (100) at 0.2 A $g^{-1}$ | 300 at 2 A $g^{-1}$ | Yao et al. (2019) |
| $Sb_2S_3$ | 77.6 | 38.6 (200) at 0.1 A $g^{-1}$ | 109.5 at 1 A $g^{-1}$, 95.1 at 2 A $g^{-1}$ | Zhao et al. (2020) |
| Flower-like $Sb_2S_3$ | 72.9 | 641.7 (100) at 0.2 A $g^{-1}$ | 597.9 at 1A $g^{-1}$, 554.6 at 2 A $g^{-1}$ | Zhu et al. (2015) |
| $Sb_2S_3$/carbon composites | | | | |
| $Sb_2S_3$@YP-43% | 42.6 | 736.2 (100) at 0.23 A $g^{-1}$ | 476.5 (1,000) at 1.2 A $g^{-1}$ | Chang et al. (2020b) |
| $Sb_2S_3$/P/C | 79 | 611 (100) at 0.05 A $g^{-1}$ | 390 at 2 A $g^{-1}$ | Choi et al. (2016) |
| $Sb_2S_3$/C | 78 | 538 (100) at 0.2 A $g^{-1}$ | 579 at 0.5A $g^{-1}$, 557 at 1 A $g^{-1}$ | Choi et al. (2017) |
| $Sb_2S_3$@C | 38.2 | 267 (100) at 0.1 A $g^{-1}$ | 283 at 1 A $g^{-1}$ | Dashairya et al. (2021) |
| $Sb_2S_3$/SCS | 68.8 | 455.8 (100) at 0.1 A $g^{-1}$ | 392 (15) at 0.5 A $g^{-1}$, 263 (20) at 1 A $g^{-1}$ | Deng et al. (2019) |
| $Sb_2S_3$@N-C | 80 | 765 (10) at 0.1 A $g^{-1}$ | 625 (1,000) at 1 A $g^{-1}$ | Dong et al. (2019) |
| $Sb_2S_3$@C rods | 68.5 | 699.1 (100) at 0.1 A $g^{-1}$ | 578 at 1.5A $g^{-1}$, 429 at 3.2 A $g^{-1}$ | Hongshuai Hou et al. (2015) |
| $Sb_2S_3$/C | – | 545.6 (100) at 0.2 A $g^{-1}$ | 550.8 (70) at 0.2 A $g^{-1}$ | Ge et al. (2018) |
| M-$Sb_2S_3$@DC | – | 326 (100) at 0.5 A $g^{-1}$ | 451 at 1 A $g^{-1}$,366 at 3 A $g^{-1}$ | Ge et al. (2020) |
| $Sb_2S_3$/CM | 64.7 | 426 (150) at 0.1 A $g^{-1}$ | – | Jaramillo-Quintero et al. (2021) |
| $Sb_2S_3$/Sb-CM | 67.1 | 608 (150) at 0.1 A $g^{-1}$ | – | Jaramillo-Quintero et al. (2021) |
| $Sb_2S_3$/S-CM | 66.9 | 675 (150) at 0.1 A $g^{-1}$ | 552 at 1 A $g^{-1}$, 481 at 2 A $g^{-1}$ | Jaramillo-Quintero et al. (2021) |
| $Sb_2S_3$@CNTs | 66.4 | 732 (110) at 0.05 A $g^{-1}$ | 668 at 1 A $g^{-1}$, 584 at 2 A $g^{-1}$ | Jiang et al. (2021) |
| $Sb_2S_3$@MWCNTs | 79.2 | 412.3 (50) at 0.05 A $g^{-1}$ | 368.8 at 0.5 A $g^{-1}$, 339.1 at 1 A $g^{-1}$ | Li et al. (2017b) |
| Amorphous $Sb_2S_3$/CNT | 77.8 | 704 (50) at 0.1 A $g^{-1}$ | 601 at 2 A $g^{-1}$,474 at 3 A $g^{-1}$ | Li et al. (2019) |
| $Sb_2S_3$/CFC | 76 | 736 (650) at 0.5 A $g^{-1}$ | 649 (400) at 2 A $g^{-1}$, 585 (400) at 5 A $g^{-1}$ | Liu et al. (2017) |
| CPC/$Sb_2S_3$ | 80 | 443 at 0.1 A $g^{-1}$ | 220 (200) at 1 A $g^{-1}$ | Mullaivananathan and Kalaiselvi, (2019) |
| $Sb_2S_3$/CS | 60 | 321 (200) at 0.2 A $g^{-1}$ | 221 at 5 A $g^{-1}$ | Xie et al. (2019b) |
| $Sb_2S_3$@CNF | 57.4 | 267.8 (100) at 0.1 A $g^{-1}$ | 221 at 1 A $g^{-1}$,178 at 5 A $g^{-1}$ | Zhai et al. (2020) |
| $Sb_2S_3$@NCFs | 56.5 | 412 (50) at 0.05 A $g^{-1}$ | 291 at 1 A $g^{-1}$, 244 at 2 A $g^{-1}$ | Zhang et al. (2021b) |
| SS/Sb@C-1 | 70.9 | 171 (200) at 0.1 A $g^{-1}$ | 253.2 at 1A $g^{-1}$, 202.8 at 2 A $g^{-1}$ | Zhao et al. (2020) |
| SS/Sb@C-2 | 66.4 | 474.6 (200) at 0.1 A $g^{-1}$ | 367 (150) at 1 A $g^{-1}$,311.1 (150) at 2 A $g^{-1}$ | Zhao et al. (2020) |
| $Sb_2S_3$/graphite | 84 | 733 at 0.1 A $g^{-1}$ | 656 (100) at 1 A $g^{-1}$, 495 (100) at 10 A $g^{-1}$ | Zhao. and Manthiram, (2015) |
| $Sb_2S_3$/graphene composites | | | | |
| SN-RGO/$Sb_2S_3$ | 57 | 507 (150) at 0.1 A $g^{-1}$ | 443.46 at 1 A $g^{-1}$, 364.89 at 2 A $g^{-1}$ | Bag et al. (2019) |
| $Sb_2S_3$/RGO | 55.9 | 262 (100) at 0.1 A $g^{-1}$ | 210 at 1 A $g^{-1}$ | Dashairya et al. (2021) |
| $Sb_2S_3$/RGO | 75.6 | 220 (50) at 0.05 A $g^{-1}$ | – | Dashairya and Saha, (2020) |
| Sn@$Sb_2S_3$-RGO | 69.8 | 597.6 (60) at 0.2 A $g^{-1}$ | 541 (70) at 0.5 A $g^{-1}$ | Deng et al. (2018) |
| $Sb_2S_3$/RGO | 66.4 | 555 (70) at 0.1 A $g^{-1}$ | – | Fan and Xie, (2019) |
| $Sb_2S_3$/graphene | – | 760 (100) at 0.05 A $g^{-1}$ | 420 (100) at 1.5 A $g^{-1}$ | Li et al. (2017a) |
| $Sb_2S_3$/RGO | – | 687.7 (80) at 0.05 A $g^{-1}$ | 495.1 (80) at 0.2 A $g^{-1}$,414.8 (100) at 0.5 A $g^{-1}$ | Pan et al. (2018b) |
| $Sb_2S_3$/RGO | 52.6 | 652 (60) at 0.1 A $g^{-1}$ | 527 at 1 A $g^{-1}$, 381 at 2 A $g^{-1}$ | Wen et al. (2019) |
| $Sb_2S_3$/RGO | 85.7 | 581.2 (50) at 0.05 A $g^{-1}$ | 309.8 (10) at 2 A $g^{-1}$ | Wu et al. (2017) |
| $Sb_2S_3$/SGS | – | 524.4 (900) at 2 A $g^{-1}$ | 591.6 at 5 A $g^{-1}$ | Xiong et al. (2016) |
| RGO/$Sb_2S_3$ | 69.2 | 670 (50) at 0.05 A $g^{-1}$ | 611 (5) at 1.5 A $g^{-1}$, 520 (5) at 3 A $g^{-1}$ | Yu et al. (2013) |
| $Sb_2S_3$@N-C/RGO | 57.6 | 368 (200) at 0.2 A $g^{-1}$ | 338 at 1 A $g^{-1}$, 253 at 5 A $g^{-1}$ | Zhan et al. (2021) |
| $Sb_2S_3$–graphene | 55.9 | 881.2 (50) at 0.1 A $g^{-1}$ | 536.4 at 1 A $g^{-1}$ | Zhao et al. (2021) |
| S-RGO/$Sb_2S_3$ | 63.9 | 509 (200) at 0.1 A $g^{-1}$ | 239 (2000) at 5 A $g^{-1}$ | Zhou et al. (2020b) |
| Sb2S3/MxSy composites | | | | |
| $Sb_2S_3$@$FeS_2$/N-graphene (SFS/C) | 82.4 | 725.4 at 0.1 A $g^{-1}$ | 645.6 at 1A $g^{-1}$, 564.3 at 5 A $g^{-1}$ | Cao et al. (2020) |
| $Sb_2S_3$-$SnS_2$ | 77.9 | 616 (50) at 0.5 A $g^{-1}$ | 510 at 10 A $g^{-1}$ | Fang et al. (2019) |
| $In_2S_3$-$Sb_2S_3$@MCNTs | – | 454 (40) at 0.2 A $g^{-1}$ | 402 at 1.6 A $g^{-1}$,355 at 3.2 A $g^{-1}$ | Huang et al. (2018) |
| $Sb_2S_3$/$MoS_2$ NWs | 82.9 | 800 at 0.1 A $g^{-1}$ | 570 at 3.2 A $g^{-1}$ | Li P. et al. (2020) |
| $Sb_2S_3$-$Bi_2S_3$@C@RGO | 68.1 | 600.7 (150) at 1 A $g^{-1}$ | 514.5 at 5 A $g^{-1}$, 485.8 at 8 A $g^{-1}$ | Li et al. (2021) |
| $Sb_2S_3$@SnS@C | 79 | 516 (100) at 0.1 A $g^{-1}$ | 442 (200) at 1 A $g^{-1}$, 200 (1,300) at 5 A $g^{-1}$ | Lin et al. (2021) |

(Continued on following page)

**TABLE 1 |** (*Continued*) Electrochemical performances of $Sb_2S_3$-based nanomaterials as anodes for SIBs.

| Materials | Initial Coulomb Efficiency [%] | Capacity [mAh $g^{-1}$/ Cycles] | Rate capability [mAh $g^{-1}$] | Ref |
|---|---|---|---|---|
| ZnS-$Sb_2S_3$@C | 61.4 | 630 (120) at 0.1 A $g^{-1}$ | 390.6 at 0.8 A $g^{-1}$ | Dong et al. (2017) |
| $SnS_2$/$Sb_2S_3$@RGO | 82.3 | 642 (100) at 0.2 A $g^{-1}$ | 593 at 2 A $g^{-1}$, 567 at 4 A $g^{-1}$ | Wang et al. (2018) |
| $Sb_2S_3$/$MoS_2$@C (SMS@C) | 79.5 | 623.2 at 0.1 A $g^{-1}$ | 465.6 (100) at 1 A $g^{-1}$, 411.5 (650) at 5 A $g^{-1}$ | Wang et al. (2021a) |
| $Sb_2S_3$/$MoS_2$ | 75.9 | 568.4 at 0.1 A $g^{-1}$ | 423.2 (100) at 1 A $g^{-1}$ | Wang et al. (2021a) |
| $Sb_2S_3$/$MoS_2$ | 48.5 | 561 (100) at 0.1 A $g^{-1}$ | 628 at 1A $g^{-1}$, 507 at 2 A $g^{-1}$ | Zhang et al. (2018) |
| α-$Sb_2S_3$@$CuSbS_2$ | 82.2 | 506.7 (50) at 0.05 A $g^{-1}$ | 293 at 3 A $g^{-1}$ | Zhou et al. (2020a) |
| Other composites | | | | |
| $Sb_2S_3$@$SnO_2$ | 54.2 | 582.9 (100) at 0.05 A $g^{-1}$ | 441.6 at 1A $g^{-1}$, 237.1 at 5 A $g^{-1}$ | Chang et al. (2020a) |
| L-$Sb_2S_3$/$Ti_3C_2$ | 65.7 | 445.5 (100) at 0.1 A $g^{-1}$ | 339.5 at 2 A $g^{-1}$ | He et al. (2021) |
| $Sb_2S_3$@$Ti_3C_2T_x$ | | 329 (100) at 0.1 A $g^{-1}$ | 118 (500) at 2 A $g^{-1}$ | Ren et al. (2021) |
| $Sb_2S_3$@PPy | 63.7 | 881 (50) at 0.1 A $g^{-1}$ | 390 (400) at 2 A $g^{-1}$ | Shi et al. (2019) |
| $Sb_2S_3$/MMCN@PPy | – | 446 (50) at 0.1 A $g^{-1}$ | 269 (300) at 1 A $g^{-1}$ | Yin et al. (2019) |
| $Sb_2S_3$@m-$Ti_3C_2T_x$ | 51 | 156 (100) at 0.1 A $g^{-1}$ | 72 (1000) at 2 A $g^{-1}$ | Zhang et al. (2021a) |
| $Sb_2S_3$/PPy | 70 | 427 (50) at 0.1 A $g^{-1}$ | 236 (50) at 0.5 A $g^{-1}$ | Zheng et al. (2018) |

*Notes: 2D-$Sb_2S_3$ = two-dimensional $Sb_2S_3$; $Sb_2S_3$@YP-43% = 43% contents $Sb_2S_3$ mixed with YP80F active carbon (YP); $Sb_2S_3$/SCS, stibnite/sulfur-doped carbon sheet; M-$Sb_2S_3$@DC, metal-sulfides with double carbon; CM, carbon matrix; CNTs, carbon nanotubes; MWCNTs, multiwalled carbon nanotubes; CFC, carbon fiber cloth; CPC, coir pith derived carbon; $Sb_2S_3$/CS, $Sb_2S_3$ embedded in carbon–silicon oxide nanofibers; CNF, multichannel N-doped carbon nanofiber; NCFs = N-doped 3D carbon nanofibers; RGO, reduced graphene oxide; $Sb_2S_3$/SGS, $Sb_2S_3$/sulfur-doped graphene sheets; SN-RGO/$Sb_2S_3$ = sulfur, nitrogen dual doped RGO/$Sb_2S_3$; $Sb_2S_3$@N-C/RGO, $Sb_2S_3$/nitrogen-doped carbon/RGO; S-RGO/$Sb_2S_3$ = sulfur-doped RGO/$Sb_2S_3$; MCNTs, multiwalled carbon nanotubes; $Sb_2S_3$/$MoS_2$ NWs, $Sb_2S_3$/$MoS_2$ core-shell nanowires; PPy, polypyrrole.*

large surface area of 2D-SS nanosheets are beneficial to the electrolyte penetration and the volume change during cycles. Therefore, 2D-SS nanosheet anodes showed remarkable rate capability and stable cycle performance in both SIBs and LIBs. When used in SIBs (**Supplementary Figure S1D**), the 2D-SS anode displayed a superior capacity of ~500 mA h $g^{-1}$ after 100 cycles at 200 mA $g^{-1}$ current rate.

Recently, $Sb_2S_3$ materials with three-dimensional (3D) hierarchical architecture were designed and synthesized to expand the contact surface area of the electrode and electrolyte and adapt it to volume expansion (Jin Pan et al., 2017; Xie et al., 2018; Xie F. et al., 2019). Xie et al. (2018) used $SbCl_3$ and $_L$-cysteine as raw materials and successfully synthesized $Sb_2S_3$ hollow microspheres by a hydrothermal method. The SEM image and cycling performance of $Sb_2S_3$ hollow microspheres are shown in **Supplementary Figures S1E,F**. However, large internal voids in hollow structures can greatly reduce bulk energy density. In order to obtain a high volumetric energy density and maintain a high gravimetric energy density, Xie F. et al. (2019) synthesized multi-shell hollow $Sb_2S_3$ structures using the metal-organic framework templates (MOFs) (**Supplementary Figure S1G**). Used as an anode in SIBs (**Supplementary Figure S1H**), the multi-shell $Sb_2S_3$ exhibited reversible capacities of 909, 806, 725, and 604 mA h $g^{-1}$ at various currents of 100, 400, 1,000, and 2,000 mA $g^{-1}$, respectively, higher than the single-shell $Sb_2S_3$ structure.

## $Sb_2S_3$/Carbon Composites

Carbon materials have received considerable attention because of their superior characteristics, such as large specific surface area, high conductivity, excellent flexibility, and chemical stability (Tao et al., 2021). During the use of SIBs, $Sb_2S_3$ will undergo transformation and alloying reaction, which results in excessive volume expansion/contraction of the material, and hinders the application of $Sb_2S_3$ energy storage effect. Therefore, $Sb_2S_3$ is usually combined with carbon materials to inhibit the volume change, such as $Sb_2S_3$/carbon-rods (Hongshuai Hou et al., 2015), $Sb_2S_3$/carbon-nanotubes (Li J. et al., 2017; Li et al., 2019), $Sb_2S_3$/carbon-nanofiber (Zhai et al., 2020; Zhang Q. et al., 2021), or $Sb_2S_3$/heteroatom-doped carbon (Dong et al., 2019; Jaramillo-Quintero et al., 2021).

For instance, Hongshuai Hou et al. (2015) designed one-dimensional (1D) $Sb_2S_3$@C rods as a distinctive anode material to improve the electrochemical performance of SIBs *via* a solvothermal method (**Supplementary Figure S2A**). The $Sb_2S_3$@C rod electrode could deliver 699.1 mA h $g^{-1}$ at a current rate of 100 mA $g^{-1}$ after 100 cycles (**Supplementary Figure S2B**). Liu et al. (2017) reported a hydrothermal method for preparing $Sb_2S_3$ micro-nanospheres loaded on carbon fiber cloth (CFC). The obtained composite materials were denoted as SS/CFC. The flexible carbon fiber cloth was completely covered by spherical $Sb_2S_3$ in **Supplementary Figure S2C**, which could greatly accommodate the volume change (Guo et al., 2019). When used as electrodes for SIBs (**Supplementary Figure S2D**), SS/CFC electrodes exhibited an excellent initial discharge capacity of 1,048 mA h $g^{-1}$ at 0.5 A $g^{-1}$, and displayed a reversible capacity of 736 mA h $g^{-1}$ after 650 cycles in the voltage range of 0.01–2.00 V. After two initial cycles, the corresponding Coulombic efficiency of SS/CFC rapidly increased to ~100%.

To boost the storage performance of SIBs, $Sb_2S_3$ can be combined with carbon doped with heteroatoms (e.g., N, S, P, and Sb), thus improving the conductivity, the storage regions, and the active sites (Choi et al., 2016; Dong et al., 2019; Zhai et al., 2020; Jaramillo-Quintero et al., 2021). For instance, Zhao et al. (2020) utilized the oxygen-function group of phenolic resin and

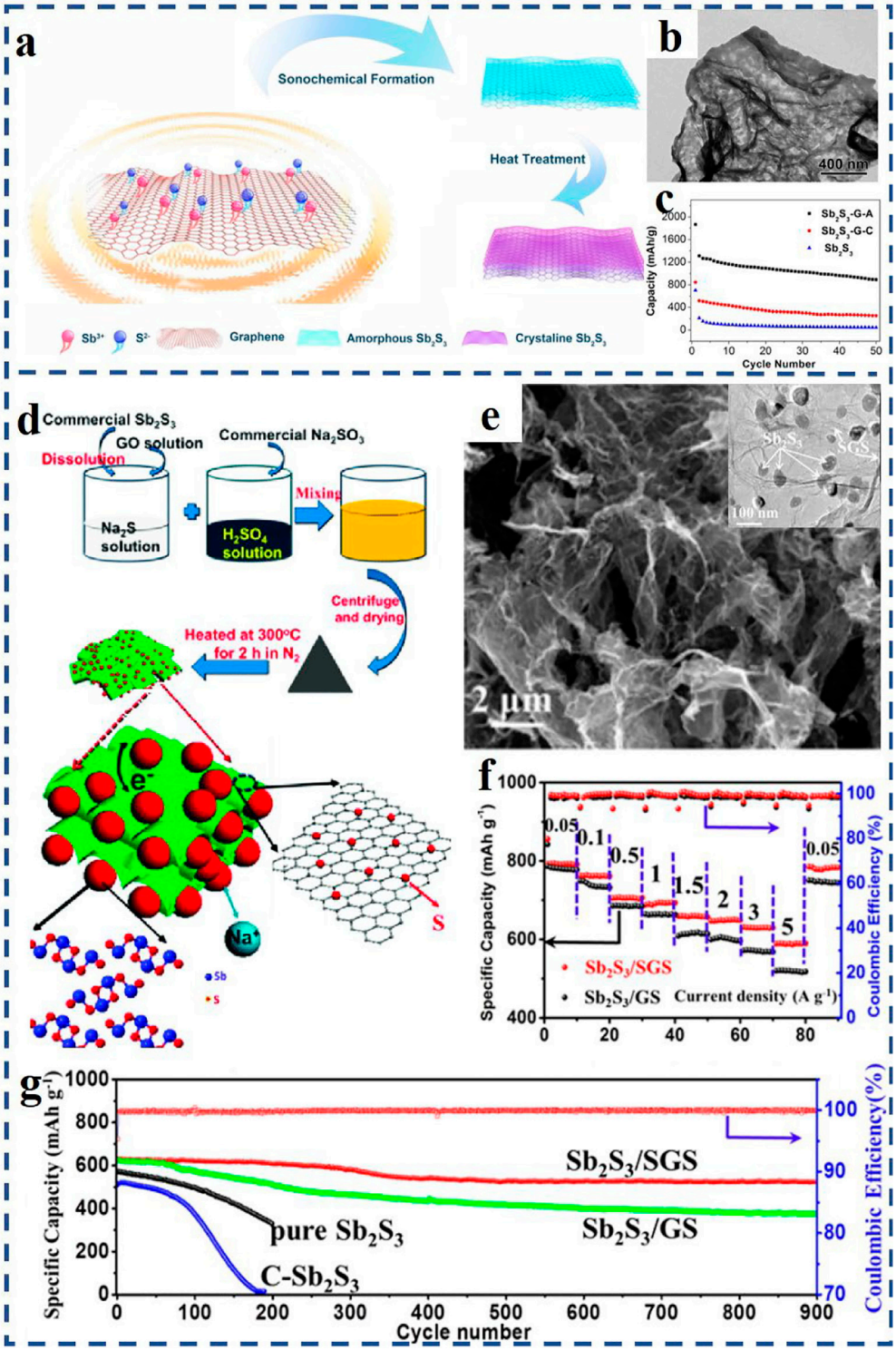


**FIGURE 2 | (A)** Schematic illustration of the preparation process of the amorphous and crystalline $Sb_2S_3$/graphene composites; **(B)** TEM image of the amorphous $Sb_2S_3$–graphene composites; **(C)** cycle performances of the pristine $Sb_2S_3$ and amorphous and crystalline $Sb_2S_3$–graphene electrodes (denoted as $Sb_2S_3$-G-A and $Sb_2S_3$-G-C); **(D)** formation process of the $Sb_2S_3$/S-doped graphene nanocomposite ($Sb_2S_3$/SGS); **(E)** SEM and TEM images of the $Sb_2S_3$/SGS nanocomposite; **(F)** rate performances of the $Sb_2S_3$/SGS electrode and $Sb_2S_3$–graphene electrode ($Sb_2S_3$/GS) under different current density; **(G)** cycle performances of three experimental electrodes at 2 A $g^{-1}$. **(A–C)** Reproduced with permission from Zhao et al. (2021). Copyright 2020, Elsevier. **(D–G)** Reproduced with permission from Xiong et al. (2016), Copyright 2016, American Chemical Society.

constructed $Sb_2S_3$ with hierarchical interfaces (antimony and sulfur-doped carbon) (**Supplementary Figure S2E**). The final obtained composites were denoted as SS/Sb@C. When evaluated as electrode materials for SIBs (**Supplementary Figure S2F**), SS/Sb@C delivered a reversible capacity of 474.6 mA h $g^{-1}$ and a capacity retention rate of 97.1% after 200 cycles at 0.1 A $g^{-1}$, showing better cyclic stability and superior rate capability than those of the $Sb_2S_3$ anodes without heteroatoms (38.6 mA h $g^{-1}$). This was due to the double control synergy of Sb-shell structure and S-doped carbon structure, which effectively expanded the polysulfide diffusion path, enhanced the reversibility of conversion reaction, and thus improved the Na-storage capacity of SIBs (Yu et al., 2020; Wang et al., 2021b). This kind of reasonable design was expected to bring bright prospects for the design of metal sulfides as advanced anodes of SIBs.

## $Sb_2S_3$/Graphene Composites

Graphene has high specific surface area, which is convenient for constructing interconnected pore structures to form conductive networks. In addition, it can also provide a platform for the growth of active materials (Lv et al., 2016; Sui et al., 2020; Wang X. et al., 2021; Liu et al., 2021). The combination of $Sb_2S_3$ with graphene can provide excellent $Na^+$ energy storage properties. Therefore, many composites have been designed in recent years, such as $Sb_2S_3$/RGO (RGO = reduced graphene oxide) (Yu et al., 2013; Wen et al., 2019), Sn@$Sb_2S_3$-RGO (tin assisted $Sb_2S_3$ decorated on RGO) (Deng et al., 2018), S-RGO/$Sb_2S_3$ (sulfur-doped RGO-based composite with $Sb_2S_3$) (Zhou X. et al., 2020), and $Sb_2S_3$/N-C/RGO ($Sb_2S_3$@nitrogen-doped carbon decorated on RGO) (Zhan et al., 2021), to improve the storage properties of SIBs.

For example, Yu et al. (2013) received a uniform coating of $Sb_2S_3$ on RGO (RGO/$Sb_2S_3$) through a solution-based synthesis method and applied it as SIB anode materials. The RGO/$Sb_2S_3$ composite with a small particle size of 15–30 nm allows $Na^+$ to move in and out of the particles rapidly during charge and discharge process. In addition, the 2D-layered structure of graphene and $Sb_2S_3$ can form oriented layered composites with excellent properties. Compared with traditional synthesis techniques, the ultrasound sonochemical method can create particular reaction conditions, and make it possible to prepare nanostructured materials with special properties by acoustic cavitation effects. Zhao et al. (2021) synthesized a special amorphous nanostructure composite material of $Sb_2S_3$/graphene by an ultrasound sonochemical synthesis technique (**Figure 2A**). As can be seen from **Figure 2B**, $Sb_2S_3$ nanoparticles were tightly covered on the graphene nanosheets and evenly distributed on both sides. The $Sb_2S_3$/graphene nanocomposites with amorphous structure had good tolerance and adaptability to drastic volume changes. Compared to the crystalline counterpart (Li C.-Y. et al., 2017), the amorphous $Sb_2S_3$/graphene nanocomposite displayed a superior electrochemical property with a higher reversible capacity of 881.2 mA h $g^{-1}$ at 0.1 A $g^{-1}$ after 50 cycles (**Figure 2C**).

Furthermore, doping heteroatoms (e.g., N, P, S, Sn) on graphene-based materials by surface chemical modification can effectively improve the properties of SIBs (Xiong et al., 2016; Deng et al., 2018; Zhou X. et al., 2020; Zhan et al., 2021). For example, Xiong et al. (2016) obtained a unique $Sb_2S_3$/S-doped graphene anode material (denoted as $Sb_2S_3$/SGS) *via* firm chemical binding of nano-$Sb_2S_3$ structure on S-doped graphene nanosheets (SGS). Schematic illustration of the preparation process of the $Sb_2S_3$/SGS composite is displayed in **Figure 2D**. As shown in **Figure 2E**, $Sb_2S_3$ nanoparticles are wrapped by flexible SGS and exhibit a size of 30–80 nm. When tested at 0.05 A $g^{-1}$ current rate, the $Sb_2S_3$/SGS anode reaches a high specific capacity of 792.8 mA h $g^{-1}$ after 90 cycles (see **Figure 2F**). After 900 cycles at a higher current rate of 2 A $g^{-1}$ (in **Figure 2G**), the $Sb_2S_3$/SGS anode still has an excellent cycle life, and the capacity retention rate is ~83%.

## $Sb_2S_3$/$M_xS_y$ Composites

Most metal sulfides ($M_xS_y$) have hierarchical structures, and $Na^+$ can easily move in the interlayers of metal sulfides without damaging their hierarchical structures (Tao et al., 2021). Thus, the use of binary metal sulfides to construct heterostructures to reduce the huge internal stress of alloy-based anodes and maintain the integrity of nanostructures has attracted extensive attention (Wang et al., 2018; Lin et al., 2021; Wang et al., 2019a). In this context, common metal sulfides ($M_xS_y$), including $SnS_2$ (Wang et al., 2018), ZnS (Dong et al., 2017), $FeS_2$ (Cao et al., 2020), $In_2S_3$ (Huang et al., 2018), and $Bi_2S_3$ (Li et al., 2021), have been combined with $Sb_2S_3$ as anode materials of SIBs.

For example, a composite of multiwalled carbon nanotubes (MCNTs) and $In_2S_3$-$Sb_2S_3$ particles (denoted as I-S@MCNTs) with a unique morphology of formicary microspheres was formed to solve the poor cycling stability and rate performance of SIBs (Huang et al., 2018). As shown in **Supplementary Figure S3A**, the hierarchical spheres are assembled by crumpled nanosheets (5–8 nm), which significantly shorten the diffusion path and accelerate the transport rate of $Na^+$. Similarly, Wang D. et al. (2021) designed an armored hydrangea-like $Sb_2S_3$/$MoS_2$ heterostructure composite (denoted as SMS@C) as a superior SIB anode material (**Supplementary Figure S3B**). After 650 cycles at a higher current density of 5 A $g^{-1}$, the SMS@C anode exhibited an enhanced cycling performance of 411.5 mA h $g^{-1}$ (**Supplementary Figure S3E**). Additionally, Dong et al. (2017) designed a polyhedron composite (~1.5 μm) with a ZnS inner-core structure and $Sb_2S_3$/C double-shell structure (ZnS-$Sb_2S_3$@C), capitalizing on full advantages of the zeolitic imidazolate framework (ZIF-8). The structure of ZnS-$Sb_2S_3$@C core-double shell composites had enough space to greatly adapt to the volume expansion during the repeated insertion/extraction of $Na^+$, and exhibited a superior reversible capacity of 630 mA h $g^{-1}$ at a current density of 0.1 A $g^{-1}$ after 120 cycles with a high Coulombic efficiency of ~100% (**Supplementary Figures S3C,F**).

Recently, a breakthrough about $Sb_2S_3$@$FeS_2$ hollow nanorods used as high-performance SIB electrode materials was reported. Cao et al. (2020) embedded $Sb_2S_3$@$FeS_2$ hollow nanorods (SFS) into a nitrogen-doped graphene matrix, and synthesized $Sb_2S_3$@$FeS_2$/N-doped graphene composite (denoted as SFS/C) *via* a simple two-step solvothermal synthesis technique

(**Supplementary Figures S3D,G**). The clever design of the heterostructure extremely accelerated the $Na^+$ transport, and greatly alleviated the volume expansion under long-period performance (1,000 cycles) (Wu et al., 2019a; Wu et al., 2019b; Liu et al., 2022). The SFS/C anode displayed a superior reversible capacity of 725.4 mA h $g^{-1}$ after 90 cycles at 0.1 A $g^{-1}$ (see **Supplementary Figure S3H**). When tested even at 5 A $g^{-1}$, the SFS/C anode had an excellent cycle performance with a capacity retention of ~85.7% after 1,000 cycles (**Supplementary Figure S3I**).

## Other Composites

In addition to the aforementioned $Sb_2S_3$-based nanomaterials, polypyrrole (PPy) (Wang et al., 2016; Zheng et al., 2018), MXene ($M_{n+1}X_nT_x$, where M is the early transition metal, X represents C/N, and $T_x$ is the surface functional group (-O, -OH or -F), n = 0,1,2,3,4. e.g., $Ti_3C_2T_x$, $Ti_3C_2$) (Wang et al., 2019b; Zhang H. et al., 2021; He et al., 2021), and metal oxides (e.g., $SnO_2$) (Chang et al., 2020a) can also be combined with $Sb_2S_3$ to fabricate better SIB anodes.

For instance, Shi et al. (Yin et al., 2019) prepared $Sb_2S_3$/meso@microporous carbon nanofibers@polypyrrole composites (denoted as $Sb_2S_3$/MMCN@PPy) though a novel multi-step method combining polymerization, sulfidation and solvothermal process (**Supplementary Figure S4A**). SEM image of $Sb_2S_3$/MMCN@PPy composites is shown in **Supplementary Figure S4B**. When investigated as SIB anode, $Sb_2S_3$/MMCN@PPy composite exhibited a discharge capacity of 535.3 mA h $g^{-1}$ at a current density of 100 mA $g^{-1}$, and the discharge specific capacity could recover to 446 mA h $g^{-1}$ after 50 cycles when returned to 100 mA $g^{-1}$ current rate (**Supplementary Figure S4C**). Shi et al. (2019) synthesized $Sb_2S_3$@PPy coaxial nanorods *via* a hydrothermal method. When tested at 100 mA $g^{-1}$, it showed a superior reversible capacity as high as 881 mA h $g^{-1}$ after 50 cycles, which was higher than those reported of MWNTs@$Sb_2S_3$@PPy composites (Wang et al., 2016), flower-like $Sb_2S_3$/PPy microspheres (Zheng et al., 2018), and $Sb_2S_3$/MMCN@PPy composites (Yin et al., 2019).

Furthermore, MXene is considered as an outstanding matrix because of the effective diffusion and mobility for $Na^+$ and excellent electronic conductivity. $Ti_3C_2T_x$ is one of the most studied MXene materials, and the theoretical capacity is 352 mA h $g^{-1}$ when used as the anode of SIBs (Zhang H. et al., 2021; He et al., 2021; Ren et al., 2021). For instance, Zhang H. et al. (2021); Ren et al. (2021) prepared $Sb_2S_3$@$Ti_3C_2T_x$ composite and $Sb_2S_3$@m-$Ti_3C_2T_x$ composite by a wet chemical method, in which $Sb_2S_3$ nanoparticles were *in situ* nucleated and grown uniformly on the surface of $Ti_3C_2T_x$ nanosheets. It was found that $Ti_3C_2T_x$, as a conductive skeleton, could effectively alleviate the volume expansion of $Sb_2S_3$ during charge/discharge progress. In 2021, inspired by the stomatal structure from natural leaves, He et al. (2021) successfully synthesized $Sb_2S_3$/nitrogen-doped $Ti_3C_2$ composites (denoted as L-$Sb_2S_3$/$Ti_3C_2$) *via* a solvothermal method (**Supplementary Figure S4D**). L-$Sb_2S_3$/$Ti_3C_2$ composite showed a unique elm leaf-like morphology in **Supplementary Figure S4E**, with a length of 60–80 nm and a width of 30–40 nm, respectively. When used as SIB anode, L-$Sb_2S_3$/$Ti_3C_2$ composite displayed a high capacity of 502.2 mA h $g^{-1}$ at a current rate of 100 mA $g^{-1}$ from 0.01 to 3 V (**Supplementary Figure S4F**).

# CONCLUSION AND OUTLOOK

In this review, we briefly summarize the applications of $Sb_2S_3$-based nanomaterials for high-performance SIBs, mainly including $Sb_2S_3$, $Sb_2S_3$/carbon composites, $Sb_2S_3$/graphene composites, $Sb_2S_3$/$M_xS_y$ composites, and other related composites. Although many significant works have been made in SIBs, there are still some problems that need to be solved, and we propose some possible directions for the anode research of SIBs in the future:

1) During the charge/discharge cycles, $Sb_2S_3$ nanoparticles are easy to accumulate because of their high surface activity energy. This results in a significant volume change and capacity declining. Therefore, it is necessary to design and fabricate more reasonable nanostructures, such as hierarchical hollow nanotubes or hierarchical spheres (Xie F. et al., 2019), to fully buffer the strain of volume change and further improve the cycling performance. In addition, some soft materials could be added to improve the flexibility, so as to avoid the collapse of the anode due to the volume expansion.

2) Carbonaceous materials are often the main choice to combine with $Sb_2S_3$ to build dense conductive physical barriers. However, the content of $Sb_2S_3$ and the corresponding specific capacity of composite materials are reduced. Therefore, the carbon content should be optimized so that the $Sb_2S_3$-based materials achieve better electrochemical performance. In addition, $Sb_2S_3$/carbonaceous composites fabricated by traditional synthesis techniques suffer from the poor mechanical adhesion and high interface resistance between $Sb_2S_3$ and carbonaceous materials. It is highly desirable to optimize the preparation methods and explore more carbonaceous materials (e.g., biochar, amorphous carbon) to establish compact conductive physical barriers to further enhance the electrochemical performance of $Sb_2S_3$-based materials.

3) Until now, the cycle lives of many $Sb_2S_3$-based materials have been tested at room temperature. In order to satisfy the demands of different applications, it is very urgent to explore $Sb_2S_3$-based anode materials that can cycle under either higher temperature (up to 60 °C) or lower (−20°C).

4) The mechanism of $Na^+$ storage in $Sb_2S_3$-based nanomaterials and the phase changes during repeated charging/discharging still need to be explored. Operating technologies, such as *in situ* X-ray technology, *in situ* scanning probe microscopy, technologies based on synchronized X-rays, as well as *in situ* electron microscopy, are very helpful in acquiring time-related information and studying the mechanism of $Na^+$ storage of $Sb_2S_3$-based nanomaterials. Therefore, more research using operating technology is needed to deeply understand $Sb_2S_3$-based electrode nanomaterials used in SIBs.

## AUTHOR CONTRIBUTIONS

YL and GW conceived the idea. MG and GW wrote the draft. All authors contributed to the writing, discussion, and revision of the final version of the article.

## FUNDING

This work was financially supported by the Chinese 02 Special Fund (Grant No.2017ZX02408003) and the Chinese 1000 Plan for High Level Foreign Experts (Grant No. WQ20154100278).

## SUPPLEMENTARY MATERIAL

The Supplementary Material for this article can be found online at: https://www.frontiersin.org/articles/10.3389/fchem.2022.870564/full#supplementary-material

**Supplementary Figure S1 | (A)** SEM image of α-$Sb_2S_3$ nanoparticles; **(B)** cycle performance of α-$Sb_2S_3$ at 0.05 A $g^{-1}$; **(C)** SEM image of the few-layer 2D-$Sb_2S_3$ nanosheets; **(D)** cyclic capacity of 2D-SS measured at 0.2 A $g^{-1}$; **(E)** SEM image of $Sb_2S_3$ hollow microspheres; **(F)** cycling performances of three experimental $Sb_2S_3$ electrodes at 1A $g^{-1}$; (g) SEM and TEM images of multi-shell $Sb_2S_3$; **(H)** comparison of the rate performance of multi-shell $Sb_2S_3$, single-shell $Sb_2S_3$, and pristine $Sb_2S_3$. **(A,B)** Adapted with permission from Hwang et al. (2016). Copyright 2013, The Royal Society of Chemistry. **(C,D)** Adapted with permission from Yao et al. (2019). Copyright 2018, Elsevier. **(E,F)** Adapted with permission from Xie et al. (2018). Copyright 2018, Springer. **(G,H)** Adapted with permission from Xie et al. (2019a). Copyright 2019, Elsevier.

**Supplementary Figure S2 | (A)** SEM image of $Sb_2S_3$@C rods; **(B)** cycle performance of $Sb_2S_3$@C rods at 0.1 A $g^{-1}$; **(C)** SEM image of SS/CFC; **(D)** cycle performances of SS/CFC and SS powder at 0.5 A $g^{-1}$; **(E)** SEM image of SS/Sb@C nanocomposites; **(F)** cycling performances of SS/Sb@C and $Sb_2S_3$ nanocomposites at 0.1 A $g^{-1}$. **(A,B)** Adapted with permission from Hongshuai Hou et al. (2015). Copyright 2015, American Chemical Society. **(C,D)** Adapted with permission from Liu et al. (2017). Copyright 2017, The Royal Society of Chemistry. **(E,F)** Adapted with permission from Zhao et al. (2020). Copyright 2020, The Royal Society of Chemistry.

**Supplementary Figure S3 |** SEM images: **(A)** $In_2S_3$-$Sb_2S_3$@MCNTs microsphere, **(B)** $Sb_2S_3$/$MoS_2$@C composite (SMS@C), **(C)** ZnS-$Sb_2S_3$@C polyhedron, and **(D)** $Sb_2S_3$@$FeS_2$/N-graphene composite (SFS/C); **(E)** sodium storage properties of the SMS@C and SMS heterostructure at 5 A $g^{-1}$; **(F)** rate capability of ZnS-$Sb_2S_3$@C core-shell SIB anode; **(G)** schematic illustration of the fabrication process of the SFS/C composite; (h) charge capability of the SFS/C anode at various rates; **(I)** cycle performances of $Sb_2S_3$, SFS, and SFS/C composites at a high rate of 5 A $g^{-1}$. **(A)** Adapted with permission from Huang et al. (2018). Copyright 2018, Wiley-VCH. **(B, E)** Adapted with permission from Wang et al. (2021a). Copyright 2021, Elsevier. **(c,f)** Adapted with permission from Dong et al. (2017). Copyright 2017, American Chemical Society. **(D,G–I)** Adapted with permission from Cao et al. (2020). Copyright 2020, American Chemical Society.

**Supplementary Figure S4 | (A)** Schematic diagram of the formation process of the $Sb_2S_3$/MMCN@PPy composite; **(B)** SEM image of $Sb_2S_3$/MMCN@PPy composite; **(C)** rate capability performances of pure $Sb_2S_3$ and $Sb_2S_3$/MMCN@PPy composite; **(D)** schematic illustration of the synthetic process of L-$Sb_2S_3$/$Ti_3C_2$ composite; **(E)** SEM image of L-$Sb_2S_3$/$Ti_3C_2$ composite; **(F)** Rate capability performances of $Sb_2S_3$, $Sb_2S_3$/$Ti_3C_2$, and L-$Sb_2S_3$/$Ti_3C_2$. **(A–C)** Adapted with permission from Yin et al. (2019). Copyright 2019, Elsevier. **(D–F)** Adapted with permission from He et al. (2021). Copyright 2021, Science China Press and Springer-Verlag GmbH Germany, part of Springer Nature.

## REFERENCES


Bag, S., Roy, A., and Mitra, S. (2019). Sulfur, Nitrogen Dual Doped Reduced Graphene Oxide Supported Two-Dimensional Sb 2 S 3 Nanostructures for the Anode Material of Sodium-Ion Battery. *ChemistrySelect* 4 (22), 6679–6686. doi:10.1002/slct.201901153

Cao, L., Gao, X., Zhang, B., Ou, X., Zhang, J., and Luo, W.-B. (2020). Bimetallic Sulfide Sb2S3@FeS2 Hollow Nanorods as High-Performance Anode Materials for Sodium-Ion Batteries. *ACS Nano* 14 (3), 3610–3620. doi:10.1021/acsnano.0c00020

Chang, G., Yin, X., Shi, S., Zhao, Y., and Zhang, J. (2020a). Sb2S3@SnO2 Hetero-Nanocomposite as High-Performance Anode Material for Sodium-Ion Battery. *Int. J. Green Energ.* 17 (15), 1044–1050. doi:10.1080/15435075.2020.1821692

Chang, G., Yin, X., Shi, S., Zhao, Y., and Zhang, J. (2020b). Sb2S3@YP Nanostructured Anode Material Synthesized by a Novel Vaporization-Condensation Method for Long Cycle-Life Sodium-Ion Battery. *J. Electrochem. Soc.* 167 (14), 140531. doi:10.1149/1945-7111/abc658

Choi, J.-H., Ha, C.-W., Choi, H.-Y., Shin, H.-C., and Lee, S.-M. (2017). High Performance Sb2S3/carbon Composite with Tailored Artificial Interface as an Anode Material for Sodium Ion Batteries. *Met. Mater. Int.* 23 (6), 1241–1249. doi:10.1007/s12540-017-7105-y

Choi, J.-H., Ha, C.-W., Choi, H.-Y., Shin, H.-C., Park, C.-M., Jo, Y.-N., et al. (2016). Sb2S3 Embedded in Amorphous P/C Composite Matrix as High-Performance Anode Material for Sodium Ion Batteries. *Electrochimica Acta* 210, 588–595. doi:10.1016/j.electacta.2016.05.190

Chong, W. G., Xiao, Y., Huang, J.-Q., Yao, S., Cui, J., Qin, L., et al. (2018). Highly Conductive Porous Graphene/sulfur Composite Ribbon Electrodes for Flexible Lithium-Sulfur Batteries. *Nanoscale* 10 (45), 21132–21141. doi:10.1039/c8nr06666c

Cui, J., Yao, S., Lu, Z., Huang, J.-Q., Chong, W. G., Ciucci, F., et al. (2018). Revealing Pseudocapacitive Mechanisms of Metal Dichalcogenide SnS2 / Graphene-CNT Aerogels for High-Energy Na Hybrid Capacitors. *Adv. Energ. Mater.* 8 (10), 1702488. doi:10.1002/aenm.201702488

Dashairya, L., Das, D., and Saha, P. (2021). Elucidating the Role of Graphene and Porous Carbon Coating on Nanostructured Sb2S3 for superior Lithium and Sodium Storage. *J. Alloys Comp.* 883, 160906–160913. doi:10.1016/j.jallcom.2021.160906

Dashairya, L., and Saha, P. (2020). Antimony Sulphide Nanorods Decorated onto Reduced Graphene Oxide Based Anodes for Sodium-Ion Battery. *Mater. Today Proc.* 21, 1899–1904. doi:10.1016/j.matpr.2020.01.247

Deng, M., Li, S., Hong, W., Jiang, Y., Xu, W., Shuai, H., et al. (2019). Natural Stibnite Ore (Sb2S3) Embedded in Sulfur-Doped Carbon Sheets: Enhanced Electrochemical Properties as Anode for Sodium Ions Storage. *RSC Adv.* 9 (27), 15210–15216. doi:10.1039/c9ra02301a

Deng, P., Yang, J., He, W., Li, S., Zhou, W., Tang, D., et al. (2018). Tin-Assisted Sb2S3Nanoparticles Uniformly Grafted on Graphene Effectively Improves Sodium-Ion Storage Performance. *ChemElectroChem* 5 (5), 811–816. doi:10.1002/celc.201800016

Dong, S., Li, C., Ge, X., Li, Z., and Yin, X. L. (2017). ZnS-Sb2S3@C Core-Double Shell Polyhedron Structure Derived from Metal-Organic Framework as Anodes for High Performance Sodium Ion Batteries. *Acs Nano* 11 (6), 6474–6482. doi:10.1021/acsnano.7b03321

Dong, Y., Hu, M., Zhang, Z., Zapien, J. A., Wang, X., Lee, J.-M., et al. (2019). Nitrogen-Doped Carbon-Encapsulated Antimony Sulfide Nanowires Enable High Rate Capability and Cyclic Stability for Sodium-Ion Batteries. *ACS Appl. Nano Mater.* 2 (3), 1457–1465. doi:10.1021/acsanm.8b02335

Fan, T.-E., and Xie, H.-F. (2019). Sb2S3-rGO for High-Performance Sodium-Ion Battery Anodes on Al and Cu Foil Current Collector. *J. Alloys Comp.* 775, 549–553. doi:10.1016/j.jallcom.2018.10.103

Fang, L., Lan, Z., Guan, W., Zhou, P., Bahlawane, N., Sun, W., et al. (2019). Hetero-interface Constructs Ion Reservoir to Enhance Conversion Reaction Kinetics for Sodium/lithium Storage. *Energ. Storage Mater.* 18, 107–113. doi:10.1016/j.ensm.2018.10.002

Fu, L., Shang, C., Li, G., Hu, L., Zhang, X., Huang, L., et al. (2019). Lithium Pre-cycling Induced Fast Kinetics of Commercial Sb 2 S 3 Anode for Advanced Sodium Storage. *Energy Environ. Mater.* 2 (3), 209–215. doi:10.1002/eem2.12037

Ge, P., Hou, H., Ji, X., Huang, Z., Li, S., and Huang, L. (2018). Enhanced Stability of Sodium Storage Exhibited by Carbon Coated Sb2S3 Hollow Spheres. *Mater. Chem. Phys.* 203, 185–192. doi:10.1016/j.matchemphys.2017.10.003

Ge, P., Zhang, L., Zhao, W., Yang, Y., Sun, W., and Ji, X. (2020). Interfacial Bonding of Metal-Sulfides with Double Carbon for Improving Reversibility of Advanced Alkali-Ion Batteries. *Adv. Funct. Mater.* 30 (16), 1910599. doi:10.1002/adfm.201910599

Guo, D., Yang, M., Li, Y., Xue, Y., Liu, G., Wu, N., et al. (2020). Hydrogel-derived VPO4/porous Carbon Framework for Enhanced Lithium and Sodium Storage. *Nanoscale* 12 (6), 3812–3819. doi:10.1039/d0nr00460j

Guo, D., Yang, M., Zhang, L., Li, Y., Wang, J., Liu, G., et al. (2019). Cr2O3 Nanosheet/carbon Cloth Anode with strong Interaction and Fast Charge Transfer for Pseudocapacitive Energy Storage in Lithium-Ion Batteries. *RSC Adv.* 9 (57), 33446–33453. doi:10.1039/c9ra07465a

Hao, X., Zhao, Q., Su, S., Zhang, S., Ma, J., Shen, L., et al. (2019). Constructing Multifunctional Interphase between Li 1.4 Al 0.4 Ti 1.6 (PO 4 ) 3 and Li Metal by Magnetron Sputtering for Highly Stable Solid-State Lithium Metal Batteries. *Adv. Energ. Mater.* 9 (34), 1901604. doi:10.1002/aenm.201901604

He, F., Tang, C., Zhu, G., Liu, Y., Du, A., Zhang, Q., et al. (2021). Leaf-inspired Design of Mesoporous Sb2S3/N-Doped Ti3C2Tx Composite towards Fast Sodium Storage. *Sci. China Chem.* 64 (6), 964–973. doi:10.1007/s11426-020-9942-9

Hou, H., Jing, M., Huang, Z., Yang, Y., Zhang, Y., Chen, J., et al. (2015). One-Dimensional Rod-like Sb2S3-Based Anode for High-Performance Sodium-Ion Batteries. *ACS Appl. Mater. Inter.* 7 (34), 19362–19369. doi:10.1021/acsami.5b05509

Huang, Y., Wang, Z., Jiang, Y., Li, S., Wang, M., Ye, Y., et al. (2018). Conductivity and Pseudocapacitance Optimization of Bimetallic Antimony-Indium Sulfide Anodes for Sodium-Ion Batteries with Favorable Kinetics. *Adv. Sci.* 5 (10), 1800613. doi:10.1002/advs.201800613

Hwang, S. M., Kim, J., Kim, Y., and Kim, Y. (2016). Na-ion Storage Performance of Amorphous Sb2S3nanoparticles: Anode for Na-Ion Batteries and Seawater Flow Batteries. *J. Mater. Chem. A.* 4 (46), 17946–17951. doi:10.1039/c6ta07838a

Jaramillo-Quintero, O. A., Barrera-Peralta, R. V., El Hachimi, A. G., Guillén-López, A., Pérez, O., Reguera, E., et al. (2021). Understanding the Interaction between Heteroatom-Doped Carbon Matrix and Sb2S3 for Efficient Sodium-Ion Battery Anodes. *J. Colloid Interf. Sci.* 585, 649–659. doi:10.1016/j.jcis.2020.10.044

Jiang, Q., Zhang, W.-q., Zhao, J.-c., Rao, P.-h., and Mao, J.-f. (2021). Superior Sodium and Lithium Storage in Strongly Coupled Amorphous Sb2S3 Spheres and Carbon Nanotubes. *Int. J. Miner Metall. Mater.* 28 (7), 1194–1203. doi:10.1007/s12613-021-2259-5

Jin Pan, Z.-L. Z., Deng, J.-Q., Wang, J., Fang, C.-C., and Yao, Q.-R. (2017). Template-free Synthesis of Sb2S3 Micro Tubes as the Anode Materials for Sodium-Ion Batteries. *ADVANCED MATERIALS ENERGY SUSTAINABILITY*, 81–89. doi:10.1142/9789813220393_0010

Kravchyk, K. V., Kovalenko, M. V., and Bodnarchuk, M. I. (2020). Colloidal Antimony Sulfide Nanoparticles as a High-Performance Anode Material for Li-Ion and Na-Ion Batteries. *Sci. Rep.* 10 (1), 2554–2561. doi:10.1038/s41598-020-59512-3

Li, C.-Y., Patra, J., Yang, C.-H., Tseng, C.-M., Majumder, S. B., Dong, Q.-F., et al. (2017a). Electrolyte Optimization for Enhancing Electrochemical Performance of Antimony Sulfide/Graphene Anodes for Sodium-Ion Batteries-Carbonate-Based and Ionic Liquid Electrolytes. *ACS Sust. Chem. Eng.* 5 (9), 8269–8276. doi:10.1021/acssuschemeng.7b01939

Li, J., Yan, D., Zhang, X., Hou, S., Li, D., Lu, T., et al. (2017b). *In Situ* growth of Sb2S3 on Multiwalled Carbon Nanotubes as High-Performance Anode Materials for Sodium-Ion Batteries. *Electrochimica Acta* 228, 436–446. doi:10.1016/j.electacta.2017.01.114

Li, K., Liu, X., Qin, Y., Zhao, Z., Xu, Y., Yi, Y., et al. (2021). Sb2S3-Bi2S3 Microrods with the Combined Action of Carbon Encapsulation and rGO Confinement for Improving High Cycle Stability in Sodium/potassium Storage. *Chem. Eng. J.* 414, 128787–128795. doi:10.1016/j.cej.2021.128787

Li, M., Huang, F., Pan, J., Li, L., Zhang, Y., Yao, Q., et al. (2019). Amorphous Sb2S3 Nanospheres *In-Situ* Grown on Carbon Nanotubes: Anodes for NIBs and KIBs. *Nanomaterials* 9 (9), 1323. doi:10.3390/nano9091323

Li, P., Jeong, J. Y., Jin, B., Zhang, K., and Park, J. H. (2020). Large and Reversible Sodium Storage through Interlaced Reaction Design. *Energ. Storage Mater.* 25, 687–694. doi:10.1016/j.ensm.2019.09.018

Li, P., Wang, P., Zheng, X., Yu, H., Qian, S., Shui, M., et al. (2015). Enhanced Sodium Storage Property of Copper Nitrate Hydrate by Carbon Nanotube. *J. Electroanalytical Chem.* 755, 92–99. doi:10.1016/j.jelechem.2015.07.043

Li, Y. X., Zhai, X. L., Liu, Y., Wei, H. J., Ma, J. Q., Chen, M., et al. (2020). WO3-Based Materials as Electrocatalysts for Hydrogen Evolution Reaction. *Frontiers in Materials* 7, 105. doi:10.3389/fmats.2020.00105

Lin, J., Yao, L., Zhang, C., Ding, H., Yuanhui, W., Li, S., et al. (2021). Construction of Sb2S3@SnS@C Tubular Heterostructures as High-Performance Anode Materials for Sodium-Ion Batteries. *ACS Sust. Chem. Eng.* 9 (33), 11280–11289. doi:10.1021/acssuschemeng.1c04497

Liu, G., Cui, J., Luo, R., Liu, Y., Huang, X., Wu, N., et al. (2019a). 2D MoS2 Grown on Biomass-Based Hollow Carbon Fibers for Energy Storage. *Appl. Surf. Sci.* 469, 854–863. doi:10.1016/j.apsusc.2018.11.067

Liu, G., Li, M., Wu, N., Cui, L., Huang, X., Liu, X., et al. (2018a). Single-Crystalline Particles: An Effective Way to Ameliorate the Intragranular Cracking, Thermal Stability, and Capacity Fading of the LiNi0.6Co0.2Mn0.2O2 Electrodes. *J. Electrochem. Soc.* 165 (13), A3040–A3047. doi:10.1149/2.0491813jes

Liu, G., Xu, L., Li, Y., Guo, D., Wu, N., Yuan, C., et al. (2022). Metal-organic Frameworks Derived Anatase/rutile Heterostructures with Enhanced Reaction Kinetics for Lithium and Sodium Storage. *Chem. Eng. J.* 430, 132689. doi:10.1016/j.cej.2021.132689

Liu, Q., Wang, H., Jiang, C., and Tang, Y. (2019b). Multi-ion Strategies towards Emerging Rechargeable Batteries with High Performance. *Energ. Storage Mater.* 23, 566–586. doi:10.1016/j.ensm.2019.03.028

Liu, S., Cai, Z., Zhou, J., Zhu, M., Pan, A., and Liang, S. (2017). High-performance Sodium-Ion Batteries and Flexible Sodium-Ion Capacitors Based on Sb2X3(X = O, S)/carbon Fiber Cloth. *J. Mater. Chem. A.* 5 (19), 9169–9176. doi:10.1039/c7ta01895a

Liu, X., Du, Y., Xu, X., Zhou, X., Dai, Z., and Bao, J. (2016). Enhancing the Anode Performance of Antimony through Nitrogen-Doped Carbon and Carbon Nanotubes. *J. Phys. Chem. C* 120 (6), 3214–3220. doi:10.1021/acs.jpcc.5b11926

Liu, Y., Wang, Y., Wang, F., Lei, Z., Zhang, W., Pan, K., et al. (2019c). Facile Synthesis of Antimony Tungstate Nanosheets as Anodes for Lithium-Ion Batteries. *Nanomaterials* 9 (12), 1689. doi:10.3390/nano9121689

Liu, Y., Wei, H., Zhai, X., Wang, F., Ren, X., Xiong, Y., et al. (2021). Graphene-based Interlayer for High-Performance Lithium-Sulfur Batteries: A Review. *Mater. Des.* 211, 110171. doi:10.1016/j.matdes.2021.110171

Liu, Z., Song, T., and Paik, U. (2018b). Sb-based Electrode Materials for Rechargeable Batteries. *J. Mater. Chem. A.* 6 (18), 8159–8193. doi:10.1039/c8ta01782d

Lv, W., Li, Z., Deng, Y., Yang, Q.-H., and Kang, F. (2016). Graphene-based Materials for Electrochemical Energy Storage Devices: Opportunities and Challenges. *Energ. Storage Mater.* 2, 107–138. doi:10.1016/j.ensm.2015.10.002

Ma, J., Wei, H., Liu, Y., Ren, X., Li, Y., Wang, F., et al. (2020). Application of Co3O4-Based Materials in Electrocatalytic Hydrogen Evolution Reaction: A Review. *Int. J. Hydrogen Energ.* 45 (41), 21205–21220. doi:10.1016/j.ijhydene.2020.05.280

Mullaivananathan, V., and Kalaiselvi, N. (2019). Sb2S3 Added Bio-Carbon: Demonstration of Potential Anode in Lithium and Sodium-Ion Batteries. *Carbon* 144, 772–780. doi:10.1016/j.carbon.2019.01.001

Pan, J., Zuo, Z., Deng, J., Yao, Q., Wang, Z., and Zhou, H. (2018a). Sb 2 S 3 Single crystal Nanowires with Comparable Electrochemical Properties as an Anode for Sodium Ion Batteries. *Surf. Inter.* 10, 170–175. doi:10.1016/j.surfin.2017.10.010

Pan, Z.-Z., Yan, Y., Cui, N., Xie, J.-C., Zhang, Y.-B., Mu, W.-S., et al. (2018b). Ionic Liquid-Assisted Preparation of Sb2S3/Reduced Graphene Oxide Nanocomposite for Sodium-Ion Batteries. *Adv. Mater. Inter.* 5 (5), 1701481. doi:10.1002/admi.201701481

Pang, P., Wang, Z., Tan, X., Deng, Y., Nan, J., Xing, Z., et al. (2019). LiCoO2@LiNi0.45Al0.05Mn0.5O2 as High-Voltage Lithium-Ion Battery Cathode Materials with Improved Cycling Performance and thermal Stability. *Electrochimica Acta* 327, 135018–135026. doi:10.1016/j.electacta.2019.135018

Qin, L., Zhai, D., Lv, W., Yang, W., Huang, J., Yao, S., et al. (2017). A High-Performance Lithium Ion Oxygen Battery Consisting of Li2O2 Cathode and Lithiated Aluminum Anode with Nafion Membrane for Reduced O2 Crossover. *Nano Energy* 40, 258–263. doi:10.1016/j.nanoen.2017.08.029

Ren, M., Cao, D., Jiang, W., Su, K., Pan, L., Jiang, Y., et al. (2021). Hierarchical Composite of Sb2S3 Decorated on Highly Crumpled Ti3C2Tx Nanosheets for

Enhanced Sodium Storage Properties. *Electrochimica Acta* 373, 137835–137844. doi:10.1016/j.electacta.2021.137835

Schmuch, R., Wagner, R., Hörpel, G., Placke, T., and Winter, M. (2018). Performance and Cost of Materials for Lithium-Based Rechargeable Automotive Batteries. *Nat. Energ.* 3 (4), 267–278. doi:10.1038/s41560-018-0107-2

Shan, Y., Li, Y., and Pang, H. (2020). Applications of Tin Sulfide-Based Materials in Lithium-Ion Batteries and Sodium-Ion Batteries. *Adv. Funct. Mater.* 30 (23), 2001298. doi:10.1002/adfm.202001298

Shi, F., Chen, C., and Xu, Z.-L. (2021). Recent Advances on Electrospun Nanofiber Materials for Post-lithium Ion Batteries. *Adv. Fiber Mater.* 3 (5), 275–301. doi:10.1007/s42765-021-00070-2

Shi, Y., Li, F., Zhang, Y., He, L., Ai, Q., and Luo, W. (2019). Sb2S3@PPy Coaxial Nanorods: A Versatile and Robust Host Material for Reversible Storage of Alkali Metal Ions. *Nanomaterials* 9 (4), 560–571. doi:10.3390/nano9040560

Sui, D., Chang, M., Peng, Z., Li, C., He, X., Yang, Y., et al. (2021a). Graphene-Based Cathode Materials for Lithium-Ion Capacitors: A Review. *Nanomaterials* 11 (10), 2771. doi:10.3390/nano11102771

Sui, D., Xu, L., Zhang, H., Sun, Z., Kan, B., Ma, Y., et al. (2020). A 3D Cross-Linked Graphene-Based Honeycomb Carbon Composite with Excellent Confinement Effect of Organic Cathode Material for Lithium-Ion Batteries. *Carbon* 157, 656–662. doi:10.1016/j.carbon.2019.10.106

Sui, Y., Zhou, J., Wang, X., Wu, L., Zhong, S., and Li, Y. (2021b). Recent Advances in Black-Phosphorus-Based Materials for Electrochemical Energy Storage. *Mater. Today* 42, 117–136. doi:10.1016/j.mattod.2020.09.005

Tao, F., Liu, Y., Ren, X., Jiang, A., Wei, H., Zhai, X., et al. (2021). Carbon Nanotube-Based Nanomaterials for High-Performance Sodium-Ion Batteries: Recent Advances and Perspectives. *J. Alloys Comp.* 873, 159742. doi:10.1016/j.jallcom.2021.159742

Tao, F., Liu, Y., Ren, X., Wang, J., Zhou, Y., Miao, Y., et al. (2022). Different Surface Modification Methods and Coating Materials of Zinc Metal Anode. *J. Energ. Chem.* 66, 397–412. doi:10.1016/j.jechem.2021.08.022

Wang, D., Cao, L., Luo, D., Gao, R., Li, H., Wang, D., et al. (2021a). Chain Mail Heterostructured Hydrangea-like Binary Metal Sulfides for High Efficiency Sodium Ion Battery. *Nano Energy* 87, 106185. doi:10.1016/j.nanoen.2021.106185

Wang, F., Feng, T., Jin, X., Zhou, Y., Xu, Y., Gao, Y., et al. (2021b). Atomic Co/Ni Active Sites Assisted MOF-Derived Rich Nitrogen-Doped Carbon Hollow Nanocages for Enhanced Lithium Storage. *Chem. Eng. J.* 420, 127583. doi:10.1016/j.cej.2020.127583

Wang, F., Liu, Y., Wei, H.-J., Li, T.-F., Xiong, X.-H., Wei, S.-Z., et al. (2021c). Recent Advances and Perspective in Metal Coordination Materials-Based Electrode Materials for Potassium-Ion Batteries. *Rare Met.* 40 (2), 448–470. doi:10.1007/s12598-020-01649-1

Wang, F., Liu, Y., Zhao, Y., Wang, Y., Wang, Z., Zhang, W., et al. (2017). Facile Synthesis of Two-Dimensional Porous MgCo2O4 Nanosheets as Anode for Lithium-Ion Batteries. *Appl. Sci.* 8 (1), 22. doi:10.3390/app8010022

Wang, G., Chen, C., Chen, Y., Kang, X., Yang, C., Wang, F., et al. (2020). Self-Stabilized and Strongly Adhesive Supramolecular Polymer Protective Layer Enables Ultrahigh-Rate and Large-Capacity Lithium-Metal Anode. *Angew. Chem. Int. Ed.* 59 (5), 2055–2060. doi:10.1002/anie.201913351

Wang, S., Liu, S., Li, X., Li, C., Zang, R., Man, Z., et al. (2018). SnS 2 /Sb 2 S 3 Heterostructures Anchored on Reduced Graphene Oxide Nanosheets with Superior Rate Capability for Sodium-Ion Batteries. *Chem. Eur. J.* 24 (15), 3873–3881. doi:10.1002/chem.201705855

Wang, S., Yuan, S., Yin, Y.-B., Zhu, Y.-H., Zhang, X.-B., and Yan, J.-M. (2016). Green and Facile Fabrication of MWNTs@Sb2S3@PPy Coaxial Nanocables for High-Performance Na-Ion Batteries. *Part. Part. Syst. Charact.* 33 (8), 493–499. doi:10.1002/ppsc.201500227

Wang, P. Y., Pu, Z. H., Li, W. Q., Zhu, J. W., Zhang, C. T., and Zhao, Y. F. (2019a). Coupling NiSe2-Ni2P Heterostructure Nanowrinkles for Highly Efficient Overall Water Splitting. *Journal of Catalysis* 377, 600–608. doi:10.1016/j.jcat.2019.08.005

Wang, X., Huang, R.-q., Niu, S.-z., Xu, L., Zhang, Q.-c., Amini, A., et al. (2021d). Research Progress on Graphene-Based Materials for High-Performance Lithium-Metal Batteries. *New Carbon Mater.* 36 (4), 711–728. doi:10.1016/s1872-5805(21)60081-1

Wang, X., Yang, C., Xiong, X., Chen, G., Huang, M., Wang, J.-H., et al. (2019b). A Robust Sulfur Host with Dual Lithium Polysulfide Immobilization Mechanism for Long Cycle Life and High Capacity Li-S Batteries. *Energ. Storage Mater.* 16, 344–353. doi:10.1016/j.ensm.2018.06.015

Wen, S., Zhao, J., Zhao, Y., Xu, T., and Xu, J. (2019). Reduced Graphene Oxide (RGO) Decorated Sb2S3 Nanorods as Anode Material for Sodium-Ion Batteries. *Chem. Phys. Lett.* 716, 171–176. doi:10.1016/j.cplett.2018.12.031

Wu, F., Guo, X., Li, M., and Xu, H. (2017). One-step Hydrothermal Synthesis of Sb 2 S 3 /reduced Graphene Oxide Nanocomposites for High-Performance Sodium Ion Batteries Anode Materials. *Ceramics Int.* 43 (8), 6019–6023. doi:10.1016/j.ceramint.2017.01.141

Wu, N., Qiao, X., Shen, J., Liu, G., Sun, T., Wu, H., et al. (2019a). Anatase Inverse Opal TiO2-x@N-Doped C Induced the Dominant Pseudocapacitive Effect for Durable and Fast Lithium/sodium Storage. *Electrochimica Acta* 299, 540–548. doi:10.1016/j.electacta.2019.01.040

Wu, N., Shen, J., Sun, L., Yuan, M., Shao, Y., Ma, J., et al. (2019b). Hierarchical N-Doped Graphene Coated 1D Cobalt Oxide Microrods for Robust and Fast Lithium Storage at Elevated Temperature. *Electrochimica Acta* 310, 70–77. doi:10.1016/j.electacta.2019.04.115

Xie, F., Zhang, L., Gu, Q., Chao, D., Jaroniec, M., and Qiao, S.-Z. (2019a). Multi-shell Hollow Structured Sb2S3 for Sodium-Ion Batteries with Enhanced Energy Density. *Nano Energy* 60, 591–599. doi:10.1016/j.nanoen.2019.04.008

Xie, J., Liu, L., Xia, J., Zhang, Y., Li, M., Ouyang, Y., et al. (2018). Template-Free Synthesis of Sb2S3 Hollow Microspheres as Anode Materials for Lithium-Ion and Sodium-Ion Batteries. *Nano-micro Lett.* 10 (1), 1–12. doi:10.1007/s40820-017-0165-1

Xie, J., Xia, J., Yuan, Y., Liu, L., Zhang, Y., Nie, S., et al. (2019b). Sb2S3 Embedded in Carbon-Silicon Oxide Nanofibers as High-Performance Anode Materials for Lithium-Ion and Sodium-Ion Batteries. *J. Power Sourc.* 435, 226762. doi:10.1016/j.jpowsour.2019.226762

Xing, Z., Tan, G., Yuan, Y., Wang, B., Ma, L., Xie, J., et al. (2020). Consolidating Lithiothermic-Ready Transition Metals for Li 2 S-Based Cathodes. *Adv. Mater.* 32 (31), 2002403. doi:10.1002/adma.202002403

Xiong, H., Slater, M. D., Balasubramanian, M., Johnson, C. S., and Rajh, T. (2011). Amorphous TiO2 Nanotube Anode for Rechargeable Sodium Ion Batteries. *J. Phys. Chem. Lett.* 2 (20), 2560–2565. doi:10.1021/jz2012066

Xiong, X., Wang, G., Lin, Y., Wang, Y., Ou, X., Zheng, F., et al. (2016). Enhancing Sodium Ion Battery Performance by Strongly Binding Nanostructured Sb2S3 on Sulfur-Doped Graphene Sheets. *ACS Nano* 10 (12), 10953–10959. doi:10.1021/acsnano.6b05653

Xu, B., Qi, S., He, P., and Ma, J. (2019). Antimony- and Bismuth-Based Chalcogenides for Sodium-Ion Batteries. *Chem. Asian J.* 14 (17), 2925–2937. doi:10.1002/asia.201900784

Yao, S., Cui, J., Deng, Y., Chong, W. G., Wu, J., Ihsan-Ul-Haq, M., et al. (2019). Ultrathin Sb2S3 Nanosheet Anodes for Exceptional Pseudocapacitive Contribution to Multi-Battery Charge Storage. *Energ. Storage Mater.* 20, 36–45. doi:10.1016/j.ensm.2018.11.005

Yin, W., Chai, W., Wang, K., Ye, W., Rui, Y., and Tang, B. (2019). A Highly Meso@Microporous Carbon-Supported Antimony Sulfide Nanoparticles Coated by Conductive Polymer for High-Performance Lithium and Sodium Ion Batteries. *Electrochimica Acta* 321, 134699. doi:10.1016/j.electacta.2019.134699

Yu, D. Y. W., Prikhodchenko, P. V., Mason, C. W., Batabyal, S. K., Gun, J., Sladkevich, S., et al. (2013). High-capacity Antimony Sulphide Nanoparticle-Decorated Graphene Composite as Anode for Sodium-Ion Batteries. *Nat. Commun.* 4, 1–7. doi:10.1038/ncomms3922

Yu, M., Yin, Z., Yan, G., Wang, Z., Guo, H., Li, G., et al. (2020). Synergy of Interlayer Expansion and Capacitive Contribution Promoting Sodium Ion Storage in S, N-Doped Mesoporous Carbon Nanofiber. *J. Power Sourc.* 449, 227514. doi:10.1016/j.jpowsour.2019.227514

Yu, S., Liu, Z., Tempel, H., Kungl, H., and Eichel, R.-A. (2018). Self-standing NASICON-type Electrodes with High Mass Loading for Fast-Cycling All-Phosphate Sodium-Ion Batteries. *J. Mater. Chem. A.* 6 (37), 18304–18317. doi:10.1039/c8ta07313a

Yuan, M., Guo, X., Liu, Y., and Pang, H. (2019). Si-based Materials Derived from Biomass: Synthesis and Applications in Electrochemical Energy Storage. *J. Mater. Chem. A.* 7 (39), 22123–22147. doi:10.1039/c9ta06934h

Zhai, H., Jiang, H., Qian, Y., Cai, X., Liu, H., Qiu, Y., et al. (2020). Sb2S3 Nanocrystals Embedded in Multichannel N-Doped Carbon Nanofiber for Ultralong Cycle Life Sodium-Ion Batteries. *Mater. Chem. Phys.* 240, 122139. doi:10.1016/j.matchemphys.2019.122139

Zhan, W., Zhu, M., Lan, J., Wang, H., Yuan, H., Yang, X., et al. (2021). 1D Sb2S3@nitrogen-Doped Carbon Coaxial Nanotubes Uniformly Encapsulated within 3D Porous Graphene Aerogel for Fast and Stable Sodium Storage. *Chem. Eng. J.* 408, 128007–128010. doi:10.1016/j.cej.2020.128007

Zhang, H., Ren, M., Jiang, W., Yao, J., Pan, L., and Yang, J. (2021a). Hierarchical Sb2S3@m-Ti3C2Tx Composite Anode with Enhanced Na-Ion Storage Properties. *J. Alloys Comp.* 887, 161318. doi:10.1016/j.jallcom.2021.161318

Zhang, Q., Zeng, Y., Wang, X., Wang, L., Wang, H., Xiao, J., et al. (2021b). Sb2S3 Nanoparticles Anchored on N-Doped 3D Carbon Nanofibers as Anode Material for Sodium Ion Batteries with Improved Electrochemical Performance. *J. Alloys Comp.* 881, 160594–160599. doi:10.1016/j.jallcom.2021.160594

Zhang, Z., Zhao, J., Xu, M., Wang, H., Gong, Y., and Xu, J. (2018). Facile Synthesis of Sb2S3/MoS2 Heterostructure as Anode Material for Sodium-Ion Batteries. *Nanotechnology* 29 (33), 335401. doi:10.1088/1361-6528/aac645

Zhao, W., Li, M., Qi, Y., Tao, Y., Shi, Z., Liu, Y., et al. (2021). Ultrasound Sonochemical Synthesis of Amorphous Sb2S3-Graphene Composites for Sodium-Ion Batteries. *J. Colloid Interf. Sci.* 586, 404–411. doi:10.1016/j.jcis.2020.10.104

Zhao, W., Zhang, L., Jiang, F., Chang, X., Yang, Y., Ge, P., et al. (2020). Engineering Metal Sulfides with Hierarchical Interfaces for Advanced Sodium-Ion Storage Systems. *J. Mater. Chem. A.* 8 (10), 5284–5297. doi:10.1039/c9ta13899d

Zhao, Y., and Manthiram, A. (2015). Amorphous Sb2S3 Embedded in Graphite: a High-Rate, Long-Life Anode Material for Sodium-Ion Batteries. *Chem. Commun.* 51 (67), 13205–13208. doi:10.1039/x0xx00000x10.1039/c5cc03825a

Zhao, Y., and Manthiram, A. (2015). Bi0.94Sb1.06S3 Nanorod Cluster Anodes for Sodium-Ion Batteries: Enhanced Reversibility by the Synergistic Effect of the Bi2S3-Sb2S3 Solid Solution. *Chem. Mater.* 27 (17), 6139–6145. doi:10.1021/acs.chemmater.5b02833

Zheng, T., Li, G., Zhao, L., and Shen, Y. (2018). Flowerlike Sb 2 S 3 /PPy Microspheres Used as Anode Material for High-Performance Sodium-Ion Batteries. *Eur. J. Inorg. Chem.* 2018 (10), 1224–1228. doi:10.1002/ejic.201701364

Zhou, J., Dou, Q., Zhang, L., Wang, Y., Yuan, H., Chen, J., et al. (2020a). A Novel and Fast Method to Prepare a Cu-Supported α-Sb2S3@CuSbS2 Binder-free Electrode for Sodium-Ion Batteries. *RSC Adv.* 10 (49), 29567–29574. doi:10.1039/d0ra05623e

Zhou, X., Zhang, Z., Yan, P., Jiang, Y., Wang, H., and Tang, Y. (2020b). Sulfur-doped Reduced Graphene oxide/Sb2S3 Composite for superior Lithium and Sodium Storage. *Mater. Chem. Phys.* 244, 122661–122668. doi:10.1016/j.matchemphys.2020.122661

Zhu, Y., Nie, P., Shen, L., Dong, S., Sheng, Q., Li, H., et al. (2015). High Rate Capability and superior Cycle Stability of a Flower-like Sb2S3anode for High-Capacity Sodium Ion Batteries. *Nanoscale* 7 (7), 3309–3315. doi:10.1039/c4nr05242k

**Conflict of Interest:** Author ZC was employed by the company Luoyang Bearing Research Institute Co., Ltd.

The remaining authors declare that the research was conducted in the absence of any commercial or financial relationships that could be construed as a potential conflict of interest

**Publisher's Note:** All claims expressed in this article are solely those of the authors and do not necessarily represent those of their affiliated organizations, or those of the publisher, the editors, and the reviewers. Any product that may be evaluated in this article, or claim that may be made by its manufacturer, is not guaranteed or endorsed by the publisher.

frontiers | Frontiers in Chemistry

ORIGINAL RESEARCH
published: 08 April 2022
doi: 10.3389/fchem.2022.870541

# Electrochemical Performance of $MnO_2$/Graphene Flower-like Microspheres Prepared by Thermally-Exfoliated Graphite

*Xuyue Liu*[1], *Bing Liang*[1]*, *Xiaodong Hong*[2] *and Jiapeng Long*[1]

[1]School of Material Science and Technology, Shenyang University of Chemical Technology, Shenyang, China, [2]School of Materials Science and Energy Engineering, Foshan University, Foshan, China

To enhance the electrochemical performance of $MnO_2$/graphene composite, herein, thermally-exfoliated graphite (TE-G) is adopted as a raw material, and a hydrothermal reaction is conducted to achieve the exfoliation of TE-G and the loading of $MnO_2$ nanosheets. Through optimizing the TE-G/$KMnO_4$ ratio in the redox reaction between carbon and $KMnO_4$, flower-like $MnO_2$/G microspheres ($MnO_2$/G-10) are obtained with 83.2% $MnO_2$ and 16.8% residual graphene. Meanwhile, corresponding $MnO_2$/rGO composites are prepared by using rGO as raw materials. Serving as a working electrode in a three-electrode system, $MnO_2$/G-10 composite displays a specific capacitance of 500 F $g^{-1}$ at 1 A $g^{-1}$, outstanding rate performance, and capacitance retention of 85.3% for 5,000 cycles. The performance is much better than that of optimized $MnO_2$/rGO composite. We ascribe this to the high carbon fraction in TE-G resulting in a high fraction of $MnO_2$ in composite, and the oxygen-containing groups in rGO reduce the resulting $MnO_2$ fraction in the composite. The superior electrochemical performance of $MnO_2$/G-10 is dependent on the hierarchical porous structure constructed by $MnO_2$ nanosheet arrays and the residual graphene layer in the composite. In addition, a supercapacitor assembled by TE-G negative electrode and $MnO_2$/G positive electrode also exhibits superior performance. In consideration of the low cost of raw materials, the $MnO_2$/G composite exhibits great application potential in the field of supercapacitors.

**Keywords: $MnO_2$, thermally-exfoliated graphite, supercapacitors, electrochemical performance, flower-like microspheres**

OPEN ACCESS

***Edited by:***
*Jinlin Lu,*
*Guangzhou Maritime College, China*

***Reviewed by:***
*Hongtao Fan,*
*Liaoning Shihua University, China*
*Xinhua Gao,*
*Ningxia University, China*
*Lisheng Guo,*
*Anhui University, China*

***Correspondence:**
*Bing Liang*
*lb1007@163.com*

***Specialty section:***
*This article was submitted to Nanoscience, a section of the journal Frontiers in Chemistry*

***Received:*** *07 February 2022*
***Accepted:*** *14 February 2022*
***Published:*** *08 April 2022*

***Citation:***
*Liu X, Liang B, Hong X and Long J (2022) Electrochemical Performance of $MnO_2$/Graphene Flower-like Microspheres Prepared by Thermally-Exfoliated Graphite. Front. Chem. 10:870541. doi: 10.3389/fchem.2022.870541*

## INTRODUCTION

Among the existing energy storage devices, the supercapacitor is an important device for high power density, rapid charge/discharge, and long cycling life. The fabrication of electrode materials is a major task for developing high-performance supercapacitors (Raj et al., 2020; Oncu et al., 2021; Zhang et al., 2021). To achieve the rapid transport and transfer of ions/electrons, various carbon materials have been developed in the field of supercapacitors, including carbon nanotubes (Lei et al., 2020), graphene (Sha et al., 2021), carbon nanosheets (Sevilla and Fuertes, 2014), porous carbon (Zhao et al., 2020), carbon fibers (Srimuk et al., 2015), and so on. Nevertheless, the poor specific capacitance of these carbon materials affects their wide application in supercapacitors, due to the electrical double

layer capacitance (EDLC) feature (Sevilla and Fuertes, 2014; Ferrero et al., 2015). To enhance the specific capacitance, carbon materials have been hybridized with various metal oxides for introducing high pseudocapacitance (Yan et al., 2014, 2021). Among those transition metal oxides, $MnO_2$ has been regarded as the most promising electrode material, due to the large theoretical specific capacitance of 1370 F $g^{-1}$, natural abundance, and low price (Xu et al., 2007, 2018; Zhang et al., 2020c).

Lots of methods have been reported to prepare $MnO_2$/rGO composites, such as the chemical precipitation method (Gong et al., 2021), alcohol infiltrated substrate method (Zhang et al., 2020b), and hydrothermal route (Liu et al., 2015). Among these methods, the hydrothermal method is the most convenient way for synthesizing $MnO_2$/rGO composites. During a hydrothermal process, a redox reaction takes place between carbon and $KMnO_4$, and $MnO_2$ nanostructures are uniformly generated on graphene nanosheets, with the consumption of a certain amount of carbon (Ping et al., 2019, 2; Hong et al., 2021; Wang T. et al., 2021). In this respect, by using sulfur-reduced graphene oxide (RGO-S) as raw materials, Tarimo et al. (Tarimo et al., 2020) synthesized RGO-S/$MnO_2$ composite via a hydrothermal method, and the optimized RGO-S/$MnO_2$ composites had a low capacitance (180.4 F $g^{-1}$). Yang et al. (Yang et al., 2012) prepared rGO firstly by using graphene oxide (GO) and then synthesized urchin-like $MnO_2$ on rGO nanosheet through a hydrothermal reaction under the presence of $KMnO_4$. The optimized rGO/$MnO_2$ composites exhibited a high capacitance of 263 F $g^{-1}$. Moreover, Liu et al. (Liu et al., 2014) prepared GO firstly by Hummers method and then synthesized $MnO_2$-GO composites via hydrothermal reaction. The $MnO_2$-GO composite presented a capacitance of 213 F $g^{-1}$ at 0.1 A $g^{-1}$. From these works about $MnO_2$/graphene composites, the graphene in composites is usually derived from GO prepared by Hummers method (Vimuna et al., 2020). In addition, the resulting $MnO_2$/rGO composites deliver the specific capacitance of less than 300 F $g^{-1}$, which further limits the development of high-performance supercapacitors. Up to now, there is no report about $MnO_2$/graphene composites prepared by using expandable graphite as raw materials.

In view of the larger specific surface area, lower oxygen content, more complete lamellar structure, and low cost and easy preparation of thermally-exfoliated graphite (TE-G), herein, TE-G was adopted as raw materials, and a hydrothermal reaction was performed to fabricate $MnO_2$/graphene composite through a redox reaction between $KMnO_4$ and C. Most importantly, the hydrothermal reaction achieves the exfoliation of TE-G. As a result, flower-like $MnO_2$/graphene microspheres were produced, in which, the residual graphene layer was wrapped by abundant thin $MnO_2$ nanosheets. The optimized $MnO_2$/graphene microspheres exhibited excellent electrochemical performance in supercapacitors. To verify the performance advantage of TE-G in preparing $MnO_2$/graphene composite, various $MnO_2$/rGO composites were fabricated by using GO as reactants, and corresponding electrochemical performance was investigated. Compared with rGO, the $MnO_2$/G composite prepared with TE-G as raw material shows better performance and a more convenient method.

# EXPERIMENT

## Materials

Potassium chloride (KCl), Expandable graphite (EG, 80 mesh), and potassium permanganate ($KMnO_4$) were obtained from Tianjin Damao Chemical Reagent Factory.

## Preparation of Thermally-Exfoliated Graphene

Thermally-exfoliated graphite (TE-G) was synthesized according to our previous work (Liu et al., 2021). Specifically, EG was heated at 500°C for 100 min under $N_2$ to obtain thermally-exfoliated graphene (TE-G).

## Preparation of $MnO_2$/Graphene ($MnO_2$/G) Composites

In a typical synthesis, 1.0 g $KMnO_4$ was put into deionized water (80 ml) and stirred for 30 min to produce a uniform solution. Meanwhile, different amounts of TE-G powders were put into the $KMnO_4$ solution and stirred for 30 min, and then, the mixture was put into a stainless-steel autoclave. The hydrothermal reaction was conducted at 180°C for 15 h. The production was filtered, rinsed repeatedly by deionized water, and dried at 60°C for 12 h to obtain $MnO_2$/G composites. The redox reaction equation of C and $KMnO_4$ can be described as: $4MnO_4^- + 3C + H_2O \rightarrow 4MnO_2 + CO_3^{2-} + 2HCO_3^-$. According to the equation, the theoretical mass ratio of KMnO4 and C can be calculated as 1/17.7. Therefore, to change the $MnO_2$ fraction in the $MnO_2$/G composite, the $KMnO_4$/TE-G mass ratio was set as 5, 10, and 20, and the resulting composites were coded as $MnO_2$/G-5, $MnO_2$/G-10, and $MnO_2$/G-20. In addition, the hydrothermal reaction of TE-G in deionized water and in KCl solution was carried out under the same condition, and the resulting samples were coded as TE-G-$H_2O$ and TE-G-KCl, respectively. The rGO was used to prepare $MnO_2$/rGO composites. The ratio of $KMnO_4$/rGO was kept the same as the ratio of $KMnO_4$/TE-G composites, and the sample was named $MnO_2$/rGO-5, $MnO_2$/rGO-10, and $MnO_2$/rGO-20.

## Testing and Characterization

The field-emission scanning electron microscopy (FE-SEM; SU8010) and transmission electron microscopy (TEM; JEM-2100) were used to observe the morphologies of samples. The crystallographic feature was performed by X-ray diffraction (XRD; D8-Advance) with Cu Kα radiation source. X-ray photoelectron spectra (XPS) were recorded by using a Thermo Scientific K-Alpha XPS spectrometer. The working voltage was 12 kV, and the X-Ray source was Al Kα. Pore size distribution and the specific surface area were tested by using the SSA-7000 device, according to the BJH model and BET method.

## Electrochemical Performance

A three-electrode system was used to test the electrochemical performance of samples in an electrolyte of 6 M KOH. The poly

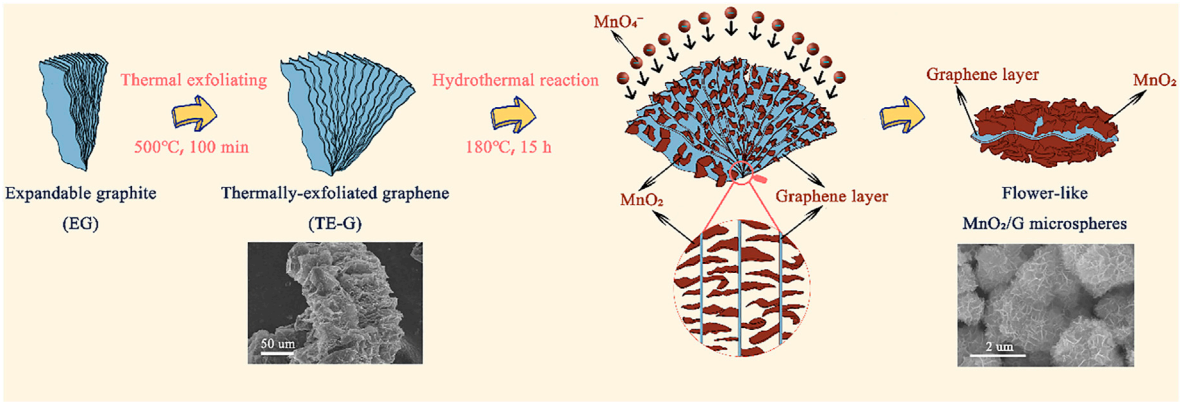


**FIGURE 1 |** Schematic presentation of the preparation of accordion structure TE-G and flower-like $MnO_2$/G microspheres, and the inset SEM images presenting the morphology of TE-G and $MnO_2$/G composites respectively.

(vinylidene fluoride)/acetylene black/active materials were weighed at the ratio of 5:10:85, and dissolved in N-methyl-2-pyrrolidone (NMP) to prepare a slurry. Foam nickel ($1 \times 1$ $cm^2$) was used to support the slurry and served as the working electrode. The platinum sheet was acted as the counter electrode, and the saturated calomel electrode (SCE) was used as the reference electrode. A CHI 660E electrochemical workstation (Shanghai Chenhua Co. Ltd.) was used to test electrochemical impedance spectroscopy (EIS), galvanostatic charge/discharge curves (GCD), cycling stability, and cyclic voltammetry (CV) curves. Asymmetric supercapacitor (ASCs) devices were assembled by using TE-G as the negative electrode and $MnO_2$/G composite as a positive electrode with 6 M KOH electrolyte. The separator was glass fiber filter paper. In the ASCs device, Formula I (Wang et al., 2018): $R = m^+/m^- = (C^- \times \Delta V^-)/(C^+ \times \Delta V^+)$ can be applied to obtain the ratio of positive/negative electrode material. Formula II (Brousse et al., 2007; Hong et al., 2021): $C = I \times \Delta t/\Delta V$, was employed in calculating the specific capacitance (C) in a three-electrode system. Formula III (Brousse et al., 2007): $Cs = 4C/M$, Formula IV (Li et al., 2021): $E = 0.5C\ (\Delta V)^2/3.6$ and Formula V (Brousse et al., 2007): $P = E/\Delta t$ can be applied to obtain specific capacitance (Cs), the energy density (E) and power density (P) of the ASCs, respectively.

# RESULTS AND DISCUSSION

## Preparation Process of $MnO_2$/G Composite

**Figure 1** exhibits the preparation process of flower-like $MnO_2$/G microspheres. Firstly, under the presence of $N_2$, the expandable graphite (EG) was heated at 500°C to prepare TE-G. Under a high temperature, the intercalation agent in EG expands and violently decomposes, resulting in a large amount of gas spilling and forming micropores, mesopores, and macropores. As shown in **Figure 1**, TE-G shows an accordion structure with a thick lamella. Moreover, abundant cavity structures can be observed on TE-G. Secondly, under a hydrothermal process, $KMnO_4$ reacts with C to generate $MnO_2$, in which, each single-layer of graphene in TE-G reacts with $KMnO_4$ and is then wrapped by abundant $MnO_2$ nanosheets. The loading of $MnO_2$ thick nanosheets on graphene layers leads to the exfoliation of TE-G. From the inset SEM image, after the redox reaction, graphene nanosheets were wrapped by $MnO_2$ nanosheet arrays in different directions to produce flower-like microspheres. Compared with rGO, the consumption of graphene nanosheets and the generation of thick $MnO_2$ layers lead to the delamination of TE-G. In order to confirm the advantage of $MnO_2$/G composite, corresponding $MnO_2$/rGO composites were prepared, and the microstructure and electrochemical performance were investigated.

## Microstructure of $MnO_2$/G Composites

The morphologies of TE-G and different $MnO_2$/G composites samples were characterized by using TEM and SEM. From **Figure 2A,B**, pure TE-G presents an accordion structure with a large number of holes, and **Figure 2C** indicates the stacking structure of abundant graphene nanosheets. From these $MnO_2$/G samples, under a low ratio of $KMnO_4$/TE-G, a few graphene sheets in TE-G participate in the redox reaction with $KMnO_4$. Hence, a few $MnO_2$ nanosheets are generated on the graphene surface (**Figure 2D**). When the ratio of $KMnO_4$/TE-G increases to 10, dense $MnO_2$ nanosheet arrays are generated in all directions of graphene nanosheets, presenting a flower spherical structure (**Figure 2F**). From the high magnification SEM in **Figure 2F**, the resulting $MnO_2$ nanosheets arrays exhibit a honeycomb-like structure. The results show that the redox reaction between carbon and $KMnO_4$ produces $MnO_2$ nanosheets on graphene, which achieves the delamination of TE-G. From **Figure 2G,H**, there are dense $MnO_2$ nanosheets arrays dispersed on the graphene surface. Moreover, the TEM image also shows the connection of different $MnO_2$/G flower spheres, which may be resulted from the fracture of large graphene nanosheets during the high-temperature hydrothermal reaction process. As shown in **Figure 2I**, we can observe the diffraction fringes of $MnO_2$ on the graphene surface. The fringe spacing of ~0.8 nm corresponds to the (001) facet of δ-$MnO_2$ (Wang J. et al., 2021). When the ratio of $KMnO_4$/TE-G

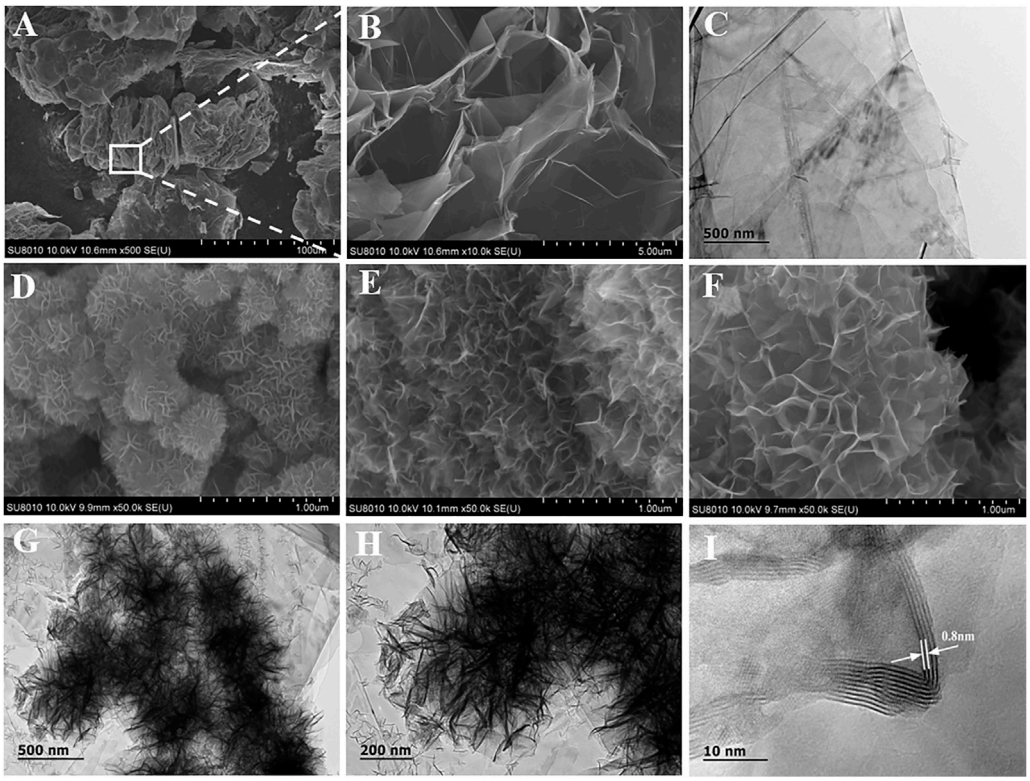


**FIGURE 2 |** The microstructure of pure TE-G **(A–C)** and the composites with the $KMnO_4$/TE-G ratio of 5 **(D)**, 20 **(E)**, and 10 **(F–I)** by SEM and TEM.

reaches 20, excessive $MnO_2$ nanosheets are generated and piled up on the surface of the $MnO_2$/G composite (**Figure 2E**).

In order to prove that the exfoliating of TE-G is related to the $KMnO_4$-assisted hydrothermal reaction, two controls are designed by using only deionized water and KCl solution, respectively. In the absence of $KMnO_4$, the hydrothermal reaction cannot exfoliate the TE-G. As shown in **Figure 3A**, the accordion structure is kept the same as pure TE-G (**Figure 2A**). Under the presence of $K^+$ derived from KCl, the resulting TE-G also keeps the same structure with pure TE-G in **Figure 2A**. Therefore, the exfoliation of TE-G is dependent on $KMnO_4$-assisted hydrothermal reaction, and the *in-situ* reaction between graphene nanosheet and $KMnO_4$ consumes carbon and introduces $MnO_2$ nanosheet arrays, which effectively exfoliate TE-G. To disclose the advantage of TE-G in preparing $MnO_2$/G composites, rGO was used as reductants, and resulting $MnO_2$/rGO composites were shown in **Figure 3C,D**. The $MnO_2$/rGO composite shows the same flower spheres as $MnO_2$/G composite (**Figure 2D–F**). The result indicates that the reaction between rGO and $KMnO_4$ is kept the same as the reaction between TE-G and $KMnO_4$, that is, the redox reaction of graphene nanosheets and $KMnO_4$. However, the major difference between the two reactions is the carbon precursors. TE-G has condensed graphene nanosheets with no oxygen-containing groups, while rGO is the exfoliated graphene containing oxygen-containing groups. Compared with rGO, TE-G has a low cost and high carbon content, which would consume more $KMnO_4$ and introduce much more $MnO_2$, while some rGO nanosheets are not wrapped by $MnO_2$ nanosheets arrays (**Figure 3C**), and much more $MnO_2$ nanosheets would enhance the electrochemical performance of $MnO_2$/G composites, which will be discussed further.

## Elemental Distribution of $MnO_2$/G Composites

Elemental mapping and EDS were conducted to verify residual graphene in $MnO_2$/G composite. $MnO_2$ nanosheets (**Figure 4A**) keep the same with the SEM morphology (**Figure 2F**). The distribution of O is in accordance with the Mn (**Figure 4C**), which reflects the generation of $MnO_2$. In addition, the dispersed C signals verify the residual graphene in the $MnO_2$/G composite. From **Figure 4E**, the C content is at 35.31%, further demonstrating the residual carbon derived from graphene. To detect the precise carbon content in composite, TG curves of TE-G, $MnO_2$/G-5, $MnO_2$/G-10, and $MnO_2$/G-20 are given in **Figure 4F**. When the temperature is higher than 600°C, TE-G begins to decompose, and no residual carbon remains at 800°C. Compared with TE-G, the residual fractions of three composites are 72.5, 75.5, and 81.0% at 800°C in air. Based on the principle in Ref. (Wang J. et al., 2021), the final product of $MnO_2$/G composite is $Mn_2O_3$ at 800°C. According to the same Mn content, we can calculate the fraction of $MnO_2$, that is, 80.0, 83.2, and 89.3%, respectively. The residual carbon fractions in

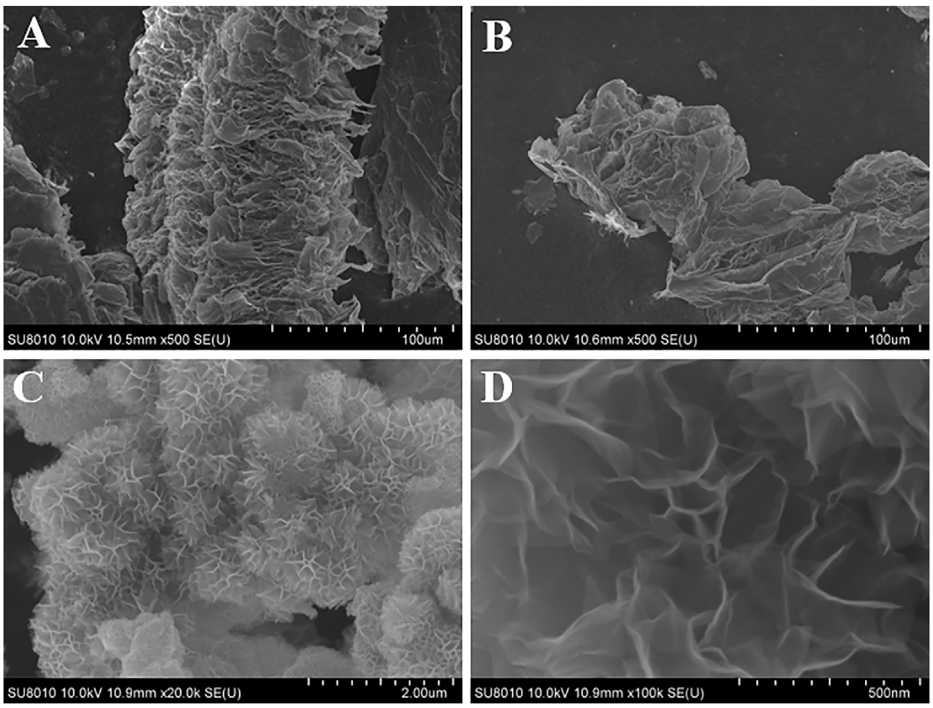


**FIGURE 3 |** The microstructure of TE-G-$H_2O$ **(A)**, TE-G-KCl **(B)**, and $MnO_2$/rGO composites **(C,D)**.

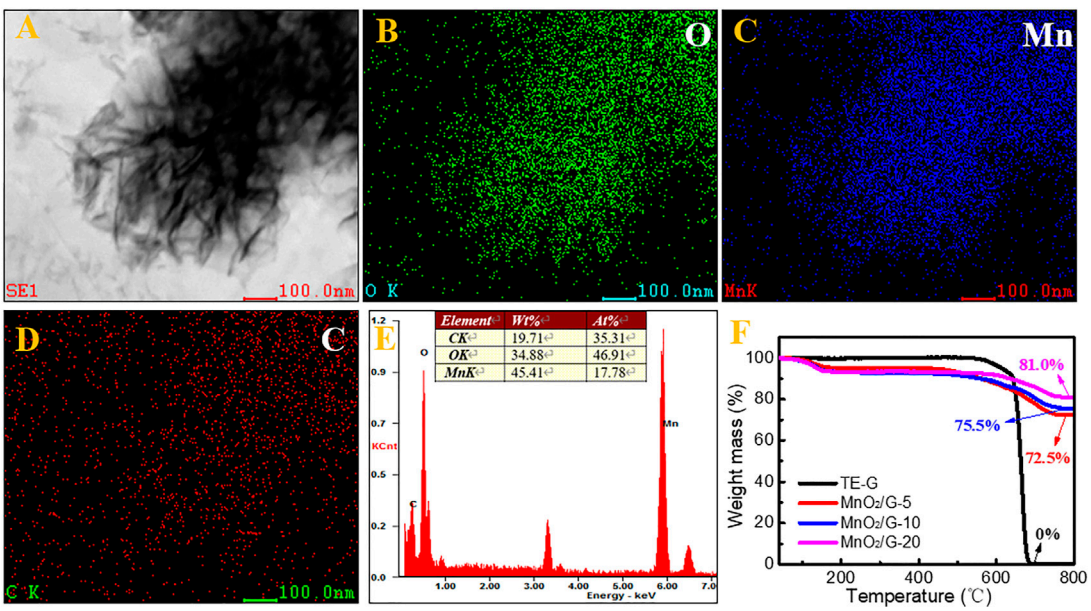


**FIGURE 4 |** The microstructure of the $MnO_2$/G-10 composite observed by STEM **(A)**, the elemental mapping of O **(B)**, Mn **(C)**, and C **(D)**, corresponding elemental fraction **(E)**, and thermogravimetric curves of TE-G and $MnO_2$/G composites **(F)**.

$MnO_2$/G-5, $MnO_2$/G-10, and $MnO_2$/G-20 are 20.0, 16.8, and 10.7%, respectively. Therefore, the TG result affirms the incomplete reaction of carbon (TE-G), and residual graphene nanosheet still exists in the $MnO_2$/G composite.

Fourier transform infra-red (FTIR) was provided in **Supplementary Figure S1**, the peak at ~3,425 $cm^{-1}$ is attributed to the O-H vibration of GO or rGO. The peaks of ~1,633 $cm^{-1}$ and 1,313 $cm^{-1}$ correspond to the stretching

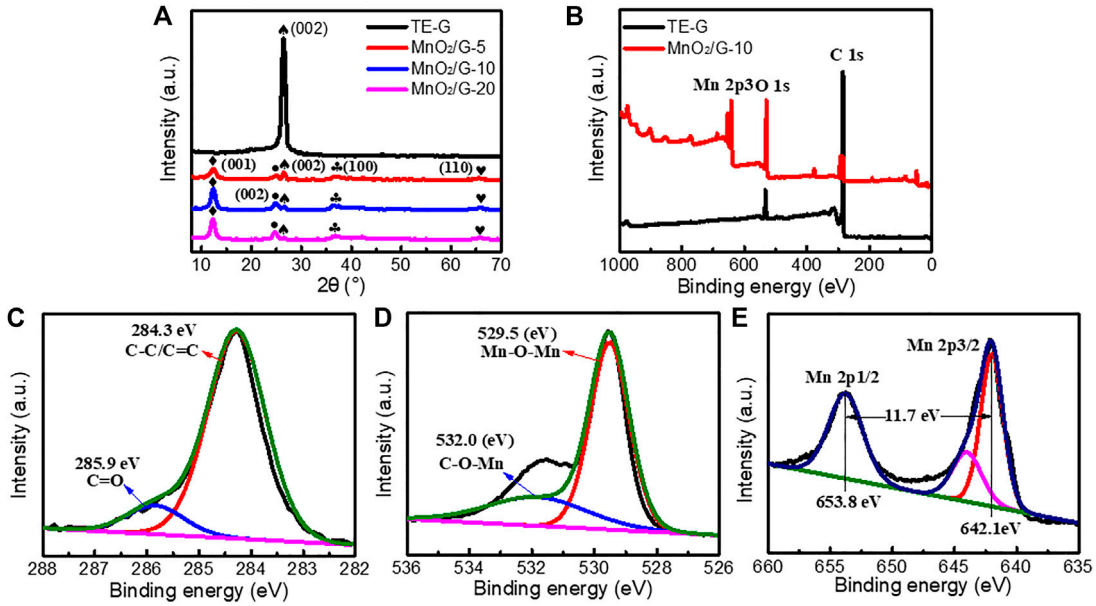


**FIGURE 5 |** The XRD patterns **(A)** and XPS survey spectra **(B)** of pure TE-G and $MnO_2$/G-10 sample, and the magnified C **(C)**, O **(D)**, and Mn **(E)** XPS spectrum.

and bending vibration of C-O, respectively. Compared with GO or rGO, there are a few oxygen-containing groups in TE-G, which is conducive to the redox reaction between TE-G and $KMnO_4$, and a high fraction of carbon would consume a large amount of $KMnO_4$ and generate many more $MnO_2$ nanosheets. To verify the high fraction of $MnO_2$ in $MnO_2$/G composites, the TG curves of $MnO_2$/rGO-5 and $MnO_2$/rGO-20 were measured to obtain the content of $MnO_2$ in $MnO_2$/rGO composites. As given in **Supplementary Figure S2**, the residual fractions of $MnO_2$/rGO-5 and $MnO_2$/rGO-20 are 57.7 and 67.0%, respectively. Therefore, the fraction of $MnO_2$ can be calculated as 63.6 and 73.8%, respectively. The result shows that the $MnO_2$ content of $MnO_2$/rGO is much lower than that of the corresponding $MnO_2$/G composite. The reason can be ascribed to the low C fraction in rGO, resulting in fewer $MnO_2$ nanosheets.

## Crystal Structure and Surface Chemistry of TE-G and $MnO_2$/G

In order to analyze the crystal structure of samples, XRD testing was performed. As given in **Figure 5A** sharp diffraction peak at 26.4° is attributed to the (002) crystal plane of TE-G (Thommes and Cychosz, 2014). According to the Bragg equation: $2d\sin\theta = n\lambda$, the layer spacing d is calculated as 0.34 nm. After reacted with $KMnO_4$, four peaks can be observed at 12.2°, 24.7°, 36.6°, and 65.6°, these peaks correspond to the (001), (002), (100), and (110) facets of δ-$MnO_2$ (JCPDS # 80–1098) (Wei et al., 2012; Zhu et al., 2017). When the amount of $KMnO_4$ increased, the (002) peak of carbon (TE-G) at 26.4° disappears, which is assigned to the loading of $MnO_2$ thick nanosheets on graphene layers leads to the exfoliation of TE-G. This phenomenon indicates the consumption of TE-G and results in a low fraction of carbon in $MnO_2$/G composites. Compared with $MnO_2$/G composite, hydrothermally-treated TE-G samples under deionized water or KCl both show a sharp diffraction peak at 26.4° (as shown in **Supplementary Figure S3**), which confirms that the TE-G cannot be exfoliated by $H_2O$ or KCl under hydrothermal reaction. Therefore, the exfoliation of TE-G is dependent on $KMnO_4$. In addition, the chemical bonds and valance state of TE-G and $MnO_2$/G-10 samples were characterized by XPS. From the general spectra in **Figure 5B**. The TE-G spectrum shows the peaks of C and O elements. After reacting with $KMnO_4$, the peak of C weakens, and the peaks of O and Mn elements are stronger obviously, due to the generation of $MnO_2$ and the consumption of TE-G nanosheets. **Figure 5C–E** shows the magnified C, O, and Mn spectrum. From **Figure 5C**, the magnified C 1s spectrum can be divided into two peaks at 284.3 and 285.9 eV, which are attributed to the C-C/C=C bond and C=O bond (Yang et al., 2020), respectively. The high-resolution O 1s can be convoluted into two main peaks at 532.0 and 529.5 eV (**Figure 5D**) corresponding to the bond of C-O-Mn generated between graphene and $MnO_2$, and the bond of Mn-O-Mn in $MnO_2$ (Yang and Park, 2018; Yang et al., 2020). From the magnified Mn 2p spectrum (**Figure 5E**), the 2p orbital of Mn has two major peaks at 642.1 and 653.8 eV, corresponding to Mn $2p_{3/2}$ and Mn $2p_{1/2}$. The distance of the two peaks is around 11.7 eV, which reflects the +4 valence of the Mn element (Yang and Park, 2018; Li et al., 2020). Hence, the $MnO_2$ in the composite is further proved by XPS.

## BET Analysis

**Figure 6** shows the $N_2$ adsorption-desorption isotherms curves and pore distribution of different samples according to the BJH model and BET method. TE-G exhibits a high adsorption capacity and a big specific surface area at low pressure. The

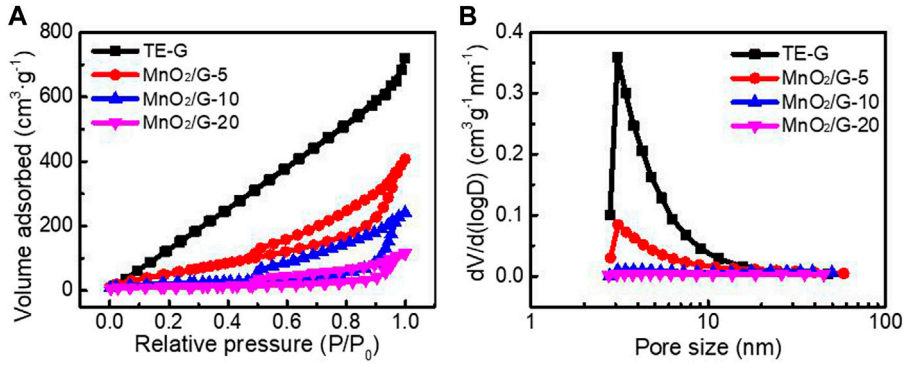


**FIGURE 6 |** $N_2$ adsorption-desorption isotherms **(A)** and pore size distribution **(B)** of pure TE-G, $MnO_2$/G-5, $MnO_2$/G-10, and $MnO_2$/G-10 composite.

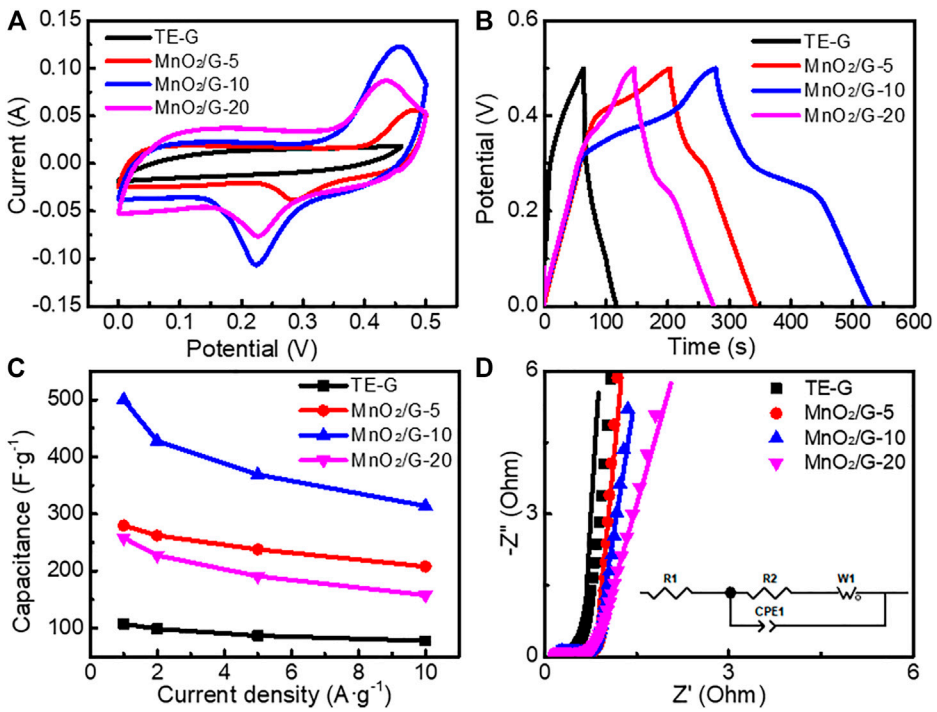


**FIGURE 7 |** Electrochemical performance of TE-G and different $MnO_2$/G composites in a three-electrode cell **(A)** CV curves tested at 20 mV s−1 **(B)** the charge-discharge curves tested at 1 A $g^{-1}$ **(C)** the specific capacitance **(D)** EIS plots, equivalent circuit and fitting curves (solid line).

specific surface area of TE-G is 1055.7 $m^2$ $g^{-1}$, and a big specific surface area facilitates the infiltration and stripping of TE-G. When increased the amount of $KMnO_4$, abundant $MnO_2$ nanosheets loading on graphene surface decreases the specific surface area. The specific surfaces of $MnO_2$/G-5, $MnO_2$/G-10, and $MnO_2$/G-20 are 252.3 $m^2$ $g^{-1}$, 76.1 $m^2$ $g^{-1}$, and 39.4 $m^2$ $g^{-1}$. From **Figure 6B**, TE-G has much more micropores and mesopores. The loading of $MnO_2$ on graphene decreases the fraction of micropores and mesopores. However, the macroporous structure of $MnO_2$/G composite would accelerate the charge transfer and ion diffusion, further improving the electrochemical performance.

## Electrochemical Performance

A three-electrode system was used to investigate the electrochemical performance of different samples, by using 6 M KOH electrolyte. **Figure 7A** presents the CV curves of TE-G and different $MnO_2$/G composites at 20 mV $s^{-1}$. The CV curve of TE-G displays a quasi-rectangular shape, reflecting the EDLC characteristic of TE-G. When introducing $MnO_2$, the resulting $MnO_2$/G composites show two pseudocapacitive peaks of $MnO_2$ corresponding to the faradic redox reaction of $MnO_2$. The faradic redox reaction mechanism of $MnO_2$ is verified as the valence shift between $Mn^{4+}$/$Mn^{3+}$ and $Mn^{3+}$/$Mn^{2+}$ (Zhou et al., 2015; Xie et al., 2019). The redox peaks centered at ~0.1 and

~0.4 V (vs Hg/HgO) can be assigned to the reversible redox reaction: $Mn^{4+} \leftrightarrow Mn^{3+} + e^-$, while the other pair of redox peaks around ~0.3 and ~0.6 V (vs Hg/HgO) originate from the faradic redox reactions related to $Mn^{3+} \leftrightarrow Mn^{2+} + e^-$ (Toupin et al., 2004; Zhou et al., 2015; Xie et al., 2019), corresponding to the two faradic redox peaks in CV curve further reflecting the pseudocapacitance characteristics from $MnO_2$. In addition, the CV curve of the $MnO_2$/G-10 sample has the largest area among these samples, revealing the maximum specific capacitance. **Figure 7B** exhibits the GCD curves of TE-G and different $MnO_2$/G samples. TE-G shows a linear symmetrical triangle, reflecting a typical EDLCs feature related to the adsorption and desorption of ions. When increased the amount of $KMnO_4$, the pseudocapacitive feature can be verified by the shape of GCD curves. The $MnO_2$/G-10 composite exhibits the longest discharge time of 250.0 s, much longer than that of pure TE-G (53.8s). On the basis of the equation of SC = I·Δt/(mV), the specific capacitance would be obtained. From **Figure 7C**, TE-G has a specific capacitance of 107.6 F $g^{-1}$ at 1 A $g^{-1}$. When hybridizing with $MnO_2$, $MnO_2$/G composites show high specific capacitances. Among these composites, the $MnO_2$/G-10 sample has the maximum specific capacitance of 500 F $g^{-1}$ at 1 A $g^{-1}$. Even operated at 10 A $g^{-1}$, the capacitance is 314 F $g^{-1}$, which is assigned to a large number of $MnO_2$ nanosheets with high capacitance content loaded to the surface of graphene. In comparison with $MnO_2$/G-10, the $MnO_2$/G-20 composite has a capacitance of 158 F $g^{-1}$, because of the stacked $MnO_2$ aggregation on graphene (**Figure 2E**). The $MnO_2$ aggregations obstruct the fast transfer of charges/ions, further decreasing the capacitance. Therefore, the $MnO_2$/G-20 composite exhibit a lower specific capacitance and poor electrochemical performance.

**Figure.7D** shows the EIS plots of different samples. Each EIS curve consists of an oblique line in the low-frequency range and a hemisphere in the high-frequency range. The Warburg impedance (W1) can be reflected by an oblique line, which reflects the diffusive resistance of the electrode in the electrolyte. The intercept in the *X*-axis and the diameter of the hemisphere reflect the internal resistance (R1) and charge transfer resistance (R2), respectively. ZView software was used to obtain the fitting curves (solid line) in **Figure.7D**. The fitting data were listed in **Supplementary Table S1**. The R1 values of TE-G, $MnO_2$/G-5, $MnO_2$/G-10, and $MnO_2$/G-20 are 0.484, 0.480, 0.213, and 0.217 Ω, respectively. In addition, the R2 values are 0.341, 0.669, 0.332 and 0.379 Ω, respectively. Therefore, the $MnO_2$/G-10 composite exhibits the minimum value of R1 and R2 among these samples, which indicates the minimum internal resistance and charge transfer resistance. The reason can be explained as the residual graphene in composite enhances the electronic conductivity. Moreover, hierarchical porous flower spheres of $MnO_2$ promote the fast transfer of charges/ions, which facilitate the pseudocapacitive reaction of $MnO_2$ in the electrolyte. Unfortunately, abundant $MnO_2$ aggregated clusters impede the rapid transfer of charges/ions, increase the internal resistance, which leads to the poor electrochemical performance of $KMnO_4$/G-20 composite.

To further verify the performance advantage of $MnO_2$/G composite, the electrochemical performance of $MnO_2$/rGO composites are given in **Supplementary Figure S4**. Both CV curves and GCD curves of different $MnO_2$/rGO composites show the pseudocapacitive feature of $MnO_2$, the area of $MnO_2$/rGO composites enclosed by the CV curve is much smaller than that of the $MnO_2$/G-10 composite. In addition, the maximum discharge time of $MnO_2$/rGO-20 is 64.7 s, the specific capacitance can be calculated as 129.4 F $g^{-1}$, much lower than that of the $MnO_2$/G composite. The reason is the less carbon fraction in rGO limits the redox reaction with $KMnO_4$, resulting in less $MnO_2$ nanosheets loading on rGO (in **Supplementary Figure S2**). Therefore, TE-G shows an obvious performance advantage to high-cost rGO.

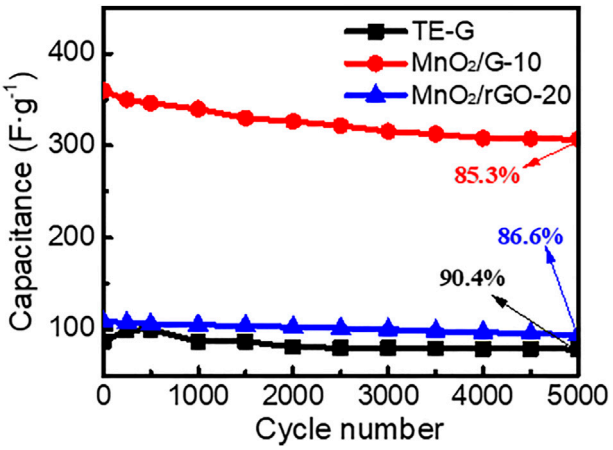


**FIGURE 8 |** Cycling stability of TE-G, $MnO_2$/G-10and $MnO_2$/rGO-20 composites electrode tested in three-electrode system.

The cycling stability of TE-G, $MnO_2$/G-10, and $MnO_2$/rGO-20 composite was tested at a current density of 5 A $g^{-1}$. As given in **Figure 8**, the specific capacitance of TE-G increases and then decreases during the first 500 cycles, which is assigned to poor wettability between TE-G and the electrolyte. As TE-G only contains a small amount of oxygen-containing groups, the wettability between TE-G and the electrolyte is poor. With the progress of the charge-discharge cycle, the wettability between TE-G and the electrolyte is improved, and the specific capacitance gradually increases. However, due to the limitation of the material itself, the specific capacitance content of TE-G decreases gradually with the increase of the cycle numbers. The specific capacitance of TE-G declines from the original 87.0 F $g^{-1}$ to 78.6 F $g^{-1}$ after 5,000 cycles. The capacitance retention rate is 90.4%, for the EDLC feature. The capacitance of $MnO_2$/rGO composites decreases from an initial 108.6 F $g^{-1}$–94.1 F $g^{-1}$, and the capacitance retention rate is 86.6%, which was attributed to the lower content of $MnO_2$ and more graphene lamellar residues (as shown in **Supplementary Figure S2**). In comparison with $MnO_2$/rGO, the $MnO_2$/G-10 composite has a low capacitance retention rate of 85.3%, and the capacitance decreases to 307.0 F $g^{-1}$ from 340.1 F $g^{-1}$. The low capacitance retention of the $MnO_2$/G-10 sample is attributed to a high fraction of $MnO_2$ nanosheets in the composite. However, considering the high specific capacitance, $MnO_2$/G-10 composite still presents

**TABLE 1 |** Summary of the electrochemical performance of existing C/MnO2 composites.

| Electrode materials | Electrolyte | Capacitance ($F \cdot g^{-1}$) | Cycling stability | Ref |
|---|---|---|---|---|
| $MnO_2$/RGO | 1 M $Na_2SO_4$ | 467 at 1 A $g^{-1}$ | 93.1%-2500 cycle | Zhang et al. (2020b) |
| $MnO_2$/rGO (NMG) | 1M $Na_2SO_4$ | 140.3 at 1 mA | 99.4%-5,000 cycle | Vimuna et al. (2020) |
| $MnO_2$@PCN | 1 M $Na_2SO_4$ | 225 at 0.5 A $g^{-1}$ | — | Yang et al. (2020) |
| $MnO_2$/C | 1M $Na_2SO_4$ | 480.3 at 0.5 mAcm$^{-2}$ | 71%-10000 cycle | Jeong et al. (2021) |
| PWC/$MnO_2$/GQDs | 1 M $Na_2SO_4$ | 188.4 at 1 mA $cm^{-2}$ | 95.3%-2000 cycle | Zhang et al. (2020d) |
| RGO-S/$MnO_2$ | 2.5 $MKNO_3$ | 180.4 at 1 A $g^{-1}$ | — | Tarimo et al. (2020) |
| $MnO_2$/GH | 1 M KOH | 445.7 at 0.5 A $g^{-1}$ | 82.4%-5000cycle | Zhang et al. (2016) |
| $MnO_2$/PC-Cs/$MnO_2$ | 1 M KOH | 397 at 1 A $g^{-1}$ | 93.1%-5,000 cycles | Hong et al. (2021) |
| rGO/C/$MnO_2$ | 3 M KOH | 215.2 at 0.15 A g–1 | 72%-2500 cycles | Zhang et al. (2020a) |
| $MnO_2$/G | 6 M KOH | 500 at 1 A $g^{-1}$ | 85.3%-5,000 cycles | This work |

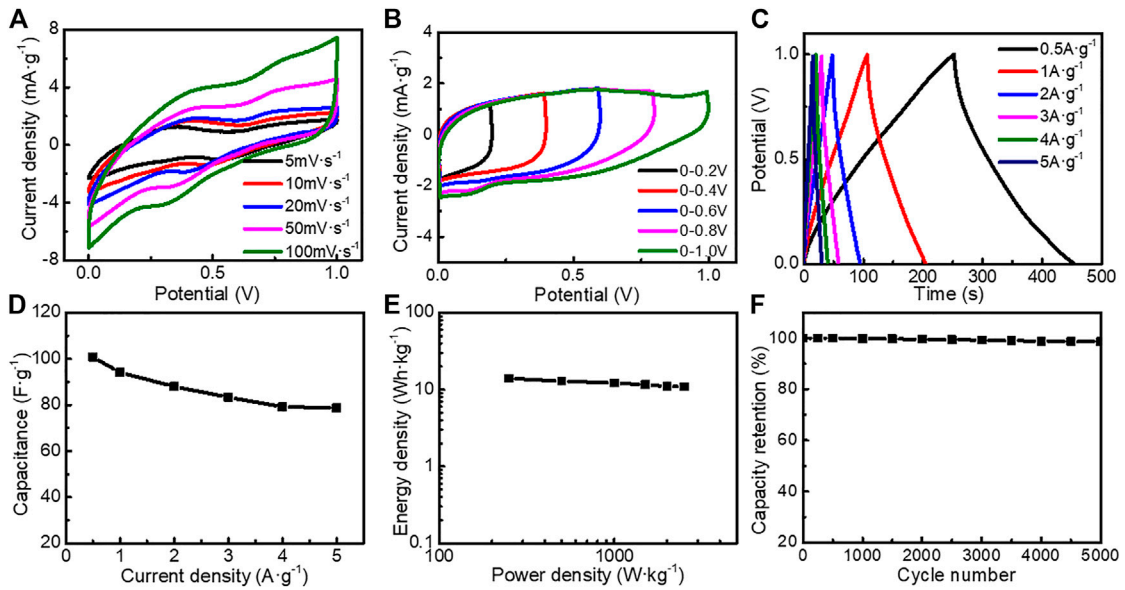


**FIGURE 9 |** Electrochemical performance of the asymmetric supercapacitor tested in 6 M KOH electrolyte **(A)** CV curves at different scan rates **(B)** CV curves at different potential ranges **(C)** GCD curves at different current densities **(D)** GCD curves at different potential ranges **(E)** Ragone plots of the asymmetric supercapacitor **(F)** cycling stability tested at 5 A $g^{-1}$.

outstanding cycling stability, which is attributed to the residual graphene layer remaining in the flower spherical structure.

To testify the outstanding performance of $MnO_2$/G composite with a flower spherical structure, we list the capacitance and long-term cycling performance of reported $MnO_2$/graphene in **Table 1**. Considering the difference in testing conditions, the $MnO_2$/C electrode material has the largest specific capacitance of 480.3 F $g^{-1}$ (Jeong et al., 2021). The maximum capacitance retention is 99.4% for 5,000 cycles (Vimuna et al., 2020). Although our $MnO_2$/G composite ($MnO_2$/G-10) has a low capacitance retention rate of 85.3%. Particularly, the specific capacitance of our $MnO_2$/G composite is 500 F $g^{-1}$, much higher than reported samples. Therefore, the $MnO_2$/G composite with flower spheres structure displays an excellent electrochemical performance, which can be ascribed to two aspects. First of all, a large amount of $MnO_2$ nanosheets arrays loading on graphene constructs a homogeneous hierarchical porous structure, which promotes the transport of electrons and ions, and reduces the charge transfer resistance. Moreover, the special microstructure facilitates the interface contact between $MnO_2$ nanosheets and electrolyte and releases a high specific capacitance. Secondly, TE-G is composed of stacking graphene layers, which facilitates the redox reaction between $KMnO_4$ and C, resulting in a high fraction of $MnO_2$ in composite, which increases the pseudocapacitance. Moreover, the residual graphene layer in composite improves the conductivity of electrode material and decreases the internal resistance, which enables an outstanding rate capability and cycling performance.

In addition, we assembled an asymmetric supercapacitor (ASC) with TE-G negative electrode and $MnO_2$/G-10 positive electrode. From **Figure 9A**, the CV curves show quasi-rectangular shapes. With an increase of scan rate, the area of the CV curve increases, with a shape of quasi-rectangular, further indicating the EDLC feature. The ASC can be operated stably under a broad voltage window of 0–1.0 V (**Figure 9B**). From

**Figure 9C**, the longest discharge time reaches 201.6 s, corresponding to the maximum specific capacitance of 100.8 F $g^{-1}$ at 0.5 A $g^{-1}$. The capacitance reduces to 78.8 F $g^{-1}$ at a large current density of 5 A $g^{-1}$, indicating an excellent rate capability. **Figure 9E** provides the energy density (E) and power density (P) at different current densities. The energy density is 14.0 Wh $kg^{-1}$ at the power density of 250.0 W $kg^{-1}$. With an increase of power density, the energy density drops to 10.94 Wh $kg^{-1}$ (2500 W $kg^{-1}$), further reflecting the excellent power/energy combination. **Figure 9F** shows the cycling stability of ASC. When measured at 5 A $g^{-1}$, the capacitance retention rate is 98.4% after 5,000 cycles, reflecting the superior cycling stability. Therefore, flower-like $MnO_2$/G microspheres exhibit outstanding performance in ASC.

## CONCLUSION

To hybridize thermally-exfoliated graphite (TE-G) and $MnO_2$, a $KMnO_4$-assisted hydrothermal method was adopted to achieve the exfoliation of TE-G and the loading of $MnO_2$ nanosheets. Through changing the ratio of TE-G and $KMnO_4$, flower-like $MnO_2$/G microspheres ($MnO_2$/G-10) were fabricated containing 83.2% $MnO_2$ and 16.8% residual graphene layer. To confirm the advantage of TE-G reactants, corresponding $MnO_2$/rGO composites were prepared by using rGO as raw materials. When tested in a three-electrode system, the $MnO_2$/G-10 sample displays a maximum specific capacitance of 500 F $g^{-1}$, an outstanding rate of performance, and a high capacitance retention rate (85.3% for 5,000 cycles). The performance is much better than that of the optimized $MnO_2$/rGO composite. The reason can be explained as the high carbon fraction in TE-G resulting in a high fraction of $MnO_2$ in flower-like $MnO_2$/G microspheres, and the oxygen-containing groups in rGO reduce the effective redox reaction between $KMnO_4$ and carbon. The superior electrochemical performance of $MnO_2$/G-10 is related to the hierarchical porous structure constructed by $MnO_2$ nanosheet arrays and conductive graphene in the composite. Moreover, the ASC consisted of $MnO_2$/G positive electrode and TE-G negative electrode has a capacitance of 100.8 F $g^{-1}$ at 0.5A $g^{-1}$, with a high capacitance retention of 98.6% for 5,000 cycles. The energy density is 14.0 Wh $kg^{-1}$ at the power density of 250.0 W $kg^{-1}$. In consideration of the low cost of raw materials, the $MnO_2$/G composite shows great application potential in the supercapacitors field.

## DATA AVAILABILITY STATEMENT

The original contributions presented in the study are included in the article/**Supplementary Material**, further inquiries can be directed to the corresponding author.

## AUTHOR CONTRIBUTIONS

XL: Conceptualization, Methodology, Experiment, Original draft preparation. BL: Conceptualization, Supervision, Reviewing and Editing. XH: Writing- Reviewing and Editing, Software JL: Investigation, Data curation.

## FUNDING

BL: The Department of Education of Liaoning Province, Liaoning Distinguished Professor Fund (512003,007021); Department of Science and Technology of Liaoning Province, Liaoning province unveils science and technology project (2021JH1/10400101); General project of national Natural Science Foundation of China (21777021) JL: Liaoning Provincial Department of Education Youth Seedling Project (LQ2020010) the PhD Start-up Research Foundation of Department of Science and Technology of Liaoning Province (2021-BS-184).

## SUPPLEMENTARY MATERIAL

The Supplementary Material for this article can be found online at: https://www.frontiersin.org/articles/10.3389/fchem.2022.870541/full#supplementary-material

## REFERENCES

Brousse, T., Taberna, P.-L., Crosnier, O., Dugas, R., Guillemet, P., Scudeller, Y., et al. (2007). Long-term Cycling Behavior of Asymmetric Activated carbon/MnO2 Aqueous Electrochemical Supercapacitor. *J. Power Sourc.* 173, 633–641. doi:10.1016/j.jpowsour.2007.04.074

Ferrero, G. A., Sevilla, M., and Fuertes, A. B. (2015). Mesoporous Carbons Synthesized by Direct Carbonization of Citrate Salts for Use as High-Performance Capacitors. *Carbon* 88, 239–251. doi:10.1016/j.carbon.2015.03.014

Gong, D., Tong, H., Xiao, J., Li, T., Liu, J., Wu, Y., et al. (2021). Self-standing Manganese Dioxide/graphene Carbon Nanotubes Film Electrode for Symmetric Supercapacitor with High Energy Density and superior Long Cycling Stability. *Ceramics Int.* 47, 33020–33027. doi:10.1016/j.ceramint.2021.08.202

Hong, X., Wang, X., Li, Y., Fu, J., and Liang, B. (2021). Sandwich Structured MnO2/carbon nanosheet/MnO2 Composite for High-Performance Supercapacitors. *J. Alloys Compd.* 889, 161821. doi:10.1016/j.jallcom.2021.161821

Jeong, J. M., Park, S. H., Park, H. J., Jin, S. B., Son, S. G., Moon, J. M., et al. (2021). Alternative-Ultrathin Assembling of Exfoliated Manganese Dioxide and Nitrogen-Doped Carbon Layers for High-Mass-Loading Supercapacitors with Outstanding Capacitance and Impressive Rate Capability. *Adv. Funct. Mater.* 31, 2009632. doi:10.1002/adfm.202009632

Lei, R., Gao, J., Qi, L., Ye, L., Wang, C., Le, Y., et al. (2020). Construction of MnO2 Nanosheets@graphenated Carbon Nanotube Networks Core-Shell Heterostructure on 316L Stainless Steel as Binder-free Supercapacitor Electrodes. *Int. J. Hydrogen Energ.* 45, 28930–28939. doi:10.1016/j.ijhydene.2019.09.070

Li, D., Lin, J., Lu, Y., Huang, Y., He, X., Yu, C., et al. (2020). MnO2 Nanosheets Grown on N-Doped Agaric-Derived Three-Dimensional Porous Carbon for Asymmetric Supercapacitors. *J. Alloys Compd.* 815, 152344. doi:10.1016/j.jallcom.2019.152344

Li, K., Hu, Z., Zhao, R., Zhou, J., Jing, C., Sun, Q., et al. (2021). A Multidimensional Rational Design of Nickel-Iron Sulfide and Carbon Nanotubes on Diatomite via

Synergistic Modulation Strategy for Supercapacitors. *J. Colloid Interf. Sci.* 603, 799–809. doi:10.1016/j.jcis.2021.06.131

Liu, X., Liang, B., and Long, J. (2021). Preparation of Novel Thick Sheet Graphene and its Effect on the Properties of Polyolefins with Different Crystallinities. *Polym. Bull.* doi:10.1007/s00289-021-03791-x

Liu, Y., He, D., Wu, H., Duan, J., and Zhang, Y. (2015). Hydrothermal Self-Assembly of Manganese Dioxide/Manganese Carbonate/Reduced Graphene Oxide Aerogel for Asymmetric Supercapacitors. *Electrochimica Acta* 164, 154–162. doi:10.1016/j.electacta.2015.01.223

Liu, Y., Yan, D., Li, Y., Wu, Z., Zhuo, R., Li, S., et al. (2014). Manganese Dioxide Nanosheet Arrays Grown on Graphene Oxide as an Advanced Electrode Material for Supercapacitors. *Electrochimica Acta* 117, 528–533. doi:10.1016/j.electacta.2013.11.121

Oncu, A., Cetinkaya, T., and Akbulut, H. (2021). Enhancement of the Electrochemical Performance of Free-Standing Graphene Electrodes with Manganese Dioxide and Ruthenium Nanocatalysts for Lithium-Oxygen Batteries. *Int. J. Hydrogen Energ.* 46, 17173–17186. doi:10.1016/j.ijhydene.2021.02.154

Ping, Y., Liu, Z., Li, J., Han, J., Yang, Y., Xiong, B., et al. (2019). Boosting the Performance of Supercapacitors Based Hierarchically Porous Carbon from Natural Juncus Effuses by Incorporation of MnO2. *J. Alloys Compd.* 805, 822–830. doi:10.1016/j.jallcom.2019.07.125

Raj, C. J., Manikandan, R., Cho, W.-J., Yu, K. H., and Kim, B. C. (2020). High-performance Flexible and Wearable Planar Supercapacitor of Manganese Dioxide Nanoflowers on Carbon Fiber Cloth. *Ceramics Int.* 46, 21736–21743. doi:10.1016/j.ceramint.2020.05.282

Sevilla, M., and Fuertes, A. B. (2014). Direct Synthesis of Highly Porous Interconnected Carbon Nanosheets and Their Application as High-Performance Supercapacitors. *ACS Nano* 8, 5069–5078. doi:10.1021/nn501124h

Sha, Z., Huang, F., Zhou, Y., Zhang, J., Wu, S., Chen, J., et al. (2021). Synergies of Vertical Graphene and Manganese Dioxide in Enhancing the Energy Density of Carbon Fibre-Based Structural Supercapacitors. *Composites Sci. Technol.* 201, 108568. doi:10.1016/j.compscitech.2020.108568

Srimuk, P., Luanwuthi, S., Krittayavathananon, A., and Sawangphruk, M. (2015). Solid-type Supercapacitor of Reduced Graphene Oxide-Metal Organic Framework Composite Coated on Carbon Fiber Paper. *Electrochimica Acta* 157, 69–77. doi:10.1016/j.electacta.2015.01.082

Tarimo, D. J., Oyedotun, K. O., Mirghni, A. A., Sylla, N. F., and Manyala, N. (2020). High Energy and Excellent Stability Asymmetric Supercapacitor Derived from sulphur-reduced Graphene Oxide/manganese Dioxide Composite and Activated Carbon from Peanut Shell. *Electrochimica Acta* 353, 136498. doi:10.1016/j.electacta.2020.136498

Thommes, M., and Cychosz, K. A. (2014). Physical Adsorption Characterization of Nanoporous Materials: Progress and Challenges. *Adsorption* 20, 233–250. doi:10.1007/s10450-014-9606-z

Toupin, M., Brousse, T., and Bélanger, D. (2004). Charge Storage Mechanism of MnO2 Electrode Used in Aqueous Electrochemical Capacitor. *Chem. Mater.* 16, 3184–3190. doi:10.1021/cm049649j

Vimuna, V. M., Athira, A. R., Dinesh Babu, K. V., and Xavier, T. S. (2020). Simultaneous Stirring and Microwave Assisted Synthesis of Nanoflakes MnO2/rGO Composite Electrode Material for Symmetric Supercapacitor with Enhanced Electrochemical Performance. *Diamond Relat. Mater.* 110, 108129. doi:10.1016/j.diamond.2020.108129

Wang, J., Yang, H., Sun, Q., Zhou, C., Zhang, X., Ge, L., et al. (2021a). Synthesis of δ-MnO2/C Assisted with Carbon Sheets by Directly Carbonizing from Corn Stalk for High-Performance Supercapacitor. *Mater. Lett.* 285, 129116. doi:10.1016/j.matlet.2020.129116

Wang, T., Li, K., Le, Q., Zhu, S., Guo, X., Jiang, D., et al. (2021b). Tuning Parallel Manganese Dioxide to Hollow Parallel Hydroxyl Oxidize Iron Replicas for High-Performance Asymmetric Supercapacitors. *J. Colloid Interf. Sci.* 594, 812–823. doi:10.1016/j.jcis.2021.03.075

Wang, X., Chen, S., Li, D., Sun, S., Peng, Z., Komarneni, S., et al. (2018). Direct Interfacial Growth of MnO2 Nanostructure on Hierarchically Porous Carbon for High-Performance Asymmetric Supercapacitors. *ACS Sustain. Chem. Eng.* 6, 633–641. doi:10.1021/acssuschemeng.7b02960

Wei, C., Xu, C., Li, B., Du, H., and Kang, F. (2012). Preparation and Characterization of Manganese Dioxides with Nano-Sized Tunnel Structures for Zinc Ion Storage. *J. Phys. Chem. Sol.* 73, 1487–1491. doi:10.1016/j.jpcs.2011.11.038

Xie, Y., Yang, C., Chen, P., Yuan, D., and Guo, K. (2019). MnO2-decorated Hierarchical Porous Carbon Composites for High-Performance Asymmetric Supercapacitors. *J. Power Sourc.* 425, 1–9. doi:10.1016/j.jpowsour.2019.03.122

Xu, M.-W., Zhao, D.-D., Bao, S.-J., and Li, H.-L. (2007). Mesoporous Amorphous MnO2 as Electrode Material for Supercapacitor. *J. Solid State. Electrochem.* 11, 1101–1107. doi:10.1007/s10008-006-0246-4

Xu, Z., Sun, S., Cui, W., Lv, J., Geng, Y., Li, H., et al. (2018). Interconnected Network of Ultrafine MnO2 Nanowires on Carbon Cloth with weed-like Morphology for High-Performance Supercapacitor Electrodes. *Electrochimica Acta* 268, 340–346. doi:10.1016/j.electacta.2018.02.138

Yan, C., Tong, X., Qu, Y., Zhou, Y., Pang, N., Xu, S., et al. (2021). Porous Manganese Dioxide Nanosheets on Modified Graphite Felt for Cathodes in High-Capacity Flexible Zinc-MnO2 Batteries. *Vacuum* 191, 110353. doi:10.1016/j.vacuum.2021.110353

Yan, D., Zhang, H., Li, S., Zhu, G., Wang, Z., Xu, H., et al. (2014). Formation of Ultrafine Three-Dimensional Hierarchical Birnessite-type MnO2 Nanoflowers for Supercapacitor. *J. Alloys Compd.* 607, 245–250. doi:10.1016/j.jallcom.2014.04.077

Yang, G., and Park, S.-J. (2018). MnO2 and Biomass-Derived 3D Porous Carbon Composites Electrodes for High Performance Supercapacitor Applications. *J. Alloys Compd.* 741, 360–367. doi:10.1016/j.jallcom.2018.01.108

Yang, W., Gao, Z., Wang, J., Wang, B., Liu, Q., Li, Z., et al. (2012). Synthesis of Reduced Graphene Nanosheet/urchin-like Manganese Dioxide Composite and High Performance as Supercapacitor Electrode. *Electrochimica Acta* 69, 112–119. doi:10.1016/j.electacta.2012.02.081

Yang, Y., Niu, H., Qin, F., Guo, Z., Wang, J., Ni, G., et al. (2020). MnO2 Doped Carbon Nanosheets Prepared from Coal Tar Pitch for Advanced Asymmetric Supercapacitor. *Electrochimica Acta* 354, 136667. doi:10.1016/j.electacta.2020.136667

Zhang, H., Lin, L., Wu, B., and Hu, N. (2020a). Vertical Carbon Skeleton Introduced Three-Dimensional MnO2 Nanostructured Composite Electrodes for High-Performance Asymmetric Supercapacitors. *J. Power Sourc.* 476, 228527. doi:10.1016/j.jpowsour.2020.228527

Zhang, M., Yang, D., and Li, J. (2020b). Effective Improvement of Electrochemical Performance of Electrodeposited MnO2 and MnO2/reduced Graphene Oxide Supercapacitor Materials by Alcohol Pretreatment. *J. Energ. Storage* 30, 101511. doi:10.1016/j.est.2020.101511

Zhang, M., Zheng, H., Zhu, H., Xu, Z., Liu, R., Chen, J., et al. (2020c). Graphene-wrapped MnO2 Achieved by Ultrasonic-Assisted Synthesis Applicable for Hybrid High-Energy Supercapacitors. *Vacuum* 176, 109315. doi:10.1016/j.vacuum.2020.109315

Zhang, N., Fu, C., Liu, D., Li, Y., Zhou, H., and Kuang, Y. (2016). Three-Dimensional Pompon-like MnO2/Graphene Hydrogel Composite for Supercapacitor. *Electrochimica Acta* 210, 804–811. doi:10.1016/j.electacta.2016.06.004

Zhang, W., Yang, Y., Xia, R., Li, Y., Zhao, J., Lin, L., et al. (2020d). Graphene-quantum-dots-induced MnO2 with Needle-like Nanostructure Grown on Carbonized wood as Advanced Electrode for Supercapacitors. *Carbon* 162, 114–123. doi:10.1016/j.carbon.2020.02.039

Zhang, W., Yuan, X., Yan, X., You, M., Jiang, H., Miao, J., et al. (2021). Tripotassium Citrate Monohydrate Derived Carbon Nanosheets as a Competent Assistant to Manganese Dioxide with Remarkable Performance in the Supercapacitor. *Front. Chem. Sci. Eng.* doi:10.1007/s11705-021-2065-7

Zhao, N., Deng, L., Luo, D., and Zhang, P. (2020). One-step Fabrication of Biomass-Derived Hierarchically Porous carbon/MnO Nanosheets Composites for Symmetric Hybrid Supercapacitor. *Appl. Surf. Sci.* 526, 146696. doi:10.1016/j.apsusc.2020.146696

Zhou, D., Lin, H., Zhang, F., Niu, H., Cui, L., Wang, Q., et al. (2015). Freestanding MnO2 Nanoflakes/porous Carbon Nanofibers for High-Performance Flexible Supercapacitor Electrodes. *Electrochimica Acta* 161, 427–435. doi:10.1016/j.electacta.2015.02.085

Zhu, L., Wang, J., Rong, S., Wang, H., and Zhang, P. (2017). Cerium Modified Birnessite-type MnO2 for Gaseous Formaldehyde Oxidation at Low

Temperature. *Appl. Catal. B: Environ.* 211, 212–221. doi:10.1016/j.apcatb.2017.04.025

**Conflict of Interest:** The authors declare that the research was conducted in the absence of any commercial or financial relationships that could be construed as a potential conflict of interest.

**Publisher's Note:** All claims expressed in this article are solely those of the authors and do not necessarily represent those of their affiliated organizations, or those of the publisher, the editors and the reviewers. Any product that may be evaluated in this article, or claim that may be made by its manufacturer, is not guaranteed or endorsed by the publisher.

frontiers | Frontiers in Chemistry

ORIGINAL RESEARCH
published: 12 April 2022
doi: 10.3389/fchem.2022.891640

# Self-Assembled Pt/$MoC_x$/MWCNTs Nano Catalyst for Ethanol Electrooxidation of Fuel Cells

*Xiaochang Cao*[1], *Zhongming Qiu*[2], *Jianjun Chen*[2] *and Tianyu Ai*[1,3]*

[1]School of Mechanical Engineering, Dongguan University of Technology, Dongguan, China, [2]Dongguan JoySun New Energy Co. Ltd., Dongguan, China, [3]School of Materials and Metallurgy, University of Science and Technology Liaoning, Anshan, China

Direct ethanol fuel cells (DEFCs) have attracted more and more attention because of their unique advantages such as low cost and low toxicity. However, sluggish C-C bond cleavage during the ethanol electrooxidation reaction (EOR) in acidic media results in a lower energy yield and gravely hinders the commercialization of DEFCs. Therefore, it is very necessary to develop an anode catalyst with high performance, high stability and low cost to solve this problem. In this paper, Pt/$MoC_x$/MWCNTs nanocomposites with different mass ratios of PtMo were obtained through a molecular self-assembly technology. The structure and morphology of Pt/$MoC_x$/MWCNTs nanocomposites were characterized by several techniques such as XRD, FESEM, XPS, etc. The electrochemical performance and stability of Pt/$WC_x$/MWCNTs electrocatalysts toward EOR were investigated in acid electrolytes. The results show that PtMo exists in the form of alloy. The size of Pt/$MoC_x$ nanoparticles is very uniform with an average size of ~24 nm. The Pt/$MoC_{0.25}$/MWCNTs exhibits excellent electrocatalytic activities with an electrochemically active surface area of 37.1 $m^2\ g^{-1}$, a peak current density of 610.4 mA $mg_{Pt}^{-1}$ and a steady-state current density of 39.8 mA $mg_{Pt}^{-1}$ after 7,200 s, suggesting that the Pt/$MoC_{0.25}$/MWCNTs is a very promising candidate for application in EOR of DEFCs.

**Keywords: direct ethanol fuel cell, electrocatalyst, platinum, self-assembly, molybdenum carbon**

OPEN ACCESS

***Edited by:***
*Feng Gu,*
*Jiangxi University of Science and Technology, China*

***Reviewed by:***
*Wei Xiao,*
*Yangtze University, China*
*Haisheng Fang,*
*Kunming University of Science and Technology, China*

***Correspondence:**
*Tianyu Ai*
*tianyuai90@126.com*

***Specialty section:***
*This article was submitted to Physical Chemistry and Chemical Physics, a section of the journal Frontiers in Chemistry*

***Received:*** *08 March 2022*
***Accepted:*** *28 March 2022*
***Published:*** *12 April 2022*

***Citation:***
*Cao X, Qiu Z, Chen J and Ai T (2022) Self-Assembled Pt/$MoC_x$/MWCNTs Nano Catalyst for Ethanol Electrooxidation of Fuel Cells. Front. Chem. 10:891640. doi: 10.3389/fchem.2022.891640*

## INTRODUCTION

Direct ethanol fuel cells (DEFCs) have many advantages such as high power density, environmental friendliness, rapid start-up and mobility, so they are believed as the most promising high energy conversion system for practical applications in mobile devices such as automotive and portable power (Singla et al., 2017; Jiang et al., 2018; Oh et al., 2019; Wang et al., 2022). However, there are still many challenges in the energy conversion processes of DEFCs, such as the difficulty in splitting the C-C bond of ethanol and the sluggish kinetics of electrocatalytic oxidation (Du et al., 2017; Zamanzad Ghavidel et al., 2017; Zhang et al., 2018). Reasonable use of catalysts can improve the energy output efficiency and overall performance of fuel cells, the problem of incomplete oxidation of ethanol can be effectively solved in DEFCs (Corradini et al., 2015; Huang et al., 2015; Bach Delpeuch et al., 2016). At present, the most promising and active catalysts for EOR are Pt in acid media of DEFCs. However, the high price, rare reserve and its low tolerance to CO severely limit its extensive commercialization (Pech-Rodríguez et al., 2017; Yang et al., 2019; Zhu et al., 2021). Therefore, it is significant and urgent to fabricate Pt-based nanocatalysts with active C-C bond cleavage ability and enhanced CO tolerance for efficient EOR.

Transition metal carbides (TMC) with high metal conductivity, strong corrosion-resistance, high stability and rich sources have a similar catalytic activity to platinum group metals (PGMs) (Hamo

et al., 2019; Zhang et al., 2019; Jiang et al., 2020; Fang et al., 2021). They have been widely concerned and applied as catalysts for fuel cells, such as WC (Hunt et al., 2014; Kelly et al., 2014; Oh et al., 2014), TaC (Myochi et al., 2018; Gao et al., 2020a), TiC (Hunt et al., 2016), $Mo_2C$ (Lin et al., 2017; Hassan and Ticianelli, 2018). The WC/p-CNFs composite catalyst was prepared and used in alkaline media (Oh et al., 2014). Due to the unique structure of p-CNFs and the synergistic effect between WC and p-CNFs, WC/p-CNFs composite catalyst increased the electrocatalytic performance for ethanol oxidation in DEFCs. Hunt et al. (2014) synthesized WC nanoparticles through a multi-step method. WC nanoparticles showed high electrocatalytic activity and stability under acid conditions. However, compared with Pt, TMC has lower catalytic activity for EOR, but it shows strong stability and anti-poisoning ability. Therefore, the Pt and TMC composite catalysts have been widely studied to reduce costs and further improve performance. Kelly et al. (2014) investigated ethanol electrooxidation of Pt/WC by density functional theory (DFT) and surface science experiments. The results showed that Pt/WC could oxidize ethanol to $CO_2$ more effectively than Pt and improve the output power of DEFCs. Subsequently, Pt/TaC electrocatalyst was prepared by the wet impregnation method (Jiang et al., 2018). The results showed that 1.5 wt% Pt/TaC demonstrated higher activity and stability for EOR than 40 wt% Pt/C. For 1.5 wt% Pt/TaC, the Pt surface was less poisoned by EOR intermediates and had a higher CO selectivity. Besides, the DFT study showed that the binding energy of EOR intermediates on Pt (111) surface was higher than that on Pt/TaC (111) surface, which further proved that the poison tolerance of Pt/TaC was increased. $Pt/Mo_2C$/C-cp catalyst was synthesized by a coprecipitation method (Li et al., 2015; Lin et al., 2017; Hassan and Ticianelli, 2018). The direct chemical bonding of Pt and MoC in $Pt/Mo_2C$/C-cp catalyst significantly reduced the onset CO oxidation potential and anti-CO poisoning ability to intermediates species. The above results show that the addition of TMC to Pt nanocatalysts can diminish the overpotentials, partially facilitate the C-C bond cleavage towards $CO_2$ and increase EOR activity. However, the synthesis of Pt/TMC catalyst usually requires multiple steps. TMC nanoparticles are easy to agglomerate, resulting in the reduction of specific surface area and catalytic activity.

In this work, we designed a simple molecular self-assembly technology to synthesize platinum/molybdenum carbide/multi-walled carbon nanotubes ($Pt/MoC_x$/MWCNTs) as active electrocatalysts for EOR in acid media. MWCNTs have a high specific surface area and excellent electrical properties at room temperature, which are especially suitable for high-performance catalysts (Lu et al., 2012; Nie et al., 2012; Sabnis et al., 2015). $Pt/MoC_x$/MWCNTs catalyst exhibits high catalytic activity and anti-CO poisoning ability. The outstanding performance of the catalyst is attributed to the complete exposure of the active sites and the synergistic effect between Pt and MoC.

# EXPERIMENT

## Materials

Hexachloroplatinic acid ($H_2PtCl_6{\cdot}6H_2O$), MWCNTs, sodium molybdate dihydrate ($Na_2MoO_3{\cdot}2H_2O$) were purchased from Shanghai Micklin Biochemical Co. Ltd. PDDA [$(C_8H_{16}CIN)_n$], ethanol ($CH_3CH_2OH$), concentrated sulfuric acid ($H_2SO_4$) were purchased from AiKe reagent. Concentrated nitric acid ($HNO_3$), Nafion solution (5 wt% in isopropanol and water) was purchased from Shanghai Aladdin Biochemical Technology Co. Ltd. All reagents were used in this work without further treatment.

## Synthesis of $Pt/MoC_x$/MWCNTs

The samples of $Pt/MoC_x$/MWCNTs were obtained by adjusting the addition amount of sodium molybdate. First, MWCNTs were treated in acid solution (90 ml $H_2SO_4$ and 30 ml $HNO_3$) by stirring for 60 min and ultrasound for 60 min to form a homogeneous solution. This slurry was centrifuged and washed three times with deionized water to obtain acid-MWCNTs. Then acid-MWCNTs and PDDA were dissolved in 200 ml deionized water by ultrasonic treatment for 60 min. The mixed solution was filtered and dispersed with deionized water. Second, 0.1 mmol sodium molybdate and 0.4 mmol chloroplatinic acids were added to the above solution under magnetic stirring for 40 min. The nanopowder was obtained by freeze-drying overnight. Subsequently, the powder were sintered under $Ar/H_2$ atmosphere at 1,200°C for 180 min at 2°C $min^{-1}$. Finally, the $Pt/MoC_{0.25}$/MWCNTs was recieved after cooling to room temperature.

## Characterization

The crystal structures were characterized by X-ray diffraction (XRD, PANalytical B.V) patterns. The data was collected from 10° to 90° at a scan speed of 15 $min^{-1}$. The morphology and the size of $Pt/MoC_x$/MWCNTs were observed by transmission electron microscopy (TEM, JEOL 2010) operating at 200 kV. The three-dimensional structure, distribution and element composition of nanoparticles on MWCNTs were observed by field emission scanning electron microscope (FESEM, JEOL JSM-6340F, 5 kV) in combination with energy-dispersive X-ray spectroscopy (EDS). The surface elemental composition and valence analysis of spherical nanoparticles were measured by X-ray photoelectron spectroscopy (XPS, PHI-5702) with a monochromatized Al Ka X-ray source (1,486.6 eV photons) and pass energy of 40 eV. The anode voltage was 15 mV with a current of 10 mA. To compensate for the effects of surface charging, all core-level spectra were referenced to the C1s hydrocarbon peak at 284.8 eV. The Raman spectrum of spherical nanoparticles was obtained by using a Renishaw RW1000 Raman spectroscope.

The electrochemical tests were performed on Autolab (PGSTAT 302N) at room temperature. The counter electrode is made of the platinum sheet with a size of 7 mm × 15 mm. For the reference electrode silver chloride (Ag/AgCl) is selected in this work. Glassy carbon electrode (GCE) with a diameter of 5 mm is used for the working electrode (WE). Catalyst inks were produced

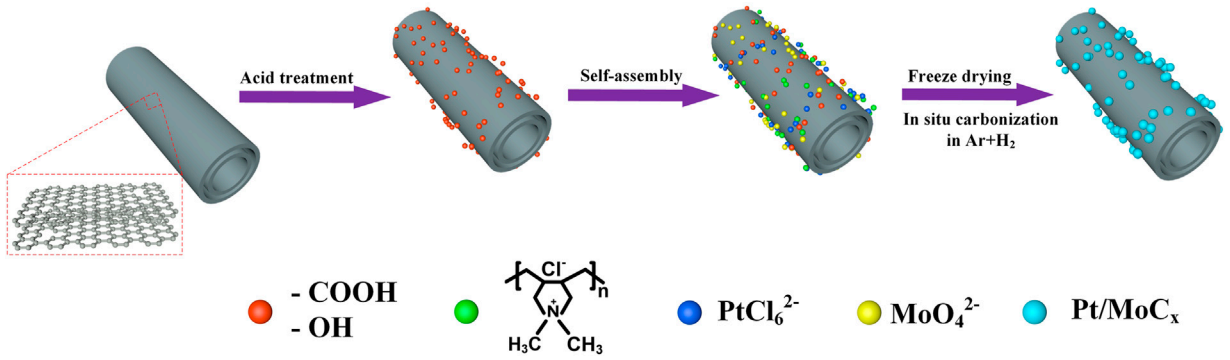


**FIGURE 1 |** Schematic diagram for synthesizing Pt/$MoC_x$/MWCNTs.

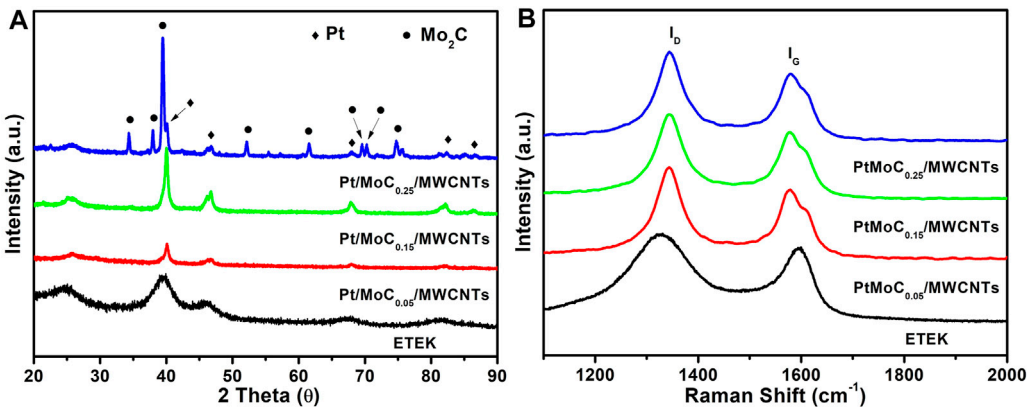


**FIGURE 2 | (A)** Wide-angle XRD patterns and **(B)** Raman spectra of ETEK and Pt/$MoC_x$/MWCNTs.

by mixing 5 mg Pt/$MoC_x$/MWCNTs nanoparticles with 1 ml 0.5 wt% Nafion/isopropanol. Then, the catalyst ink was ultrasound for 20 min. Finally, 10 μl catalyst ink was dropped on the surface of GCE and dried in air. The ECSA of ETEK and Pt/$MoC_x$/MWCNTs electrocatalysts was measured in a nitrogen-saturated 0.5 M $H_2SO_4$ solution at a scan rate of 50 mV $s^{-1}$. The electrocatalytic activity for EOR was characterized by the CV measurements in a nitrogen-purged 0.5 M $H_2SO_4$ + 1.0 M ethanol solution at a scan rate of 50 mV $s^{-1}$. Te stability was examined by CA tests at a constant potential of 0.6 V vs. Ag/AgCl.

## RESULTS AND DISCUSSION

The synthesis route of Pt/$MoC_x$/MWCNTs nanoparticles by molecular self-assembly is illustrated in **Figure 1**. Negative charges (–OH, –COOH), strong cationic polyelectrolyte PDDA, $PtCl_6^{2-}$ and $MoO_4^{2-}$ were adsorbed on MWCNTs through electrostatic adsorption to realize layer-by-layer assembly. Then, the precursors were dried under freeze-drying conditions and calcined in a weak reducing atmosphere to obtain Pt/$MoC_x$/MWCNTs nanoparticles.

The XRD spectra of ETEK and Pt/$MoC_x$/MWCNTs are shown in **Figure 2A**. The diffraction peaks at 39.44°, 46.56°, 67.98°, and 81.91° closely matched with standard values of diffraction peaks for Pt (PDF#03-065-5035) (Sabnis et al., 2015), which indicates that $H_2PtCl_6$ has been successfully reduced to Pt. However, not only the characteristic peaks of Pt but also the diffraction peaks at 34.34°, 37.98°, 39.42°, 52.14°, 61.5°, 69.56°, and 74.73° are very consistent with the standard values of $Mo_2C$ (PDF#00-035-0787) in the Pt/$MoC_{0.25}$/MWCNTs (Li et al., 2019). When the content of Mo continues to increase, Mo forms PtMo alloy and $Mo_2C$. The average diameters of PtMo alloy nanoparticles are calculated by the Scherrer equation, as shown in **Table 1**. The Scherrer constant is 0.9 and the wavelength is 1.54 Å in this case for Cu Kα radiation in the Scherrer equation. The grain sizes of Pt/$MoC_{0.05}$/MWCNTs, Pt/$MoC_{0.15}$/MWCNTs and Pt/$MoC_{0.25}$/MWCNTs are about 23.72, 23.82 and 23.84 nm. Because the radius of doping $Mo^{4+}$ ionic is large than $Pt^{6+}$, the lattice constant of Mo doped all increase to some extent in Pt/$MoC_x$/MWCNTs, compared to ETEK. These results indicate that Pt/$MoC_x$/MWCNTs can be directly prepared by using the molecular self-assembly method.

**TABLE 1 |** Physicochemical parameters of different sample.

| Samples | Average diameter (nm) | Lattice parameters (nm) | Pt: Mo ratio (at %) |
|---|---|---|---|
| ETEK | 4.36 | 0.389 | 100:0 |
| $Pt/MoC_{0.05}$/MWCNTs | 23.72 | 0.391 | 95:5 |
| $Pt/MoC_{0.15}$/MWCNTs | 23.82 | 0.391 | 85:15 |
| $Pt/MoC_{0.25}$/MWCNTs | 23.84 | 0.391 | 75:25 |

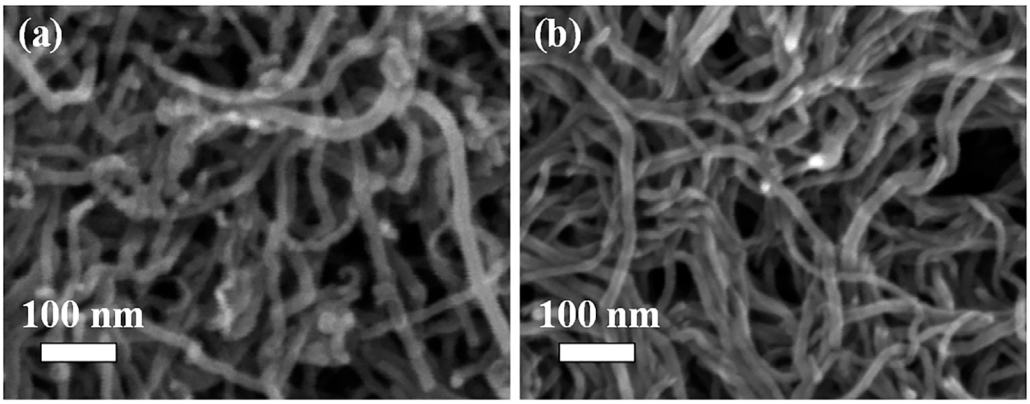


**FIGURE 3 |** FESEM images of **(A)** MWCNTs and **(B)** acid-treated MWCNTs.

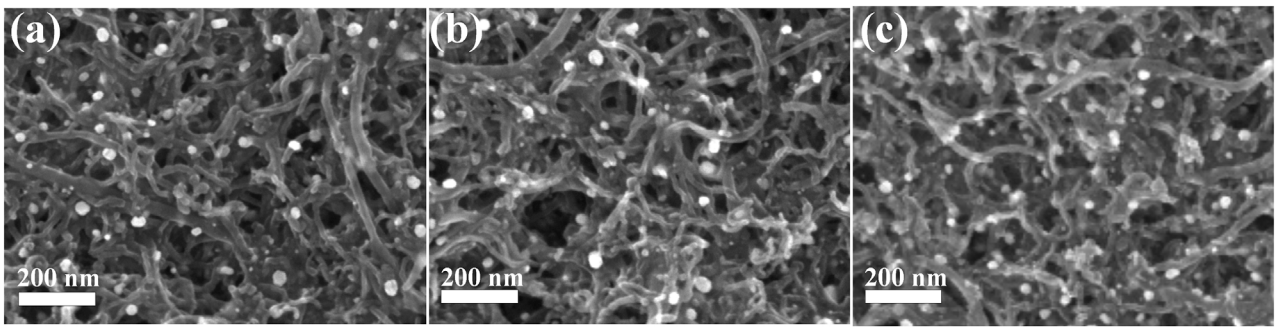


**FIGURE 4 |** FESEM images of **(A)** $Pt/MoC_{0.05}$/MWCNTs, **(B)** $Pt/MoC_{0.15}$/MWCNTs and **(C)** $Pt/MoC_{0.25}$/MWCNTs.

There are two main peaks at about 1,580 $cm^{-1}$ (G band, represents $E_{2g}$ vibration) and 1,343 $cm^{-1}$ (D band, represents $A_{1g}$ vibration). The graphitization degree of MWCNTs is expressed by the relative strength of D-band ($I_D$) and G-band ($I_G$) (Dietrich et al., 2014). The $I_G/I_D$ ratios of ETEK, $Pt/MoC_{0.05}$/MWCNTs, $Pt/MoC_{0.15}$/MWCNTs and $Pt/MoC_{0.25}$/MWCNTs are 0.9, 0.8, 0.9, and 0.9, respectively. The corresponding results indicate that the graphitization degrees of ETEK and $Pt/MoC_x$/MWCNTs are similar.

The SEM images of MWCNTs before and after treatment in mixed acid solution are shown in **Figure 3**. It can be seen that the MWCNTs have no fracture and the diameter and morphology do not change significantly after ultrasonic and mixed acid treatment. The FESEM images of $Pt/MoC_{0.05}$/MWCNTs, $Pt/MoC_{0.15}$/MWCNTs and $Pt/MoC_{0.25}$/MWCNTs are shown in **Figure 4**. As a support material, the morphology of MWCNTs has no obvious change after composite with $Mo_xC$ nanoparticles, indicating that its structure has not been damaged in the synthesis process (Wang et al., 2019). $Pt/Mo_x$ nanoparticles are uniformly dispersed on the surface of MWCNTs without agglomeration. The size of $Pt/Mo_x$ is uniform and its particle size is about 24 nm, which is consistent with Scherrer's calculation results. The successful preparation of $Pt/Mo_x$ nanoparticles is closely related to the addition of ionic surfactant PDDA. PDDA is hydrolyzed in the precursor solution to form ion pairs. The existence of ion pairs slows down the reduction process and controls the growth rate of nanoparticles.

**Figure 5** shows the EDS results of $Pt/MoC_x$/MWCNTs samples. There are characteristic peaks of C, Pt and Mo in Pt/

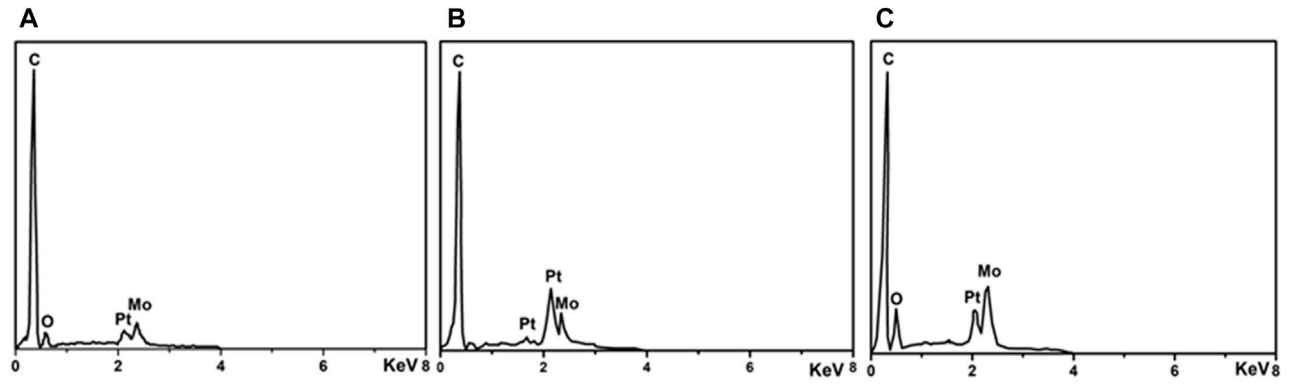


**FIGURE 5 |** EDX analysis of **(A)** Pt/$MoC_{0.05}$/MWCNTs, **(B)** Pt/$MoC_{0.15}$/MWCNTs and **(C)** Pt/$MoC_{0.25}$/MWCNTs.

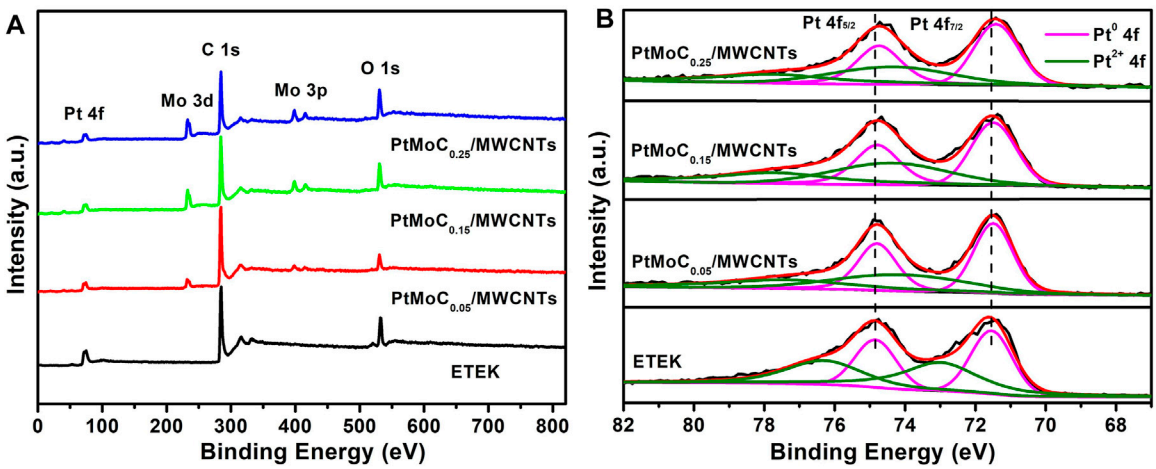


**FIGURE 6 | (A)** Survey scanned XPS spectrum and **(B)** high-resolution Pt 4f spectra of ETEK, Pt/$MoC_x$/MWCNTs.

**TABLE 2 |** Binding energies of XPS spectra of Pt in ETEK and Pt/$MoC_x$/MWCNTs.

| Sample | Species | | | |
|---|---|---|---|---|
| | $Pt^0$ $4f_{7/2}$ | $Pt^{2+}$ $4f_{7/2}$ | $Pt^0$ $4f_{5/2}$ | $Pt^{2+}$ $4f_{5/2}$ |
| ETEK | 71.55 | 73.05 | 74.85 | 76.35 |
| Pt/$MoC_{0.05}$/MWCNTs | 71.47 | 74.2 | 74.77 | 77.5 |
| Pt/$MoC_{0.15}$/MWCNTs | 71.45 | 74.39 | 74.75 | 77.69 |
| Pt/$MoC_{0.25}$/MWCNTs | 71.42 | 74.47 | 74.72 | 77.77 |

$MoC_x$/MWCNTs composites and no other element peaks. **Figure 6** investigates the surface elements and chemical states of Pt/$MoC_x$/MWCNTs composites by XPS. The characteristic peaks of C, Pt and Mo were observed in Pt/$MoC_x$/MWCNTs composites and the intensities of characteristic peaks for Mo 3d and Mo 3p gradually increased with the increase of Mo element content as shown in **Figure 6A**. The surface valence state of Pt in Pt/$MoC_x$/MWCNTs composites is shown in **Figure 6B**. The Pt 4f spectra of Pt/$MoC_x$/MWCNTs show two peaks of Pt $4f_{7/2}$ and Pt $4f_{5/2}$ and can be further divided into two doublet peaks, which associates with metal Pt and Pt oxide. It is worth noting that, compared with ETEK, the bond energy of Pt 4f in Pt/$MoC_x$/MWCNTs shifts slightly to the negative phase and the peak binding energy is shown in **Table 2**. The shift of bond energy is caused by the electronegativity of Pt, which may cause the more charges transformation from Mo to Pt. The decrease of Pt bond energy will weaken the adsorption energy of Pt and $CO_{ads}$, promote the removal of $CO_{ads}$ and promote the breaking of C-H (Lu et al., 2016; Gao et al., 2020b).

The electrocatalytic activity of Pt/$MoC_x$/MWCNTs composites catalyst in acid medium is shown in **Figure 7**. **Figure 7A** shows the cyclic voltammetry (CV) curves of ETEK, Pt/$MoC_{0.05}$/MWCNTs, Pt/$MoC_{0.15}$/MWCNTs and Pt/$MoC_{0.25}$/MWCNTs catalysts in a $N_2$-saturated 0.5 M $H_2SO_4$ solution. In **Figure 7B**, the electrochemically active surface area (ECSA) can be obtained from the hydrogen adsorption/desorption region in a 0.5 M $H_2SO_4$ solution. The specific value of ECSA for the Pt/$MoC_{0.25}$/MWCNTs is 37.1 $m^2\ g^{-1}$, which is

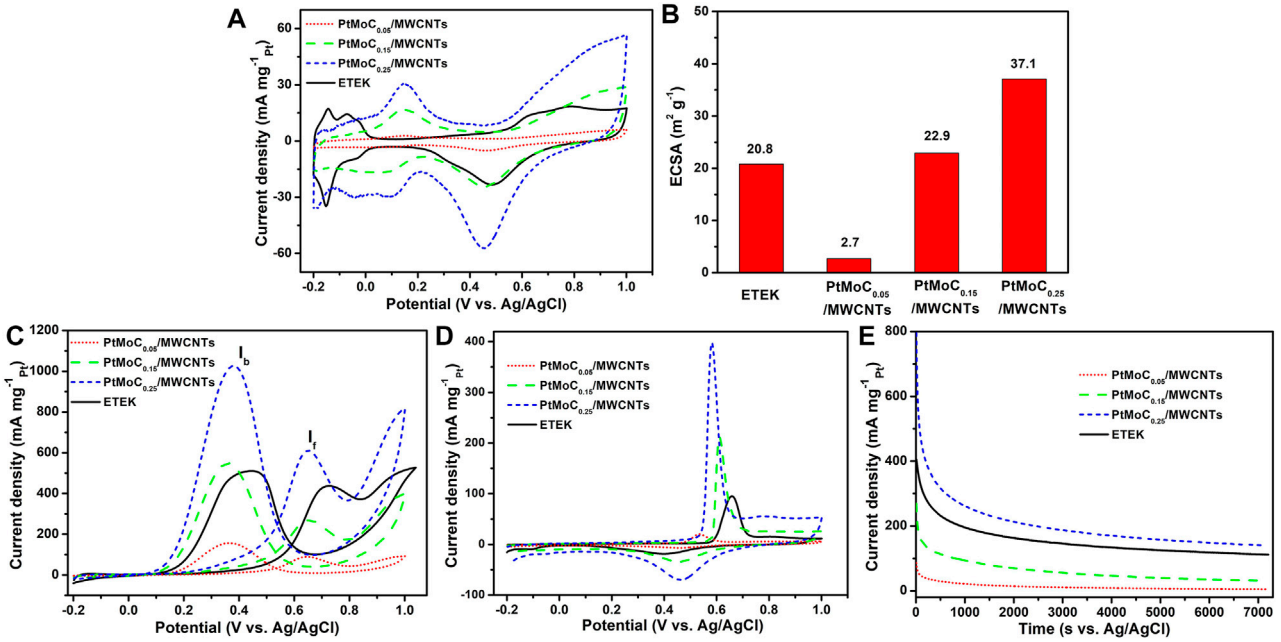


**FIGURE 7 |** CV of the catalysts **(A)** in a $N_2$-saturated 0.5 M $H_2SO_4$ solution, **(B)** ECSA, **(C)** in a $N_2$-saturated 0.5 M $H_2SO_4$ + 1 M $CH_3CH_2OH$ solution, **(D)** CO stripping voltammograms in a 0.5 M $H_2SO_4$ solution at 25°C with a scan rate of 50 mV $s^{-1}$ and **(E)** CA curves of the catalysts in a $N_2$-saturated 0.5 M $H_2SO_4$ + 1 M $CH_3CH_2OH$ solution at 25°C.

**TABLE 3 |** Comparisons of the EOR performance for Pt based catalysts in recently published papers.

| Refs. | Catalyst | ECSA ($m^2$ $g_{Pt}^{-1}$) | Electrolyte | Mass activity (mA $mg_{Pt}^{-1}$) | Methods |
|---|---|---|---|---|---|
| 13 | Pt/BC | 52.7 | 0.5 M $H_2SO_4$ + 1.0 M $CH_3CH_2OH$ | 770 | Solvent heating method |
| 30 | Rh@Pt d-CNCs | 34.65 | 0.1 M $HClO_4$ + 0.2 M $CH_3CH_2OH$ | 860 | Solvent heating method |
| 34 | PtCo@N-GNS-3 | — | 0.5 M $H_2SO_4$ + 0.5 M $CH_3CH_2OH$ | 196 | Hydrolysis-pyrolysis method |
| 35 | Pt-AuSn$O_x$ | 44.1 | 0.5 M $H_2SO_4$ + 1.0 M $CH_3CH_2OH$ | 305 | Improved impregnation method |
| 37 | Pt/α-Pt$O_x$/$WO_3$ | 151.6 | 0.1 M NaOH + 1.0 M $CH_3CH_2OH$ | 2,760 | One-pot solvothermal method |
| This work | Pt/Mo$C_x$/MWCNTs | 37.1 | 0.5 M $H_2SO_4$ + 1.0 M $CH_3CH_2OH$ | 610.4 | Molecular self-assembly method |

slightly higher than that commercial TETK electrocatalyst (20.8 $m^2$ $g^{-1}$). Due to the uniform distribution of Pt/MoC nanoparticles and the electronic structure change caused by the introduction of Mo, the ECSA area is increasing. These results indicate that more Pt active sites on Pt/$MoC_{0.25}$/MWCNTs are exposed for EOR (Dai et al., 2020).

In **Figure 7C**, the electrocatalytic activities of Pt/Mo$C_x$/MWCNTs and ETEK for EOR were tested in a $N_2$-saturated 0.5 $H_2SO_4$ with 1.0 M $CH_3CH_2OH$ solution. During the EOR forward scanning of Pt/Mo$C_x$/MWCNTs electrocatalysts, there is one peak at 0.65 V, which is caused by the fracture of the C-C or C-O bond (ethanol oxidations to acetaldehyde, acetic acid and $CO_2$). During the reverse scanning, the peak current appeared at 0.38 V related to the oxidation of intermediates from ethanol dissociative adsorption (e.g., CO). It is known that the excessive accumulation of intermediates leads to catalyst poisoning. Therefore, the current density ratio between peak f and b ($I_f$/$I_b$) has been used to evaluate the anti-poison capability of electrocatalysts. According to the calculation results, the surface of Pt/Mo$C_x$/MWCNTs shows higher anti-CO poisoning ability than ETEK. As can be seen from **Figure 7C**, the peak current densities of Pt/$MoC_{0.25}$/MWCNTs is 610.4 mA $mg_{Pt}^{-1}$, which is about 1.4 times that of ETEK (449.2 mA $mg_{Pt}^{-1}$). Due to the synergistic effect between Pt and MoC and the promotion of MoC in the adsorption of reaction and the desorption of products, the EOR activity of

the composite catalyst is significantly increased (Robinson et al., 2016; Xiao et al., 2021). EOR performance and the synthesis method of the current work were compared to relevant reports, as shown in **Table 3**.

The anti-poisoning of $Pt/MoC_x$/MWCNTs catalyst is a very important parameter in practical application. The CO stripping voltammetry curve was tested in 0.5 M $H_2SO_4$, as shown in **Figure 7D**. The onset potentials of CO for ETEK, $Pt/MoC_{0.05}$/MWCNTs, $Pt/MoC_{0.15}$/MWCNTs and $Pt/MoC_{0.25}$/MWCNTs were 0.58, 0.45, 0.57, and 0.48 V, respectively. The $Pt/MoC_x$/MWCNTs catalyst can oxidize CO at low potential, which makes CO easier to desorb from the surface of nanoparticles, releases more active sites and improves the performance of $Pt/MoC_x$/MWCNTs catalyst. In addition, the peak voltage of $Pt/MoC_{0.25}$/MWCNTs is about 80 mV lower than ETEK, indicating that $Pt/MoC_{0.25}$/MWCNTs catalyst has higher CO oxidation activity.

In **Figure 7E**, the stability of $Pt/MoC_x$/MWCNTs catalyst is tested by the chronoamperometric (CA) method at a constant potential of 0.6 V for 7,200 s. As shown in the current-time curves, the initial current values of ETEK, $Pt/MoC_{0.05}$/MWCNTs, $Pt/MoC_{0.15}$/MWCNTs and $Pt/MoC_{0.25}$/MWCNTs catalysts are 404.6, 85.8, 268.9 and 820.2 mA $mg_{Pt}^{-1}$, respectively. The polarization current of all catalysts decreases sharply within 200 s, which is caused by the poisoning of $Pt/MoC_x$ and the reduction of catalytic active sites caused by the intermediates during the electrooxidation of ethanol (Mao et al., 2017). In the following time, the current gradually reaches a plateau due to the established balance between the adsorption and oxidation of the intermediates. After 7,200 s, the current of $Pt/MoC_{0.25}$/MWCNTs still reached 139.8 mA $mg_{Pt}^{-1}$, which is higher than that of ETEK. MoC can significantly improve the stability of $Pt/MoC_{0.25}$/MWCNTs catalyst and reduce the adsorption of intermediate products on the catalyst surface. The higher stability current achieved on $Pt/MoC_{0.25}$/MWCNTs compared to ETEK, together with the results from the above CV tests, confirms the best EOR performance of $Pt/MoC_{0.25}$/MWCNTs.

## CONCLUSION

In summary, $Pt/MoC_x$/MWCNTs nanocomposites were successfully synthesized by the molecular self-assembly technology. The structural characterization shows that $Pt/MoC_x$ nanoparticles are evenly dispersed and anchored on MWCNTs. The structure of MWCNTs is not significantly damaged during the synthesis process. The electrochemical measurement results show that $Pt/MoC_{0.25}$/MWCNTs electrocatalyst has the highest catalytic activity and the best stability. The significant improvement of electrochemical performance is attributed to the introduction of MoC, which changes the electronic structure of $Pt/MoC_x$, provides more active sites for the EOR, enhancing the electrocatalytic activity. The synergistic effect between Pt and MoC provides more active sites for intermediates and improves the catalytic activity. And the MoC interface is beneficial to the adsorption of reaction products and the desorption of intermediate products, which improves the catalytic activity of the composite catalyst. The newly developed self-assembly technique has a great deal of potential for synthesizing Pt/carbide nanocomposite electrocatalysts and the as-prepared $Pt/MoC_{0.25}$/MWCNTs demonstrates a promising prospect as anode catalyst for applying in DEFCs.

## DATA AVAILABILITY STATEMENT

The original contributions presented in the study are included in the article/Supplementary Material, further inquiries can be directed to the corresponding authors.

## AUTHOR CONTRIBUTIONS

XC is mainly responsible for the operation of the experiment. ZQ and JC are mainly responsible for sorting of experimental date, and TA is mainly responsible for designing the experimental scheme and writing the paper.

## FUNDING

This work was supported by Program of DGUT Innovation Center of Robotics and Intelligent Equipment of China (No. KCYCXPT2017006), KEY Laboratory of Robotics and Intelligent Equipment of Guangdong Regular Institutions of Higher Education (No. 2017KSYS009), Dongguan Sci-Tech Commissoner Program (No. 20201800500252).

## REFERENCES

Bach Delpeuch, A., Maillard, F., Chatenet, M., Soudant, P., and Cremers, C. (2016). Ethanol Oxidation Reaction (EOR) Investigation on Pt/C, Rh/C, and Pt-Based Bi- and Tri-metallic Electrocatalysts: A DEMS and *In Situ* FTIR Study. *Appl. Catal. B: Environ.* 181, 672–680. doi:10.1016/j.apcatb.2015.08.041

Corradini, P. G., Antolini, E., and Perez, J. (2015). Electro-oxidation of Ethanol on Ternary Non-alloyed Pt-Sn-Pr/C Catalysts. *J. Power Sourc.* 275, 377–383. doi:10.1016/j.jpowsour.2014.11.026

Dai, S., Huang, T.-H., Chien, P.-C., Lin, C.-A., Liu, C.-W., Lee, S.-W., et al. (2020). Optimization of Pt-Oxygen-Containing Species Anodes for Ethanol Oxidation Reaction: High Performance of Pt-AuSnOx Electrocatalyst. *J. Phys. Chem. Lett.* 11, 2846–2853. doi:10.1021/acs.jpclett.0c00213

Dietrich, P. J., Sollberger, F. G., Akatay, M. C., Stach, E. A., Delgass, W. N., Miller, J. T., et al. (2014). Structural and Catalytic Differences in the Effect of Co and Mo as Promoters for Pt-Based Aqueous Phase Reforming Catalysts. *Appl. Catal. B: Environ.* 156-157, 236–248. doi:10.1016/j.apcatb.2014.03.016

Du, C., Gao, X., Zhuang, Z., Cheng, C., Zheng, F., Li, X., et al. (2017). Epitaxial Growth of Zigzag PtAu alloy Surface on Au Nano-Pentagrams with Enhanced Pt Utilization and Electrocatalytic Performance toward Ethanol Oxidation Reaction. *Electrochimica Acta* 238, 263–268. doi:10.1016/j.electacta.2017.03.198

Fang, H., Wu, L., Chen, W., and Yuan, Y. (2021). Synergy of Carbon Defect and Transition Metal on Tungsten Carbides for Boosting the Selective Cleavage of Aryl Ether C O Bond. *Appl. Catal. A: Gen.* 613, 118023–118032. doi:10.1016/j.apcata.2021.118023

Gao, J., Zhang, F., Gan, W., Gui, Y., Qiu, H., Li, H., et al. (2020). MOF-derived 2D/3D Hierarchical N-Doped Graphene as Support for Advanced Pt Utilization in

Ethanol Fuel Cell. *ACS Appl. Mater. Inter.* 12, 47667–47676. doi:10.1021/acsami.0c15493

Gao, W., Liu, T., Zhang, Z., Dou, M., and Wang, F. (2020). Stabilization of Pt Nanoparticles at the Ta2O5-TaC Binary junction: an Effective Strategy to Achieve High Durability for Oxygen Reduction. *J. Mater. Chem. A.* 8, 5525–5534. doi:10.1039/C9TA12596E

Hamo, E. R., Tereshchuk, P., Zysler, M., Zitoun, D., Natan, A., and Rosen, B. A. (2019). Corrosion Resistance and Acidic ORR Activity of Pt-Based Catalysts Supported on Nanocrystalline Alloys of Molybdenum and Tantalum Carbide. *J. Electrochem. Soc.* 166, F1292–F1300. doi:10.1149/2.0251916jes

Hassan, A., and Ticianelli, E. A. (2018). Activity and Stability of Dispersed Multi Metallic Pt-Based Catalysts for CO Tolerance in Proton Exchange Membrane Fuel Cell Anodes. *Acad. Bras. Ciênc.* 90, 697–718. doi:10.1590/0001-3765201820170559

Huang, M., Wu, W., Wu, C., and Guan, L. (2015). Pt2SnCu Nanoalloy with Surface Enrichment of Pt Defects and SnO2 for Highly Efficient Electrooxidation of Ethanol. *J. Mater. Chem. A.* 3, 4777–4781. doi:10.1039/c4ta06695b

Hunt, S. T., Milina, M., Wang, Z., and Román-Leshkov, Y. (2016). Activating Earth-Abundant Electrocatalysts for Efficient, Low-Cost Hydrogen Evolution/oxidation: Sub-monolayer Platinum Coatings on Titanium Tungsten Carbide Nanoparticles. *Energy Environ. Sci.* 9, 3290–3301. doi:10.1039/c6ee01929c

Hunt, S. T., Nimmanwudipong, T., and Román-Leshkov, Y. (2014). Engineering Non-sintered, Metal-Terminated Tungsten Carbide Nanoparticles for Catalysis. *Angew. Chem. Int. Ed.* 53, 5131–5136. doi:10.1002/anie.201400294

Jiang, H., Li, J., Xiao, Z., Wang, B., Fan, M., Xu, S., et al. (2020). The Rapid Production of Multiple Transition Metal Carbides via Microwave Combustion under Ambient Conditions. *Nanoscale* 12, 16245–16252. doi:10.1039/D0NR05223J

Jiang, Z., Zhang, Q., Liang, Z., and Chen, J. G. (2018). Pt-modified TaC as an Efficient Electrocatalyst for Ethanol Oxidation in Acid and Alkaline Electrolytes. *Appl. Catal. B: Environ.* 234, 329–336. doi:10.1016/j.apcatb.2018.04.052

Kelly, T. G., Stottlemyer, A. L., Yang, X., and Chen, J. G. (2014). Theoretical and Experimental Studies of Ethanol Decomposition and Electrooxidation over Pt-Modified Tungsten Carbide. *J. Electrochem. Soc.* 161, E3165–E3170. doi:10.1149/2.017408jes

Li, P., Liu, K., Ye, J., Xue, F., Cheng, Y., Lyu, Z., et al. (2019). Facilitating the C-C Bond Cleavage on Sub-10 Nm Concavity-Tunable Rh@Pt Core-Shell Nanocubes for Efficient Ethanol Electrooxidation. *J. Mater. Chem. A.* 7, 17987–17994. doi:10.1039/c9ta04867g

Li, X., Fang, Y., Lin, X., Tian, M., An, X., Fu, Y., et al. (2015). MOF Derived Co3O4nanoparticles Embedded in N-Doped Mesoporous Carbon Layer/MWCNT Hybrids: Extraordinary Bi-functional Electrocatalysts for OER and ORR: Extraordinary Bi-functional Electrocatalysts for OER and ORR. *J. Mater. Chem. A.* 3, 17392–17402. doi:10.1039/C5TA03900B

Lin, L., Sheng, W., Yao, S., Ma, D., and Chen, J. G. (2017). Pt/Mo2C/C-cp as a Highly Active and Stable Catalyst for Ethanol Electrooxidation. *J. Power Sourc.* 345, 182–189. doi:10.1016/j.jpowsour.2017.02.001

Lu, J. L., Li, Z. H., Jiang, S. P., Shen, P. K., and Li, L. (2012). Nanostructured Tungsten Carbide/carbon Composites Synthesized by a Microwave Heating Method as Supports of Platinum Catalysts for Methanol Oxidation. *J. Power Sourc.* 202, 56–62. doi:10.1016/j.jpowsour.2011.11.018

Lu, S., Eid, K., Lin, M., Wang, L., Wang, H., and Gu, H. (2016). Hydrogen Gas-Assisted Synthesis of Worm-like PtMo Wavy Nanowires as Efficient Catalysts for the Methanol Oxidation Reaction. *J. Mater. Chem. A.* 4, 10508–10513. doi:10.1039/c6ta02053d

Mao, J., Chen, W., He, D., Wan, J., Pei, J., Dong, J., et al. (2017). Design of Ultrathin Pt-Mo-Ni Nanowire Catalysts for Ethanol Electrooxidation. *Sci. Adv.* 3, e1603068–e1603076. doi:10.1126/sciadv.1603068

Myochi, R., Nagao, T., Fugane, Y., Takahashi, S., Todoroki, N., and Wadayama, T. (2018). Oxygen Reduction Reaction Properties for Dry-Process Synthesized Pt/TaCx Nanoparticles. *ECS Trans.* 86, 519–524. doi:10.1149/08613.0519ecst

Nie, R., Liang, D., Shen, L., Gao, J., Chen, P., and Hou, Z. (2012). Selective Oxidation of Glycerol with Oxygen in Base-free Solution over MWCNTs Supported PtSb alloy Nanoparticles. *Appl. Catal. B: Environ.* 127, 212–220. doi:10.1016/j.apcatb.2012.08.026

Oh, A., Kim, H. Y., Baik, H., Kim, B., Chaudhari, N. K., Joo, S. H., et al. (2019). Topotactic Transformations in an Icosahedral Nanocrystal to Form Efficient Water-Splitting Catalysts. *Adv. Mater.* 31, 1805546. doi:10.1002/adma.201805546

Oh, Y., Kim, S.-K., Peck, D.-H., Jang, J.-s., Kim, J., and Jung, D.-H. (2014). Improved Performance Using Tungsten Carbide/carbon Nanofiber Based Anode Catalysts for Alkaline Direct Ethanol Fuel Cells. *Int. J. Hydrogen Energ.* 39, 15907–15912. doi:10.1016/j.ijhydene.2014.02.010

Pech-Rodríguez, W. J., González-Quijano, D., Vargas-Gutiérrez, G., Morais, C., Napporn, T. W., and Rodríguez-Varela, F. J. (2017). Electrochemical and *In Situ* FTIR Study of the Ethanol Oxidation Reaction on PtMo/C Nanomaterials in Alkaline media. *Appl. Catal. B: Environ.* 203, 654–662. doi:10.1016/j.apcatb.2016.10.058

Robinson, A. M., Mark, L., Rasmussen, M. J., Hensley, J. E., and Medlin, J. W. (2016). Surface Chemistry of Aromatic Reactants on Pt- and Mo-Modified Pt Catalysts. *J. Phys. Chem. C* 120, 26824–26833. doi:10.1021/acs.jpcc.6b08415

Sabnis, K. D., Akatay, M. C., Cui, Y., Sollberger, F. G., Stach, E. A., Miller, J. T., et al. (2015). Probing the Active Sites for Water-Gas Shift over Pt/molybdenum Carbide Using Multi-Walled Carbon Nanotubes. *J. Catal.* 330, 442–451. doi:10.1016/j.jcat.2015.07.032

Singla, G., Singh, K., and Pandey, O. P. (2017). Catalytic Activity of Tungsten Carbide-Carbon (WC@C) Core-Shell Structured for Ethanol Electro-Oxidation. *Mater. Chem. Phys.* 186, 19–28. doi:10.1016/j.matchemphys.2016.07.022

Wang, J., Liu, C., Xu, G., Miao, C., Wen, M., Xu, M., et al. (2022). Strengthened the Structural Stability of *In-Situ* F– Doping Ni-Rich LiNi0.8Co0.15Al0.05O2 Cathode Materials for Lithium-Ion Batteries. *Chem. Eng. J.* 438, 135537. doi:10.1016/j.cej.2022.135537

Wang, Q., Chen, S., Li, P., Ibraheem, S., Li, J., Deng, J., et al. (2019). Surface Ru Enriched Structurally Ordered Intermetallic PtFe@PtRuFe Core-Shell Nanostructure Boosts Methanol Oxidation Reaction Catalysis. *Appl. Catal. B: Environ.* 252, 120–127. doi:10.1016/j.apcatb.2019.04.023

Xiao, L., Li, G., Yang, Z., Chen, K., Zhou, R., Liao, H., et al. (2021). Engineering of Amorphous PtO X Interface on Pt/WO 3 Nanosheets for Ethanol Oxidation Electrocatalysis. *Adv. Funct. Mater.* 31, 2100982. doi:10.1002/adfm.202100982

Yang, Z., Shi, Y., Wang, X., Zhang, G., and Cui, P. (2019). Boron as a superior Activator for Pt Anode Catalyst in Direct Alcohol Fuel Cell. *J. Power Sourc.* 431, 125–134. doi:10.1016/j.jpowsour.2019.05.052

Zamanzad Ghavidel, M. R., Monteverde Videla, A. H. A., Specchia, S., and Easton, E. B. (2017). The Relationship between the Structure and Ethanol Oxidation Activity of Pt-Cu/C alloy Catalysts. *Electrochimica Acta* 230, 58–72. doi:10.1016/j.electacta.2017.01.129

Zhang, Q., Jiang, Z., Tackett, B. M., Denny, S. R., Tian, B., Chen, X., et al. (2019). Trends and Descriptors of Metal-Modified Transition Metal Carbides for Hydrogen Evolution in Alkaline Electrolyte. *ACS Catal.* 9, 2415–2422. doi:10.1021/acscatal.8b03990

Zhang, Q., Mellinger, Z. J., Jiang, Z., Chen, X., Wang, B., Tian, B., et al. (2018). Palladium-modified Tungsten Carbide for Ethanol Electrooxidation: from Surface Science Studies to Electrochemical Evaluation. *J. Electrochem. Soc.* 165, J3031–J3038. doi:10.1149/2.0061815jes

Zhu, X., Huang, L., Wei, M., Tsiakaras, P., and Shen, P. K. (2021). Highly Stable Pt-Co Nanodendrite in Nanoframe with Pt Skin Structured Catalyst for Oxygen Reduction Electrocatalysis. *Appl. Catal. B: Environ.* 281, 119460–119468. doi:10.1016/j.apcatb.2020.119460

**Conflict of Interest:** ZQ and JC were employed by Dongguan JoySun New Energy Co. Ltd.

The remaining authors declare that the research was conducted in the absence of any commercial or financial relationships that could be construed as a potential conflict of interest.

**Publisher's Note:** All claims expressed in this article are solely those of the authors and do not necessarily represent those of their affiliated organizations, or those of the publisher, the editors and the reviewers. Any product that may be evaluated in this article, or claim that may be made by its manufacturer, is not guaranteed or endorsed by the publisher.

frontiers | Frontiers in Chemistry

ORIGINAL RESEARCH
published: 27 April 2022
doi: 10.3389/fchem.2022.899287

# Preparation and Properties of Indium Ion Modified Graphite Felt Composite Electrode

*Yang Su[1,2], Na Chen[1], Hai-lin Ren[1], Li-li Guo[1], Zhen Li[1] and Xiao-min Wang[1]**

[1]Liaoning Key Laboratory of Chemical Additive Synthesis and Separation, School of Materials Science and Engineering, Yingkou Institute of Technology, Yingkou, China, [2]School of Materials Science and Metallurgy, University of Science and Technology Liaoning, Anshan, China

Iron-chromium redox flow batteries (ICRFBs) have the advantages of high safety, long cycle life, flexible design, and low maintenance costs. Polyacrylonitrile-based graphite felt composite material has good temperature resistance, corrosion resistance, large surface area and excellent electrical conductivity, and is often used as the electrode material of ICRFB, but its chemical activity is poor. In order to improve the activity of the graphite felt electrode, $In^{3+}$ was used for modification in this paper, and the modified graphite felt was used as the electrode material for iron-chromium batteries. The structure and surface morphology of the modified graphite felt were analyzed by the specific surface area analyzer and scanning electron microscope; the electrochemical impedance spectroscopy and cyclic voltammetry experiments were carried out on the electrochemical workstation to study the electro catalytic activity of $In^{3+}$ modified graphite felt and its performance in ICRFBS. The results show that the graphite felt electrode modified with a concentration of 0.2 M $In^{3+}$ was activated at 400°C for 2 h, and its surface showed a lot of grooves, and the specific surface area reached 3.889 $m^2$/g, while the specific surface area of the untreated graphite felt was only 0.995 $m^2$/g significantly improved. Electrochemical tests show that the electrochemical properties of graphite felt electrodes are improved after $In^{3+}$ modification. Therefore, the $In^{3+}$ modified graphite felt electrode can improve the performance of ICRFB battery, and also make it possible to realize the engineering application of ICRFB battery.

**Keywords: iron-chromium flow battery, graphite felt, indium ion, specific surface area, electrochemical performance**

OPEN ACCESS

***Edited by:***
*Hailong Wang,*
*Ningxia University, China*

***Reviewed by:***
*Bin Lu,*
*Ningbo University, China*
*Ping Liang,*
*Liaoning Shihua University, China*

****Correspondence:***
*Xiao-min Wang*
*ty.com.cn@126.com*

***Specialty section:***
*This article was submitted to Physical Chemistry and Chemical Physics, a section of the journal Frontiers in Chemistry*

***Received:*** *18 March 2022*
***Accepted:*** *28 March 2022*
***Published:*** *27 April 2022*

***Citation:***
*Su Y, Chen N, Ren H-l, Guo L-l, Li Z and Wang X-m (2022) Preparation and Properties of Indium Ion Modified Graphite Felt Composite Electrode. Front. Chem. 10:899287. doi: 10.3389/fchem.2022.899287*

## INTRODUCTION

In recent years, with the depletion of non-renewable resources such as coal, oil, and natural gas, renewable energy such as wind, hydro, and tidal energy has developed rapidly (Mankge et al., 2021; Hargreaves et al., 2020). Therefore, it is very important to develop large-scale and high-efficiency energy storage systems (Ani 2021; Züttel et al., 2022). As a large-scale power storage system, flow batteries have the characteristics of high capacity and wide application fields (environments), and will usher in a period of rapid development (Yang et al., 2021; Sankaralingam et al., 2021; Huang et al., 2021). In most flow batteries, iron-chromium flow batteries use low-cost $Cr^{3+}/Cr^{2+}$ pairs to reduce $Cr^{2+}$ and $Fe^{3+}/Fe^{2+}$ pairs to oxidize $Fe^{3+}$, respectively. Electrochemical redox reaction is carried out in $Cr^{3+}$ electrolyte and acidic $Fe^{2+}$ electrolyte (Zhang et al., 2020; Wu et al., 2021; Ahn

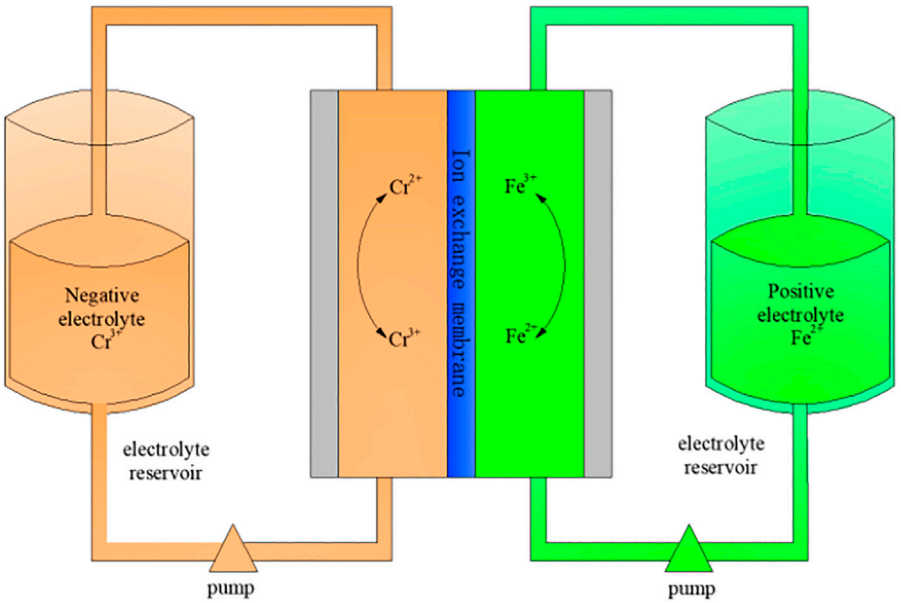


**FIGURE 1 |** Composition diagram of iron-chromium flow battery.

et al., 2021). A typical iron-chromium flow battery system is shown in **Figure 1**, which consists of a point stack unit, an electrolyte, electrolyte storage and supply unit, and a management and control unit (Chen et al., 2020).

The key materials of flow batteries include electrodes, membranes, electrolytes, etc. Among them, graphite felt is the most commonly used electrode material in flow batteries (Zhang et al., 2017; Yue et al., 2010). At present, the activation methods of graphite felt are generally divided into two methods: adding oxygen-containing functional groups on the surface and introducing surface catalytic substances (Zhang et al., 2019). In terms of increasing the oxygen-containing functional groups on the surface, methods such as acidified $K_2Cr_2O_7$ solution (Hassan et al., 2019), $KMnO_4$ solution (Hassan et al., 2020), and laser coating modification (Daugherty et al., 2020) and aerogel modification (Jiang et al., 2019) are generally used. The introduction of oxygen-containing functional groups can not only increase the carbon and oxygen sites of the graphite felt modified electrode, increase the electrode activity, but also accelerate the charge transfer speed and improve the dynamic performance of the electrode (Na et al., 2018). The specific surface area of the felt (Jiang et al., 2019). In terms of introducing surface catalytic substances, electrostatic spraying graphene oxide coating (Anantha et al., 2021), rare earth composite oxide (Wang et al., 2020). and noble metal particles such as Pt and Ag are generally used as the main decoration (Xia et al., 2020; Lou et al., 2021), which can increase the current density and improve the current efficiency.

Indium and indium oxide are promising oxides (Xinyuan et al., 2021), and current research is mainly focused on the fact that indium and indium oxide can inhibit the hydrogen evolution reaction of the anode and improve the Coulombic efficiency of the battery. Leung et al. deposited zinc on a carbon composite electrode in a methane sulfonic acid medium and added $2 \times 10^{-3}$ moldm$^{-3}$ indium oxide as a hydrogen suppressor, and the energy efficiency was increased from 62 to 73% (Leung et al., 2011). Wang et al. used $In^{3+}$ as an additive to improve the stability and performance of ICFBS, and their studies showed that $In^{3+}$ can not only effectively inhibit the hydrogen evolution reaction, but also promote the reaction kinetics to a certain extent (Wang et al., 2021). The research on $In^{3+}$ modified graphite felt electrodes has not been reported in detail. Therefore, it is of great significance to study the electro catalytic activity of $In^{3+}$ modified graphite felt and its performance in ICRFBS.

## EXPERIMENT

### Preparation of Graphite Felt Electrodes

Graphite felt (GF, 5 mm, Gansu Haoshi Carbon Fiber Co., Ltd.) was heat-treated at 400°C for 2 h as the base material. Take three appropriate amounts of $In_2O_3$ powder and add them to a beaker of 3 M dilute hydrochloric acid respectively to prepare a 0.1, 0.2, and 0.3 M $InCl_3$ solution. The following chemical reactions mainly take place in this process:

$$In_2O_3 + 6HCl = 2InCl_3 + 3H_2O$$

Three groups of graphite felts of the same size were immersed in 0.1, 0.2, and 0.3 M $InCl_3$ solutions for 8 h, respectively. Then it was dried in a drying oven at 80°C for 15 h. The dried graphite felt was thermally activated in a medium-temperature experimental furnace at 400°C for 2 h. That is, the active graphite felt electrode for iron-chromium flow battery whose surface is coated with $InCl_3$ is prepared.

### Characterization of Graphite Felt Electrodes

Scanning electron microscope (SEM) was used to observe the microscopic morphology of graphite felt, and X-ray energy

dispersive spectroscopy (EDS) was used to determine the types and contents of elements on the surface of the samples. The $N_2$ adsorption and desorption isotherms and the specific surface area (BET) and pore size distribution of each sample were measured by a specific surface area and pore size tester, and the pore size distribution was compared and analyzed by the BJH method (Chen et al., 2020).

## Electrochemical Measurements

Electrochemical performance was measured at room temperature using Wuhan Koster electrochemical workstation, and the flow battery electrolyte solution consisted of 1.0 M $CrCl_3$ + 1.0 M $FeCl_2$ + 3.0 M HCl solution. A three-electrode system was used for electrochemical measurement, 0.4 $cm^2$ graphite felt was used as the working electrode, 1.0 $cm^2$ platinum sheet was used as the counter electrode, and the reference electrode was a calomel electrode. Cyclic voltammetry tests were performed at a scan rate of 5 mV/s and a voltage range of −0.8–0.8 V. Electrochemical impedance measurements were performed in the frequency range from 0.01Hz to 100 kHz with an AC voltage amplitude of 5 mV and polarization potentials of 0.4V and −0.5 V, respectively.

# RESULTS AND DISCUSSION

## Characterization of Physical Properties

The surface morphology of graphite felt electrode observed by scanning electron microscope is shown in **Figure 2**. A small amount of impurities attached to the surface is the untreated graphite felt (**Figure 2A**), and a large number of deep "grooves" appeared along the fiber axis on the surface of the heat-treated graphite felt (**Figure 2B**). **Figures 2C–E** show the heat-treated graphite felt electrodes impregnated with $InCl_3$ solutions of different concentrations, respectively. It can be seen that after immersion in the $InCl_3$ solution, the depth of the "grooves" increases on the surface and is accompanied by the generation of irregular holes. When the concentration of $InCl_3$ solution was 0.2 M (**Figure 2D**), the specific surface area of the graphite felt increased significantly to 3.889 $m^2$/g, while the specific surface area of the untreated graphite felt was only 0.995 $m^2$/g. In addition to the increase in the specific surface area of the graphite felt electrode, the EDS test results (**Figure 3**) showed that $InCl_3$ was successfully coated on the fiber surface with uniform distribution, which may increase the activation point of the graphite felt electrode, which is beneficial to improve the performance of the electrode.

Take five pieces of graphite felt of the same size and put it into the electrolyte at the same time, observe its falling speed and position in three time periods of instant, 10 and 30 min, and judge its wettability.

It can be seen from **Figure 4** that when the graphite felt is impregnated with $InCl_3$ solution, its lipophilicity is significantly improved, and it will quickly sink into the electrolyte at the moment of contact, and the sinking speed of graphite felt impregnated with 0.2 M $InCl_3$ solution will be slightly faster than Graphite felt impregnated with other concentrations of $InCl_3$ solution. This method can measure the hydrophilicity of graphite felt, but the error is large. It can also be proved that the

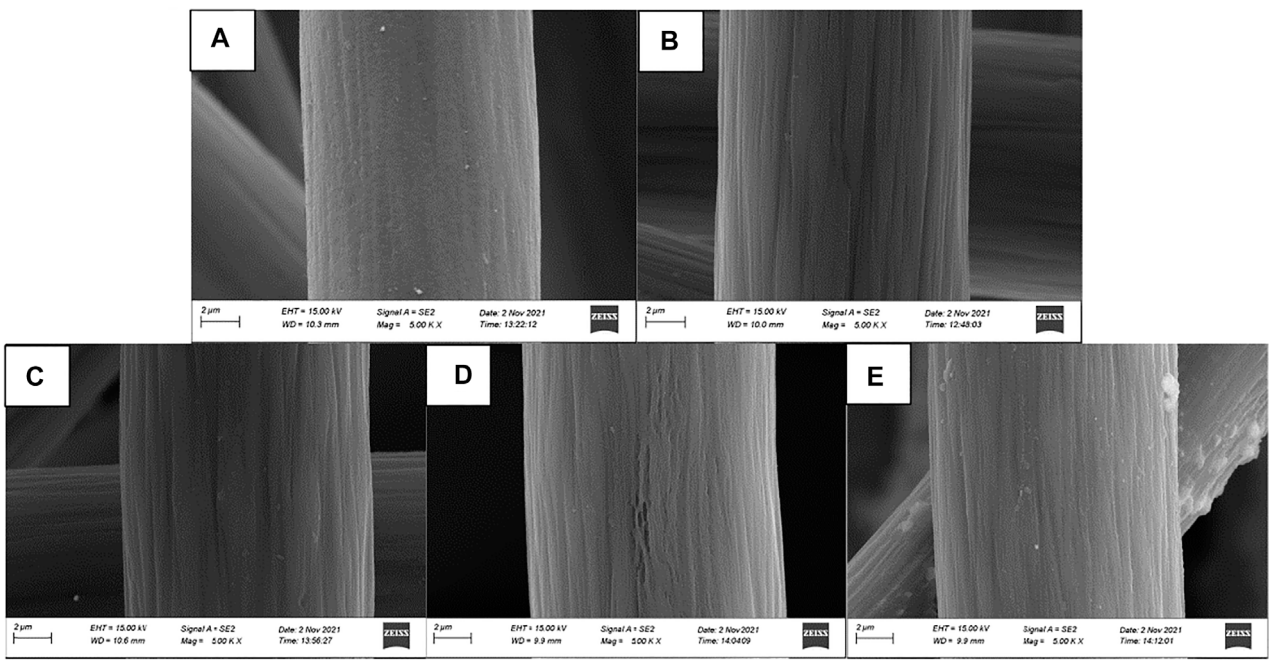


**FIGURE 2 |** 5.00 KX Scanning Electron Micrograph (SEM) **(A)**, untreated graphite felt **(B)**, heat treated graphite felt **(C)**, heat treated graphite felt impregnated with 0.1 M $InCl_3$ solution **(D)**, heat treated graphite felt impregnated with 0.2 M $InCl_3$ solution **(E),** heat treated graphite felt impregnated with 0.3 M $InCl_3$ solution.

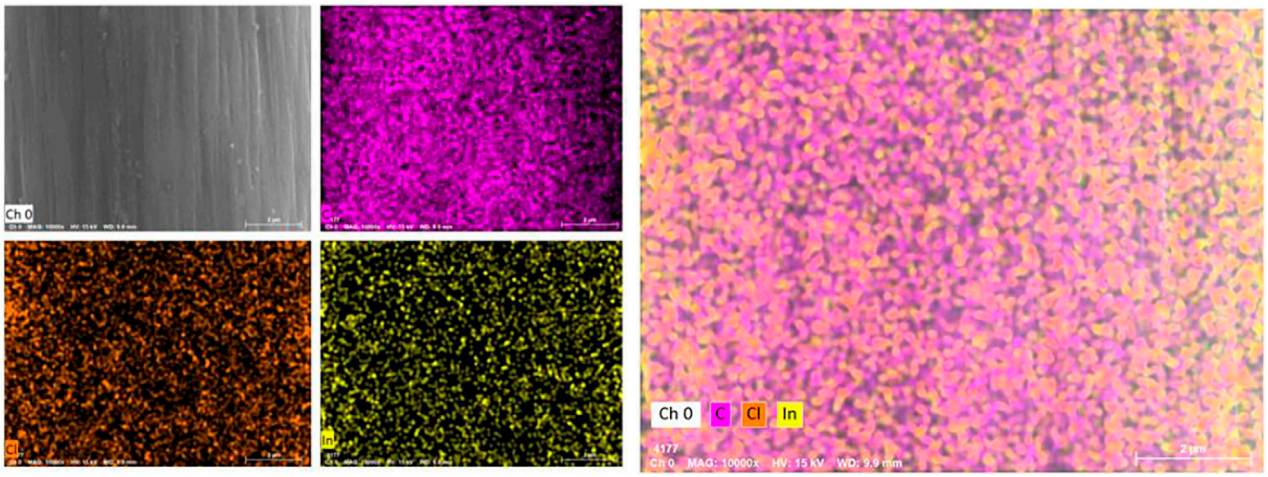


**FIGURE 3 |** EDS analysis diagram of heat-treated graphite felt after immersion in $InCl_3$ solution.

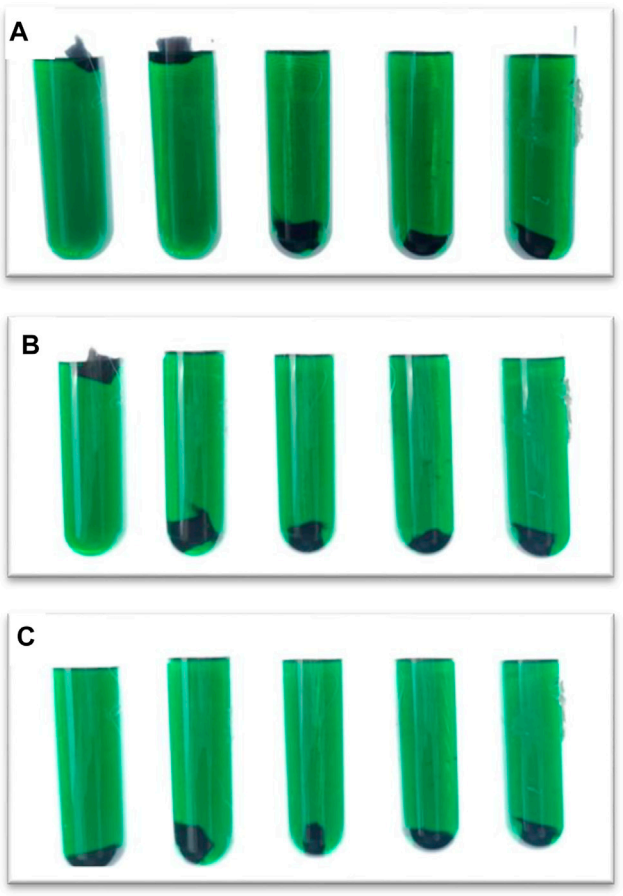


**FIGURE 4 |** Samples from left to right are untreated graphite felt, heat-treated graphite felt, heat-treated graphite felt after immersion in 0.1 M $InCl_3$ solution, heat-treated graphite felt after immersion in 0.2 M $InCl_3$ solution, and heat-treated graphite felt after immersion in 0.3 M $InCl_3$ solution, **(A),** momentary Contact; **(B),** soak for 10 min; **(C),** soak for 30 min.

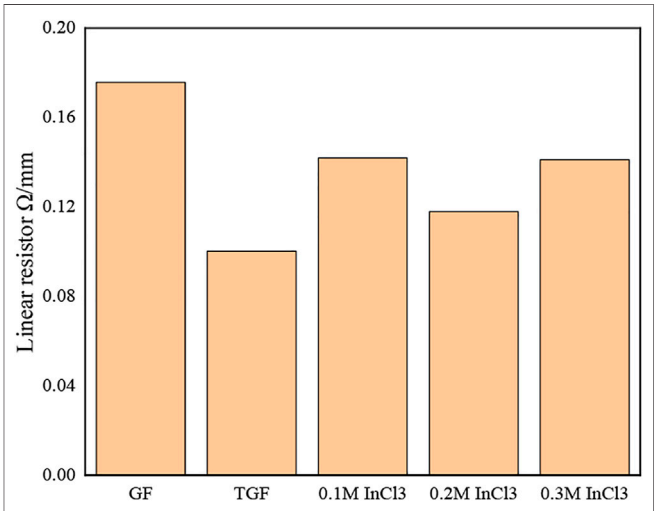


**FIGURE 5 |** respectively GF; TGF; 0.1 M $InCl_3$ solution impregnated heat-treated graphite felt; 0.2 M $InCl_3$ solution impregnated heat-treated graphite felt; 0.3 M $InCl_3$ solution impregnated heat-treated graphite felt line resistance.

hydrophilicity of graphite felt is enhanced after being impregnated with $InCl_3$ solution.

In order to better understand the properties of graphite felt after immersion in $InCl_3$ solution, we measured the resistance of each sample. **Figure 5** shows the change of the line resistance value of each sample.

It can be seen from **Figure 5** that the line resistance of GF is the largest, while the line resistance of TGF is slightly lower than that of GF, from 0.17 Ω/cm to 0.1 Ω/cm, and the reduction range is 41.17%. All have decreased, the decrease range is 17.64, 35.29, 17.65%, and it can be seen that the graphite felt impregnated with 0.2 M $InCl_3$ solution has the lowest resistance.

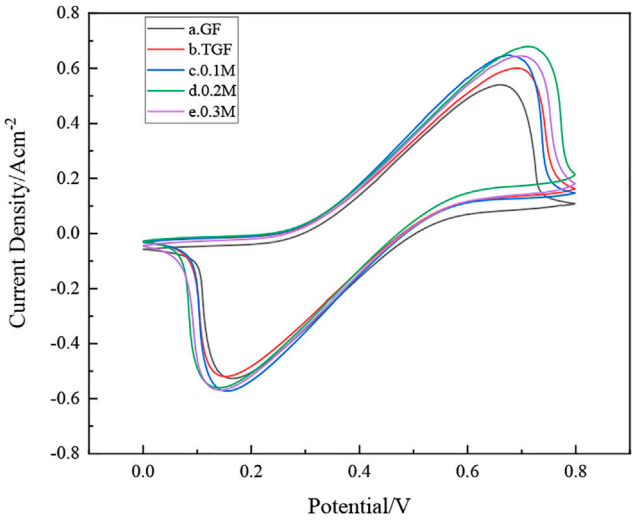


**FIGURE 6 |** how's samples **(a),** GF; **(b),** TGF; **(c),** heat-treated graphite felt after immersion in 0.1 M $InCl_3$ solution; **(d),** heat-treated graphite felt after immersion in 0.2 M $InCl_3$ solution; **(e),** heat-treated graphite felt after immersion in 0.3 M $InCl_3$ solution, cycle Voltammetry curve.

## Electrochemical Characterization

As shown in **Figure 6**, the redox peak intensity of the cyclic voltammetry of the untreated graphite felt electrode is small, indicating that its electrochemical activity is low, and it is not suitable for direct use as an electrode material for iron-chromium batteries. The heat-treated graphite felt electrodes showed more obvious redox peaks after heat treatment and $InCl_3$ solution immersion, indicating that the electrochemical performance of the heat-treated graphite felt electrodes was significantly improved compared with the untreated ones. Among them, the electrochemical performance of graphite felt electrode (d) after impregnation with $InCl_3$ solution concentration of 0.2 M is the best, and the peak value of its wave peak is also stronger. It can be observed from **Figure 6** that the peak current values of the positive electrode of the heat-treated graphite felt electrode and the graphite felt after being impregnated with $InCl_3$ solution and then heat-treated are 587 mA, 642 mA, 692 mA, and 644 mA, all of which are greater than 524 mA. It can be proved that heat treatment after immersion in $InCl_3$ solution can improve the electrochemical activity of the redox pair in Fe-Cr batteries.

Electrochemical impedance spectroscopy further analyzed the effect of heat treatment after immersion in $InCl_3$ solution on the electrochemical performance of iron-chromium batteries. **Figure 7** shows the Nyquist plots of a-e graphite felt electrodes. It can be observed from the figure that in all Nyquist diagrams, the semicircular part exists in the high frequency region, and the linear part exists in the low frequency region, which can indicate the interaction between iron ions and chromium ions on the graphite felt electrode. Redox reactions are affected by both the rate of charge transfer and the rate of diffusion. In **Figure 7**, when the electron transfer step at the electrode/electrolyte interface is the control step, the electrode process is corresponding to the semicircle arc located in the high frequency region, and the difficulty of the electron transfer is determined by the semicircle arc. Reflected by the radius of the arc (Rct), the smaller the resistance, the less difficult the transfer of electrons will be, and the smaller the radius will be; the diffusion coefficient of the reaction particles in the solution is the control step. Corresponding to the slash (Rs). Observing **Figure 7**, it can be seen that heat treatment after immersion in $InCl_3$ solution can significantly reduce the charge transfer resistance of the iron-chromium redox couple, and the high-frequency arc radius is significantly smaller than that before treatment, indicating that heat treatment after immersion in $InCl_3$ solution can accelerate the redox couple of iron-chromium. Reaction and charge transfer rates. However, it is easier for electrons to transfer on the graphite felt after being immersed in $InCl_3$ solution and then heat-treated, that is, and the charge transfer resistance of the graphite felt is greatly reduced at this time, which further indicates that the heat-treated graphite felt electrode after being immersed in $InCl_3$ solution is in iron. The electrochemical performance of chromium flow batteries has been greatly improved.

## CONCLUSION

In this paper, the graphite felt was immersed in $InCl_3$ solution and then heat treated, so that indium ions were successfully introduced into the surface of the graphite felt to prepare an active electrode. The comprehensive SEM, EDS, BET, resistance, lipophilicity, and electrochemical test results can get conclusion:

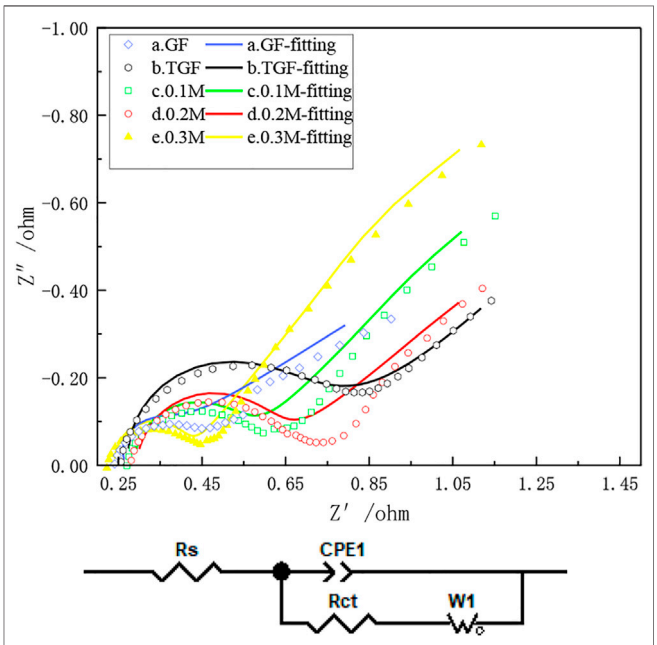


**FIGURE 7 |** Samples **(a),** GF; **(b),** TGF; **(c),** heat-treated graphite felt after immersion in 0.1 MM $InCl_3$ solution; **(d),** heat-treated graphite felt after immersion in 0.2 MM $InCl_3$ solution; **(e),** heat-treated graphite felt after immersion in 0.3 MM $InCl_3$ solution, electrochemical impedance Diagram and Equivalent Circuit Diagram.

1) $In^{3+}$ was successfully coated on the surface of the fiber, and the distribution was uniform, which increased the activation point of the graphite felt electrode, which was beneficial to improve the performance of the electrode. When the $In^{3+}$ concentration was 0.2 M, the specific surface area of the graphite felt increased significantly to 3.889 $m^2$/g, while the specific surface area of the untreated graphite felt is only 0.995 $m^2$/g.
2) The hydrophilicity of graphite felt impregnated with $InCl_3$ solution is obviously enhanced, and it can be seen that the graphite felt impregnated with 0.2 M $InCl_3$ solution has the lowest resistance.
3) Heat treatment after immersion in $InCl_3$ solution can accelerate the redox reaction and charge transfer rate of iron-chromium charge, and the charge transfer resistance of the graphite felt after immersion in $InCl_3$ solution is greatly reduced, thereby further improving its electrochemical performance.

## DATA AVAILABILITY STATEMENT

The original contributions presented in the study are included in the article/Supplementary Material, further inquiries can be directed to the corresponding author.

## AUTHOR CONTRIBUTIONS

YS is the experimental designer and executor of this study, completing the data analysis and writing the first draft of the paper; NC, H-LR, L-LG, and ZL participated in the experimental design and analysis of the experimental results; X-MW is the designer and responsible for the project People, instructed experimental design, data analysis, thesis writing and revision. All authors read and agree to the final text.

## FUNDING

This work is funding by the National Key Research and Development Program (2020YFC1909300), Regional joint fund project of Liaoning Provincial Department of science and technology (2020-YKLH-27), the Foundation of Liaoning Key Laboratory of Chemical Additive Synthesis and Separation (ZJNK 2001) and the Yingkou Institute of Technology Innovation Team Project (TD201901).

## REFERENCES

Ahn, Y., Moon, J., Park, S. E., Shin, J., Wook Choi, J., and Kim, K. J. (2021). High-performance Bifunctional Electrocatalyst for Iron-Chromium Redox Flow Batteries. *Chem. Eng. J.* 421, 127855. doi:10.1016/j.cej.2020.127855

Anantha, M. S., Anarghya, D., Hu, C., Reddy, N., Venkatesh, K., and Muralidhara, H. B. (2021). Electrochemical Performance of Graphene Oxide Modified Graphite Felt as a Positive Electrode in All-Iron Redox Flow Batteries. *J. Appl. Electrochem.* 51 (2), 331–344. doi:10.1007/s10800-020-01490-5

Ani, V. A. (2021). Development of an Intelligent Power Management System for Solar PV-Wind-Battery-Fuel-Cell Integrated System. *Front. Energ. Res.* 9. doi:10.3389/fenrg.2021.613958

Chen, N., Zhang, H., Luo, X.-D., and Sun, C.-Y. (2020). SiO2-decorated Graphite Felt Electrode by Silicic Acid Etching for Iron-Chromium Redox Flow Battery. *Electrochimica Acta* 336, 135646. doi:10.1016/j.electacta.2020.135646

Daugherty, M. C., Hsieh, C.-T., Aaron, D. S., Ashraf Gandomi, Y., Li, J., Zheng, Y., et al. (2020). Enabling High Rate Capability, Low Internal Resistance, and Excellent Cyclability for Vanadium Redox Flow Batteries Utilizing Ultrafast Laser-Structured Graphite Felt. *Electrochimica Acta* 344, 136171. doi:10.1016/j.electacta.2020.136171

Hargreaves, J. J., and Jones, R. A. (2020). Long Term Energy Storage in Highly Renewable Systems. *Front. Energ. Res.* 8. doi:10.3389/fenrg.2020.00219

Hassan, A., and Tzedakis, T. (2019). Enhancement of the Electrochemical Activity of a Commercial Graphite Felt for Vanadium Redox Flow Battery (VRFB), by Chemical Treatment with Acidic Solution of K2Cr2O7. *J. Energ. Storage* 26, 100967. doi:10.1016/j.est.2019.100967

Hassan, A., and Tzedakis, T. (2020). Facile Chemical Activation of Graphite Felt by KMnO4 Acidic Solution for Vanadium Redox Flow Batteries. *Appl. Surf. Sci.* 528, 146808. doi:10.1016/j.apsusc.2020.146808

Huang, Z., Mu, A., Wu, L., Wang, H., and Zhang, Y. (2021). Electrolyte Flow Optimization and Performance Metrics Analysis of Vanadium Redox Flow Battery for Large-Scale Stationary Energy Storage. *Int. J. Hydrogen Energ.* 46 (63), 31952–31962. doi:10.1016/j.ijhydene.2021.06.220

Jiang, F., He, Z., Guo, D., and Zhou, X. (2019). Carbon Aerogel Modified Graphite Felt as Advanced Electrodes for Vanadium Redox Flow Batteries. *J. Power Sourc.* 440, 227114. doi:10.1016/j.jpowsour.2019.227114

Leung, P. K., Ponce-de-León, C., Low, C. T. J., and Walsh, F. C. (2011). Zinc Deposition and Dissolution in Methanesulfonic Acid onto a Carbon Composite Electrode as the Negative Electrode Reactions in a Hybrid Redox Flow Battery. *Electrochimica Acta* 56 (18), 6536–6546. doi:10.1016/j.electacta.2011.04.111

Lou, Y., Fu, D., Fabre, B., Fourcade, F., Amrane, A., Pasturel, M., et al. (2021). Bismuth Coated Graphite Felt Modified by Silver Particles for Selective Electroreduction of CO2 into Formate in a Flow Cell. *Electrochimica Acta* 371, 137821. doi:10.1016/j.electacta.2021.137821

Mankge, N. S., Madito, M. J., Hlongwa, N. W., and Kuvarega, A. T. (2022). Review of Electrochemical Production of Doped Graphene for Energy Storage Applications. *J. Energ. Storage* 46, 103527. doi:10.1016/j.est.2021.103527

Na, Z., Sun, X., and Wang, L. (2018). Surface-functionalized Graphite Felts: Enhanced Performance in Cerium-Based Redox Flow Batteries. *Carbon* 138 (18), 363–368. doi:10.1016/j.carbon.2018.07.052

Sankaralingam, R. K., Seshadri, S., Sunarso, J., Bhatt, A. I., and Kapoor, A. (2021). Overview of the Factors Affecting the Performance of Vanadium Redox Flow Batteries. *J. Energ. Storage* 41, 102857. doi:10.1016/j.est.2021.102857

Wang, H., Li, D., Chen, L., and Han, H. (2020). La and Sr Composite Oxides-Modified Graphite Felt for Aqueous Organic Redox Flow Batteries. *Chem. Res. Chin. Univ.* 36 (6), 1255–1260. doi:10.1007/s40242-020-0108-0

Wang, S., Xu, Z., Wu, X., Zhao, H., Zhao, J., Liu, J., et al. (2021). Excellent Stability and Electrochemical Performance of the Electrolyte with Indium Ion for Iron-Chromium Flow Battery. *Electrochimica Acta* 368, 137524. doi:10.1016/j.electacta.2020.137524

Wang, X., and Lu, B. (2021). Influences of Silica Additive on Sintering and Hall Effect of Novel Transparent In2O3 Semiconductive Ceramics. *Scripta Materialia* 193, 137–141. doi:10.1016/j.scriptamat.2020.10.053

Wu, S., Lv, X., Ge, Z., Wang, L., Dai, L., and He, Z. (2021). Thiourea-Grafted Graphite Felts as Positive Electrode for Vanadium Redox Flow Battery. *Front. Chem.* 8. doi:10.3389/fchem.2020.626490

Xia, L., Long, T., Li, W., Zhong, F., Ding, M., Long, Y., et al. (2020). Highly Stable Vanadium Redox-Flow Battery Assisted by Redox-Mediated Catalysis. *Small* 16 (38), 2003321. doi:10.1002/smll.202003321

Yang, Z., Wei, Y., Zeng, Y., and Yuan, Y. (2021). Effects of Iin-Ssitu Bismuth Catalyst Electrodeposition on Performance of Vanadium Redox Flow Batteries. *J. Power Sourc.* 506, 230238. doi:10.1016/j.jpowsour.2021.230238

Yue, L., Li, W., Sun, F., Zhao, L., and Xing, L. (2010). Highly Hydroxylated Carbon Fibres as Electrode Materials of All-Vanadium Redox Flow Battery. *Carbon* 48 (11), 3079–3090. doi:10.1016/j.carbon.2010.04.044

Zhang, H., Chen, N., Sun, C., and Luo, X. (2020). Investigations on Physicochemical Properties and Electrochemical Performance of Graphite Felt and Carbon Felt for Iron-chromium Redox Flow Battery. *Int. J. Energ. Res* 44 (5), 3839–3853. doi:10.1002/er.5179

Zhang, H., Tan, Y., Li, J., and Xue, B. (2017). Studies on Properties of Rayon- and Polyacrylonitrile-Based Graphite Felt Electrodes Affecting Fe/Cr Redox Flow Battery Performance. *Electrochimica Acta* 248, 603–613. doi:10.1016/j.electacta.2017.08.016

Zhang, H., Tan, Y., Luo, X. D., Sun, C. Y., and Chen, N. (2019). Polarization Effects of a Rayon and Polyacrylonitrile Based Graphite Felt for Iron-Chromium Redox Flow Batteries. *Chem. Electro Chem.* 6 (12), 3175–3188. doi:10.1002/celc.201900518

Züttel, A., Gallandat, N., Dyson, P. J., Schlapbach, L., Gilgen, P. W., and Orimo, S.-I. (2022). Future Swiss Energy Economy: The Challenge of Storing Renewable Energy. *Front. Energ. Res.* 9. doi:10.3389/fenrg.2021.785908

**Conflict of Interest:** The authors declare that the research was conducted in the absence of any commercial or financial relationships that could be construed as a potential conflict of interest.

frontiers | Frontiers in Chemistry

ORIGINAL RESEARCH
published: 30 June 2022
doi: 10.3389/fchem.2022.936679

# Porous ZnO Nanosphere Inherently Encapsulated in Carbon Framework as a High-Performance Anode For Ni–Zn Secondary Batteries

*Zhuo Li*[1], *Xianwei Hu*[1]*, *Jian Kang*[2], *Xiaoli Wang*[1], *Lingyu Kong*[1], *Zhongning Shi*[2] *and Zhaowen Wang*[1]

[1]Key Laboratory for Ecological Metallurgy of Multimetallic Mineral (Ministry of Education), School of Metallurgy, Northeastern University, Shenyang, China, [2]State Key Laboratory of Rolling and Automation, Northeastern University, Shenyang, China

Nickel–zinc (Ni-Zn) secondary battery that is environmentally friendly and inexpensive has been regarded as a promising rechargeable battery system. However, the generation of deformation and dendrites of the traditional zinc anode during the cycling can cause capacity degradation and impede its practical application. Herein, we design a hierarchical ZnO nanosphere coated with an inherently derived ZIF-8 porous carbon shell (ZnO@$C_{ZIF-8}$) using a simple controllable method. The conductive carbon shell and porous ZnO core can provide more active sites, allow the fast transfer of electrons, and buffer the volume expansion of the electrode effectively. Benefiting from the synergistic effect amid the inherently ZIF-8–derived carbon shell and ZnO core, ZnO@$C_{ZIF-8}$ nanospheres exhibit a satisfying capacity of 316 mAh $g^{-1}$ at a current density of 1 A $g^{-1}$ after 50 cycles and an outstanding rate capacity when acting as the anode for a Ni-Zn secondary battery with merchant agglomerative $Ni(OH)_2$ as the cathode. These results imply that the ZnO@$C_{ZIF-8}$ nanosphere is a hopeful anode for a high-energy Ni-Zn secondary battery.

**Keywords: intrinsic regulation, porous carbon shell, zinc oxide, anode, Ni-Zn batteries**

OPEN ACCESS

***Edited by:***
*Feng Gu,*
*Jiangxi University of Science and Technology, China*

***Reviewed by:***
*Fang Zhao,*
*Xi'an University of Architecture and Technology, China*
*Zongliang Zhang,*
*Central South University, China*

***Correspondence:**
*Xianwei Hu*
*huxw@smm.neu.edu.cn*

***Specialty section:***
*This article was submitted to Nanoscience, a section of the journal Frontiers in Chemistry*

***Received:*** *05 May 2022*
***Accepted:*** *23 May 2022*
***Published:*** *30 June 2022*

***Citation:***
*Li Z, Hu X, Kang J, Wang X, Kong L, Shi Z and Wang Z (2022) Porous ZnO Nanosphere Inherently Encapsulated in Carbon Framework as a High-Performance Anode For Ni–Zn Secondary Batteries. Front. Chem. 10:936679. doi: 10.3389/fchem.2022.936679*

## INTRODUCTION

Energy demand is increasing as societies continue to develop. Fossil fuels have caused severe pollution of the environment, so the development of environmentally friendly and renewable rechargeable battery systems is becoming increasingly important (Lund, 2007; Dunn et al., 2011; Wang et al., 2016). Rechargeable battery systems such as lithium-ion and nickel–hydrogen have received extensive attention because they are environment friendly and have considerable capacity (Yu et al., 2008; Lu et al., 2015; Xu et al., 2016). However, most existing rechargeable battery systems have limitations that hinder their further development. For example, the operating temperature range of the nickel–hydrogen battery is limited, and it often confronts a low operating voltage (Li et al., 2018). Lithium-ion batteries have high manufacturing costs, and the matched organic electrolyte has serious safety problems, such as toxicity and possibility of explosion (Stock et al., 2018; Yan et al., 2018). Compared with these battery systems, the nickel–zinc (Ni-Zn) secondary battery is a better alternative energy storage system with great prospects because of advantages such as cheap cost, safety, environmental friendliness, and outstanding specific energy density (Li and Dai, 2014; Yuan et al., 2014; Sun et al., 2016).

The anode is an important part of the nickel–zinc battery. However, the traditional zinc anode used in the Ni-Zn secondary battery suffers from deformation, dendrite, and corrosion during the

charge and discharge processes. This results in capacity degradation, which severely limits the development of the Ni-Zn secondary battery (Lan et al., 2007; Wu et al., 2009; Nakata et al., 2015; Guo et al., 2017; Chen et al., 2021). Researchers have performed many studies to solve problems including surface modification (Park et al., 2018; He et al., 2021), structural optimization (Zeng et al., 2019a), and the use of active additives to improve the performance of zinc anode (Xie et al., 2015; Yi et al., 2021). Among them, carbon-shell–coated zinc oxide (ZnO) materials have shown great application potential. The carbon layer is coated on the surface of ZnO, which not only inhibits the dissolution of ZnO but also improves the conductivity of the base material and results in a symmetrical dispersion of electrons on the surface of the ZnO particles (Feng et al., 2015; Xia et al., 2019; Zhou et al., 2020). Long's group prepared carbon-coated ZnO through the ball-milling pattern using glucose as the carbon source (Long et al., 2013). The material exhibited great cycling performance when used as an anode for Ni-Zn secondary battery. Other researchers prepared the ZnO/carbon nanotube composites by controlling the vertical growth of ZnO on carbon nanotubes (Cui et al., 2019). The unique heterostructure can efficiently improve the contact surface between the electrode and electrolyte to promote ion transport (Huang et al., 2014; Li et al., 2017a; Zeng et al., 2020). However, these strategies are only applied to modify the surface of ZnO by directly introducing the carbon source, which decreases the contact surface between the carbon material and ZnO and incompletely restrains the growth of dendrites. Therefore, it is necessary to realize a carbon-coating strategy that inherently evolves on the surface of ZnO to further enhance the electrochemical performance of zinc anode materials.

Zeolitic-imidazolate frameworks (ZIFs) are novel 3D framework materials that have received wide attention due to their well-designed morphology, ordered pore structure, and high stability (Lin et al., 2020; Huo et al., 2021; Xu et al., 2022). The pyrolysis product of ZIFs is a porous carbon material with a considerable specific area and conductivity under anaerobic conditions (Jiang et al., 2017; Li et al., 2020). Based on the aforementioned summary, we successfully synthesized a unique hierarchical ZnO nanosphere coated with ZIF-8 inherently derived porous carbon shell (ZnO@$C_{ZIF-8}$) by using a simple hydrothermal method following pyrolysis. The electrochemical properties of ZnO@$C_{ZIF-8}$ employed as an anode for the Ni-Zn secondary battery were investigated. Benefiting from the unique core-shell heterostructure consisting of the ZIF-8 inherently derived carbon shell and porous ZnO core with abundant active sites, the ZnO@$C_{ZIF-8}$ nanocomposites present a stable base structure and improved cycling stability.

# EXPERIMENT

## Synthesis of ZIF-8

Zn $(NO_3)_2{\cdot}6H_2O$ (1.1158 g) was dissolved in 30 ml methanol under ultrasonic treatment. 2-Methylimidazole (1.2337 g) was dissolved in 30 ml methanol. Then, the aforementioned solutions were mixed. The mixed solution was continuously stirred for 20 h. After that, the white precipitate was washed with methanol 3 times and vacuum dried.

## Synthesis of ZnO@ZIF-8

Zn $(CH_3COO)_2$ (6.5 g) was first hemolyzed in 300 ml diethylene glycol under ultrasonication for half of an hour to obtain a clear solution and then transferred into a flask. This mixture was heated at 150°C in an oil slot with continuous stirring for 0.5 h. During this step, the solution gradually changed from colorless to a milky white color. After the solution cooled to indoor temperature, the ZnO nanospheres were obtained and dried at 60°C for 10 h. The as-prepared ZnO nanospheres were dispersed in 30 ml methanol with 1.2337 g 2-methylimidazole and stirred for 0.5 h. The aforementioned mixture was poured into a reaction still and held at 70°C for 20 h. Then, ZnO@ZIF-8 was obtained by centrifugation at 8,000 rpm for 5 min, washed with methanol, and dried at 60°C.

## Synthesis of ZnO@$C_{ZIF-8}$

The ZnO@ZIF-8 powders were annealed in an Ar atmosphere at 600°C for 3 h at a heating rate of 3°C $min^{-1}$. After cooling to indoor temperature, ZnO@$C_{ZIF-8}$ was obtained. For comparison, ZnO was prepared by the same process using a single ZIF-8 as a precursor, marked as ZnO (ZIF-8).

## Material Characterization

The crystalline structural characterization of the samples was investigated by X-ray diffraction (XRD, D8). Transmission electron microscopy (TEM, FEI Talos-F200S) and scanning electron microscopy (SEM, Zeiss Sigma 300) were used to observe the morphology and microstructure of the samples. Raman spectra were performed using an HR800 spectrophotometer with 633 nm laser excitation. The carbon content in the product was confirmed with thermogravimetric analysis (TGA) under an air atmosphere from 20 to 700°C. The specific area and porous property were measured via $N_2$ adsorption/desorption isotherms (Quantachrome Autosorb-IQ3). The surface element component of the sample was determined via X-ray photoelectron spectroscopy (XPS, Thermo Scientific K-Alpha).

## Electrochemical Measurements

The ZnO@$C_{ZIF-8}$ (active material, 80%), polyvinylidene fluoride (PVDF, 10%), and conductive carbon (10%) in N-methyl-2-pyrrolidone (NMP) solvent were mixed to obtain a mixed slurry. The as-prepared mixture was pasted on tinfoil and dried at 70°C in vacuum. The ZnO@$C_{ZIF-8}$ anode was punched into a wafer (diameter of 10 mm). The loading mass of the electrode was 0.8~1.0 mg. The electrochemical performances of ZnO@$C_{ZIF-8}$ were determined by assembling CR2032 coin cells using agglomerative $Ni(OH)_2$ as the cathode and a mixed solution (4 M KOH, 2 M $K_2CO_3$, and 2 M KF) as the electrolyte. A galvanostatic charge and discharge test was performed on the LAND-CT2001 batter-testing system. The cell was charged to 1.9 V and discharged to 1.5 V for a certain time. Cycle voltammogram (CV 1 mV $s^{-1}$, voltage ambit between

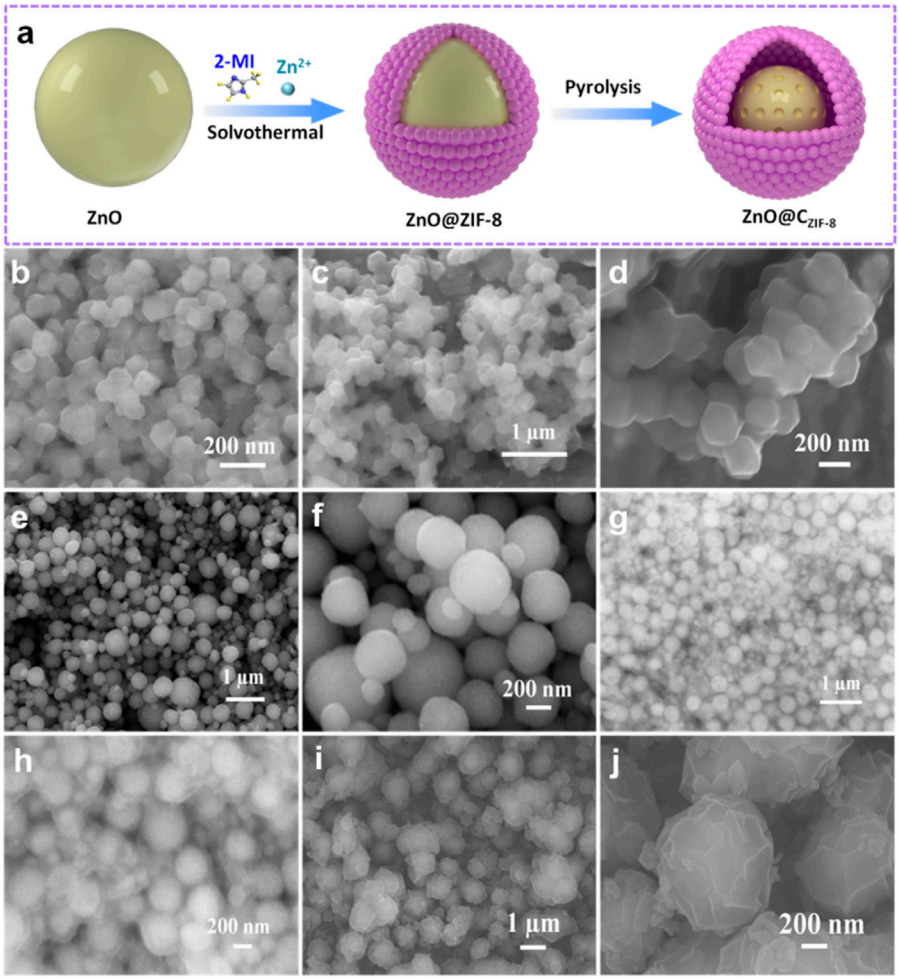


**FIGURE 1 | (A)** The preparation process of core-shell ZnO@$C_{ZIF-8}$. SEM images of **(B)** ZIF-8, **(C,D)** ZnO (ZIF-8), **(E,F)** ZnO nanosphere, **(G,H)** ZnO@ZIF-8, and **(I,J)** ZnO@$C_{ZIF-8}$.

−1.9~−1.0 V), electrochemical impedance spectroscopy (EIS, 10 kHz to 0.1 Hz), and Tafel plots were obtained by using an electrochemical workstation (CHI660D).

## RESULTS AND DISCUSSION

The core-shell structural ZnO@$C_{ZIF-8}$ nanospheres were prepared as shown schematically in **Figure 1A**. First, a ZnO nanosphere precursor with a diameter range between 300 and 500 nm is synthesized by heating in an oil bath (**Figures 1E,F**). Second, a shell layer of ZIF-8 is intrinsically grown and coated on the surface of the nanosphere precursor by the solvothermal method. It can be observed that the ZIF-8 layer forms a coating shell on the nanosphere surface, and the obtained ZnO@ZIF-8 is uniform with a diameter size of about 600 nm (**Figures 1G,H**). Moreover, ZIF-8 and ZnO (pyrolysis treatment of ZIF-8) were prepared, as presented in **Figures 1B–D**. The ZIF-8 nanoparticles presented a rhombic dodecahedron morphology with a size of about 100 nm, and the framework structure can be maintained after the pyrolysis process. Finally, the well-designed carbon shell derived from the ZIF-8 layer can be generated and coated on the surface of the ZnO core. The inherently derived porous ZIF-8 carbon shell plays a vital role in the construction of ZnO@$C_{ZIF-8}$. **Figures 1I,J** show the morphology of ZnO@$C_{ZIF-8}$. After pyrolysis treatment, the spherical structure was preserved, and the surface became rougher, which is ascribed to the decomposition of the organic-functional groups in ZIF-8 (Li et al., 2020). The average size of ZnO@$C_{ZIF-8}$ is about 600 nm.

In **Figure 2A**, the XRD pattern of ZIF-8 is consistent with the ZIF-8 crystal reported in the literature (Zhang et al., 2017) and the diffraction peaks are sharp, which indicate the high purity and great crystallinity of the material. Furthermore, the characteristic peaks of ZnO can be detected in the curve of ZnO@ZIF-8. This result confirms that the ZIF-8 layer can inherently form on the external surface of the ZnO nanosphere. All diffraction peaks of ZnO (ZIF-8) and ZnO@$C_{ZIF-8}$ can be well matched to hexagonal ZnO (PDF#70-2551). The peaks at 31.8°, 34.3°, 36.6°, 47.7°, 56.5°, 62.7°, and 68.1° for ZnO (ZIF-8) and ZnO@$C_{ZIF-8}$ were associated with the (100), (002), (101), (102), (110), (103), and (112) planes

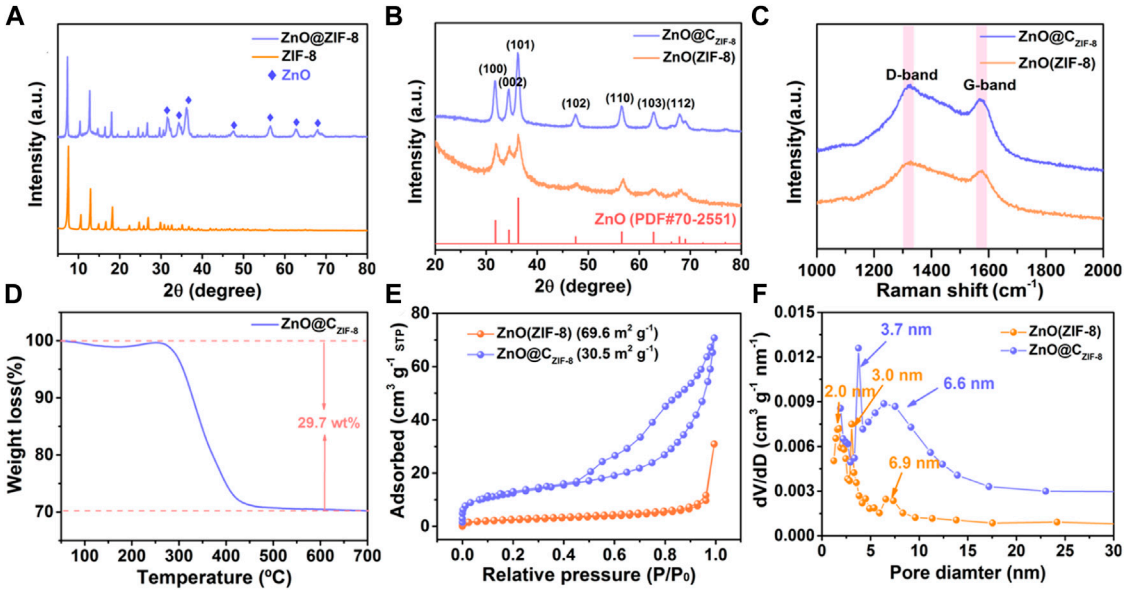


**FIGURE 2 |** XRD patterns of **(A)** ZIF-8 and ZnO@ZIF-8, **(B)** ZnO (ZIF-8), and ZnO@$C_{ZIF-8}$. **(C)** The Raman spectra of ZnO (ZIF-8) and ZnO@$C_{ZIF-8}$. **(D)** The TGA curve of ZnO@$C_{ZIF-8}$. **(E)** $N_2$ adsorption–desorption isotherms and **(F)** pore size distribution curves of ZnO (ZIF-8) and ZnO@$C_{ZIF-8}$.

of ZnO, respectively. The Zn species in ZIF-8 can be oxidized to the metal oxide (ZnO) during pyrolysis. This is ascribed to the oxygen released from the decomposition of organic-functional groups in ZIF-8. In addition, the peaks of ZnO@$C_{ZIF-8}$ are sharper than those of ZnO (ZIF-8), exhibiting the high crystallinity of ZnO@$C_{ZIF-8}$.

To further inquire about the constituents and pore diameter size of the samples, Raman, TGA, and BET tests were measured. The Raman spectra for ZnO (ZIF-8) and ZnO@$C_{ZIF-8}$ both present two distinct peaks at 1,322 $cm^{-1}$ (D-band) and 1,575 $cm^{-1}$ (G-band). These peaks are ascribed to disordered carbon and graphitic carbon, respectively, confirming the presence of a carbon shell (Li et al., 2017b). **Figure 2A** shows the TGA curves of ZnO@$C_{ZIF-8}$ in an air atmosphere. For ZnO@$C_{ZIF-8}$, a major weight loss appeared at 300°C due to the pyrolysis of the coated carbon shell. The carbon content in ZnO@$C_{ZIF-8}$ is estimated to be 29.7%. **Figures 2E,F** present the BET curves and the pore diameter size of ZnO (ZIF-8) and ZnO@$C_{ZIF-8}$, respectively. The specific surface areas for ZnO (ZIF-8) and ZnO@$C_{ZIF-8}$ (**Figure 2E**) are estimated to be 30.5 and 69.6 $m^2g^{-1}$, respectively. As shown in **Figure 2F**, the pore diameter distributions are mostly centered at 2~10 nm for ZnO (ZIF-8) and ZnO@$C_{ZIF-8}$. The result indicates that the samples mainly comprise a mesoporous structure (2–50 nm). The formation of mesoporous structure for ZnO@$C_{ZIF-8}$ is ascribed to the release of gas-phase compounds in the ZIF-8 during the carbonization (Li et al., 2020). The structural characteristics of mesoporous are helpful for the transportation of $Li^+$ ions and the improvement of the active site.

The microstructure of the products were also investigated by TEM. The ZIF-8 particles display a uniform rhombic dodecahedron (**Figure 3A**). Compared with ZIF-8, the surface of ZnO (ZIF-8) is sunken and shrunken after carbonization (**Figure 3B**), and the particle size is slightly reduced. Agglomeration occurs between the particles for both ZIF-8 and ZnO (ZIF-8). As presented in **Figure 3C**, ZnO@ZIF-8 exhibits a sphere-shaped heterostructure coated with a ~50 nm inherent growth of the ZIF-8 shell, and the particle size of ZnO@ZIF-8 is ~700 nm. **Figures 3D,E** show the TEM images of ZnO@$C_{ZIF-8}$. The microsphere structure can be maintained after carbonization. The carbon-shell–derived ZIF-8 layer is coated on the external face of the ZnO core. Furthermore, the pyrolysis of the coated ZIF-8 layer can cause volume contraction of ZnO@$C_{ZIF-8}$. Thus, the external shell of ZnO@$C_{ZIF-8}$ becomes rough, and the particle size decreases. Agglomeration can be controlled, owing to the preservation of the carbon shell. The HRTEM image of ZnO@$C_{ZIF-8}$ (**Figure 3F**) presents lattice fringes with an interplanar spacing of 0.26 nm, matching the (002) plane of ZnO.

The surface element compositions and valences of the as-prepared ZnO@$C_{ZIF-8}$ were analyzed using XPS. The full spectrum in **Figure 4A** shows the presence of Zn, N, O, and C elements in ZnO@$C_{ZIF-8}$. The Zn 2p spectrum of ZnO@$C_{ZIF-8}$ contains two characteristic peaks at 1,043.8 and 1,022.1 eV, matching Zn 2p1/2 and Zn 2p2/3, respectively. This result reveals the existence of a Zn (II) oxidation state in ZnO@$C_{ZIF-8}$. For the O 1s spectrum of ZnO@$C_{ZIF-8}$ (**Figure 4D**), the peak is fitted for three peaks at 533.1, 531.7, and 530.1 eV, respectively. The characteristic peak at 530.1 eV is matched to the lattice oxygen of ZnO, and the other two peaks at 533.1 and 531.7 eV are derived from the C-OH and C=O in the carbon shell, respectively (Zeng et al., 2019b). The N 1s spectrum of the ZnO@$C_{ZIF-8}$ is presented in **Figure 4D**. The broadband is fitted into three peaks, which are ascribed to graphitic-N (400.5 eV), pyrrolic-N (399.7 eV), and pyridinic-N (298.1 eV), respectively, derived

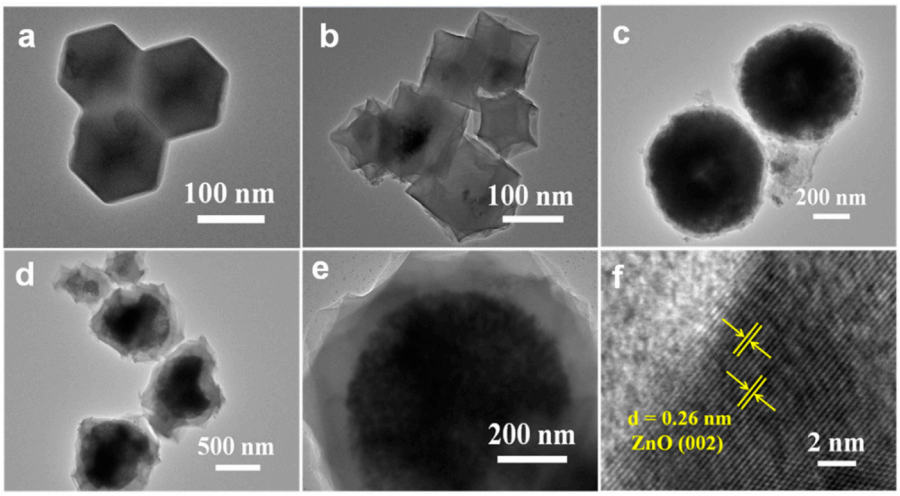


**FIGURE 3 |** TEM images of **(A)** ZIF-8, **(B)** ZnO (ZIF-8), **(C)** ZnO@ZIF-8, **(D,E)** ZnO@$C_{ZIF-8}$, and **(F)** HRTEM of ZnO@$C_{ZIF-8}$.

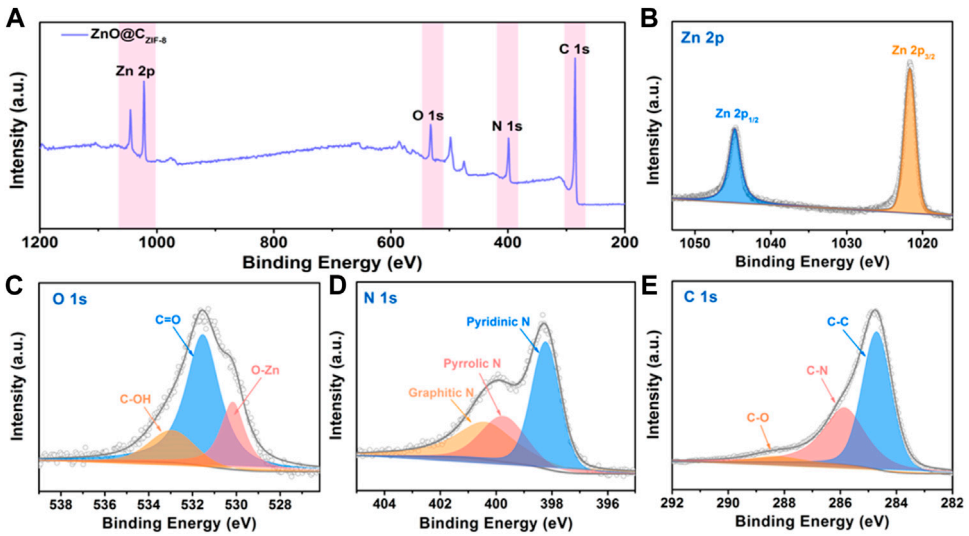


**FIGURE 4 | (A)** The Survey XPS spectrum of ZnO@$C_{ZIF-8}$ microsphere. **(B–E)** High-resolution XPS spectra of Zn 2p, C 1s, O 1s, and N 1s.

from the splitting decomposition of the organic-functional group in the ZIF-8 layer during carbonization. As is well known, N-doped graphitized carbon can be used as additional active sites to improve zinc storage (Xu et al., 2022). The C 1s spectrum of ZnO@$C_{ZIF-8}$ is also given (**Figure 4C**). The C 1s spectrum can be fitted into three spectral peaks, assigned to C-O (288.1 eV), C-N (285.9 eV), and C-C (284.6 eV). The formation of C-N bands reveals that N-atoms are anchored on the carbon shell. Moreover, the existence of N-doped carbon can also enhance the electrical conductivity of the base material (Xu et al., 2022).

The electrochemical performances of the as-prepared samples were tested by constructing a button cell using commercial sintered Ni $(OH)_2$ as the cathode, as shown in **Figure 5**. To confirm the related electrochemical behaviors during the discharge–charge processes, a cycling voltammogram (CV) was tested with a voltage window amid −1.9 and −1.0 V at a scan rate of 1 mV $s^{-1}$. It can be observed that all electrodes show similar CV curves, which include the reduction peaks for ZnO@$C_{ZIF-8}$ (−1.37 V) and ZnO (ZIF-8) (−1.34 V) and the oxidation peaks for ZnO@$C_{ZIF-8}$ (−1.35 V) and ZnO (ZIF-8) (−1.29 V). The potential intervals between the oxidation peak and the reduction peak of ZnO (ZIF-8) and ZnO@$C_{ZIF-8}$ are 0.046 and 0.03 V, respectively. The lower potential interval implies that the ZnO@$C_{ZIF-8}$ anode presents better reversibility (Yan et al., 2018). The electrochemical reactions can be presented as follows:

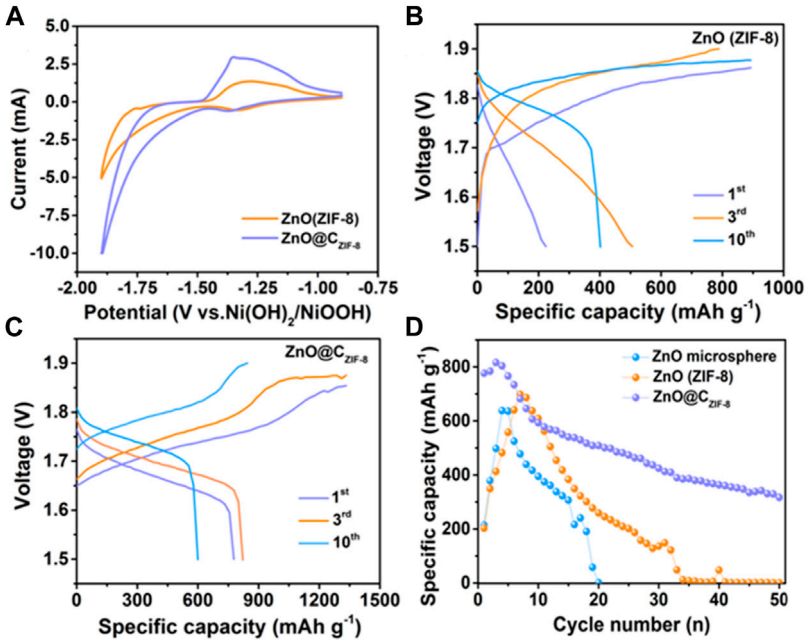


**FIGURE 5 | (A)** Cyclic voltammogram curves of ZnO (ZIF-8) and ZnO@$C_{ZIF-8}$. Galvanostatic charge and discharge curves of **(B)** ZnO (ZIF-8) and **(C)** ZnO@$C_{ZIF-8}$ at 1st, 3rd, and 10th cycles. **(D)** Cycling performance of ZnO microsphere, ZnO (ZIF-8), and ZnO@$C_{ZIF-8}$ at 1 A $g^{-1}$.

$$\text{Charge process}: ZnO + 2OH^- + H_2O \rightarrow Zn(OH)_4^{2-}, \quad (1)$$

$$Zn(OH)_4^{2-} + 2e^- \rightarrow Zn + 4OH^-, \quad (2)$$

$$\text{Discharge process}: Zn + 4OH^- \rightarrow Zn(OH)_4^{2-} + 2e^-, \quad (3)$$

$$Zn(OH)_4^{2-} \rightarrow Zno + 2OH^- + H_2O. \quad (4)$$

**Figures 5B,C** show the discharge and charge curves of ZnO (ZIF-8) and ZnO@$C_{ZIF-8}$ at different cycles (1st, 3rd, and 10th cycles). The discharge specific capacities of ZnO@$C_{ZIF-8}$ are 777, 820, and 601 mAh $g^{-1}$ at the 1st, 3rd, and 10th cycles, respectively, which are larger than those of ZnO (ZIF-8) (223, 507, and 401 mAh $g^{-1}$ at the first, third, and 10th cycles). For comparison, the cycling performances of ZnO@$C_{ZIF-8}$, ZnO (ZIF-8), and ZnO (nanosphere) are presented in **Figure 5D**. The specific capacity of ZnO (nanosphere) declined seriously and depleted after 20 cycles. The ZnO (ZIF-8) anode suffers the same experience. In contrast, the cycling performance of ZnO@$C_{ZIF-8}$ remained steady, and the discharge capacity reached 316 mAh $g^{-1}$ after 50 cycles. This benefit stemmed from the synergistic effect of the carbon shell derived from the inherent ZIF-8 layer and ZnO nanoparticle core.

**Figures 6A–C** present the rate stabilities of ZnO (ZIF-8) and ZnO@$C_{ZIF-8}$ at various current densities. The discharge specific capacities of ZnO@$C_{ZIF-8}$ at 1, 1.5, and 2 A $g^{-1}$ are 821, 562, and 396 mAh $g^{-1}$, respectively, which are larger than those of ZnO (ZIF-8) (536, 477, and 312 mAh $g^{-1}$ at 1, 1.5, and 2 A $g^{-1}$). **Figure 6D** displays the midpoint discharge voltage charts of ZnO (ZIF-8) and ZnO@$C_{ZIF-8}$, which is also a significant argument for rechargeable batteries. The better the stability and higher the midpoint discharge voltage, the higher the specific energy and the greater the electrochemical property. ZnO@$C_{ZIF-8}$ exhibits a stable and high midpoint discharge voltage during cycling. However, the midpoint discharge voltage of ZnO (ZIF-8) markedly decreases after 18 cycles. The Tafel plot curves (**Figure 6E**) of ZnO (ZIF-8) and ZnO@$C_{ZIF-8}$ are exhibited to investigate the anticorrosion performance of the electrode in alkaline solution, assessed using corrosion potential ($E_{corr}$) (Li et al., 2017a). We observed that the value of $E_{corr}$ for ZnO@$C_{ZIF-8}$ (−1.115) was more positive than that of ZnO (ZIF-8) (−1.167). This indicates that the ZnO@$C_{ZIF-8}$ electrode exhibits better corrosion resistance. The mainspring was that the coated carbon shell can control the corrosion of ZnO. Nyquist plots of the ZnO (ZIF-8) and ZnO@$C_{ZIF-8}$ electrodes are exhibited in **Figure 6F**. All plots are semi-circular in the high-frequency region and show an oblique stroke in the low-frequency region. These are related to charge transfer and ion diffusion in the electrode. Obviously, the semi-circular diameter of ZnO@$C_{ZIF-8}$ is smaller than that of ZnO (ZIF-8), implying that the coated carbon shell enhances the electronic conductivity of the base material. The morphological changes of ZnO and ZnO@$C_{ZIF-8}$ after the cycles are presented in **Figure 6G**. The ZnO (ZIF-8) suffers an inevitable volume increase during cycling, causing fracture of the material. By constructing the inherently derived core-shell structure, the ZIF-8–derived carbon shell restricts the volume expansion of the ZnO core during the cycling process. This indicates that the inherently derived carbon shell clings to the surface of ZnO and effectively ensnares the volume expansion of the active material, thereby increasing the cycling performance. The superior electrochemical performances of ZnO@$C_{ZIF-8}$ can be ascribed to its unique hierarchical structure. First, the microsize of ZnO@$C_{ZIF-8}$ guarantees more efficient infiltration between the electrolyte and the electrode. Second, the existence of a carbon

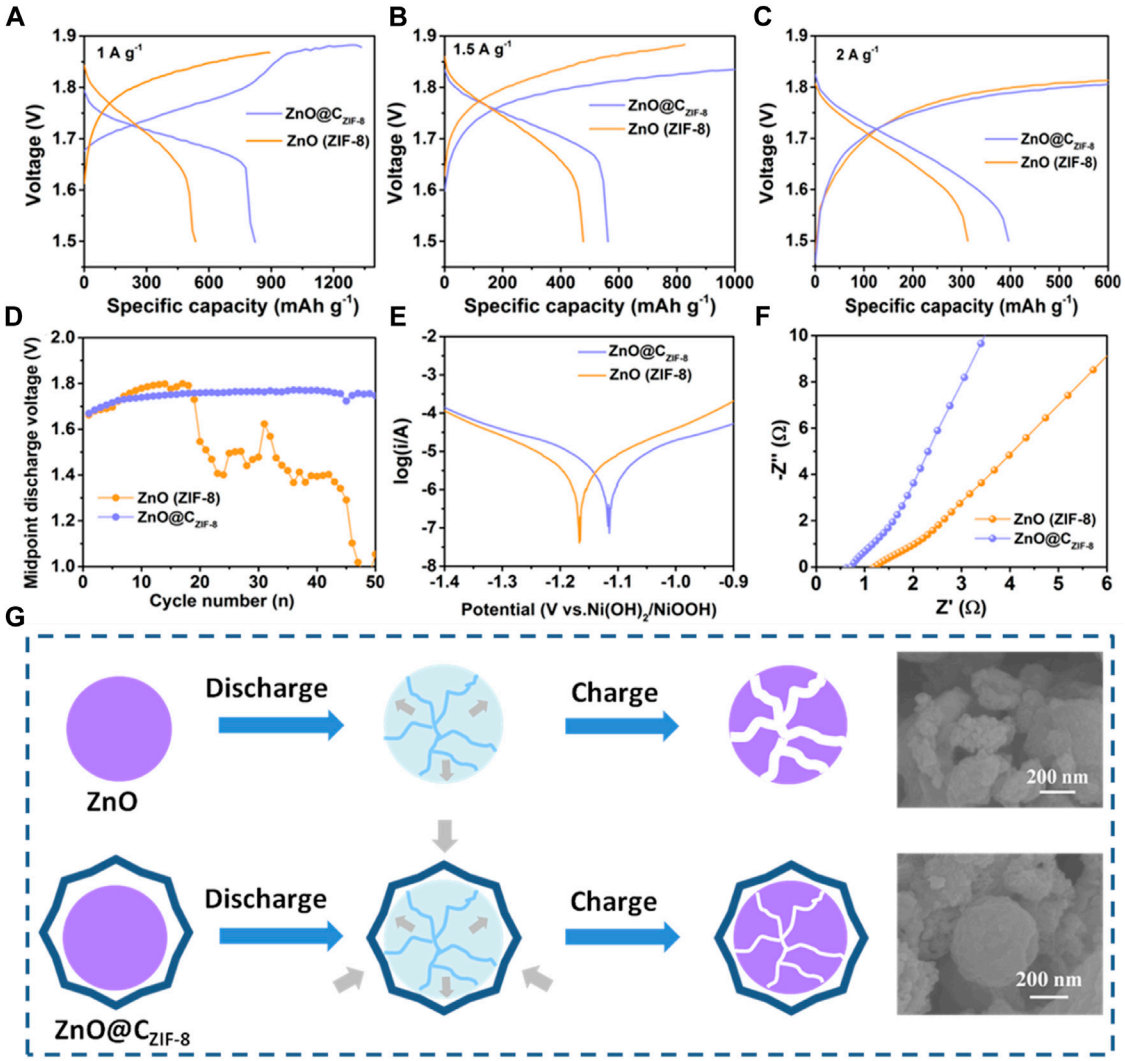


**FIGURE 6 |** Rate performance of ZnO (ZIF-8) and ZnO@$C_{ZIF-8}$ electrodes at different current densities: **(A)** 1 A $g^{-1}$, **(B)** 1.5 A $g^{-1}$, and **(C)** 2 A $g^{-1}$. **(D)** Midpoint discharge voltage curves of the Ni-Zn batteries with different anodes of ZnO (ZIF-8) and ZnO@$C_{ZIF-8}$. **(E)** The Tafel plot of ZnO (ZIF-8) and ZnO@$C_{ZIF-8}$ electrodes. **(F)** Nyquist plots of ZnO (ZIF-8) and ZnO@$C_{ZIF-8}$ electrodes. **(G)** Morphological changes after the charge/discharge processes.

shell derived from the inherent ZIF-8 layer can not only weaken the dissolution of ZnO and be the detriment of zinc dendrites but can also increase the electronic conductivity of the electrode.

## CONCLUSION

In summary, a unique core-shell ZnO@$C_{ZIF-8}$ nanocomposite was successfully synthesized using a ZnO nanosphere as the core and an inherent ZIF-8 layer as the coated carbon source by using a simple hydrothermal method and subsequent pyrolysis process. The inherent ZIF-8–derived carbon shell with N-doping can improve the electronic conductivity and offer abundant active sites. Meanwhile, this hierarchical structure provides an extreme self-adaptive framework that can efficiently control the volume expansion of the electrode. Benefiting from the unique hierarchical structure, the ZnO@$C_{ZIF-8}$ nanocomposite exhibits superior electrochemical properties when used as anode material in the Ni-Zn secondary battery. In particular, the ZnO@$C_{ZIF-8}$ electrode presents a discharge-specific capacity of 820 mAh $g^{-1}$, which is larger than that of the ZnO (ZIF-8) (507 mAh $g^{-1}$) and ZnO (nanosphere) precursor (410 mAh $g^{-1}$). In addition, the ZnO@$C_{ZIF-8}$ presents remarkable cycling stability and outstanding rate stability. The advanced electrochemical performances of the ZnO@$C_{ZIF-8}$ electrode can be attributed to the conductivity improvement, structure stability, anticorrosion property, and reaction reversibility of the inherent combination between the carbon shell and ZnO core. Therefore, this study offers a guide to constructing hierarchical inherent carbon-coated ZnO with outstanding electrochemical performances.

## DATA AVAILABILITY STATEMENT

The original contributions presented in the study are included in the article/Supplementary Material; further inquiries can be directed to the corresponding author.

## AUTHOR CONTRIBUTIONS

ZL: Conceptualization and writing—original draft. XW: Investigation and formal analysis. LK: Investigation and formal analysis. ZS: Validation. ZW: Validation. XH: Supervision, funding acquisition, and writing—review and editing.

## FUNDING

This work was financially supported by the National Natural Science Foundation of China (Grant no. 51974081), the Fundamental Research Funds for the Central Universities (Grant no. N2125005), and the Open Program of the State Key Laboratory of Rolling and Automation (2020RALKFKT008).

## REFERENCES

Chen, Z., Chen, H., Che, Y., Cheng, L., Zhang, H., Chen, J., et al. (2021). Arginine Cations Inhibiting Charge Accumulation of Dendrites and Boosting Zn Metal Reversibility in Aqueous Rechargeable Batteries. *ACS Sustain. Chem. Eng.* 9, 6855–6863. doi:10.1021/acssuschemeng.1c01609

Cui, C., Li, M., Zhou, X., and Zhang, X. (2019). Synthesis of ZnO/carbon Nanotube Composites for Enhanced Electrochemical Performance of Ni-Zn Secondary Batteries. *Mater. Res. Bull.* 112, 261–268. doi:10.1016/j.materresbull.2018.12.036

Dunn, B., Kamath, H., and Tarascon, J.-M. (2011). Electrical Energy Storage for the Grid: a Battery of Choices. *Science* 334, 928–935. doi:10.1126/science.1212741

Feng, Z., Yang, Z., Huang, J., Xie, X., and Zhang, Z. (2015). The Superior Cycling Performance of the Hydrothermal Synthesized Carbon-Coated ZnO as Anode Material for Zinc-Nickel Secondary Cells. *J. Power Sources* 276, 162–169. doi:10.1016/j.jpowsour.2014.11.121

Guo, W., Tian, Z., Yang, C., Lai, Y., and Li, J. (2017). ZIF-8 Derived Nano-SnO 2 @ZnO as Anode for Zn/Ni Secondary Batteries. *Electrochem. Commun.* 82, 159–162. doi:10.1016/j.elecom.2017.08.009

He, H., Qin, H., Wu, J., Chen, X., Huang, R., Shen, F., et al. (2021). Engineering Interfacial Layers to Enable Zn Metal Anodes for Aqueous Zinc-Ion Batteries. *Energy Storage Mater.* 43, 317–336. doi:10.1016/j.ensm.2021.09.012

Huang, J., Yang, Z., Yang, B., Wang, R., and Wang, T. (2014). Ultrasound Assisted Polymerization for Synthesis of ZnO/Polypyrrole Composites for Zinc/nickel Rechargeable Battery. *J. Power Sources* 271, 143–151. doi:10.1016/j.jpowsour.2014.07.140

Huo, Y., Teng, Y., Cai, K., and Chen, H. (2021). Honeycomb ZnO/N/C Obtained from Cornsilk and ZIF-8 Dual Induced Method for Long-Life Aqueous Zinc-Ion Batteries. *J. Alloys Compd.* 855, 157398. doi:10.1016/j.jallcom.2020.157398

Jiang, Y., Liu, H., Tan, X., Guo, L., Zhang, J., Liu, S., et al. (2017). Monoclinic ZIF-8 Nanosheet-Derived 2D Carbon Nanosheets as Sulfur Immobilizer for High-Performance Lithium Sulfur Batteries. *ACS Appl. Mat. Interfaces* 9, 25239–25249. doi:10.1021/acsami.7b04432

Lan, C. J., Lee, C. Y., and Chin, T. S. (2007). Tetra-alkyl Ammonium Hydroxides as Inhibitors of Zn Dendrite in Zn-Based Secondary Batteries. *Electrochimica Acta* 52, 5407–5416. doi:10.1016/j.electacta.2007.02.063

Li, J., Zhao, T., Shangguan, E., Li, Y., Li, L., Wang, D., et al. (2017). Enhancing the Rate and Cycling Performance of Spherical ZnO Anode Material for Advanced Zinc-Nickel Secondary Batteries by Combined *In-Situ* Doping and Coating with Carbon. *Electrochimica Acta* 236, 180–189. doi:10.1016/j.electacta.2017.03.164

Li, P., Jin, Z., and Xiao, D. (2018). Three-dimensional Nanotube-Array Anode Enables a Flexible Ni/Zn Fibrous Battery to Ultrafast Charge and Discharge in Seconds. *Energy Storage Mater.* 12, 232–240. doi:10.1016/j.ensm.2017.11.017

Li, Q., Li, L., Owusu, K. A., Luo, W., An, Q., Wei, Q., et al. (2017). Self-adaptive Mesoporous CoS@alveolus-like Carbon Yolk-Shell Microsphere for Alkali Cations Storage. *Nano Energy* 41, 109–116. doi:10.1016/j.nanoen.2017.09.022

Li, Y., and Dai, H. (2014). Recent Advances in Zinc-Air Batteries. *Chem. Soc. Rev.* 43, 5257–5275. doi:10.1039/c4cs00015c

Li, Z., Hu, X., Shi, Z., Lu, J., and Wang, Z. (2020). MOFs-Derived Metal Oxides Inlayed in Carbon Nanofibers as Anode Materials for High-Performance Lithium-Ion Batteries. *Appl. Surf. Sci.* 531, 147290. doi:10.1016/j.apsusc.2020.147290

Lin, Y., Zhang, L., Xiao, J., and Liu, H. (2020). MnO/C Cubo-Polyhedrons Derived from α-MnO2@ZIF-8 as Anode Materials for High-Performance Lithium-Ion Batteries. *Sustain. Energy Fuels* 4, 633–642. doi:10.1039/c9se00637k

Long, W., Yang, Z., Fan, X., Yang, B., Zhao, Z., and Jing, J. (2013). The Effects of Carbon Coating on the Electrochemical Performances of ZnO in Ni-Zn Secondary Batteries. *Electrochimica Acta* 105, 40–46. doi:10.1016/j.electacta.2013.04.162

Lu, X., Shang, Y., Zhang, S., and Deng, C. (2015). Enhanced Lithium Ion Transport by Superionic Pathways Formed on the Surface of Two-Dimensional Structured Li0.85Na0.15V3O8 for High-Performance Lithium Ion Batteries. *Electrochimica Acta* 155, 148–156. doi:10.1016/j.electacta.2014.12.119

Lund, H. (2007). Renewable Energy Strategies for Sustainable Development. *Energy* 32, 912–919. doi:10.1016/j.energy.2006.10.017

Nakata, A., Murayama, H., Fukuda, K., Yamane, T., Arai, H., Hirai, T., et al. (2015). Transformation of Leaf-like Zinc Dendrite in Oxidation and Reduction Cycle. *Electrochimica Acta* 166, 82–87. doi:10.1016/j.electacta.2015.03.076

Park, D.-J., Aremu, E. O., and Ryu, K.-S. (2018). Bismuth Oxide as an Excellent Anode Additive for Inhibiting Dendrite Formation in Zinc-Air Secondary Batteries. *Appl. Surf. Sci.* 456, 507–514. doi:10.1016/j.apsusc.2018.06.079

Stock, D., Dongmo, S., Walther, F., Sann, J., Janek, J., and Schröder, D. (2018). Homogeneous Coating with an Anion-Exchange Ionomer Improves the Cycling Stability of Secondary Batteries with Zinc Anodes. *ACS Appl. Mat. Interfaces* 10, 8640–8648. doi:10.1021/acsami.7b18623

Sun, L., Yi, Z., Lin, J., Liang, F., Wu, Y., Cao, Z., et al. (2016). Fast and Energy Efficient Synthesis of ZnO@RGO and its Application in Ni-Zn Secondary Battery. *J. Phys. Chem. C* 120, 12337–12343. doi:10.1021/acs.jpcc.6b01025

Wang, C.-Y., Zhang, G., Ge, S., Xu, T., Ji, Y., Yang, X.-G., et al. (2016). Lithium-ion Battery Structure that Self-Heats at Low Temperatures. *Nature* 529, 515–518. doi:10.1038/nature16502

Wu, J. Z., Tu, J. P., Yuan, Y. F., Ma, M., Wang, X. L., Zhang, L., et al. (2009). Ag-modification Improving the Electrochemical Performance of ZnO Anode for Ni/Zn Secondary Batteries. *J. Alloys Compd.* 479, 624–628. doi:10.1016/j.jallcom.2009.01.013

Xia, A., Pu, X., Tao, Y., Liu, H., and Wang, Y. (2019). Graphene Oxide Spontaneous Reduction and Self-Assembly on the Zinc Metal Surface Enabling a Dendrite-free Anode for Long-Life Zinc Rechargeable Aqueous Batteries. *Appl. Surf. Sci.* 481, 852–859. doi:10.1016/j.apsusc.2019.03.197

Xie, X., Yang, Z., Feng, Z., Zhang, Z., and Huang, J. (2015). Electrochemical Properties of ZnO Added with Zn-Al-Hydrotalcites as Anode Materials for Zinc/Nickel Alkaline Secondary Batteries. *Electrochimica Acta* 154, 308–314. doi:10.1016/j.electacta.2014.12.101

Xu, C., Liao, J., Yang, C., Wang, R., Wu, D., Zou, P., et al. (2016). An Ultrafast, High Capacity and Superior Longevity Ni/Zn Battery Constructed on Nickel Nanowire Array Film. *Nano Energy* 30, 900–908. doi:10.1016/j.nanoen.2016.07.035

Xu, J., Wang, J., Ge, L., Sun, J., Ma, W., Ren, M., et al. (2022). ZIF-8 Derived Porous Carbon to Mitigate Shuttle Effect for High Performance Aqueous Zinc-Iodine Batteries. *J. Colloid Interface Sci.* 610, 98–105. doi:10.1016/j.jcis.2021.12.043

Yan, X., Chen, Z., Wang, Y., Li, H., and Zhang, J. (2018). *In-situ* Growth of ZnO Nanoplates on Graphene for the Application of High Rate Flexible Quasi-Solid-

State Ni-Zn Secondary Battery. *J. Power Sources* 407, 137–146. doi:10.1016/j.jpowsour.2018.10.071

Yi, Z. H., Chen, G. Y., Hou, F., Wang, L. Q., and Liang, J. (2021). Strategies for the Stabilization of Zn Metal Anodes for Zn-Ion Batteries. *Adv. Energy Mat.* 11 (1-31), 2003065. doi:10.1002/aenm.202170001

Yu, L.-J., Qin, M.-J., Zhu, P., and Yang, L. (2008). Numerical Simulation and Optimization of Nickel-Hydrogen Batteries. *J. Power Sources* 179, 848–853. doi:10.1016/j.jpowsour.2007.12.126

Yuan, C., Wu, H. B., Xie, Y., and Lou, X. W. D. (2014). Mixed Transition-Metal Oxides: Design, Synthesis, and Energy-Related Applications. *Angew. Chem. Int. Ed.* 53, 1488–1504. doi:10.1002/anie.201303971

Zeng, X., Hao, J., Wang, Z., Mao, J., and Guo, Z. (2019). Recent Progress and Perspectives on Aqueous Zn-Based Rechargeable Batteries with Mild Aqueous Electrolytes. *Energy Storage Mater.* 20, 410–437. doi:10.1016/j.ensm.2019.04.022

Zeng, X., Yang, Z., Fan, M., Cui, F., Meng, J., Chen, H., et al. (2020). Shape-controlled Growth of Three-Dimensional Flower-like ZnO@Ag Composite and its Outstanding Electrochemical Performance for Ni-Zn Secondary Batteries. *J. Colloid Interface Sci.* 562, 518–528. doi:10.1016/j.jcis.2019.11.083

Zeng, X., Yang, Z., Meng, J., Chen, L., Chen, H., and Qin, H. (2019). The Cube-like Porous ZnO/C Composites Derived from Metal Organic Framework-5 as Anodic Material with High Electrochemical Performance for Ni-Zn Rechargeable Battery. *J. Power Sources* 438, 226986. doi:10.1016/j.jpowsour.2019.226986

Zhang, H., Wang, Y., Zhao, W., Zou, M., Chen, Y., Yang, L., et al. (2017). MOF-derived ZnO Nanoparticles Covered by N-Doped Carbon Layers and Hybridized on Carbon Nanotubes for Lithium-Ion Battery Anodes. *ACS Appl. Mat. Interfaces* 9, 37813–37822. doi:10.1021/acsami.7b12095

Zhou, Y., Wang, X., Shen, X., Shi, Y., Zhu, C., Zeng, S., et al. (2020). 3D Confined Zinc Plating/stripping with High Discharge Depth and Excellent High-Rate Reversibility. *J. Mat. Chem. A* 8, 11719–11727. doi:10.1039/d0ta02791j

**Conflict of Interest:** The authors declare that the research was conducted in the absence of any commercial or financial relationships that could be construed as a potential conflict of interest.

**Publisher's Note:** All claims expressed in this article are solely those of the authors and do not necessarily represent those of their affiliated organizations, or those of the publisher, the editors, and the reviewers. Any product that may be evaluated in this article, or claim that may be made by its manufacturer, is not guaranteed or endorsed by the publisher.

frontiers | Frontiers in Chemistry

ORIGINAL RESEARCH
published: 08 July 2022
doi: 10.3389/fchem.2022.933319

# Aerosol Jet Printing of Hybrid $Ti_3C_2T_x$/C Nanospheres for Planar Micro-supercapacitors

*Yu Wu[1†], Aiping Lin[1†], Jidi Zhang[2], Danjiao Zhao[1], Lanlan Fan[1], Cheng Lu[2], Shufen Wang[1], Lei Cao[1] and Feng Gu[1,2,3]**

[1]Laboratory of Advanced Materials & Manufacturing (LAMM), International Institute for Innovation, Jiangxi University of Science and Technology, Nanchang, China, [2]Institute for Process Modelling and Optimization, Jiangsu Industrial Technology Research Institute, Suzhou, China, [3]School of Energy and Environment, Southeast University, Nanjing, China

When utilized in energy devices, the restacking tendency of MXene $Ti_3C_2T_x$ inhibits its electrochemical performance. Using aerosol jet printing (AJP) technology, hybrid $Ti_3C_2T_x$/C nanospheres are synthesized with C nanoparticle-bonded MXene nanosheets, and the restacking of MXene nanosheets is blocked efficiently. The formation mechanism for hybrid $Ti_3C_2T_x$/C nanospheres has been hypothesized, and the $Ti_3C_2T_x$/C is anticipated to assemble and shape along the droplet surface in tandem with the Marangoni flow within the droplet. The planar microsupercapacitor devices generated from these hybrid spherical nanostructures with increased interlayer spacing exhibit exceptional areal capacitance performance. This concept offers a straightforward and effective method for constructing 3D-structured MXene with suppressed self-stacking for diverse high-performance micro energy storage devices.

**Keywords: aerosol jet printing, hybrid structure, nanosphere, MXene, restacking behavior**

OPEN ACCESS

***Edited by:***
*Baiquan Liu,*
*Sun Yat-sen University, China*

***Reviewed by:***
*Wei Han,*
*Jilin University, China*
*Peng Xiao,*
*Foshan University, China*

****Correspondence:***
*Feng Gu*
*feng.gu@jxust.edu.cn*

*†These authors have contributed equally to this work*

***Specialty section:***
*This article was submitted to Nanoscience, a section of the journal Frontiers in Chemistry*

***Received:*** *30 April 2022*
***Accepted:*** *21 June 2022*
***Published:*** *08 July 2022*

***Citation:***
*Wu Y, Lin A, Zhang J, Zhao D, Fan L, Lu C, Wang S, Cao L and Gu F (2022) Aerosol Jet Printing of Hybrid $Ti_3C_2T_x$/C Nanospheres for Planar Micro-supercapacitors. Front. Chem. 10:933319. doi: 10.3389/fchem.2022.933319*

## 1 INTRODUCTION

MXene has been attracting increasing attention because of its good metallicity, relatively large accessible surface area, and the availability of more active sites, endowing it with great potential for applications in energy storage (Ling et al., 2014; Naguib et al., 2014; Cao et al., 2021a; Cao et al., 2021b). However, MXene has a pronounced restacking characteristic with close contact between layers, which greatly reduces the exposed specific surface area and active sites (Xia et al., 2018; Fang et al., 2020; Cao et al., 2021c; Yang et al., 2021). Over the past few years, intensive efforts have been exerted to address this issue. Among them, three-dimensional (3D) structured MXene are expected to expose more active sites with facilitated ion transportation, which is essential for embodying the prominent electrochemical feature of MXene when developing future-related high-performance energy devices (Orangi and Beidaghi, 2020). By applying spherical poly(methyl methacrylate) (PMMA) as a template, a macroporous film of MXene has been developed with a significant increase in specific capacitance performance *($200Fg^{-1}$ at $10Vs^{-1}$)* (Lukatskaya et al., 2017). A similar method of sacrificing templates has also been applied to sodium ion storage (Zhao et al., 2017). However, these methods suffer from tedious procedures and time/energy consuming, while residuals are still in a difficult stage to be removed.

Basically, hybridization can be considered as an effective strategy to suppress MXene restacking. For example, knotted carbon nanotubes (CNTs) were developed to support the $Ti_3C_2$ network and restacking could be effectively avoided with enhanced ion accessibility (Gao et al., 2020). Graphene was embedded between $Ti_3C_2T_x$ nanosheets to form a high nanopore connectivity network to

facilitate ion transport (Fan et al., 2018). These protocols effectively suppressed the restacking behavior of MXene with enlarged interlayer spacing; however, the resultant hybrid structure was still in a facial form.

Aerosol jet printing (AJP) is a new type of additive manufacturing technology with industrialization prospects. As a non-contact, programmable, and versatile printing technique, the feature size of AJP could reach ~10 μm (Secor, 2018; Wu et al., 2021), implying the potential for precise preparation of individualized, batched, and miniaturized devices (Mahajan et al., 2013; Jabari and Toyserkani, 2015; Deiner and Reitz, 2017). Currently, AJP has been applied in the fabrication of integrated circuits (Skarzynski et al., 2021), transistors (Cao et al., 2017), memristor (Feng et al., 2019), ring oscillators (Ha et al., 2013), etc. Actually, during the AJP process, the atomized aerosol droplet could be developed as a microreactor mediating the solvent evaporation and solute migration for precisely constructing 3D nanostructures during deposition (Ha et al., 2013). Recently, our group developed a convenient AJP approach for *in situ* synthesis of MXene nanospheres with crumpled and eccentric characteristics (Wu et al., 2022). The shell of the nanosphere was still composed of densely stacked $Ti_3C_2T_x$ nanosheets.

Herein, we developed an effective AJP process for MXene hybrid nanospheres by introducing nanoscale carbon particles ($Ti_3C_2T_x$/C) inhibiting restacking and anchoring neighbouring nanosheets for integrity. The carbon nanoparticles were simply formulated with MXene for the precursor ink. The formation mechanism for the hybrid nanospheres has been proposed tentatively by considering the evaporation-induced migration and assembly process. The derived microsupercapacitor (MSC) device of MXene hybrid nanospheres shows excellent areal capacitance performance of 64.58 mF $cm^{-2}$. This work highlights the great potential of AJP for developing complex nanostructures and broadens the applications of additive manufacturing techniques for miniaturized and intelligent microelectronics.

## 2 RESULTS AND DISCUSSION

The precursor ink was simply formulated by mixing delaminated $Ti_3C_2T_x$ nanosheets and carbon nanoparticles (commercial carbon paint) of different mass ratios in deionized water. The synthesis of the delaminated $Ti_3C_2T_x$ refers previously reported methods, and the details are given in the experimental section (Lukatskaya et al., 2017; Eom et al., 2020; Li et al., 2020). The morphology of the delaminated $Ti_3C_2T_x$ nanosheets is shown in **Supplementary Figure S1** (Supporting Information), indicating the MAX phase ($Ti_3AlC_2$) was well etched to a single layer or few-layered nanosheets. **Figure 1A** shows the transmission electron microscopy (TEM) image of the carbon nanoparticles with a lateral size of 20–30 nm and thickness of 2–3 nm. The X-ray diffraction (XRD) pattern (**Supplementary Figure S2**, Supporting Information) further verified the carbon of graphite matching information with PDF card 41–1487. **Figure 1B** show the TEM image of the precursor ink, indicating that the carbon nanoparticles distribute uniformly on the MXene nanosheet surface, which can be further verified by the element mapping results (**Supplementary Figure S3**, Supporting Information). In our work, the relative mass ratio of $Ti_3C_2T_x$ and C was set at 0:1, 1:0, 1:0.5, 1:1, and 1:2, respectively. **Figure 1C** schematically illustrates the AJP procedure to fabricate hybrid $Ti_3C_2T_x$/C nanospheres. In case of the aerosol jet printing process, the precursor ink was atomized by an ultrasonic atomizer (1.7 MHz). The generated mist of

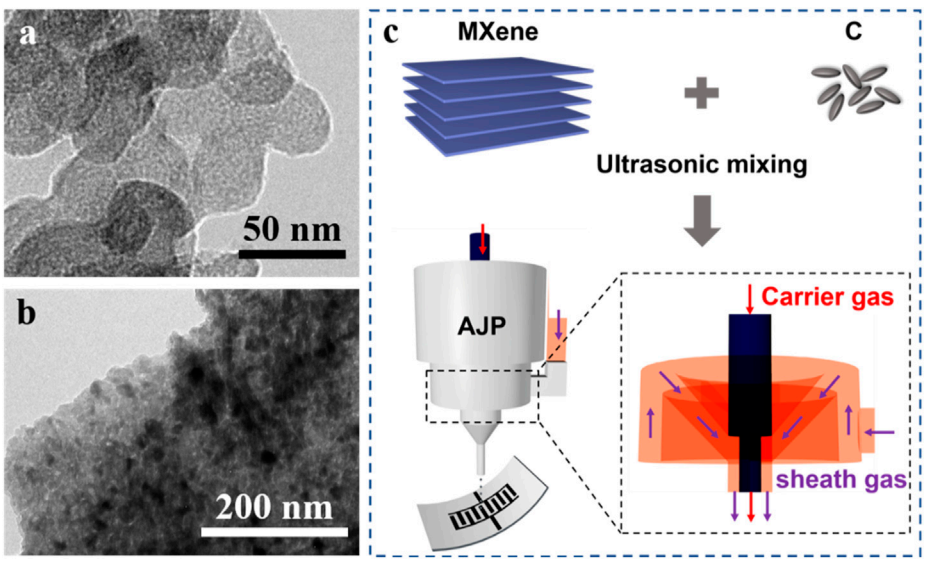


**FIGURE 1 | (A,B)** TEM images of the carbon nanoparticles and $Ti_3C_2T_x$/C ink; **(C)** schematic illustration of the AJP process for fabrication of hybrid $Ti_3C_2T_x$/C nanospheres.

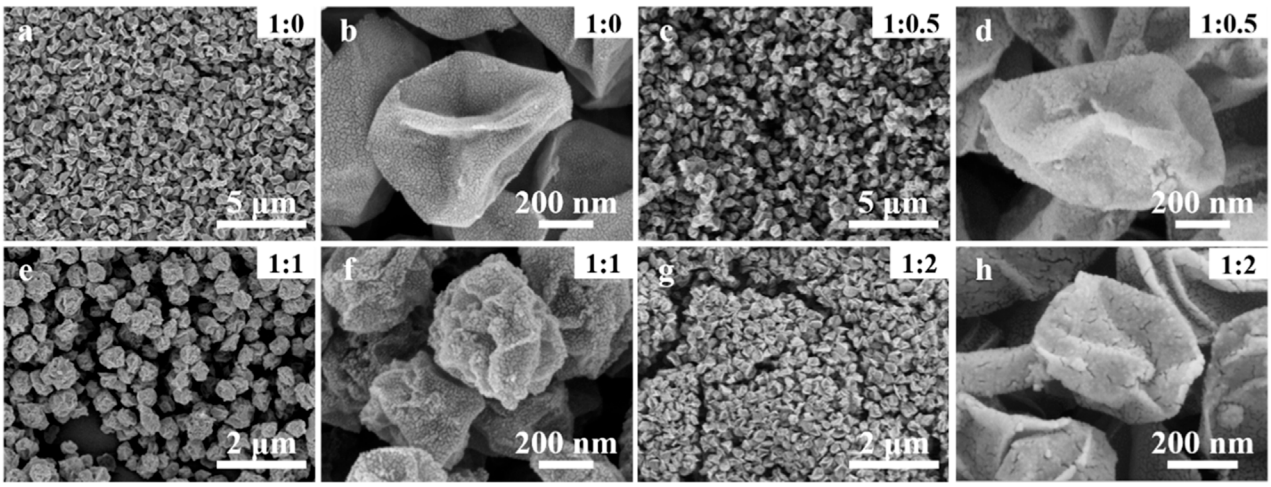


**FIGURE 2 |** SEM images of the printed hybrid $Ti_3C_2T_x$/C nanospheres with different mass ratios of MXene and carbon nanoparticles. **(A,B)** Pristine MXene nanospheres; **(C,D)** hybrid MXene nanospheres with mass ratio of 1:0.5; **(E,F)** hybrid MXene nanospheres with mass ratio of 1:1; **(G,H)** hybrid MXene nanospheres with mass ratio of 1:2.

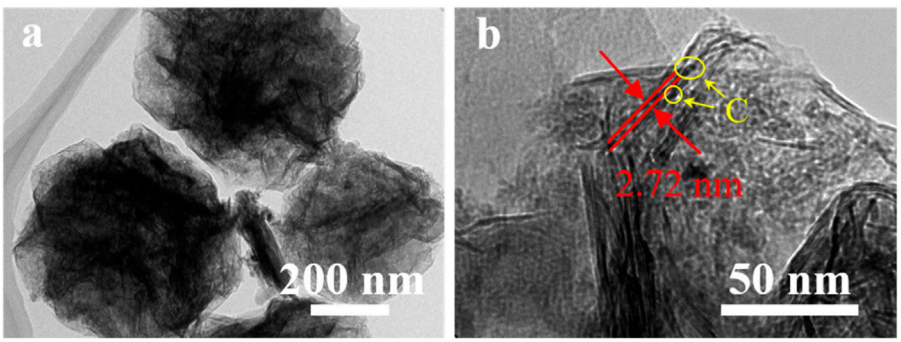


**FIGURE 3 |** HRTEM images of the printed hybrid $Ti_3C_2T_x$/C nanospheres showing the enlarged interlayer distance. The yellow circles mark the embedded carbon nanoparticles.

aerosol droplets (less than 10 μm) was transmitted to the nozzle by a carrier gas of $N_2$ and then shaped by a sheath gas of $N_2$ jetting out of the nozzle. By confining in the microscale regime of the sheath gas, the mist of aerosol droplets was tremendously focused into a microscale mist jet. The focus ration (FR), which is defined by the sheath gas rate to the carrier flow rate, determines the printing quality. In this work, the FR was fixed at 3 without obvious overspray phenomenon observed. The focused aerosol jet was subjected on the oxygen plasma–treated polyethylene terephthalate (PET) surface. The deposition temperature was 100°C for accelerating the solute migration.

The morphology and microstructure of the printed patterns were characterized by SEM and TEM, indicating the formation of crumpled nanospheres with ridges or wrinkles while the pristine facial MXene nanosheets were not detected (**Figures 2A**,**B**). The size of the formed spheres is ~500 nm, independent of carbon nanoparticles added. With the introduction of carbon nanoparticles, the spheres surface become rough and the carbon nanoparticles could be clearly observed (**Figures 2C–F**). When excessive carbon nanoparticles added (mass ratio of 1:2), a rather dense film composed of closely bonded nanospheres were formed (**Figure 2G**). It is found that the carbon nanoparticles are distributed homogeneously in the resultant hybrid products in case of the formulation of the precursor ink by simply mixing these two components. Due to the hydrophilic nature, the $Ti_3C_2T_x$ nanosheets could be dispersed in the solvent of water homogeneously. The negatively charged surface of MXene is assumed as the main reason for absorbing the carbon nanoparticles for formation of the hybrid structure. Under the ultrasonic condition for atomization, the dispersed carbon nanoparticles are prone to be adsorbed on the MXene nanosheets surface. During the assembly of $Ti_3C_2T_x$/C for the resultant spherical nanostructure, the adsorbed carbon nanoparticles could effectively inhibit the closely restacking tendency of MXene nanosheets. From **Figure 3B**, the embedded carbon nanoparticles could be clearly observed and

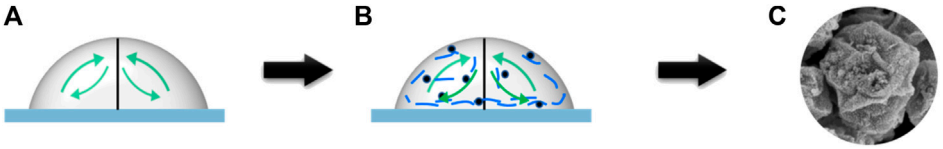


**FIGURE 4 |** Schematic illustration of the formation mechanism of hybrid MXene/C nanospheres. **(A)** Marangoni flow occurs in the deposited droplet due to the temperature gradient on heat substrate. **(B)** Carbon nanoparticles-anchored MXene nanosheets migrating from the interior to the edge; **(C)** MXene/C precipitating at the edge and shaping along the droplet surface for a spherical structure.

the interlayer distance is enlarged greatly up to 2–3 nm, consistent with the size of the carbon nanoparticles. The interlayer distance is obviously larger than its pristine MXene counterpart (less than 1 nm) (**Supplementary Figure S4**, Supporting Information). Here, the adsorbed carbon nanoparticles could also function as binders to bridge neighbouring nanosheets for integrity, which is particularly important for optimizing the electrochemical performance.

For a microscale droplet containing $Ti_3C_2T_x$/C components depositing on the heat PET surface, which is supposed to offer an isotropical evaporation regime, the temperature gradient along the liquid-vapor interface between the apex and the bottom of the drop causes a Marangoni flow inside the droplet (Girard et al., 2008). The evaporation of water from the edge is replenished by water from the interior, carrying $Ti_3C_2T_x$/C toward the edge by the Marangoni flows. As the evaporation progresses, the liquid/solid/gas three phase contact line (TCL) gradually recedes. The transmitting $Ti_3C_2T_x$/C are easily precipitated on the substrate surface at the edge and further shaped along the droplet surface during solvent evaporation to form a spherical structure with eccentric features by referring velocity field analysis of sessile water droplets on heat substrate, although $Ti_3C_2T_x$ MXene is generally resistant to bending due to high bending rigidity (Wu et al., 2021). The bending of $Ti_3C_2T_x$ nanosheets are expected to be triggered by the sonication for the aerosol droplets generation with stress inequality, which has been evidenced during the synthesis of graphene nanoscrolls previously reported (Savoskin et al., 2007). Moreover, Laplace pressure, which is correlated to the curvature radius (R) of the droplet, (Wu et al., 2022), increased greatly along with the decreasing droplet size on the heat substrate due to solvent evaporation for further bending the MXene nanosheets. With the formation of eccentric nanospheres, the anchored carbon nanoparticles are liable to bond neighbouring nanosheets with favorable interlayer distances. The formation mechanism of the hybrid $Ti_3C_2T_x$/C nanospheres is schematically illustrated in **Figure 4**.

The electrochemical performance of the hybrid MXene/C nanospheres was tentatively investigated by printing interdigital microelectrodes via the AJP process. The interdigital microelectrode was realized by multiple printing passes of feature size of 200 μm. In view of the influence of electrode configuration (e.g., line length, width, thickness and gap distance) on the electrochemical performance, in this work, the interdigital microelectrodes of hybrid MXene/C nanospheres were printed with line width of 200 μm, thickness of 95 μm, and gap distance of 170 μm, respectively, after 50-time printing passes and the working area was estimated to be 3.7 mm × 3.8 mm (**Supplementary Figure S5**, Supporting Information). The MSC devices were fabricated by applying a gel electrolyte based on poly (vinyl alcohol) (PVA)/$H_2SO_4$ onto the interdigital microelectrodes with labeling as MSC-n, where n designates the relative mass ratio of carbon nanoparticles (**Supplementary Figure S6**, Supporting Information). **Figure 5A** shows the cyclic voltammogram (CV) curves of the MSC devices at n values of 0 and 0.5. The quasi-rectangular CV curves indicate that the presence of pseudocapacitance and electric double layer capacitance behavior (Cao et al., 2018; Cao et al., 2019; Das et al., 2020). **Figure 5B** shows the GCD curves of the MSC devices at a current density of 0.2 mA $cm^{-2}$ and the approximately symmetrical curves indicates good reversibility and the non-linear curves in the potential during both charge and discharge half-cycles shows a typical feature of a hybrid supercapacitor (Yu et al., 2020). The areal capacitance was estimated to be 33.14 mF $cm^{-2}$, for MSC-0.5 device, obviously larger than the pristine MXene device. The addition of carbon nanoparticles is clear to greatly enhance the electrochemical performance of MXene-based devices. Noted that although the quantity of carbon nanoparticles is comparable to the MXene when formulating the precursor inks, actually the atomized aerosol droplets contain minimal carbon nanoparticles due to the fact that only the supernatant of the ink containing MXene nanosheet of suitable lateral size (less than the aerosol droplet size) could be successfully atomized and large quantity of carbon nanoparticles were captured by large MXene nanosheets or agglomerated under the sonication. The TEM and SEM images shown in **Figures 1–3** could verify this conjecture with dotted carbon nanoparticles present. Therefore, the contribution of carbon nanoparticles on the areal capacitance of the hybrid system could be neglected. The improved areal capacitance mainly arises from the spherical nanostructures with broadened interlayer distances, which is expected to favor the ionic transportation for a promising electrochemical performance. By optimizing the mass ratio of carbon nanoparticles (n = 1), the assembled device exhibited an optimal areal capacitance of 46.95 mF $cm^{-2}$, exceeding the values of microscale devices fabricated by other additive manufacturing techniques, e.g., direct writing and inkjet printing reported previously (Quain et al., 2019; Zhang et al., 2019). The electrochemical impedance spectroscopy (EIS) measurements were applied to explore the electronic/ionic transport behaviors of the microelectrodes. As shown in **Figure 5C**, the Nyquist plot at the high-frequency region of

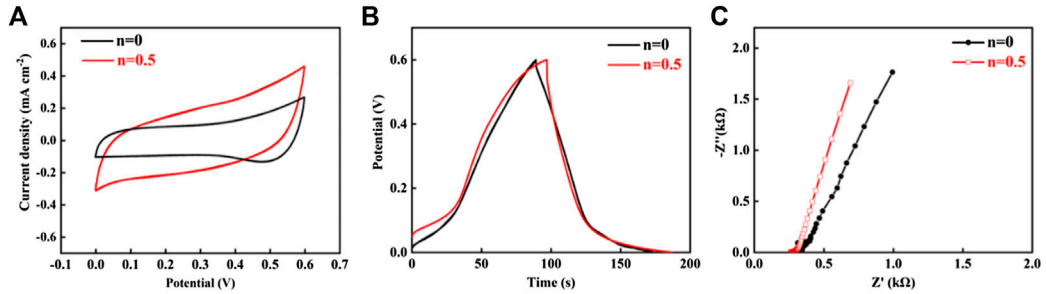


**FIGURE 5 | (A)** CV curves of the MSC devices of hybrid MXene/C nanospheres with different mass ratios at a scan rate of 20 mV s$^{-1}$. **(B)** GCD profiles at a current density of 0.2 mA cm$^{-2}$. **(C)** EIS of the microdevice of hybrid MXene/C and its pristine MXene counterpart.

the hybrid microelectrode indicates a faster ion diffusion in comparison to pristine MXene electrode. The results demonstrate that the hybrid microelectrode could accommodate more electrochemically active sites and enable the electrolyte to permeate more readily, enhancing the capacitive performance.

## 3 CONCLUSION

In conclusion, hybrid $Ti_3C_2T_x$/C nanospheres with crumpled and eccentric features have been successfully developed by a convenient AJP approach. The addition of carbon nanoparticles could effectively inhibit the closely restacking of MXene nanosheets during the assembly process. Meanwhile, the anchored carbon nanoparticles could act as binder to bridge neighbouring nanosheets and nanospheres for integrity. Arising from the temperate gradient-derived Marangoni flow, the $Ti_3C_2T_x$/C could be easily transported and further shaped along the droplet surface with the solvent evaporation. Due to the special hybrid spherical characteristic, the fabricated MSC devices derived from the hybrid $Ti_3C_2T_x$/C nanospheres demonstrate faster ion diffusion and excellent areal capacitance. Accordingly, the areal capacitance is greatly enhanced in comparison to $Ti_3C_2T_x$ counterpart. The AJP approach developed in this work highlight its potential for developing future high-performance microdevices with capabilities of structure modulation at multiscale.

## 4 MATERIALS AND METHODS

*Preparation of delaminated $Ti_3C_2T_x$ nanosheets:* Typically, LiF (0.5 g, Aladdin) was dissolved in HCl (9 M, 10 ml, Aladdin) and stirred until completely clear at room temperature. $Ti_3AlC_2$ powder (0.5 g, 11 Technology) was slowly added to the aforementioned solution accompanied by vigorous stirring in an ice bath. After being stirred at 40 °C for 48 h, the mixture was washed with deionized water and centrifuged at 7500 rpm for 5 min until the pH of the supernatant was ~6. Subsequently, the obtained sediment was dispersed in deionized water, shaken vigorously, and then sonicated for 1 h. The resulting mixture was centrifuged at 3500 rpm for 1 h, and the supernatant was transferred for freeze-drying to obtain the delaminated $Ti_3C_2T_x$ nanosheets.

*Preparation of $Ti_3C_2T_x$/C ink:* The precursor ink was formulated by mixing delaminated $Ti_3C_2T_x$ nanosheets and carbon nanoparticles (Bare Conductive Ltd.) of different mass ratios in deionized water. After shaking vigorously, the $Ti_3C_2T_x$/C ink is ready for printing.

*Printing of $Ti_3C_2T_x$/C interdigital microelectrodes:* A commercial aerosol jet printer (WE-HMP, WE Electronics) was applied for the printing process. The interdigital patterns were designed by CAD software, which can be readable by the printer. The $Ti_3C_2T_x$/C ink was atomized into droplets with the aid of an ultrasonic atomizer (1.7 MHz). The nozzle diameter was 500 μm and the stand-off height was ~8 mm. When the carrier gas ($N_2$) and the sheath gas ($N_2$) were set to 50 and 150 sccm, respectively, the aerosol beam was focused without obvious overspray. The substrate, polyethylene terephthalate (PET), was cleaned with ethanol, dried by, and then plasma-treated for 400 s (VP-R, SunJune) before use. The printing speed was fixed at 10 mm s$^{-1}$. The deposition temperature was set to 100 °C. All the interdigital microelectrodes were obtained after 50-time printing passes.

*Fabrication of $Ti_3C_2T_x$/C MSCs:* The poly(vinyl alcohol) (PVA)/$H_2SO_4$ electrolyte was prepared by dissolving 3 g of PVA (87–89% alcohol solubility) in 15 mL deionized water. After being stirred at 60 °C for 15 min, another 15 mL of deionized water was added, accompanied by being stirred at 85 °C for 3 h until the solution was completely clear and transparent. After cooling to room temperature, 3 mL of sulfuric acid (98%, Aladdin) was added dropwise for 1 h. In addition, two silver wires were connected separately with two electrodes by conductive silver enamel. After the enamel dried absolutely, the electrolyte gel was coated onto the interdigital electrodes.

*Materials Characterizations:* The morphologies and microstructures were characterized by a transmission microscope (TEM, Titan G260-300) and a scanning electron microscopy (SEM, Zeiss Gemini 300) together with an energy-dispersive X-ray spectroscope (EDX, Zeiss Smart). X-ray diffraction patterns (XRD) were obtained by

using a PIGAKV Ultima IV X-ray diffractometer with a Cu $K_\alpha$ radiation source ($\lambda$ = 0.15418 nm).

*Electrochemical Measurement:* Cyclic voltammetry (CV), galvanostatic charging/discharging (GCD), and spectroscopy (EIS) were conducted on an electrochemical workstation (Princeton, Versa STAT 4). The areal capacitance of the MSCs was calculated based on the GCD results as following: $C_A = It/(S\Delta V)$, where $C_A$ (mF $cm^{-2}$) refers to the areal capacitance, I (A) refers to the discharge current, t (s) refers to the discharge time, S ($cm^2$) refers to the geometric area of the electrode, and $\Delta V$ (V) refers to the working potential window.

## DATA AVAILABILITY STATEMENT

The original contributions presented in the study are included in the article/**Supplementary Material**; further inquiries can be directed to the corresponding author.

## AUTHOR CONTRIBUTIONS

All authors listed have made a substantial, direct, and intellectual contribution to the work and approved it for publication

## FUNDING

This work was financially supported by the Jiangsu Key R&D Plan (BE2018006-4), JITRI Youth Fellow (GC-1), Suzhou Science and Technology Development Plan (CYTS2019160), and the Key Project of Natural Science Foundation of Jiangxi Province (20212ACB203004).

## SUPPLEMENTARY MATERIAL

The Supplementary Material for this article can be found online at: https://www.frontiersin.org/articles/10.3389/fchem.2022.933319/full#supplementary-material

## REFERENCES

Cao, C., Andrews, J. B., and Franklin, A. D. (2017). Completely Printed, Flexible, Stable, and Hysteresis-free Carbon Nanotube Thin-Film Transistors via Aerosol Jet Printing. *Adv. Electron. Mat.* 3 (5), 1700057. doi:10.1002/aelm.201700057

Cao, J., Li, J., Li, D., Yuan, Z., Zhang, Y., Shulga, V., et al. (2021). Strongly Coupled 2D Transition Metal Chalcogenide-MXene-Carbonaceous Nanoribbon Heterostructures with Ultrafast Ion Transport for Boosting Sodium/potassium Ions Storage. *Nano-Micro Lett.* 13 (1), 113. doi:10.1007/s40820-021-00623-5

Cao, J., Li, J., Li, L., Zhang, Y., Cai, D., Chen, D., et al. (2019). Mn-doped Ni/Co LDH Nanosheets Grown on the Natural N-Dispersed PANI-Derived Porous Carbon Template for a Flexible Asymmetric Supercapacitor. *ACS Sustain. Chem. Eng.* 7 (12), 10699–10707. doi:10.1021/acssuschemeng.9b01343

Cao, J., Li, L., Xi, Y., Li, J., Pan, X., Chen, D., et al. (2018). Core-shell Structural PANI-Derived carbon@Co-Ni LDH Electrode for High-Performance Asymmetric Supercapacitors. *Sustain. Energy Fuels* 2 (6), 1350–1355. doi:10.1039/c8se00123e

Cao, J., Sun, Z., Li, J., Zhu, Y., Yuan, Z., Zhang, Y., et al. (2021). Microbe-Assisted Assembly of Ti3C2Tx MXene on Fungi-Derived Nanoribbon Heterostructures for Ultrastable Sodium and Potassium Ion Storage. *ACS Nano* 15 (2), 3423–3433. doi:10.1021/acsnano.0c10491

Cao, J., Wang, L., Li, D., Yuan, Z., Xu, H., Li, J., et al. (2021). Ti 3 C 2 T X MXene Conductive Layers Supported Bio-Derived Fe X −1 Se X/MXene/Carbonaceous Nanoribbons for High-Performance Half/Full Sodium-Ion and Potassium-Ion Batteries. *Adv. Mat.* 33 (34), 2101535. doi:10.1002/adma.202101535

Das, P., Shi, X. Y., Fu, Q., and Wu, Z. S. (2020). Substrate-free and Shapeless Planar Micro-supercapacitors. *Adv. Funct. Mater.* 30 (7), 10. doi:10.1002/adfm.201908758

Deiner, L. J., and Reitz, T. L. (2017). Inkjet and Aerosol Jet Printing of Electrochemical Devices for Energy Conversion and Storage. *Adv. Eng. Mat.* 19 (7), 1600878. doi:10.1002/adem.201600878

Eom, W., Shin, H., Ambade, R. B., Lee, S. H., Lee, K. H., Kang, D. J., et al. (2020). Large-scale Wet-Spinning of Highly Electroconductive MXene Fibers. *Nat. Commun.* 11 (1), 2825. doi:10.1038/s41467-020-16671-1

Fan, Z., Wang, Y., Xie, Z., Wang, D., Yuan, Y., Kang, H., et al. (2018). Modified MXene/holey Graphene Films for Advanced Supercapacitor Electrodes with Superior Energy Storage. *Adv. Sci. (Weinh)* 5 (10), 1800750. doi:10.1002/advs.201800750

Fang, Y. Z., Hu, R., Zhu, K., Ye, K., Yan, J., Wang, G., et al. (2020). Aggregation-Resistant 3D Ti 3 C 2 T X MXene with Enhanced Kinetics for Potassium Ion Hybrid Capacitors. *Adv. Funct. Mat.* 30 (50), 2005663. doi:10.1002/adfm.202005663

Feng, X., Li, Y., Wang, L., Chen, S., Yu, Z. G., Tan, W. C., et al. (2019). A Fully Printed Flexible MoS 2 Memristive Artificial Synapse with Femtojoule Switching Energy. *Adv. Electron. Mat.* 5 (12), 1900740. doi:10.1002/aelm.201900740

Gao, X., Du, X., Mathis, T. S., Zhang, M., Wang, X., Shui, J., et al. (2020). Maximizing Ion Accessibility in MXene-Knotted Carbon Nanotube Composite Electrodes for High-Rate Electrochemical Energy Storage. *Nat. Commun.* 11 (1), 6160. doi:10.1038/s41467-020-19992-3

Girard, F., Antoni, M., and Sefiane, K. (2008). On the Effect of Marangoni Flow on Evaporation Rates of Heated Water Drops. *Langmuir* 24 (17), 9207–9210. doi:10.1021/la801294x

Ha, M., Seo, J.-W. T., Prabhumirashi, P. L., Zhang, W., Geier, M. L., Renn, M. J., et al. (2013). Aerosol Jet Printed, Low Voltage, Electrolyte Gated Carbon Nanotube Ring Oscillators with Sub-5 μs Stage Delays. *Nano Lett.* 13 (3), 954–960. doi:10.1021/nl3038773

Jabari, E., and Toyserkani, E. (2015). Micro-scale Aerosol-Jet Printing of Graphene Interconnects. *Carbon* 91, 321–329. doi:10.1016/j.carbon.2015.04.094

Li, X. R., Li, H. P., Fan, X. Q., Shi, X. L., and Liang, J. J. (2020). 3D-printed Stretchable Micro-supercapacitor with Remarkable Areal Performance. *Adv. Energy Mater.* 10 (14), 12. doi:10.1002/aenm.201903794

Ling, Z., Ren, C. E., Zhao, M.-Q., Yang, J., Giammarco, J. M., Qiu, J., et al. (2014). Flexible and Conductive MXene Films and Nanocomposites with High Capacitance. *Proc. Natl. Acad. Sci. U.S.A.* 111 (47), 16676–16681. doi:10.1073/pnas.1414215111

Lukatskaya, M. R., Kota, S., Lin, Z., Zhao, M.-Q., Shpigel, N., Levi, M. D., et al. (2017). Ultra-high-rate Pseudocapacitive Energy Storage in Two-Dimensional Transition Metal Carbides. *Nat. Energy* 2 (8), 17105. doi:10.1038/nenergy.2017.105

Mahajan, A., Frisbie, C. D., and Francis, L. F. (2013). Optimization of Aerosol Jet Printing for High-Resolution, High-Aspect Ratio Silver Lines. *ACS Appl. Mat. Interfaces* 5 (11), 4856–4864. doi:10.1021/am400606y

Naguib, M., Mochalin, V. N., Barsoum, M. W., and Gogotsi, Y. (2014). 25th Anniversary Article: MXenes: A New Family of Two-Dimensional Materials. *Adv. Mat.* 26 (7), 992–1005. doi:10.1002/adma.201304138

Orangi, J., and Beidaghi, M. (2020). A Review of the Effects of Electrode Fabrication and Assembly Processes on the Structure and Electrochemical Performance of 2D MXenes. *Adv. Funct. Mat.* 30 (47), 2005305. doi:10.1002/adfm.202005305

Quain, E., Mathis, T. S., Kurra, N., Maleski, K., Van Aken, K. L., Alhabeb, M., et al. (2019). Direct Writing of Additive-free MXene-In-Water Ink for Electronics and Energy Storage. *Adv. Mater. Technol.* 4 (1), 7. doi:10.1002/admt.201800256

Savoskin, M. V., Mochalin, V. N., Yaroshenko, A. P., Lazareva, N. I., Konstantinova, T. E., Barsukov, I. V., et al. (2007). Carbon Nanoscrolls Produced from Acceptor-type Graphite Intercalation Compounds. *Carbon* 45 (14), 2797–2800. doi:10.1016/j.carbon.2007.09.031

Secor, E. B. (2018). Principles of Aerosol Jet Printing. *Flex. Print. Electron.* 3 (3), 035002. doi:10.1088/2058-8585/aace28

Skarzynski, K., Krzeminski, J., Jakubowska, M., and Sloma, M. (2021). Highly Conductive Electronics Circuits from Aerosol Jet Printed Silver Inks. *Sci. Rep.* 11 (1), 18141.

Wu, Y., Lin, A., Zhang, J., Zhao, D., Bai, X., Lu, C., et al. (2022). Crumpled and Eccentric Nanospheres of $Ti_3C_2T_x$ MXene by Aerosol Jet Printing on Heat Substrate. *Adv. Eng. Mater.*, 2101556.

Wu, Y., Zhao, D., Zhang, J., Lin, A., Wang, Y., Cao, L., et al. (2021). Microscale Curling and Alignment of Ti3C2Tx MXene by Confining Aerosol Droplets for Planar Micro-supercapacitors. *ACS Omega* 6 (48), 33067–33074. doi:10.1021/acsomega.1c05373

Xia, Y., Mathis, T. S., Zhao, M.-Q., Anasori, B., Dang, A., Zhou, Z., et al. (2018). Thickness-independent Capacitance of Vertically Aligned Liquid-Crystalline MXenes. *Nature* 557 (7705), 409–412. doi:10.1038/s41586-018-0109-z

Yang, X., Wang, Q., Zhu, K., Ye, K., Wang, G., Cao, D., et al. (2021). 3D Porous Oxidation-Resistant MXene/Graphene Architectures Induced by *In Situ* Zinc Template toward High-Performance Supercapacitors. *Adv. Funct. Mat.* 31 (20), 2101087. doi:10.1002/adfm.202101087

Yu, L., Li, W., Wei, C., Yang, Q., Shao, Y., and Sun, J. (2020). 3D Printing of NiCoP/Ti3C2 MXene Architectures for Energy Storage Devices with High Areal and Volumetric Energy Density. *Nano-Micro Lett.* 12 (1), 143. doi:10.1007/s40820-020-00483-5

Zhang, C., McKeon, L., Kremer, M. P., Park, S.-H., Ronan, O., Seral-Ascaso, A., et al. (2019). Additive-free MXene Inks and Direct Printing of Micro-supercapacitors. *Nat. Commun.* 10, 1795. doi:10.1038/s41467-019-09398-1

Zhao, M. Q., Xie, X., Ren, C. E., Makaryan, T., Anasori, B., Wang, G., et al. (2017). Hollow MXene Spheres and 3D Macroporous MXene Frameworks for Na-Ion Storage. *Adv. Mat.* 29 (37), 1702410. doi:10.1002/adma.201702410

**Conflict of Interest:** The authors declare that the research was conducted in the absence of any commercial or financial relationships that could be construed as a potential conflict of interest.

**Publisher's Note:** All claims expressed in this article are solely those of the authors and do not necessarily represent those of their affiliated organizations, or those of the publisher, the editors, and the reviewers. Any product that may be evaluated in this article, or claim that may be made by its manufacturer, is not guaranteed or endorsed by the publisher.

frontiers | Frontiers in Chemistry

ORIGINAL RESEARCH
published: 15 July 2022
doi: 10.3389/fchem.2022.957462

# $FeS_2$ Nanoparticles Encapsulated in S/N Co-Doped Carbon Nanofibers With a Three-Dimensional Multi-Channel Structure for Lithium-Ion Batteries

*Xiaochang Cao[1,2], Yi Zhang[3], Chujiang Luo[3], Yansheng Yin[3] and Yingying Huang[3]**

[1]College of Mechanical Engineering, Dongguan University of Technology, Dongguan, China, [2]Institute of Science and Technology Innovation, Dongguan University of Technology, Dongguan, China, [3]Research Center for Corrosion and Erosion Process Control of Equipment and Material in Marine Harsh Environment, Guangzhou Maritime University, Guangzhou, China

Pyrite ($FeS_2$) is one of the potential candidates for advanced rechargeable Li-ion batteries (LIBs) owing to its inherent capacity (849 mAh $g^{-1}$), environmental friendliness, and abundant natural resources. However, the volume expansion of $FeS_2$ and the dissolution of polysulfide in the electrochemical reaction severely limit its application in the field of energy conversion and storage. Herein, $FeS_2$ nanoparticles are encapsulated in S/N co-doped three-dimensional multi-channel structural carbon nanofibers ($FeS_2$@CNFs) through the electrospinning method. As a cathode material for LIBs, $FeS_2$@CNFs demonstrated excellent rate property and cyclic stability. The $3FeS_2$@CNFs (weight ratio of $FeS_2$ is 30%) present the initial capacity of 1,336.7 mAh $g^{-1}$ and the remaining 856.5 mAh $g^{-1}$ at 0.02A $g^{-1}$ after 100 circles. The favorable electrochemical properties have confirmed that carbon nanofibers can enhance the electroconductivity of electrodes, reduce the volume collapse of $FeS_2$, and remit the dissolution of polysulfide during the $Li^+$ ions insertion/de-insertion process. In addition, co-doped S/N can supply abundant active sites for electrochemical reactions, providing enough space for $Li^+$ ion storage. The results indicate that $3FeS_2$@CNFs is a cathode with a developmental prospect for LIBs.

**Keywords: $FeS_2$, carbon nanofibers, three-dimensional multi-channel structure, cathode material, lithium-ion batteries**

OPEN ACCESS

***Edited by:***
*Feng Gu,*
*Jiangxi University of Science and Technology, China*

***Reviewed by:***
*Xianwen Wu,*
*Jishou University, China*
*Yongde Yan,*
*Harbin Engineering University, China*

****Correspondence:***
*Yingying Huang*
*Yingying_Huang1991@126.com*

***Specialty section:***
*This article was submitted to Nanoscience, a section of the journal Frontiers in Chemistry*

***Received:*** *31 May 2022*
***Accepted:*** *15 June 2022*
***Published:*** *15 July 2022*

***Citation:***
*Cao X, Zhang Y, Luo C, Yin Y and Huang Y (2022) $FeS_2$ Nanoparticles Encapsulated in S/N Co-Doped Carbon Nanofibers With a Three-Dimensional Multi-Channel Structure for Lithium-Ion Batteries. Front. Chem. 10:957462. doi: 10.3389/fchem.2022.957462*

## 1 INTRODUCTION

As the population continues to increase, the energy demand is also growing rapidly (Zhao et al., 2015; Chi et al., 2018; Teng et al., 2019; Kesavan et al., 2020). The overexploitation of non-renewable fossil fuels has seriously polluted the environment (Zhang et al., 2019; Fang et al., 2021; Yang et al., 2021). Compared to traditional fossil fuels, electricity is a green, low-carbon, environment-friendly, and efficient energy system. To date, researchers have conducted numerous studies on electric energy storage. The common commercial electronic storage devices currently used contain nickel–cadmium batteries, lead–acid batteries, nickel–metal hydride batteries, Li-ion batteries (LIBs), fuel cells, etc. Among them, LIBs have been universally used in various fields such as manned crafts and small equipment because of their advantages of high energy density, excellent cyclic stability, and low self-

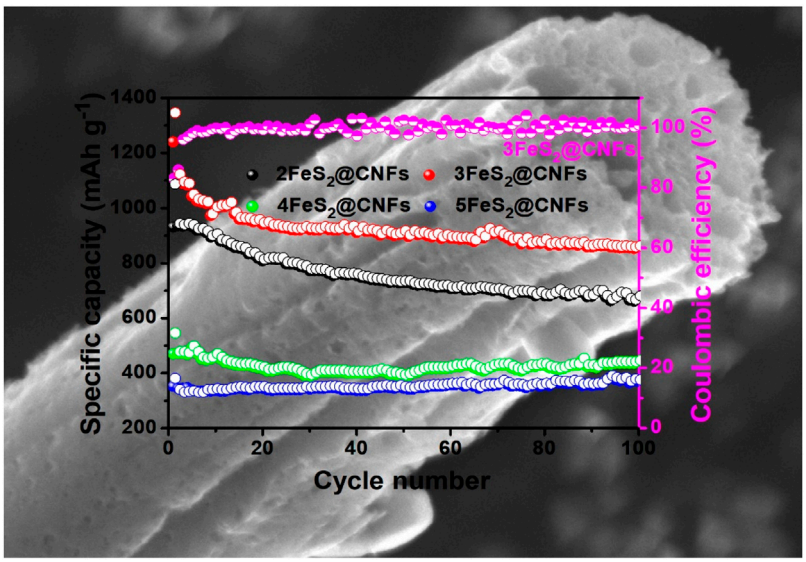


**GRAPHICAL ABSTRACT |** Graphical Abstract Novel $FeS_2$@CNFs nanocomposites with the multi-channel structure were successfully prepared using the electrospinning method. The three-dimensional interlinked multi-channel carbon nanofibers can facilitate the diffusion of $Li^+$ ions and electrons. Meanwhile, the $FeS_2$ nanoparticles are distributed on the inner wall of the carbon nanofibers, improving the phenomenon of volume expansion for $FeS_2$ and preventing the dissolution of polysulfide during the cycling process. In addition, co-doped S/N can supply abundant active sites for electrochemical reactions, providing enough space for $Li^+$ ion storage. The $FeS_2$@CNFs and the preparation method have exceptional applications in the field of energy storage.

discharge. Therefore, LIBs have attracted great attention. For instance, Gou et al. (2021) prepared $Li_3VO_4$/C through a facile agitation–drying method combined with subsequent calcination. The as-prepared composites were used as anode materials for LIBs and exhibited outstanding electrochemical properties. Zhong et al. (2018) synthesized a sandwich-type sulfur@Co/N-doped carbon ternary composite for Li–S batteries. The assembled Li–S batteries display excellent energy storage performance and provide the possibility of realizing industrially practical energy. Jiang et al. (2020) encapsulated $NaTi_2(PO_4)_3$ nanoparticles in N/S dual-doped carbon (NTP@CNS) as the anode for LIBs via the sol–gel method followed by calcination treatment. The NTP@CNS shows excellent electrochemical property. According to daily needs and the rate of production, various types of LIBs are prepared. Recently, Li–$FeS_2$ batteries are considered to be one of the power batteries having the most potential. However, the volume expansion of $FeS_2$ during the intercalation and de-intercalation of $Li^+$ ions lead to a structural collapse, reducing the cycle life of LIBs (Zhang et al., 2016; Wang et al., 2021). Meanwhile, the conversion process is accompanied by accessory substances such as lithium polysulfides ($Li_2S_x$, $2 < x < 8$). These accessory substances can make the conductivity between the anode and current collector worse. In addition, the lithium polysulfides also dissolve in the electrolyte and can gradually migrate to the cathode, leading to an increase in the impedance of the cathode (Wang et al., 2019; Li et al., 2021).

To overcome these existing issues, researchers have also attempted to nanosize $FeS_2$. Nanocrystallization can effectively alleviate the damage caused by $Li^+$ ions insertion/de-insertion of active materials during the charge and discharge processes, improving the cyclic stability (Lei et al., 2016). Meanwhile, the nanoscale of active substances also effectively shortens the ion transmission path, accelerates the $Li^+$ ions diffusion rate, and improves the rate property (Polishchuk et al., 2019). Li et al. (2014) reported the synthesis of phase-pure $FeS_2$ nanowires through thermal vulcanization of the precursor $\alpha$-$FeF_3$ $3H_2O$ nanowires. The nano-$FeS_2$ cathode retained 350 mAh $g^{-1}$ after 50 circles at 0.1°C. Liao et al. (2013) fabricated macroporous $FeS_2$ nanotubes through a solvothermal method. The macroporous $FeS_2$ nanotubes exhibited 925.2 mAh $g^{-1}$ and retained 439 mAh $g^{-1}$ at 0.2°C after 60 cycles. Nevertheless, the preparation of nanostructured single-phase $FeS_2$ has long-term challenges due to the presence of many substoichiometric Fe–S phases and orthorhombic $FeS_2$ (Ennaoui et al., 1993). Therefore, researchers began to attempt to hybrid nanostructured $FeS_2$ with carbon materials. Carbon materials can not only improve the electrical conductivity and relieve the volume expansion of electrodes but also delay the damage of polysulfides during charge and discharge processes (Xu et al., 2016; He et al., 2017). For instance, Xu et al. (2016) synthesized a $FeS_2$@HPC composite through the formation of $FeS_2$ nanocrystals in hierarchical porous carbon. The as-fabricated $FeS_2$@HPC presented 907 mAh $g^{-1}$ and maintained 720 mAh $g^{-1}$ after 100 circles at 1°C. Xu Q.-T. et al. (2018) prepared the biomass-carbon@$FeS_2$ composites from auricularia auricula after the carbonization and sulfidation procedure. The as-synthesized composite demonstrated 850 mAh $g^{-1}$ after 80 circles at 0.5°C. Wang et al. (2021) reported a raspberry-like hierarchical-structured $FeS_2$ cathode modified by the dual-carbon framework. The as-prepared cathode delivered 566 mAh $g^{-1}$ and maintained a capacity reduction rate of 0.014% for each circle at 1°C. These studies demonstrate that the development of

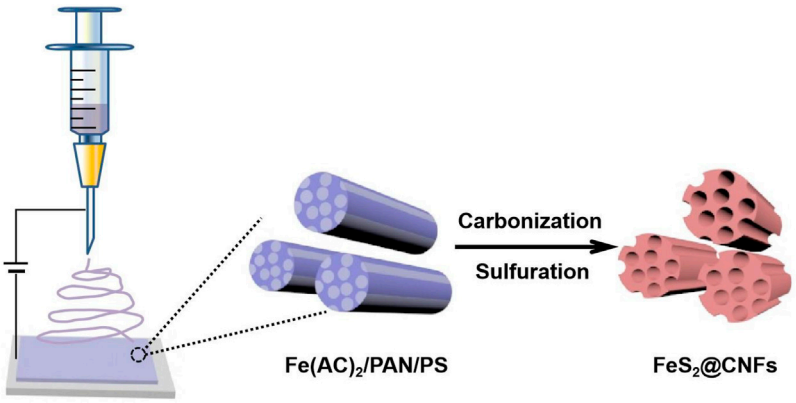


**FIGURE 1 |** Illustration of the procedure for the preparation of FeS2@CNFs.

nanocomposites combining $FeS_2$ with carbon can improve the electrochemical properties of electrodes.

Herein, a type of $FeS_2$@carbon nanofiber ($FeS_2$@CNF) nanocomposites with a multi-channel structure was successfully prepared using the electrospinning method. The three-dimensional interlinked multi-channel and S/N co-doped carbon nanofibers can improve the electroconductivity of cathodes. Meanwhile, the lotus-like structure can ameliorate the phenomenon of volume expansion for $FeS_2$ and prevent the dissolution of polysulfide during the cycling process. The effect of the $FeS_2$ content on properties was studied through examining the performances of $FeS_2$@CNFs nanocomposites with different contents of $FeS_2$. The application feasibility of $FeS_2$@CNFs as cathodes for LIBs was also explored in detail.

## 2 EXPERIMENT

### 2.1 Material Preparation

A total of 340 mg iron acetate, 400 mg polystyrene, and 500 mg polyacrylonitrile (PAN) were poured into 5 mlN, N-dimethylformamide and mixed at 65°C for 12 h. The aforementioned mixture was then electrospun with a single nozzle (21 gauge needle). The distance between the syringe and the receiver was 15 cm, the voltage was 17 kV, and the injection rate was 1 $mlh^{-1}$. The as-prepared precursor film was stabilized at 200°C for 2 h and then calcined at 800°C with 5°C $min^{-1}$ for 4 h in an $Ar/H_2$ atmosphere. After reducing to 30°C, the film was sealed with sulfur powder in a quartz tube ($V_{product}$: $V_{sulfur}$ = 1:2). Subsequently, the quartz tube was heated to 600°C and kept for 6 h. After that, the product was dissolved in $CS_2$ to eliminate redundant sulfur. Finally, it was dried in vacuum at 100°C to obtain a lotus root–like $FeS_2$@CNFs with many channels. The preparation process of $FeS_2$@CNF nanocomposites based on the electrospinning approach is illustrated in **Figure 1**. The content of $FeS_2$ in $FeS_2$@CNFs nanocomposites prepared by this process was 20 wt%, which was named 2$FeS_2$@CNFs. Samples with contents of 30, 40, and 50 wt% were also synthesized in the same way and named 2$FeS_2$@CNFs, 3$FeS_2$@CNFs, 4$FeS_2$@CNFs, and 5$FeS_2$@CNFs, respectively.

### 2.2 Characterization

The crystal structure information was obtained on a Rigaku diffractometer with Cu K$\alpha$ radiation ($\lambda$ = 1.5418) within 10–90°. Raman measurements were performed on an HR800 spectrophotometer from 400 $cm^{-1}$ to 2400 $cm^{-1}$. The information of the valence states was acquired using a Thermo ESCALAB 250 X-ray photoelectron spectrometer (XPS) with monochromatic Al K$\alpha$ (1486.6 eV). The surface morphologies were observed using scanning and transmission electron microscopes (SEM, Ultra Plus, ZEISS and TEM, Talos F200X). The SEM was obtained at 10 kV. TEM was acquired at 200 kV accelerating voltage.

### 2.3 Electrochemical Measurements

The synthesized $FeS_2$@CNFs nanocomposites were directly used as the cathodes of LIBs without any conductive agent, binder, and metal collector. The film of $FeS_2$@CNFs was cut into a circle with a diameter of 1 cm. The mass of each cathode was about 1 mg $cm^{-2}$. A total of 1 M $LiPF_6$ in a mixture of vinyl carbonate/dimethyl carbonate (1:1 in volume) was used directly as the electrolyte. Lithium disks were used as the anode, and the Celgard 2400 microporous polypropylene membrane was employed as the separator. The aforementioned materials were assembled into CR2032 coin-type cells in an argon-filled glovebox and tested for electrochemical properties. The electrochemical properties were tested by using a CHI760E workstation and a Land CT 2001A battery testing system. The cyclic voltammetry (CV) and the galvanostatic charge and discharge (GCD) performances were determined between 1.0 and 3.0 V. Electrochemical impedance spectroscopy (EIS) was conducted at the frequency of $10^5$–$10^{-2}$ Hz.

## 3 RESULTS AND DISCUSSION

The structures and phase purities of $FeS_2$@CNFs were characterized by XRD patterns, as presented in **Figure 2A**. The diffraction peaks of $FeS_2$@CNFs were consistent with the

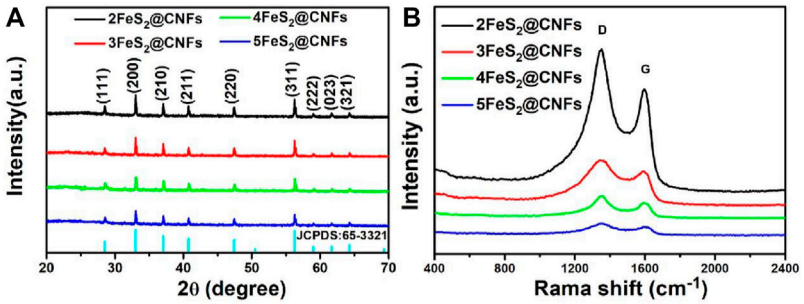


**FIGURE 2 | (A)** XRD patterns and **(B)** Raman spectra.

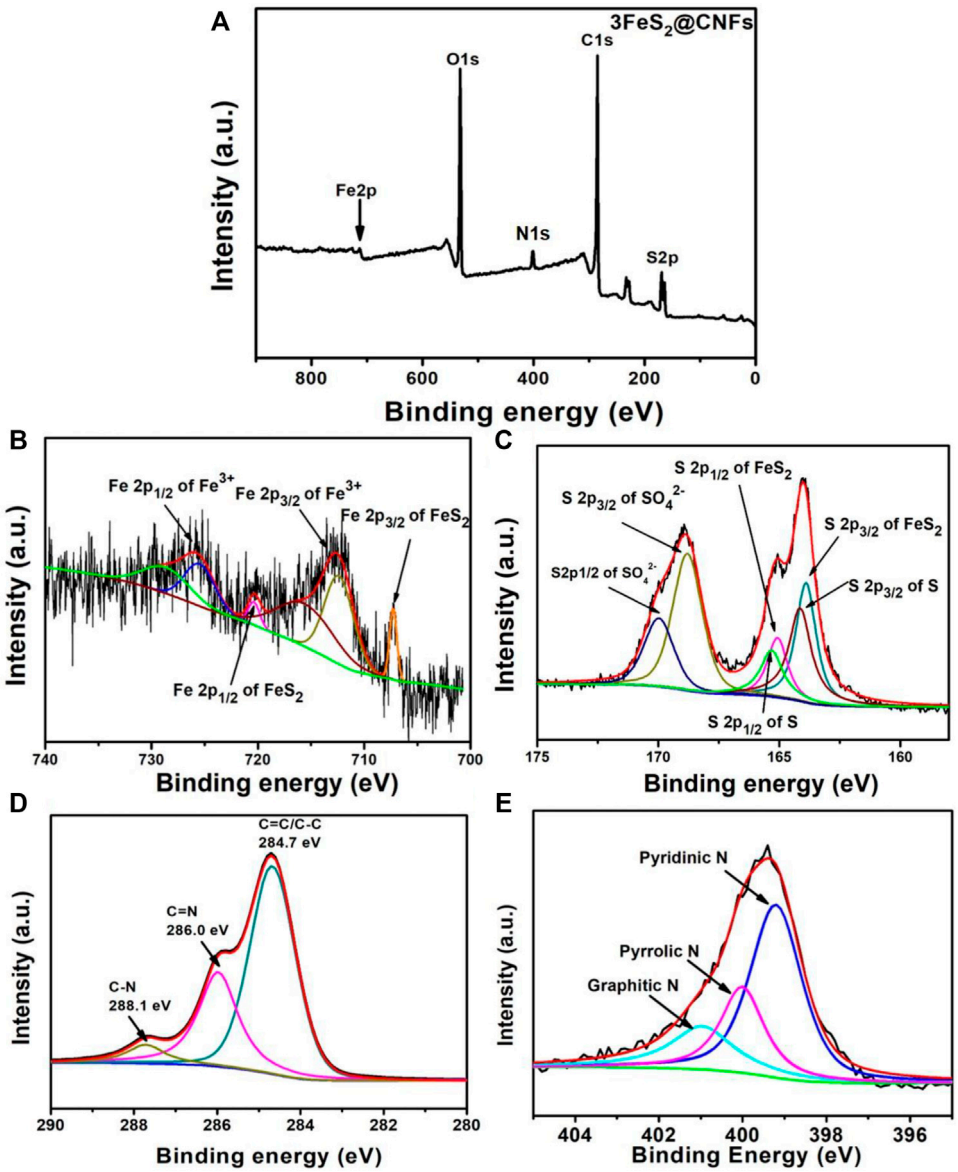


**FIGURE 3 |** XPS of 3FeS2@CNFs: **(A)** survey spectra, **(B)** Fe 2p, **(C)** S 2p, **(D)** C1s, and **(E)** N1s.

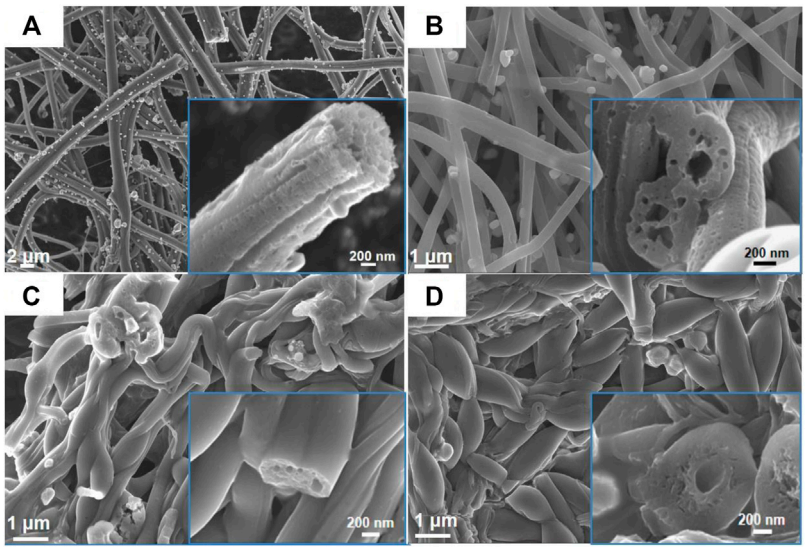


**FIGURE 4 |** FESEM images of **(A)** 2FeS2@CNFs, **(B)** 3FeS2@CNFs, **(C)** 4FeS2@CNFs, and **(D)** 5FeS2@CNFs (The figure is a high-magnification image).

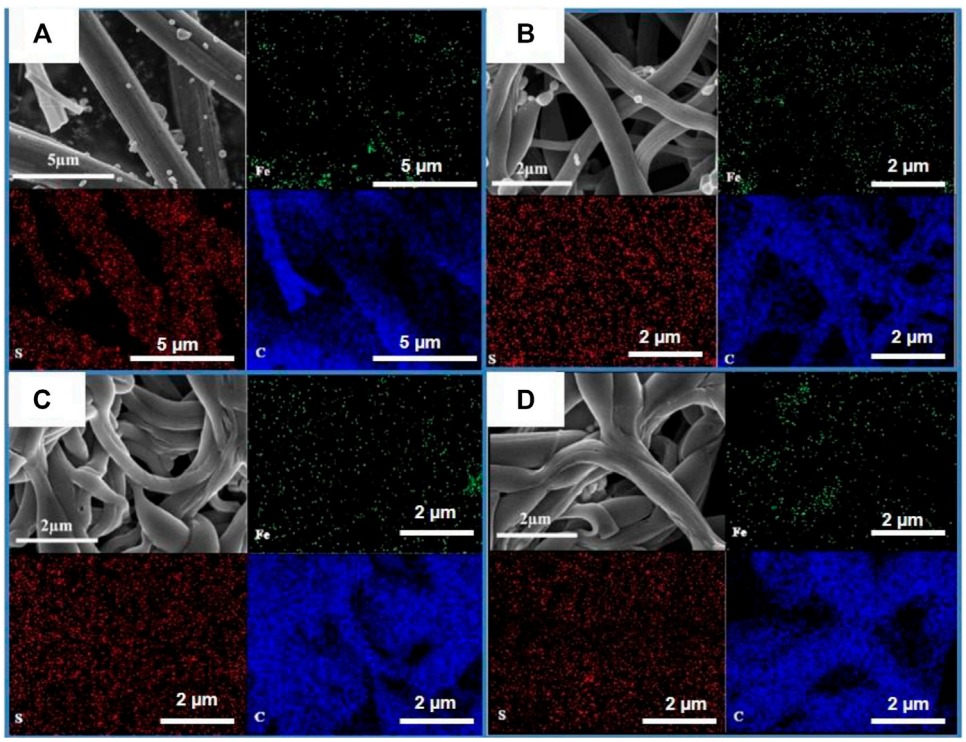


**FIGURE 5 |** Elemental mapping and distribution of **(A)** 2FeS2@CNFs, **(B)** 3FeS2@CNFs, **(C)** 4FeS2@CNFs, and **(D)** 5FeS2@CNFs.

pure phase of pyrite $FeS_2$ (JCPDS Card No. 65-3321). No diffraction peaks of the marcasite $FeS_2$ and other impurities were observed. There is no diffraction peak of CNFs, indicating the formation of disordered layered graphite structures during the carbonization of PAN. This structure is composed of tiny crystals of layered graphite. The chemical composition of different $FeS_2$@CNFs nanocomposites was determined using the Raman spectrum (**Figure 2B**). Two notable peaks at 1,352 $cm^{-1}$ and 1,594 $cm^{-1}$ in each spectrum match well with the D band and G band, respectively (Lu et al., 2020).

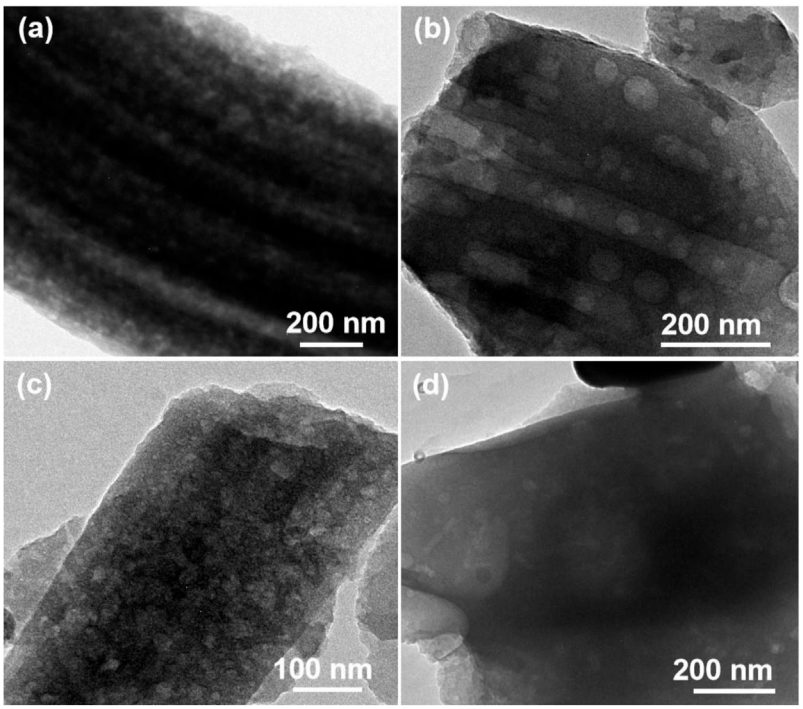


**FIGURE 6 |** TEM images of **(A)** 2FeS2@CNFs, **(B)** 3FeS2@CNFs, **(C)** 4FeS2@CNFs, and **(D)** 5FeS2@CNFs.

The D band illustrates the defects of the carbon atom lattice, and the G band indicates the first-order scattered $E_{2g}$ vibration mode (Xu X. et al., 2018). The ratio ($I_D/I_G$) is higher suggesting that there are more defects on the surface of CNFs (Huang et al., 2018). The values of $I_D/I_G$ for 2$FeS_2$@CNFs, 3$FeS_2$@CNFs, 4$FeS_2$@CNFs, and 5$FeS_2$@CNFs were calculated to be 1.36, 1.35, 1.33, and 1.27, respectively. As the content of $FeS_2$ increases, the value of $I_D/I_G$ gradually decreases, indicating that the $FeS_2$@CNFs composites transform from a disordered structure to an ordered structure. The chemical composition of 3$FeS_2$@CNFs was analyzed using the XPS spectrum (**Figure 3**). The survey spectrum (**Figure 3A**) displays four typical peaks of Fe2p, O1s, C1s, and S2p, respectively. The high-resolution spectrum of Fe2p is demonstrated in **Figure 3B**, the two feature peaks at 707.2 and 720.3 eV belong to $Fe2p_{3/2}$ and $Fe2p_{1/2}$ of pyrite $FeS_2$, while the two peaks at 712.3 and 725.4 eV belong to slight $Fe^{3+}$-S or $Fe^{3+}$-O on the surface of $FeS_2$@CNFs (Chen et al., 2019). The XPS spectra of S displayed in **Figure 3C** are fit into six peaks. The peaks at 163.8 and 165.1 eV match well with the $S2p_{3/2}$ and $S2p_{1/2}$ of $FeS_2$, the binding energy at 164.1 and 165.3 eV are assigned to $S2p_{3/2}$ and $S2p_{1/2}$ of $S^{2-}$, and the higher binding energy at 168.7 and 169.9 eV match well with $S2p_{3/2}$ and $S2p_{1/2}$ of $SO_4^{2-}$ (Zhao et al., 2017; Lin et al., 2019). In the high-resolution spectrum of C 1s (**Figure 3D**), C-N, C=C/C-C, and C = N peaks are displayed (Ma et al., 2018). The production of C=N and C-N bonds is due to the addition of PAN in the electrospinning process (Huang et al., 2020). The S/N co-doped $FeS_2$@CNFs can provide abundant active sites for redox reactions, improving the electronic conductivity of $FeS_2$@CNFs (Lu et al., 2018).

The morphology characterizations of different $FeS_2$@CNFs were carried out by SEM and TEM. **Figure 4A** displays the SEM image of 2$FeS_2$@CNFs. There are many pore channels in the CNFs (the inset of **Figure 4A**) and **Figure 5A**. As the content of $FeS_2$ increases to 30%, there are many pore channels with different diameters inside the nanofibers parallel to the radial direction of the nanofibers. Meanwhile, many holes appear on the surface of the CNFs, as demonstrated in **Figure 4B** and **Figure 5B**. This structure can reduce diffusion resistance and facilitate the diffusion of $Li^+$ ions. At the same time, $FeS_2$ nanoparticles can be firmly loaded on the inner wall of the CNFs to prevent the structure from collapsing caused by volume expansion during cycling. This multi-channel structure can also effectively prevent the dissolution of intermediate products generated during electrochemical reactions (Li et al., 2015). In the SEM and TEM images of 4$FeS_2$@CNFs (**Figure 4C** and **Figure 5C**), it can be observed that the shape of CNFs becomes irregular and the phenomenon of bending and entanglement bonding appears. Furthermore, the pores inside the nanofibers are also significantly reduced. When the $FeS_2$ content is 50%, the shape of CNFs is more irregular and the agglomeration phenomenon is more serious. There are no obvious pores inside the CNFs (**Figures 4D**, **5D**). In summary, as the proportion of $FeS_2$ increases, the structure of CNFs changes. This phenomenon can be attributed to the growth and aggregation of $FeS_2$ particles during the reaction of iron and

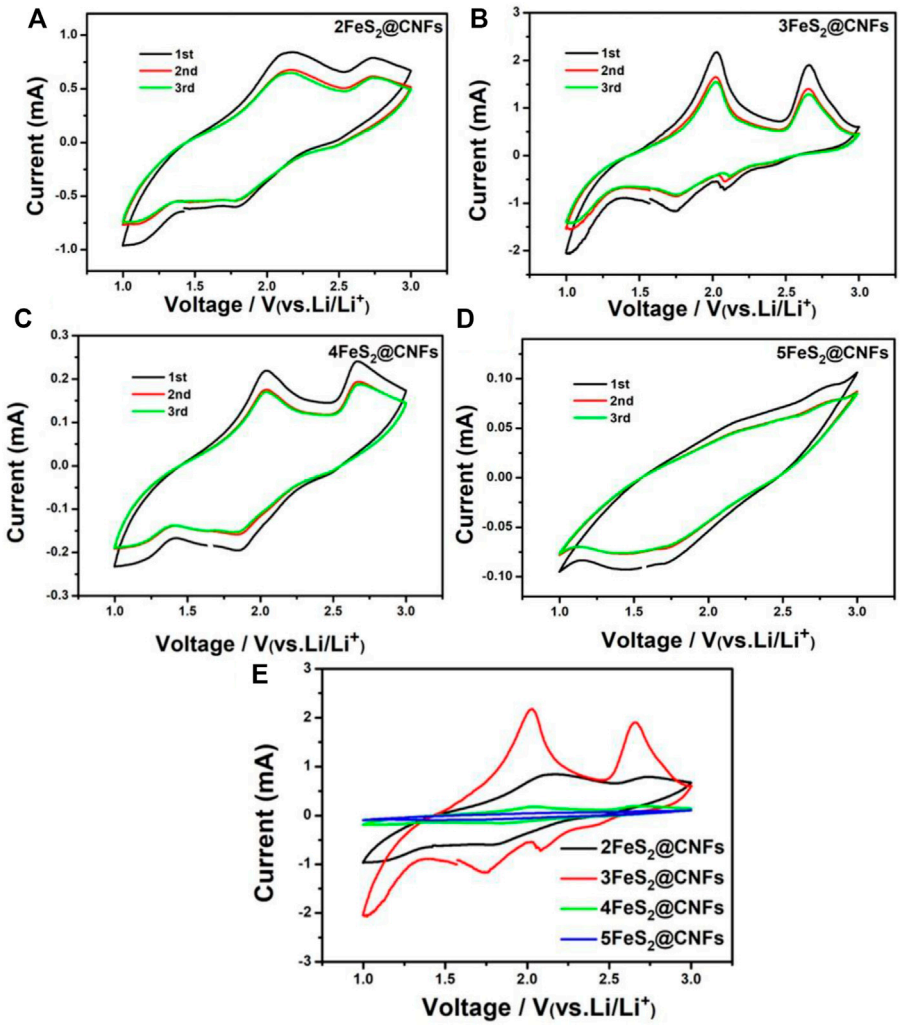


**FIGURE 7 |** CV curves of **(A)** 2FeS2@CNFs, **(B)** 3FeS2@CNFs, **(C)** 4FeS2@CNFs, and **(D)** 5FeS2@CNFs in the initial 3 cycles at 0.5 mV $s^{-1}$; **(E)** CV curves of the first cycle for different electrodes at 0.5 mV $s^{-1}$.

sulfur to form $FeS_2$, occupying the space of the pores in the nanofibers. EDS measurements of the samples were investigated, as shown in **Figure 6**. EDS mappings present that Fe, S, C, and N are evenly distributed on their inherent positions. The Fe element originates from the addition of iron acetate during the process of experiment. The C and N elements come from PAN. The presence of S element is due to the addition of sulfur powder.

CV is an important method to study the lithium storage behavior of $FeS_2$@CNF cathodes. As shown in **Figures 7A–D**, CV tests were carried out for different $FeS_2$@CNF cathodes at 0.5 mV $s^{-1}$ within 1–3 V. The CV curves of $2FeS_2$@CNFs show two oxidation peaks at 2.0 and 2.6 V, and two reduction peaks at 2.1 and 1.8 V. There are two oxidation peaks at 2.1 and 2.7 V and a reduction peak at 1.8 V in the CV curves of $3FeS_2$@CNFs and $4FeS_2$@CNFs. However, no notable redox peaks can be observed in the CV curves of $5FeS_2$@CNFs. **Figure 7E** shows the CV curves of the first cycle for different $FeS_2$@CNFs cathodes. Taking the CV curve of the $3FeS_2$@CNFs cathode as an example, the electrochemical is analyzed. The reduction peak at about 1.8 V can correspond to the below formula:

$$FeS_2 + 2Li^+ + 2e^- \rightarrow Li_2FeS_2 \quad (1)$$

$$Li_2FeS_2 + 2Li^+ + 2e^- \rightarrow 2Li_2S + Fe \quad (2)$$

The aforementioned reactions are conducted simultaneously with reaction (3). But reaction (3) can be attributed to the fact that $Li^+$ ions show relatively slow diffusion in pyrite $FeS_2$ at room temperature.

$$FeS_2 + 4Li^+ + 4e^+ \rightarrow Fe + 2Li_2S \quad (3)$$

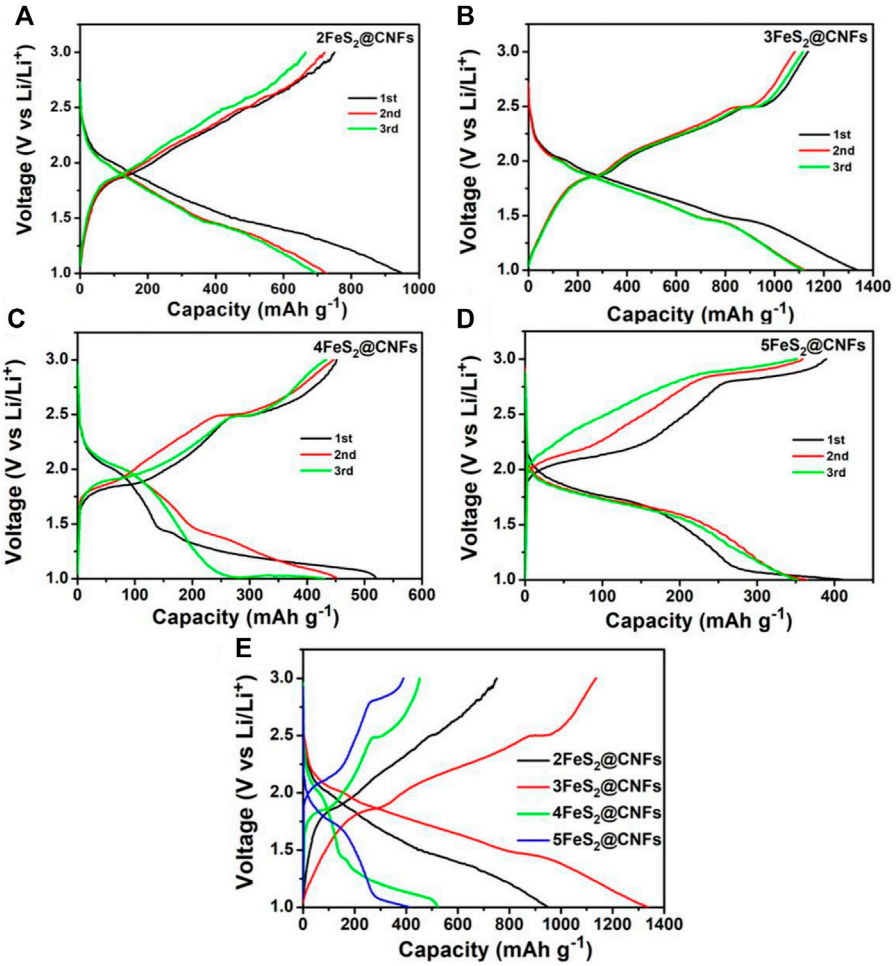


**FIGURE 8 |** Discharge–charge profiles of **(A)** 2FeS2@CNFs, **(B)** 3FeS2@CNFs, **(C)** 4FeS2@CNFs, and **(D)** 5FeS2@CNFs 20 mA $g^{-1}$ between 1 and 3 V; **(E)** the initial discharge-charge profiles of different electrodes at 20 mA $g^{-1}$.

The oxidation peak at around 2.0 V is related to the generation of $Li_{2-x}FeS_2$ according to reactions (4) and (5).

$$2Li_2S + Fe \rightarrow Li_2FeS_2 + 2Li^+ + 2e^- \quad (4)$$

$$Li_2FeS_2 \rightarrow Li_{2-x}FeS_2 + xLi^+ + xe^- \quad (5)$$

The peak at around 2.6 V can be put down to the generation of $FeS_y$ and S according to **formula (6)**.

$$Li_{2-x}FeS_2 \rightarrow FeS_y + (2-y)S + (2-x)Li^+ + (2-x)e^- \quad (6)$$

**Figures 8A–D** are the GCD curves of the first three circles for different $FeS_2$@CNFs cathodes at 20 mA $g^{-1}$. It can be observed that the charge and discharge platforms of each cathode are matched well with the CV curves. **Figure 8E** shows the GCD profiles of the initial cycle for different cathodes at 0.02 A $g^{-1}$. The initial discharge capacity of $2FeS_2$@CNFs, $3FeS_2$@CNFs, $4FeS_2$@CNFs, and $5FeS_2$@CNFs is 905.8, 1,336.7, 520.3, and 400.9 mAh $g^{-1}$, respectively. It is obvious that $3FeS_2$@CNFs composites show a relatively high specific capacity. This is mainly because CNFs can not only improve the conductivity of the electrodes, but its internal pores can also facilitate the reversible embed/de-embed of $Li^+$ ions. In addition, $FeS_2$ nanoparticles can be uniformly distributed in the pores, increasing the contact area between the $FeS_2$ and $Li^+$ ions, and effectively prevent the dissolution of polysulfides generated during the discharge process (Li et al., 2020). $2FeS_2$@CNFs also have many pores, but the content of $FeS_2$ is relatively low, so the specific capacity is less than that of $3FeS_2$@CNFs. As the content of $FeS_2$ increases, the resistance of $4FeS_2$@CNFs and $5FeS_2$@CNFs increases, so their specific capacitances decrease.

The cyclic performance of the samples was also determined, as presented in **Figure 9A**. The specific capacity of $2FeS_2$@CNFs, $3FeS_2$@CNFs, $4FeS_2$@CNFs, and $5FeS_2$@CNFs is 674.6, 856.5, 440, and 370 mAh $g^{-1}$ at 20 mA $g^{-1}$ after 100 cycles. The specific capacities of $2FeS_2$@CNFs and $3FeS_2$@CNFs decay during the cycling, which can be attributed to the dissolution of polysulfides during the electrochemical reaction and leading to the loss of active materials. As the proportion of $FeS_2$ increases, the $FeS_2$ in the pores of carbon fibers can build up and agglomerate. Therefore, the space of the pores becomes less and less,

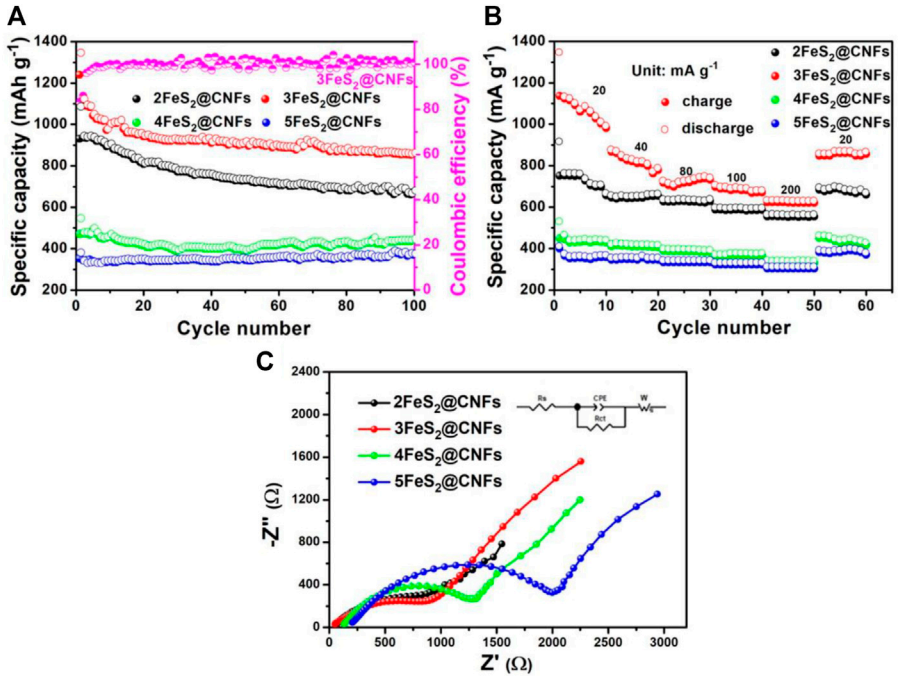


**FIGURE 9 | (A)** Cycling performance at 20 mA $g^{-1}$, **(B)** rate performance, and **(C)** EIS plots of the different electrodes.

resulting in a reduction in the contact area between $Li^+$ ions and active materials so that the phenomena of 4$FeS_2$@CNFs and 5$FeS_2$@CNFs are not obvious. **Figure 9B** shows the rate performance curves of different samples at 20, 40, 80, 100, and 200 mA $g^{-1}$, respectively. It is evident that the 3$FeS_2$@CNFs cathode exhibits the highest rate performance at various current densities among the four cathodes. The excellent electrochemical performances of the 3$FeS_2$@CNF cathode can be attributed to the multi-channel structure of CNFs, which can supply abundant paths for ion and charge transfers. The EIS of 2$FeS_2$@CNFs, 3$FeS_2$@CNFs, 4$FeS_2$@CNFs, and 5$FeS_2$@CNFs was confirmed, as displayed in **Figure 9C**. The values of the equivalent series resistance and the charge transfer resistance for 3$FeS_2$@CNFs are the smallest. The results indicate that the ratio of $FeS_2$ and CNFs is appropriate, which allows the cathode materials possess more three-dimensional hollow channels. Therefore, numerous paths are provided to promote the transport of $Li^+$ ions and electrons, improving the electroconductivity of the cathodes.

## 4 CONCLUSION

In summary, the novel $FeS_2$@CNFs nanocomposites with the multi-channel structure are successfully prepared by the electrospinning method. The 3$FeS_2$@CNFs cathode exhibits an admirable capacity of 856.5 mAh $g^{-1}$ at 20 mA $g^{-1}$ after 100 cycles. The excellent electrochemical properties can be attributed to the right ratio of $FeS_2$ and carbon nanofibers that can produce lots of hollow channels. The three-dimensional interlinked multi-channel carbon nanofibers can facilitate the diffusion of $Li^+$ ions and electrons, improving the electroconductivity of cathodes. Meanwhile, the $FeS_2$ nanoparticles are distributed on the inner wall of the carbon nanofibers, improving the phenomenon of the volume expansion for $FeS_2$ and preventing the dissolution of polysulfides during the cycling process. In addition, S/N co-doped $FeS_2$@CNFs can supply abundant active sites for electrochemical reactions, providing enough space for $Li^+$ ion storage. Thus, the as-prepared 3$FeS_2$@CNFs are a splendid cathode material for lithium-ion batteries, and it can be one of the promising candidates for next-generation secondary batteries.

## DATA AVAILABILITY STATEMENT

The original contributions presented in the study are included in the article/Supplementary Material; further inquiries can be directed to the corresponding author.

## AUTHOR CONTRIBUTIONS

XC: investigation and writing—original draft. YZ: conceptualization and formal analysis. CL: supervision and formal analysis. YY: supervision. YH: methodology, supervision, and writing—review and editing.

## FUNDING

This work was supported by Program of DGUT Innovation Center of Robotics and Intelligent Equipment of China (KCYCXPT2017006), KEY Laboratory of Robotics and Intelligent Equipment of Guangdong Regular Institutions of Higher Education (2017KSYS009), and Dongguan Sci-tech Commissioner Program (20201800500252).

## REFERENCES

Chen, C., Yang, Y., Tang, X., Qiu, R., Wang, S., Cao, G., et al. (2019). Graphene-Encapsulated FeS2 in Carbon Fibers as High Reversible Anodes for Na+/K+ Batteries in a Wide Temperature Range. *Small* 15, 1804740. doi:10.1002/smll.201804740

Chi, J.-Q., Lin, J.-H., Qin, J.-F., Dong, B., Yan, K.-L., Liu, Z.-Z., et al. (2018). A Triple Synergistic Effect from Pitaya-like MoNix-MoCx Hybrids Encapsulated in N-Doped C Nanospheres for Efficient Hydrogen Evolution. *Sustain. Energy Fuels* 2, 1610–1620. doi:10.1039/C8SE00135A

Ennaoui, A., Fiechter, S., Pettenkofer, C., Alonso-Vante, N., Büker, K., Bronold, M., et al. (1993). Iron Disulfide for Solar Energy Conversion. *Sol. Energy Mater. Sol. Cells* 29, 289–370. doi:10.1016/0927-0248(93)90095-K

Fang, K., Ma, L., Cheng, Y.-J., Xia, S., Yang, Z., Zuo, X., et al. (2021). Si/Cu/C Nanohybrid Lithium-Ion Battery Anode with *In Situ* Incorporation of Nonagglomerated Super-small Copper Nanoparticles Based on Epoxy Resin. *Energy fuels.* 35, 6250–6264. doi:10.1021/acs.energyfuels.0c04272

Gou, W.-W., Zhou, S., Cao, X.-X., Luo, Y.-L., Kong, X.-Z., Chen, J., et al. (2021). Agitation Drying Synthesis of Porous Carbon Supported Li3VO4 as Advanced Anode Material for Lithium-Ion Batteries. *Rare Mater.* 40, 3466–3476. doi:10.1007/s12598-021-01712-5

He, J., Li, Q., Chen, Y., Xu, C., Zhou, K., Wang, X., et al. (2017). Self-assembled Cauliflower-like $FeS_2$ Anchored into Graphene Foam as Free-Standing Anode for High-Performance Lithium-Ion Batteries. *Carbon* 114, 111–116. doi:10.1016/j.carbon.2016.12.001

Huang, K., Xing, Z., Wang, L., Wu, X., Zhao, W., Qi, X., et al. (2018). Direct Synthesis of 3D Hierarchically Porous carbon/Sn Composites via *In Situ* Generated NaCl Crystals as Templates for Potassium-Ion Batteries Anode. *J. Mat. Chem. A* 6, 434–442. doi:10.1039/C7TA08171E

Huang, Y., Bao, S., and Lu, J. (2020). Flower-like MnO2/polyaniline/hollow Mesoporous Silica as Electrode for High-Performance All-Solid-State Supercapacitors. *J. Alloys Compd.* 845, 156192. doi:10.1016/j.jallcom.2020.156192

Jiang, Z., Li, Y., Han, C., Huang, Z., Wu, X., He, Z., et al. (2020). Raising Lithium Storage Performances of NaTi2(PO4)3 by Nitrogen and Sulfur Dual-Doped Carbon Layer. *J. Electrochem. Soc.* 167, 020550. doi:10.1149/1945-7111/ab6c5c

Kesavan, T., Partheeban, T., Vivekanantha, M., Prabu, N., Kundu, M., Selvarajan, P., et al. (2020). Design of P-Doped Mesoporous Carbon Nitrides as High-Performance Anode Materials for Li-Ion Battery. *ACS Appl. Mat. Interfaces* 12, 24007–24018. doi:10.1021/acsami.0c05123

Li, G., Cao, S., Fu, L., Wan, S., and Liu, Q. (2021). A Two-step Hydrothermal Synthesis of TiO2/C/FeS2 Composite as High Performance Anode for Lithium Ion Batteries. *Electrochimica Acta* 386, 138470. doi:10.1016/j.electacta.2021.138470

Li, L., Cabán-Acevedo, M., Girard, S. N., and Jin, S. (2014). High-purity Iron Pyrite (FeS2) Nanowires as High-Capacity Nanostructured Cathodes for Lithium-Ion Batteries. *Nanoscale* 6, 2112–2118. doi:10.1039/C3NR05851D

Li, Z., Hu, X., Shi, Z., Lu, J., and Wang, Z. (2020). MOFs-derived Metal Oxides Inlayed in Carbon Nanofibers as Anode Materials for High-Performance Lithium-Ion Batteries. *Appl. Surf. Sci.* 531, 147290. doi:10.1016/j.apsusc.2020.147290

Li, Z., Zhang, J. T., Chen, Y. M., Li, J., and Lou, X. W. (2015). Pie-like Electrode Design for High-Energy Density Lithium-Sulfur Batteries. *Nat. Commun.* 6, 8850. doi:10.1038/ncomms9850

Liao, H. T., Wang, Y. R., Wang, J., Qian, X. F., and Cheng, S. Q. (2013). Synthesis of Macroporous FeS2 Nanotubes and Their Electrochemical Properties. *Amr* 774-776, 677–681. doi:10.4028/www.scientific.net/AMR.774-776.677

Lin, Z., Xiong, X., Fan, M., Xie, D., Wang, G., Yang, C., et al. (2019). Scalable Synthesis of FeS2 Nanoparticles Encapsulated into N-Doped Carbon Nanosheets as a High-Performance Sodium-Ion Battery Anode. *Nanoscale* 11, 3773–3779. doi:10.1039/C8NR10444A

Lu, Z., Wang, N., Zhang, Y., Xue, P., Guo, M., Tang, B., et al. (2018). Metal-Organic Framework-Derived Sea-cucumber-like FeS2@C Nanorods with Outstanding Pseudocapacitive Na-Ion Storage Properties. *ACS Appl. Energy Mat.* 1, 6234–6241. doi:10.1021/acsaem.8b01239

Lu, Z., Zhai, Y., Wang, N., Zhang, Y., Xue, P., Guo, M., et al. (2020). $FeS_2$ Nanoparticles Embedded in N/S Co-doped Porous Carbon Fibers as Anode for Sodium-Ion Batteries. *Chem. Eng. J.* 380, 122455. doi:10.1016/j.cej.2019.122455

Ma, W., Liu, X., Lei, X., Yuan, Z., and Ding, Y. (2018). Micro/nano-structured FeS2 for High Energy Efficiency Rechargeable Li-FeS2 Battery. *Chem. Eng. J.* 334, 725–731. doi:10.1016/j.cej.2017.10.122

Polishchuk, Y. V., Shembel, E. M., Volfkovich, Y. M., Reisner, D., and Yu. Volfkovich, A. (2019). Synthesized Nanostructured FeS2 for Li-Batteries Application. Influence of Microstructure. *Mater. Today Proc.* 6, 48–55. doi:10.1016/j.matpr.2018.10.074

Teng, Y., Liu, H., Liu, D., He, H., and Chen, Y. (2019). Pitaya-like Carbon-Coated ZnS/carbon Nanospheres with Inner Three-Dimensional Nanostructure as High-Performance Anode for Lithium-Ion Battery. *J. Colloid Interface Sci.* 554, 220–228. doi:10.1016/j.jcis.2019.07.012

Wang, J., Fang, J., Zhao, H., Zhang, Z., and Li, Z. (2021). Raspberry-like Hierarchical Structure FeS2 Decorated by Dual-Carbon Framework as High-Performance Cathode for Rechargeable Lithium Batteries. *Carbon* 171, 171–178. doi:10.1016/j.carbon.2020.09.006

Wang, S., Ning, P., Huang, S., Wang, W., Fei, S., He, Q., et al. (2019). Multi-functional NiS2/FeS2/N-Doped Carbon Nanorods Derived from Metal-Organic Frameworks with Fast Reaction Kinetics for High Performance Overall Water Splitting and Lithium-Ion Batteries. *J. Power Sources* 436, 226857–226857.11. doi:10.1016/j.jpowsour.2019.226857

Xu, L., Hu, Y., Zhang, H., Jiang, H., and Li, C. (2016). Confined Synthesis of FeS2 Nanoparticles Encapsulated in Carbon Nanotube Hybrids for Ultrastable Lithium-Ion Batteries. *ACS Sustain. Chem. Eng.* 4, 4251–4255. doi:10.1021/acssuschemeng.6b00741

Xu, Q.-T., Li, J.-C., Xue, H.-G., and Guo, S.-P. (2018). Effective Combination of FeS2 Microspheres and Fe3S4 Microcubes with rGO as Anode Material for High-Capacity and Long-Cycle Lithium-Ion Batteries. *J. Power Sources* 396, 675–682. doi:10.1016/j.jpowsour.2018.06.088

Xu, X., Cai, T., Meng, Z., Ying, H., Xie, Y., Zhu, X., et al. (2016). $FeS_2$ Nanocrystals Prepared in Hierarchical Porous Carbon for Lithium-Ion Battery. *J. Power Sources* 331, 366–372. doi:10.1016/j.jpowsour.2016.09.015

Xu, X., Meng, Z., Zhu, X., Zhang, S., and Han, W.-Q. (2018). Biomass Carbon Composited FeS 2 as Cathode Materials for High-Rate Rechargeable Lithium-Ion Battery. *J. Power Sources* 380, 12–17. doi:10.1016/j.jpowsour.2018.01.057

Yang, X., Chen, X., Qiu, J., Li, M., Ming, H., Zhang, S., et al. (2021). Controllable Synthesis of Silicon/carbon Hollow Microspheres Using Renewable Sources for High Energy Lithium-Ion Battery. *J. Solid State Chem.* 296, 121968. doi:10.1016/j.jssc.2021.121968

Zhang, F., Wang, C., Huang, G., Yin, D., and Wang, L. (2016). FeS2@C Nanowires Derived from Organic-Inorganic Hybrid Nanowires for High-Rate and Long-Life Lithium-Ion Batteries. *J. Power Sources* 328, 56–64. doi:10.1016/j.jpowsour.2016.07.117

Zhang, X.-Y., Guo, B.-Y., Chen, Q.-W., Dong, B., Zhang, J.-Q., Qin, J.-F., et al. (2019). Ultrafine and Highly-Dispersed Bimetal Ni2P/Co2P Encapsulated by Hollow N-Doped Carbon Nanospheres for Efficient Hydrogen Evolution. *Int. J. Hydrogen Energy* 44, 14908–14917. doi:10.1016/j.ijhydene.2019.04.108

Zhao, B., Wang, Q., Zhang, S., and Deng, C. (2015). Self-assembled Wafer-like Porous NaTi2(PO4)3 Decorated with Hierarchical Carbon as a High-Rate Anode for Aqueous Rechargeable Sodium Batteries. *J. Mat. Chem. A* 3, 12089–12096. doi:10.1039/C5TA02568K

Zhao, W., Guo, C., and Li, C. M. (2017). Lychee-like FeS2@FeSe2 Core-Shell Microspheres Anode in Sodium Ion Batteries for Large Capacity and Ultralong Cycle Life. *J. Mat. Chem. A* 5, 19195–19202. doi:10.1039/C7TA05931K

Zhong, M.-e., Guan, J., Feng, Q., Wu, X., Xiao, Z., Zhang, W., et al. (2018). Accelerated Polysulfide Redox Kinetics Revealed by Ternary Sandwich-type S@Co/N-doped Carbon Nanosheet for High-Performance Lithium-Sulfur Batteries. *Carbon* 128, 86–96. doi:10.1016/j.carbon.2017.11.084

**Conflict of Interest:** The authors declare that the research was conducted in the absence of any commercial or financial relationships that could be construed as a potential conflict of interest.

**Publisher's Note:** All claims expressed in this article are solely those of the authors and do not necessarily represent those of their affiliated organizations, or those of the publisher, the editors, and the reviewers. Any product that may be evaluated in this article, or claim that may be made by its manufacturer, is not guaranteed or endorsed by the publisher.

frontiers | Frontiers in Chemistry

TYPE Original Research
PUBLISHED 25 August 2022
DOI 10.3389/fchem.2022.960369



OPEN ACCESS

EDITED BY
Hailong Wang,
Ningxia University, China

REVIEWED BY
Houzhao Wan,
Hubei University, China
Zhongqi Shi,
Xi'an Jiaotong University, China

*CORRESPONDENCE
Adnan,
adnan_abbasi89@yahoo.com

SPECIALTY SECTION
This article was submitted to Nanoscience, a section of the journal Frontiers in Chemistry

RECEIVED 02 June 2022
ACCEPTED 22 July 2022
PUBLISHED 25 August 2022

CITATION
Adnan, Guedri K, Raizah Z, Tag-Eldin E, Ashraf W, Khan U and M. Galal A (2022), Thermal efficiency in hybrid ($Al_2O_3$-CuO/$H_2O$) and tri-hybrid ($Al_2O_3$-CuO-Cu/$H_2O$) nanofluids between converging/diverging channel with viscous dissipation function: Numerical analysis.
*Front. Chem.* 10:960369.
doi: 10.3389/fchem.2022.960369



# Thermal efficiency in hybrid ($Al_2O_3$-CuO/$H_2O$) and tri-hybrid ($Al_2O_3$-CuO-Cu/$H_2O$) nanofluids between converging/diverging channel with viscous dissipation function: Numerical analysis

Adnan[1]*, Kamel Guedri[2], Zehba Raizah[3], Elsayed Tag-Eldin[4], Waqas Ashraf[5], Umar Khan[6] and Ahmed M. Galal[7,8]

[1]Department of Mathematics, Mohi-ud-Din Islamic University, Nerian Sharif, AJ&K, Pakistan, [2]Mechanical Engineering Department, College of Engineering and Islamic Architecture, Umm Al-Qura University, Makkah, Saudi Arabia, [3]Department of Mathematics, College of Science, King Khalid University, Abha, Saudi Arabia, [4]Faculty of Engineering and Technology, Future University in Egypt New Cairo, Mansoura, Egypt, [5]Departmment of Applied Mathematics and Statistics (AM&S), Institute of Space Technology (IST), Islamabad, Pakistan, [6]Department of Mathematics and Statistics, Hazara University Mansehra, Islamabad, Pakistan, [7]Mechanical Engineering Department, College of Engineering, Prince Sattam Bin Abdulaziz University, Wadi Addawaser, Saudi Arabia, [8]Production Engineering and Mechanical Design Department, Faculty of Engineering, Mansoura University, Mansoura, Egypt

Heat transfer and energy storage remain a core problem for industrialists and engineers. So, the concept of new heat transfer fluids, namely, nanofluids and hybrid nanofluids, has been introduced so far. Recently, a new third generation of heat transfer fluids has been developed known as modified hybrid nanofluids (MHNs), synthesized by ternary nanomaterials and the host fluid. Therefore, the study was conducted to investigate the energy storage efficiency between $(Al_2O_3\text{-}CuO\text{-}Cu/H_2O)_{mhnf}$ and $(Al_2O_3\text{-}CuO/H_2O)_{hnf}$ in the presence of novel viscous dissipation effects. The problem is developed for a channel with stretchable walls *via* thermophysical attributes of binary and ternary guest nanomaterials and the host liquid. The model is tackled numerically and furnished results for the dynamics, most specifically energy storage efficiency in $(Al_2O_3\text{-}CuO\text{-}Cu/H_2O)_{mhnf}$. It is examined that the third generation of heat transfer fluids $(Al_2O_3\text{-}CuO\text{-}Cu/H_2O)_{mhnf}$ has high thermal energy storage efficiency than traditional nano and hybrid nanofluids. Therefore, these new insights in heat transfer would be beneficial and cope with the problems of energy storage in the modern technological world.

KEYWORDS

**thermal energy storage, hybrid and modified hybrid nanofluids, thermophysical attributes, engineering applications, mathematical analysis, local energy storage**

## Introduction

The significance of heat transport in the modern technological world is unavoidable due to its remarkable applications. It is a bitter truth that conventional liquids have very limited thermal performance; therefore, these fluids have very limited applications in the modern world era. However, scientists and fluid dynamists thought that how to cope with this core problem. Finally, they introduced the concept of nanofluids. These fluids are the composition of host liquid and guest nanoparticles. The nanoparticles are stably suspended in the liquid and thermally compatible. The majority of issues of the modern world were tackled after the development of nanofluids. However, researchers did not stop their efforts and moved toward the second generation of nanofluids called hybrid nanofluids.

Lately, a superior class of hybrid nanofluids has developed called modified hybrid nanofluid. In this case, further nanoparticles of third guest metals were added to the conventional hybrid nanofluid. The newly suspended additives make the resultant suspension more efficient than hybrid nanofluid. These fluids attained much fame from fluid dynamists and industrialists because of their ultra-high thermal performance than conventional nano and hybrid nanofluids. However, we can categorize the heat transfer fluids into three categories to cope with the heat transfer problems of the modern technological world. These are:

Nanofluids (Choi, 1995) or first-generation heat transfer fluids.

Hybrid nanofluids (Ahmed et al., 2020; Mohyud-Din et al., 2020) or second-generation heat transfer fluids.

Modified hybrid Nanofluids (Abbasi et al., 2021) or third-generation heat transfer fluids.

The synthetization process of the aforementioned classes is depicted in Figures 1–3 for nano, hybrid, and modified hybrid nanofluids, respectively.

The newly developed generation (first, second, and third generations) of the fluids strengthen their roots in modern world applications. These could be found in biomedical engineering, electronics, and cooling of the systems to save the drugs and different medicines from moisture in the stores, to check the interaction of biofluids in the human veins and arteries by injecting the hybrid and modified hybrid mixture of nanoparticles, aerodynamics, in the study of chemotherapy, to diagnose cancer symptoms, paint industries, and manufacturing of home appliances. Therefore, the study of heat transfer in nanofluids is significant to accomplish many industrial and engineering processes. In view of such a significant motive, the researchers and fluid dynamists started working in this direction with all of their potential.

The investigation of heat and mass transport mechanisms in opening/narrowing channel is of much interest owing to its applications in medical sciences and engineering as well.

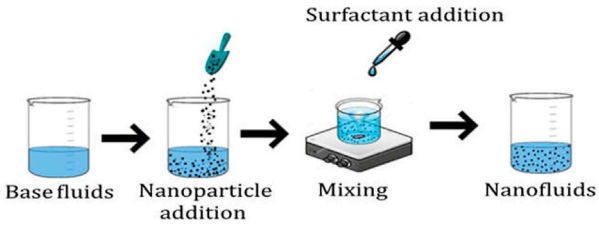


FIGURE 1
First-generation heat transfer fluids.

Therefore, fluid dynamists focused their attention on exploring the behavior of heat and mass transfer under certain flow assumptions. Such flows extensively appeared in different engineering systems and the flow of blood in human bodies. More specifically, these flows were named Jeffery–Hamel flows after the untiring efforts of Jeffery (1915) and Hamel (1916) during the era of 1915 and 1916, respectively. This concept of flow configuration became very prevalent and conferred the attention of researchers in this direction.

The exploration of thermal performance in the nanofluid under the impacts of internal heat generation/absorption source and viscous dissipation is reported in Akinshilo et al. (2020). The authors organized the study in converging/diverging walls by imposing Lorentz forces on them. The problem is modeled in a cylindrical polar frame, and a dimensionless version is attained *via* feasible similarity transforms. The mathematical section of the work is organized by using the homotopy perturbation method (HPM) and then plotting the results for the concerned flow parameters such as magnetic, Darcy, and Reynolds numbers. It is reported that by increasing the strength of Re, the fluid velocity drops and heat transfer declines at the high Darcy parameter. Although the study is fascinating, researchers performed the results with full consideration; however, it could be prolonged to the next nanofluid generation (hybrid nanofluids) by inducing the influences of Joule heating and thermal radiations.

An analytical study of JH flow for regular liquid is conducted by Patel and Meher (2018). They prolonged the concept of the traditional Adomian decomposition method (ADM) technique to modified Adomian decomposition method (MADM) and solved the problem and found satisfactory results regarding the implementation of the technique. The graphical results were explored and discussed in detail. From the critical review of the article, it is understood that the work has its own significance, but it lacks the important concept of nanofluids and other physical conditions such as slip, thermal jump, and Biot effects. Therefore, more interesting and novel results could be achieved by prolonging the work for hybrid and modified hybrid nanofluids. Further studies on JH flows by taking different physical conditions are reported in Sushila and Shishodia (2014)

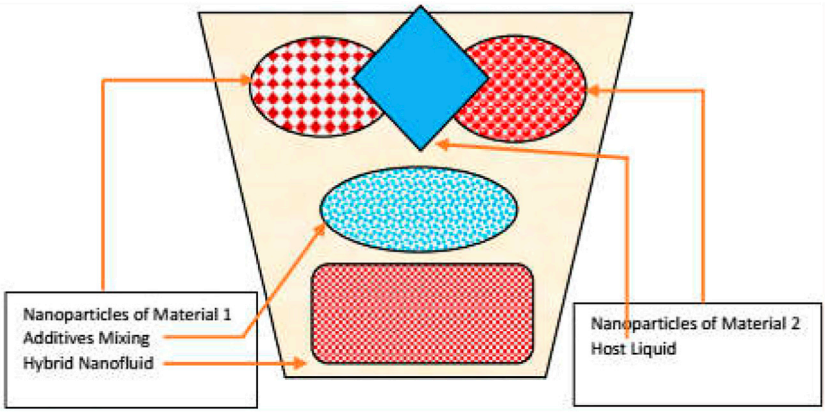


FIGURE 2
Second-generation heat transfer fluids.

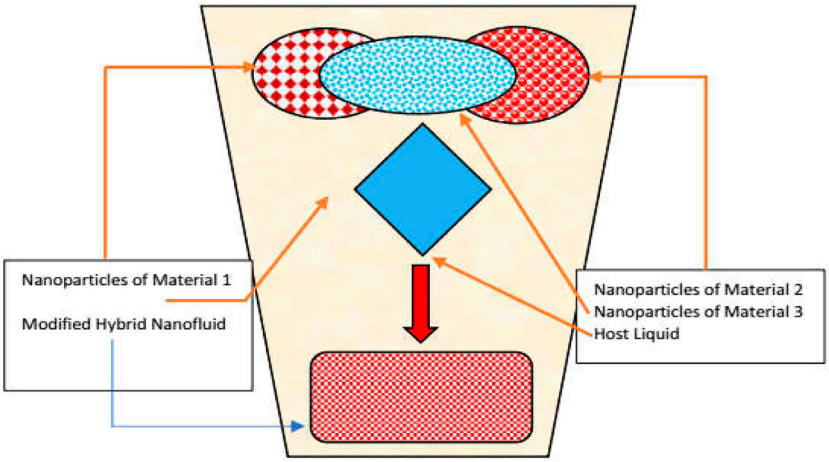


FIGURE 3
Third-generation heat transfer fluids.

and Kumbinarasaiah and Raghunatha (2022), and the relevant studies are cited therein.

The applications of nanofluids and hybrid nanofluids attracted researchers and scientists to analyze these fluids for thermal performance, which is a primary element of the modern world. Therefore, numerous studies in this regard have been reported under different flow conditions by using nanofluids synthesized by various base liquids and multiple nano-additives, for instance, the studies by Turkyilmazoglu (2014), Zangooee et al. (2019); Kumar et al. (2021), and Rout et al. (2021). Furthermore, some significant studies related to hybrid nanofluids were reported in Ahmed et al. (2017), Khan et al. (2021) Kumar (2021), Saeed et al. (2021), and Shanmugapriya et al. (2021).

The careful literature survey reveals that comparative heat transfer efficiency of second-generation $(Al_2O_3\text{-}CuO/H_2O)_{hnf}$ and third-generation $(Al_2O_3\text{-}CuO\text{-}Cu/H_2O)_{mhnf}$ nanofluids between opening/narrowing walls subject to the stretching and shrinking conditions has not been reported so far. This type of flow has numerous applications in different engineering systems, most specifically in biomedical engineering. The blood flow at the junction of veins and arteries works under the principle of Jeffery–Hamel (JH) flow. Therefore, the study is organized to explore the velocity, heat transport mechanism, trends in shear stresses, and thermal conductivity in $(Al_2O_3\text{-}CuO/H_2O)_{hnf}$ and $(Al_2O_3\text{-}CuO\text{-}Cu/H_2O)_{mhnf}$ against various parameters, particularly the volumetric fraction. The efficiency of the studied nanofluids can be compared with other reported nanofluids.

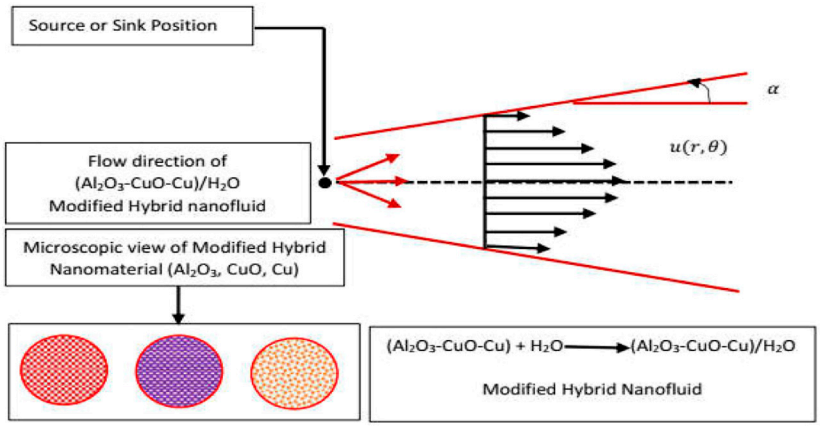


FIGURE 4
Flow scenario of $(Al_2O_3\text{-}CuO\text{-}Cu/H_2O)_{mhnf}$.

# Development of third-generation nanofluid model

## Flow configuration

The flow of $(Al_2O_3\text{-}CuO/H_2O)_{hnf}$ and $(Al_2O_3\text{-}CuO\text{-}Cu/H_2O)_{mhnf}$ subject to viscous dissipation and flexible channel walls is organized between two non-parallel walls. It is supposed that the fluid flow is due to a source/sink positioned at the junction of these two walls. The walls are separated by an angle $2\alpha$ is placed in a cylindrical polar frame. The flow is along the only direction with the velocity component $\boldsymbol{V} = (\breve{u}_r, 0, 0)$. Furthermore, the velocity at the walls is subject to $\breve{u}_r = \breve{U}_w = \frac{\breve{s}}{\breve{r}}$, where $s$ is the stretching/shrinking rate of the walls. The nanofluids synthesized are subject to the following assumptions:

- The guest hybrid nanomaterials $Al_2O_3$-CuO and $H_2O$ are thermally compatible.
- The guest hybrid nanomaterial $Al_2O_3$-CuO is uniformly suspended in $H_2O$.
- The guest modified hybrid nanomaterials $Al_2O_3$-CuO-Cu and $H_2O$ are thermally compatible.
- The guest modified hybrid nanomaterial $Al_2O_3$-CuO-Cu is uniformly suspended in $H_2O$.

The physical setup of the flow configuration is depicted in Figure 4.

## Empirical correlations

The nanoparticles of aluminum oxide, copper oxide, and copper are used to synthesize the desired nanofluid (nf), hybrid nanofluid (hnf), and modified hybrid nanofluid (mhnf) in the presence of host liquid water. The empirical correlations for nanofluids, hybrid nanofluids, and modified hybrid nanofluids are given in Tables 1–3, respectively, whereas the shape factor is given in Table 4.

TABLE 1 Empirical correlations for first-generation heat transfer fluids.

| Characteristics | Empirical correlation |
|---|---|
| Dynamic viscosity | $\frac{\breve{\mu}_{nf}}{\breve{\mu}_f} = \frac{1}{(1-\phi)^{25/10}}$ |
| Effective density | $\breve{\rho}_{nf} = \breve{\rho}_f(1-\phi) + \breve{\rho}_s\phi$ |
| Heat capacity | $(\rho\breve{c}_p)_{nf} = (\rho\breve{c}_p)_f(1-\phi) + \phi(\rho\breve{c}_p)_s$ |
| Thermal conductivity | $\frac{\breve{k}_{nf}}{\breve{k}_f} = \frac{\breve{k}_s+(\breve{n}-1)\breve{k}_f-(\breve{n}-1)\phi_s(\breve{k}_f-\breve{k}_s)}{\breve{k}_s+(\breve{n}-1)\breve{k}_f+\phi_s(\breve{k}_f-\breve{k}_s)}$ |
| Electrical conductivity | $\frac{\breve{\sigma}_{nf}}{\breve{\sigma}_f} = 1 + \frac{3(\frac{\breve{\sigma}_s}{\breve{\sigma}_f}-1)\phi}{(\frac{\breve{\sigma}_s}{\breve{\sigma}_f}+2)-(\frac{\breve{\sigma}_s}{\breve{\sigma}_f}-1)\phi}$ |
| Thermal expansion | $(\rho\beta)_{nf} = (1-\phi)(\rho\beta)_s + \phi(\rho\beta)_f$ |

The values of guest nanoparticles ($Al_2O_3$, CuO, and Cu) and the host liquid (water) are key ingredients in the study of newly generated heat transfer fluids. These attributes are given in Table 5 for the guest nanoparticles and the host liquid.

## Development of modified hybrid nanofluid

The development of the model is based on well-known mass, momentum, and energy constitutive relations in a cylindrical polar frame. For the particular study, these relations are given as follows:

TABLE 2 Empirical correlations for second-generation heat transfer fluids (hybrid nanofluids) (Ahmed et al., 2021).

| Characteristics | Empirical correlation |
|---|---|
| Dynamic viscosity | $\frac{\breve{\mu}_{(Al_2O_3-CuO)water}}{\breve{\mu}_{water}} = \frac{1}{(1-\phi_1)^{25/10}(1-\phi_2)^{25/10}}$ |
| Effective density | $\breve{\rho}_{(Al_2O_3-CuO)water} = ((1-\phi_2)((1-\phi_1)\rho_{water} + \phi_1\rho_{Al_2O_3})) + \phi_2\rho_{CuO}$ |
| Heat capacity | $(\widetilde{\rho c}_p)_{(Al_2O_3-CuO)water} = (1-\phi_2)((1-\phi_1)(\widetilde{\rho c}_p)_{water} + \phi_1(\widetilde{\rho c}_p)_{Al_2O_3}) + \phi_2(\widetilde{\rho c}_p)_{CuO}$ |
| Thermal conductivity | $\frac{\breve{k}_{(Al_2O_3-CuO)water}}{\breve{k}_{nf}} = \frac{\breve{k}_{CuO}+(\breve{n}-1)\breve{k}_{nf}-(\breve{n}-1)\phi_{CuO}(\breve{k}_{nf}-\breve{k}_{CuO})}{\breve{k}_{CuO}+(\breve{n}-1)\breve{k}_{nf}+\phi_{CuO}(\breve{k}_{nf}-\breve{k}_{CuO})}$, where<br>$\frac{k_{nf}}{k_f} = \frac{\breve{k}_{Al_2O_3}+(\breve{n}-1)\breve{k}_{water}-(\breve{n}-1)\phi_{Al_2O_3}(\breve{k}_{water}-\breve{k}_{Al_2O_3})}{\breve{k}_{Al_2O_3}+(\breve{n}-1)\breve{k}_{water}+\phi_{Al_2O_3}(\breve{k}_{water}-\breve{k}_{Al_2O_3})}$;<br>$\phi_{Al_2O_3}=\phi_1;\ \phi_{CuO=\phi_2}$ |
| Electrical conductivity | $\frac{\breve{\sigma}_{(Al_2O_3-CuO)water}}{\breve{\sigma}_{nf}} = \frac{\sigma_{CuO}+2\sigma_{nf}-2\phi_{CuO}(\sigma_{nf}-\sigma_{CuO})}{\sigma_{CuO}+2\sigma_{nf}+\phi_{CuO}(\sigma_{nf}-\sigma_{CuO})}$, where<br>$\frac{\sigma_{nf}}{\sigma_{water}} = \frac{\sigma_{Al_2O_3}+2\sigma_{water}-2\phi_{Al_2O_3}(\sigma_{water}-\sigma_{Al_2O_3})}{\sigma_{Al_2O_3}+2\sigma_{water}+\phi_{Al_2O_3}(\sigma_{water}-\sigma_{Al_2O_3})}$ |
| Thermal expansion | $(\rho\beta)_{(Al_2O_3-CuO)water} = (1-\phi_{CuO})[(1-\phi_{Al_2O_3})(\rho\beta)_{water} + \phi_{Al_2O_3}(\rho\beta)_{Al_2O_3}] + \phi_{Al_2O_3}(\rho\beta)_{CuO}$,<br>where $\phi_{Al_2O_3} = \phi_1, \quad \phi_{CuO} = \phi_2$ |

TABLE 3 Empirical correlations for third-generation heat transfer fluids (modified hybrid nanofluids).

| Characteristics | Empirical correlation |
|---|---|
| Dynamic viscosity | $\frac{\breve{\mu}_{(Al_2O_3-CuO-Cu)water}}{\breve{\mu}_{water}} = \frac{1}{(1-\phi_{Al_2O_3})^{25/10}(1-\phi_{CuO})^{25/10}(1-\phi_{Cu})^{25/10}}$<br>$\phi_{Al_2O_3} = \phi_1, \ \phi_{CuO} = \phi_2, \ \phi_{Cu} = \phi_3$ |
| Effective density | $\breve{\rho}_{(Al_2O_3-CuO-Cu)water} = (1-\phi_{Cu})[(1-\phi_{CuO})\{(1-\phi_{Al_2O_3})\rho_{water} + \phi_{Al_2O_3}\rho_{Al_2O_3}\} + \phi_{CuO}\rho_{CuO}] + \phi_{Cu}\rho_{Cu}$,<br>where $\rho_{Al_2O_3} = \phi_1, \ \phi_{CuO} = \phi_2, \ \phi_{Cu} = \phi_3$ |
| Heat capacity | $(\widetilde{\rho c}_p)_{(Al_2O_3-CuO-Cu)water} = (1-\phi_{Cu})[(1-\phi_{CuO})\{(1-\phi_{Al_2O_3})(\rho c_p)_{water} + \phi_{Al_2O_3}(\rho c_p)_{Al_2O_3}\} + \phi_{CuO}(\rho c_p)_{CuO}] + \rho_{Cu}(\rho c_p)_{Cu}$ |
| Thermal conductivity | $\frac{\breve{k}_{(Al_2O_3-CuO-Cuwater)}}{\breve{k}_{(Al_2O_3-CuO)water}} = \frac{\breve{k}_{Cu}+(\breve{n}-1)\breve{k}_{(Al_2O_3-CuO)water}-(\breve{n}-1)\phi_{Cu}(\breve{k}_{(Al_2O_3-CuO)water}-\breve{k}_{Cu})}{\breve{k}_{Cu}+(\breve{n}-1)\breve{k}_{(Al_2O_3-CuO)water}+\phi_{Cu}(\breve{k}_{(Al_2O_3-CuO)water}-\breve{k}_{Cu})}$<br>$\frac{k_{(Al_2O_3-CuO)water}}{k_{nf}} = \frac{\breve{k}_{CuO}+(\breve{n}-1)\breve{k}_{nf}-(\breve{n}-1)\phi_{CuO}(\breve{k}_{nf}-\breve{k}_{Cu})}{\breve{k}_{CuO}+(\breve{n}-1)\breve{k}_{nf}+\phi_{CuO}(\breve{k}_{nf}-\breve{k}_{Cu})}$<br>$\frac{k_{nf}}{k_f} = \frac{\breve{k}_{Al_2O_3}+(\breve{n}-1)\breve{k}_{water}-(\breve{n}-1)\phi_{Al_2O_3}(\breve{k}_{water}-\breve{k}_{Al_2O_3})}{\breve{k}_{Al_2O_3}+(\breve{n}-1)\breve{k}_{water}+\phi_{Al_2O_3}(\breve{k}_{water}-\breve{k}_{Al_2O_3})}$<br>$\phi_{Al_2O_3=\phi_1;\ \phi_{CuO=\phi_2}}, \quad \phi_{Cu=\phi_3}, \quad \breve{k}_{(Al_2O_3-CuO)water=\breve{k}_{hnf}}$ |
| Electrical conductivity | $\frac{\breve{\sigma}_{(Al_2O_3-CuO-Cu)water}}{\breve{\sigma}_{(Al_2O_3-CuO)water}} = \frac{\breve{\sigma}_{Cu}+2\breve{\sigma}_{(Al_2O_3-CuO)water}-2\phi_{Cu}(\breve{\sigma}_{(Al_2O_3-CuO)water}-\breve{\sigma}_{Cu})}{\breve{\sigma}_{Cu}+2\breve{\sigma}_{(Al_2O_3-CuO)water}+\phi_{Cu}(\breve{\sigma}_{(Al_2O_3-CuO)water}-\breve{\sigma}_{Cu})}$, where<br>$\frac{\breve{\sigma}_{(Al_2O_3-CuO)water}}{\breve{\sigma}_{nf}} = \frac{\breve{\sigma}_{CuO}+2\breve{\sigma}_{nf}-2\phi_{CuO}(\breve{\sigma}_{nf}-\breve{\sigma}_{CuO})}{\breve{\sigma}_{CuO}+2\breve{\sigma}_{nf}+\phi_{CuO}(\breve{\sigma}_{nf}-\breve{\sigma}_{CuO})}$<br>$\frac{\breve{\sigma}_{nf}}{\breve{\sigma}_{water}} = \frac{\breve{\sigma}_{Al_2O_3}+2\breve{\sigma}_{water}-2\phi_{Al_2O_3}(\breve{\sigma}_{water}-\breve{\sigma}_{Al_2O_3})}{\breve{\sigma}_{Al_2O_3}+2\breve{\sigma}_{water}+\phi_{Al_2O_3}(\breve{\sigma}_{water}-\breve{\sigma}_{Al_2O_3})}$<br>$\breve{\sigma}_{(Al_2O_3-CuO-Cu)water} = \breve{\sigma}_{mhnf}, \ \breve{\sigma}_{(Al_2O_3-CuO)water} = \breve{\sigma}_{hnf}$<br>$\breve{\sigma}_{Al_2O_3} = \breve{\sigma}_{s1}, \ \breve{\sigma}_{CuO} = \breve{\sigma}_{s2}, \ \breve{\sigma}_{Cu} = \breve{\sigma}_{s3}$ |

$$\frac{1}{\breve{r}}\frac{\partial\left(\breve{r}\breve{u}_r\right)}{\partial\breve{r}} = 0, \tag{1}$$

$$\breve{\rho}_{mhnf}\left(\breve{u}_r\frac{\partial\left(\breve{u}_r\right)}{\partial\breve{r}}\right) + \frac{\partial\breve{p}}{\partial\breve{r}} - \breve{\mu}_{mhnf}\left(\frac{\partial^2\breve{u}_r}{\partial\breve{r}^2} + \frac{1}{\breve{r}}\frac{\partial\breve{u}_r}{\partial\breve{r}} + \frac{1}{\breve{r}^2}\frac{\partial^2\breve{u}_r}{\partial\breve{\theta}^2} - \frac{\breve{u}_r}{\breve{r}^2}\right) = 0, \tag{2}$$

$$-\frac{1}{\breve{\rho}_{mhnf}}\frac{\partial\breve{p}}{\partial\breve{\theta}} + \frac{2\breve{\mu}_{mhnf}}{\breve{r}^2\breve{\rho}_{mhnf}}\frac{\partial\breve{u}_r}{\partial\breve{\theta}} = 0, \tag{3}$$

$$\breve{u}_r\frac{\partial\breve{T}}{\partial\breve{r}} - \frac{\breve{k}_{mhnf}}{\left(\rho c_p\right)_{mhnf}}\left(\frac{\partial^2\breve{T}}{\partial\breve{r}^2} + \frac{1}{\breve{r}}\frac{\partial\breve{T}}{\partial\breve{r}} + \frac{1}{\breve{r}^2}\frac{\partial^2\breve{T}}{\partial\breve{\theta}^2}\right) - \frac{\breve{\mu}_{mhnf}}{\left(\rho c_p\right)_{mhnf}}\left(4\left(\frac{\partial\breve{u}_r}{\partial\breve{r}}\right)^2 + \frac{1}{\breve{r}^2}\left(\frac{\partial\breve{u}_r}{\partial\breve{\theta}}\right)^2\right) = 0. \tag{4}$$

TABLE 4 Attributes for different shape factors.

| Nanomaterial's shape | Attribute |
|---|---|
| Bricks | 3.7 |
| Cylinders | 4.9 |
| Platelets | 5.7 |
| Blades | 8.6 |

TABLE 5 Thermophysical values of the guest nanoparticles and the host liquid.

| Properties | $\hat{\rho}(kg/m^3)$ | $\hat{c}_p\,(J/Kg\,K)$ | $\hat{k}(W/mk)$ | $\breve{\sigma}(\Omega m)^{-1}$ |
|---|---|---|---|---|
| Pure water ($H_2O$) | 997.1 | 4180 | 0.6071 | $5.5 \times 10^{-6}$ |
| $Al_2O_3$ | 3,970 | 765 | 40 | $35 \times 10^{6}$ |
| Cu | 8,933 | 385 | 400 | $59.6 \times 10^{6}$ |
| CuO | 6,500 | 540 | 18 | $6.9 \times 10^{-2}$ |

The flow conditions that are fixed on the flexible walls are described in the following expressions:

$$\breve{u}_r = \frac{\breve{U}_c}{\breve{r}}\downarrow_{\theta=0},\ \frac{\partial \breve{u}_r}{\partial \breve{\theta}}\downarrow_{\theta=0} = 0,\ \frac{\partial \breve{T}}{\partial \breve{\theta}}\downarrow_{\theta=0} = 0\,, \tag{5}$$

$$\breve{u}_r\downarrow_{\theta=\pm\alpha} = \breve{U}_w = \frac{s}{\breve{r}},\ \breve{T}\downarrow_{\theta=\pm\alpha} = \frac{\breve{T}_w}{\breve{r}^2}. \tag{6}$$

In the constitutive relations, $\breve{U}_c$, $\breve{U}_w$, $\breve{T}_w$, and $mhnf$ stands for velocity at the central line, velocity at flexible walls, wall temperature, and modified hybrid nanofluid, respectively. The simplification of mass conservation in a cylindrical polar frame is reduced to the following version:

$$f\left(\breve{\theta}\right) = \breve{r}\breve{u}_r\,. \tag{7}$$

Furthermore, for non-dimensionalization of the model, the following similarity relations are introduced:

$$F(\eta) = \frac{f\left(\breve{\theta}\right)}{\breve{U}_c},\ \eta = \frac{\breve{\theta}}{\alpha},\ \beta = \frac{\breve{T}}{\breve{T}_w}\breve{r}^2. \tag{8}$$

In the implementation of desired partial differentiation from Eq. 8, in the constitutive model, the following dimensionless model is acquired:

$$F''' + \frac{2\alpha R_e\left[\left(1-\phi_{Al_2O_3}\right)^{\frac{25}{10}}\left(1-\phi_{CuO}\right)^{\frac{25}{10}}\left(1-\phi_{Cu}\right)^{\frac{25}{10}}\right]}{\left(\left(1-\phi_{Cu}\right)\left[\left(1-\phi_{CuO}\right)\left\{\left(1-\phi_{Al_2O_3}\right)+\phi_{Al_2O_3}\frac{\rho_{Al_2O_3}}{\rho_{water}}\right\}+\phi_{CuO}\frac{\rho_{CuO}}{\rho_{water}}\right]+\frac{\phi_{Cu}\rho_{Cu}}{\rho_{water}}\right)^{-1}}FF' + 4\alpha^2F' = 0, \tag{9}$$

$$\beta'' + 4\alpha^2\beta + \frac{\left[\left(1-\phi_{Cu}\right)\left[\left(1-\phi_{CuO}\right)\left\{\left(1-\phi_{Al_2O_3}\right)+\frac{\phi_{Al_2O_3}\left(\rho c_p\right)_{Al_2O_3}}{\left(\rho c_p\right)_{water}}\right\}+\frac{\phi_{CuO}\left(\rho c_p\right)_{CuO}}{\left(\rho c_p\right)_{water}}\right]+\frac{\rho_{Cu}\left(\rho c_p\right)_{Cu}}{\left(\rho c_p\right)_{water}}\right]}{\frac{\breve{k}_{Cu}+\left(\breve{n}-1\right)\breve{k}_{(Al_2O_3-CuO)water}-\left(\breve{n}-1\right)\phi_{Cu}\left(\breve{k}_{(Al_2O_3-CuO)water}-\breve{k}_{Cu}\right)}{\breve{k}_{Cu}+\left(\breve{n}-1\right)\breve{k}_{(Al_2O_3-CuO)water}+\phi_{Cu}\left(\breve{k}_{(Al_2O_3-CuO)water}-\breve{k}_{Cu}\right)}}\left(2Pr\alpha^2F\beta+\frac{PrEc}{R_e\left[\left(1-\phi_{Al_2O_3}\right)^{\frac{25}{10}}\left(1-\phi_{CuO}\right)^{\frac{25}{10}}\left(1-\phi_{Cu}\right)^{\frac{25}{10}}\right]}\left(4\alpha^2F^2+F'^2\right)\right) = 0. \tag{10}$$

The functions $F$ and $\beta$ in the abovementioned model depend on the variable $\eta$. Furthermore, the conditions imposed on the channel walls transformed in the following version after utilizing the similarity equations:

$$F(\eta_{=0}) = 1,\quad F'(\eta_{=0}) = 0,\quad \beta'(\eta_{=0}) = 0$$
$$F(\eta_{=1}) = S,\quad \beta(\eta_{=1}) = 1$$

The parameters involved in the model are summarized in Table 6 with mathematical expressions.

TABLE 6 Parameters ingrained in the model with expressions and physical ranges.

| Parameter | Name | Expression | Ranges |
|---|---|---|---|
| Reynolds number | $Re$ | $\frac{\breve{U}_c\alpha}{\breve{\nu}_f}$ | Within laminar regimes |
| Prandtl number | $Pr$ | $\frac{(\rho c_p)_f\breve{U}_c}{\breve{k}_{hnf}}$ | 6.2 |
| Eckert number | $Ec$ | $Ec = \frac{\breve{U}_c^2\alpha}{\breve{k}_{hnf}}$ | Within physical domain |

## Shear stresses and local energy storage

The investigation of shear stresses and local energy storage capability in $(Al_2O_3\text{-}CuO\text{-}Cu/H_2O)_{mhnf}$ under multiple flow conditions is very imperative from an industrial and engineering point of view. The quantities can be described by the following mathematical formula in the dimensional form:

$$C_F = \frac{\breve{\mu}_{(Al_2O_3-CuO-Cu)water}\left(\tau_{\breve{r}\breve{\theta}}\right)}{\breve{\rho}_{(Al_2O_3-CuO-Cu)water}}\downarrow_{\eta=1}, \tag{11}$$

$$Nu = -\frac{l\breve{k}_f\left(\breve{q}_w\right)}{k\breve{T}_w}. \tag{12}$$

By endorsing the attributes of $(Al_2O_3\text{-}CuO\text{-}Cu/H_2O)_{mhnf}$ and performing the calculation, the following version is obtained:

$$Re_rC_F = \frac{\left[\left(1-\phi_{Al_2O_3}\right)^{\frac{25}{10}}\left(1-\phi_{CuO}\right)^{\frac{25}{10}}\left(1-\phi_{Cu}\right)^{\frac{25}{10}}\right]^{-1}F'(1)}{\left[\left(1-\phi_{Cu}\right)\left[\left(1-\phi_{CuO}\right)\left\{\left(1-\phi_{Al_2O_3}\right)+\frac{\phi_{Al_2O_3}\left(\rho_{Al_2O_3}\right)}{\rho_{water}}\right\}+\frac{\phi_{CuO}\left(\rho_{CuO}\right)}{\rho_{water}}\right]+\frac{\phi_{Cu}\left(\rho_{Cu}\right)}{\rho_{water}}\right]}, \tag{13}$$

$$\alpha Nu = -\frac{\breve{k}_{Cu}+\left(\breve{n}-1\right)\breve{k}_{(Al_2O_3-CuO)water}-\left(\breve{n}-1\right)\phi_{Cu}\left(\breve{k}_{(Al_2O_3-CuO)water}-\breve{k}_{Cu}\right)}{\breve{k}_{Cu}+\left(\breve{n}-1\right)\breve{k}_{(Al_2O_3-CuO)water}+\phi_{Cu}\left(\breve{k}_{(Al_2O_3-CuO)water}-\breve{k}_{Cu}\right)}\beta'(1). \tag{14}$$

## Mathematical investigation of $[(Al_2O_3\text{-}CuO\text{-}Cu)/water]_{mhnf}$

The mathematical models appearing in the fields of medical sciences, engineering (deflection of beams, load over the bridge,

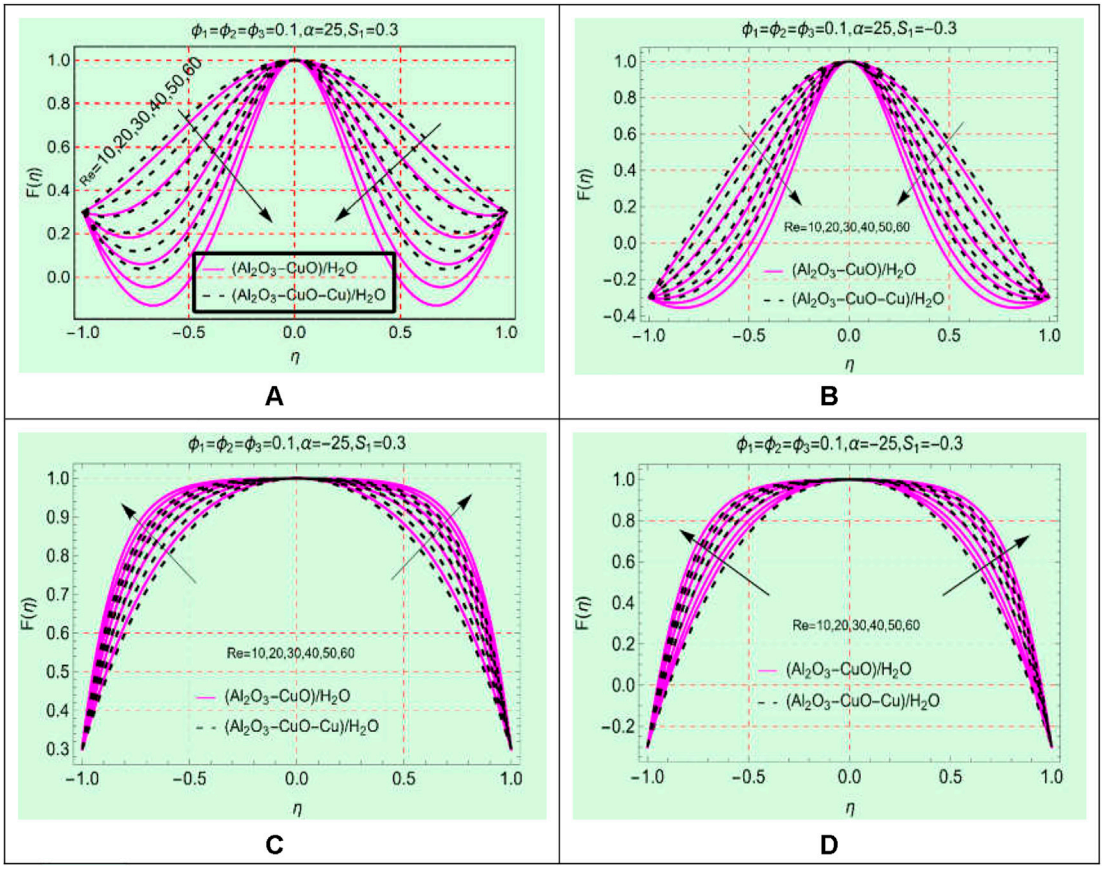


FIGURE 5
$F(\eta)$ against Re **(A)** stretching and divergent, **(B)** shrinking and divergent, **(C)** stretching and convergent, and **(D)** shrinking and convergent.

etc.), and biomedical engineering are highly nonlinear in nature. For such models, it is almost impossible to handle the model in the form of an exact solution. However, numerical techniques are best suited to solve and analyze the impacts of various parameters on the dynamics of the model.

The under consideration model is very tedious due to the induction of ternary nanoparticles and their thermophysical attributes; therefore, the numerical technique is helpful to tackle the model and explore the results by altering the flow parameters. For said purpose, we adopted a numerical technique coupled with a shooting algorithm. Primarily, the setup of this technique is based on the development of a first-order initial value problem (IVP) from the higher-order model by means of feasible transformations. After that, the model is then solved by implementing the aforementioned algorithm. The calculation in the under consideration model is very lengthy; therefore, we omit the mathematical procedure. However, the results are plotted against various ranges of the flow parameters and discussed in the next section.

## Results with discussion

### $(Al_2O_3$-CuO-Cu/water$)_{mhnf}$ flow against Re

The Reynolds number, which is a quotient of viscous and inertial forces, is a significant parameter in the study of channel flow. The influences of this parameter on the flow behavior of $(Al_2O_3$-CuO/$H_2O)_{hnf}$ and $(Al_2O_3$-CuO-Cu/$H_2O)_{mhnf}$ in stretching/shrinking and opening/narrowing channels are pictured in Figure 2. It is worthy to mention that the values of the opening/narrowing parameter $\alpha$ are taken in degree.

The analysis of Figures 5A and B ensures that the fluid motion drops in a divergent channel for both stretching and shrinking walls. It is noticeable that a backflow phenomenon occurs near the walls because by increasing the Reynolds number, the fluid reverses its motion along the wall instead of mainstream ($\eta = 0$). For smaller ranges of Re, the backflow reduces toward the mainstream flow. The maximum fluid motion occurs along the central line for both $(Al_2O_3$-CuO/$H_2O)_{hnf}$ and $(Al_2O_3$-CuO-

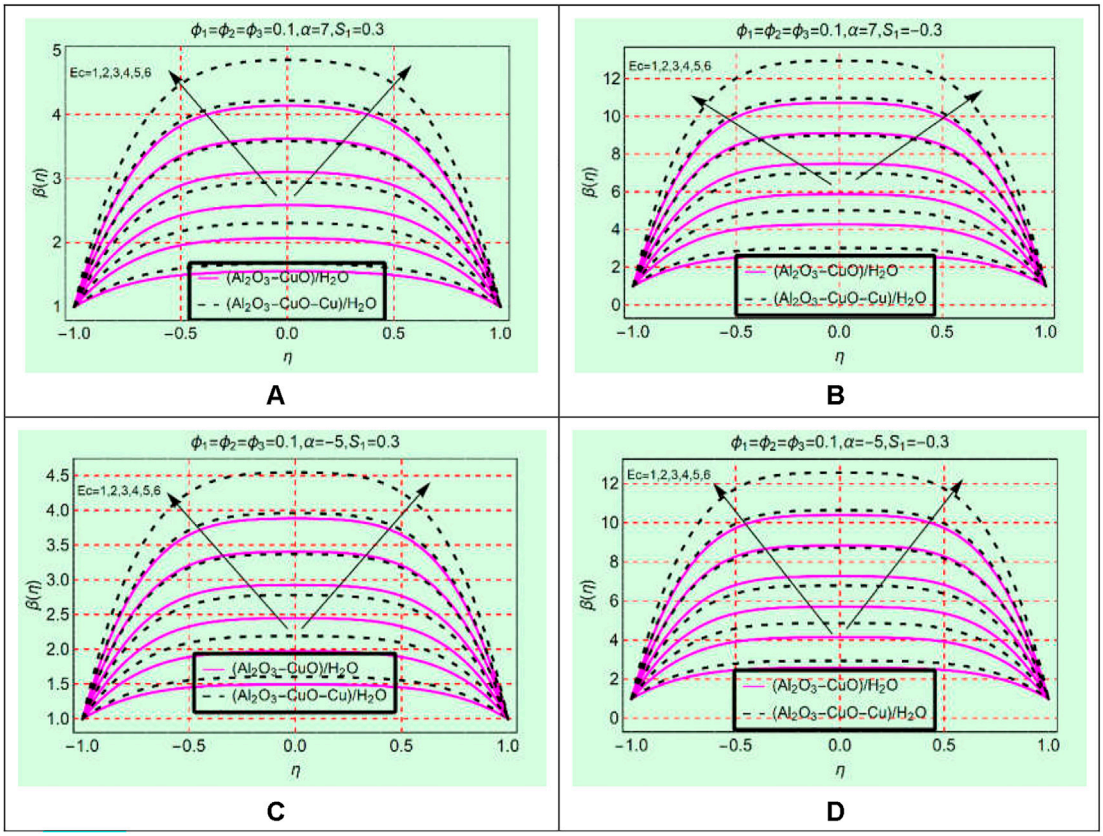


FIGURE 6
$\beta(\eta)$ against Ec **(A)** stretching and divergent, **(B)** shrinking and divergent, **(C)** stretching and convergent, and **(D)** shrinking and convergent.

$Cu/H_2O)_{mhnf}$. Furthermore, shrinking of the walls leads to reduced backflow as well.

Figures 5C and D elaborate on the behavior of $(Al_2O_3$-CuO/$H_2O)_{hnf}$ and $(Al_2O_3$-CuO-Cu/$H_2O)_{mhnf}$ in the narrowing channel. Physically, the flowing area reduces in the narrowing channel due to which force per unit area enhances which leads to an increment in the motion. The flow profile becomes more flattened at the central position due to the higher strength of Re and narrowing parameter $\alpha$. The maximum fluid motion is observed near the vicinity of the central portion, and it gradually slows down toward the channel walls.

## $(Al_2O_3$-CuO-Cu/water$)_{mhnf}$ thermal behavior against Ec

The viscous dissipation is an important physical phenomenon regarding the energy storage in $(Al_2O_3$-CuO/$H_2O)_{hnf}$ and $(Al_2O_3$-CuO-Cu/$H_2O)_{mhnf}$. The Eckert number is a parameter that appeared due to viscous dissipation. Therefore, Figures 3A–D are organized to explore the influences of Ec on the thermal behavior $\beta(\eta)$ of $(Al_2O_3$-CuO/$H_2O)_{hnf}$ and $(Al_2O_3$-CuO-Cu/$H_2O)_{mhnf}$. From the analysis of Figure 6, it is found that the temperature rises significantly in both sorts of heat transfer fluids for stretching/shrinking and opening/narrowing channels. Physically, the appearance of viscous dissipation enhances the internal energy of the liquids due to which the temperature rises significantly.

The nanofluid containing ternary nanoparticles $(Al_2O_3$-CuO-Cu/$H_2O)_{mhnf}$ has more capability to store energy than binary-based $(Al_2O_3$-CuO/$H_2O)_{hnf}$ heat transfer fluids. Physically, the thermal conductivity of $(Al_2O_3$-CuO-Cu/$H_2O)_{mhnf}$ becomes greater than $(Al_2O_3$-CuO/$H_2O)_{hnf}$ which increases its energy storage ability. The maximum increasing behavior of binary- and ternary-based nanomaterial liquids is observed along the central line.

## $(Al_2O_3$-CuO-Cu/water$)_{mhnf}$ thermal behavior against Re

The set of Figures 7A–D elaborates the thermal behavior of $(Al_2O_3$-CuO/$H_2O)_{hnf}$ and $(Al_2O_3$-CuO-Cu/$H_2O)_{mhnf}$

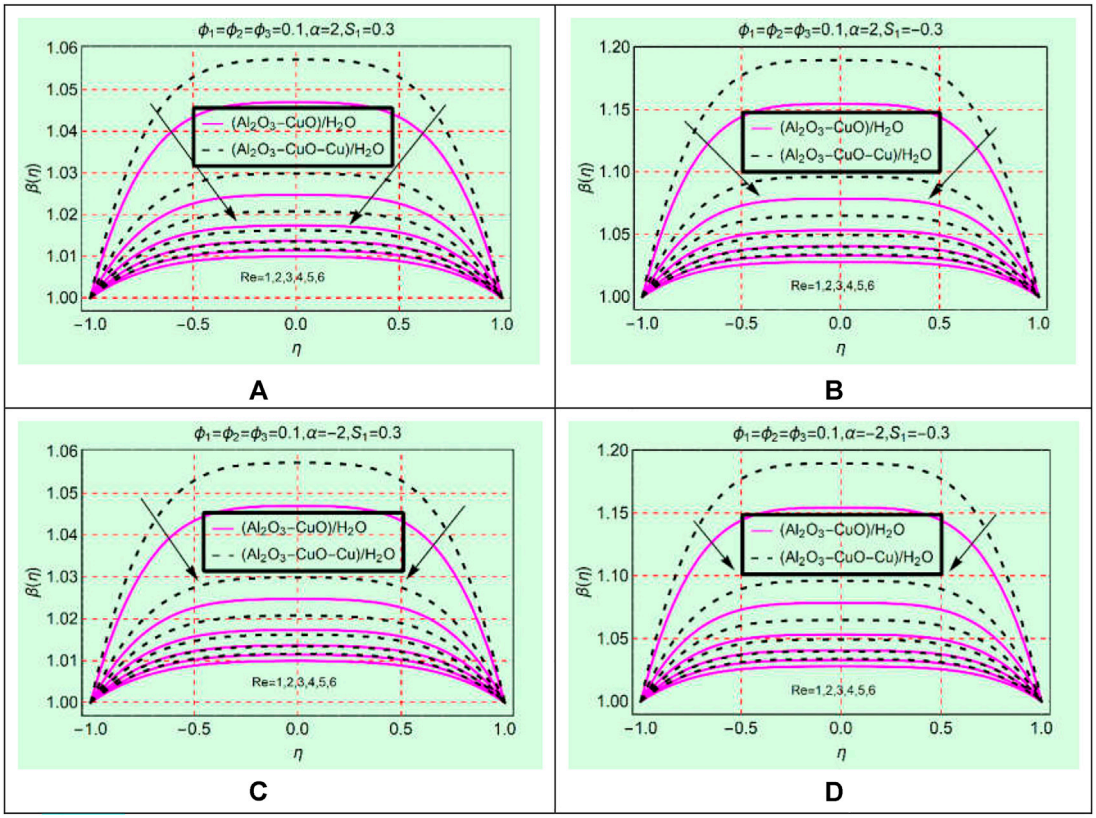


FIGURE 7
$\beta(\eta)$ against Re **(A)** stretching and divergent, **(B)** shrinking and divergent, **(C)** stretching and convergent, and **(D)** shrinking and convergent.

against Re. The keen study of Figure 7 reveals that the fluid temperature declines by strengthening Re within the physical domain. The temperature in $(Al_2O_3\text{-}CuO/H_2O)_{hnf}$ reduces more abruptly than in $(Al_2O_3\text{-}CuO\text{-}Cu/H_2O)_{mhnf}$ for both stretching/shrinking and opening/narrowing walls. Physically, $(Al_2O_3\text{-}CuO\text{-}Cu/H_2O)_{mhnf}$ has high thermal conductivity due to the addition of the third additive Cu due to which its energy storage ability becomes maximum than $(Al_2O_3\text{-}CuO/H_2O)_{hnf}$. All these effects are elaborated in Figures 7A–D in both opening and narrowing channels.

## Local energy storage in $(Al_2O_3\text{-}CuO/water)_{hnf}$ and $(Al_2O_3\text{-}CuO\text{-}Cu/water)_{mhnf}$

This subsection is devoted to analyzing the local energy storage in $(Al_2O_3\text{-}CuO/H_2O)_{hnf}$ and $(Al_2O_3\text{-}CuO\text{-}Cu/H_2O)_{mhnf}$ for varying flow parameters such as Ec, Re, and $\alpha$. For said purpose, Figures 8 and 9 displayed over the region of interest.

From Figures 8A–D, it is evident that the local energy storage in $(Al_2O_3\text{-}CuO\text{-}Cu/H_2O)_{mhnf}$ is higher than that in $(Al_2O_3\text{-}CuO/H_2O)_{hnf}$. Physically, the ternary mixture of $Al_2O_3$, CuO, and Cu increases the thermal conductivity of $(Al_2O_3\text{-}CuO\text{-}Cu/H_2O)_{mhnf}$, while $(Al_2O_3\text{-}CuO/H_2O)_{hnf}$ has low thermal conductivity due to the binary mixture of $Al_2O_3$ and CuO. Due to the high thermal conductance of $(Al_2O_3\text{-}CuO\text{-}Cu/H_2O)_{mhnf}$, the temperature increases rapidly. Moreover, imposed viscous dissipation effects provide extra energy to the fluid, which ultimately boosts the energy ability of $(Al_2O_3\text{-}CuO\text{-}Cu/H_2O)_{mhnf}$ than $(Al_2O_3\text{-}CuO/H_2O)_{hnf}$. Similarly, from Figure 9, it can be seen that drops in the local energy storage in $(Al_2O_3\text{-}CuO\text{-}Cu/H_2O)_{mhnf}$ is slower than $(Al_2O_3\text{-}CuO/H_2O)_{hnf}$. Therefore, modified hybrid nanofluids will be very effective for industrial and engineering applications because of their high energy storage capability.

The streamlines pattern due to $\alpha$ is furnished in Figure 10. It is noted that the streamlines pattern becomes more parabolic shapes for smaller values of $\alpha$, while it becomes flattened by increasing the value of $\alpha$.

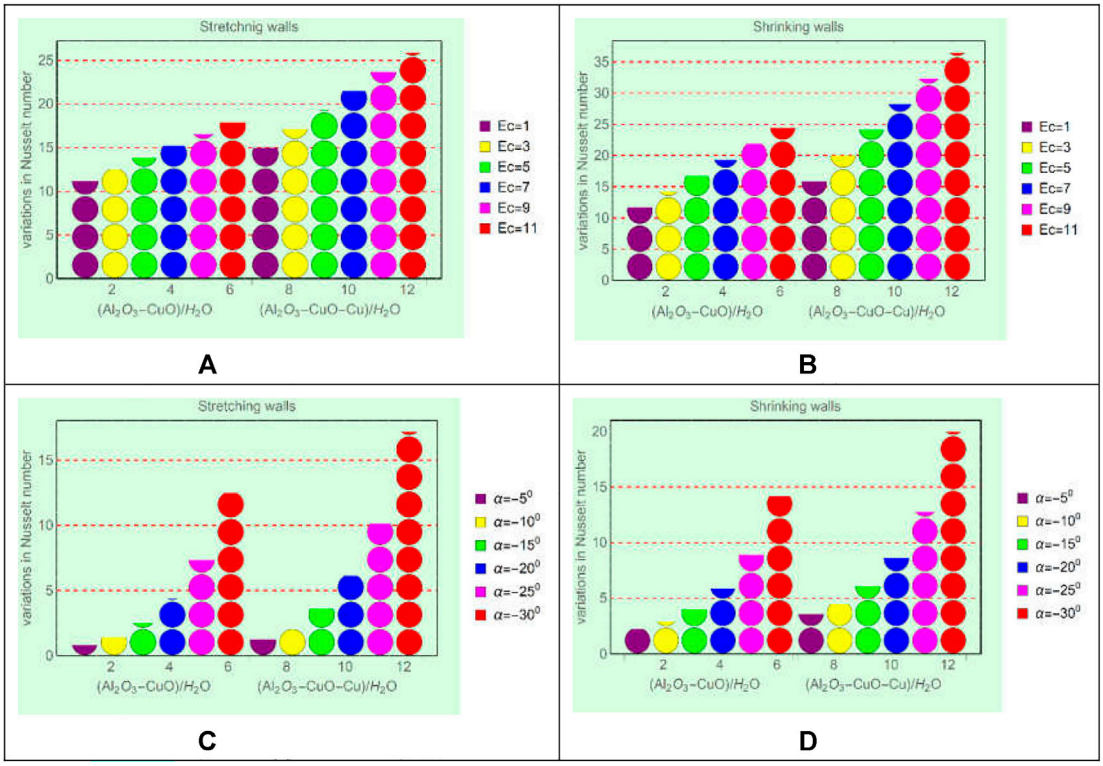


FIGURE 8
Local energy storage against **(A)** stretching and Ec, **(B)** shrinking and Ec, **(C)** stretching and $\alpha$, and **(D)** shrinking and $\alpha$.

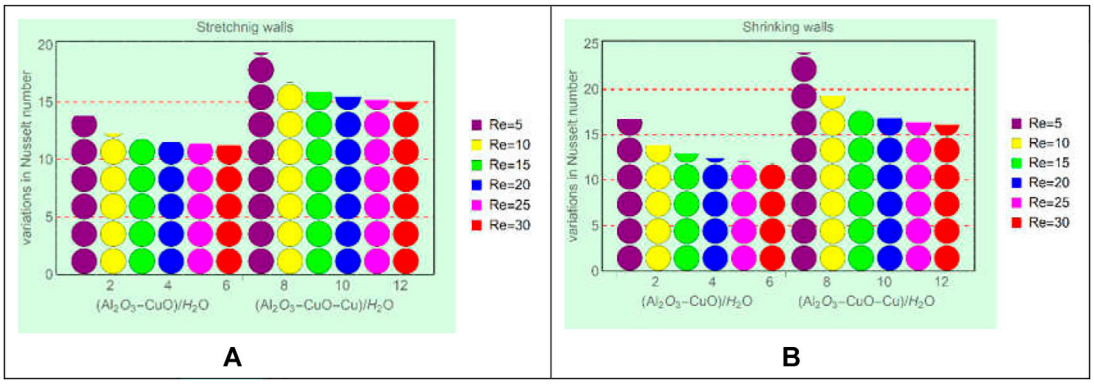


FIGURE 9
Local energy storage against **(A)** stretching and Re and **(B)** shrinking and Re.

## Concluding remarks

The study of $(Al_2O_3\text{-}CuO/H_2O)_{hnf}$ and $(Al_2O_3\text{-}CuO\text{-}Cu/H_2O)_{mhnf}$ heat transfer fluids is organized between opening/narrowing channels. The channel walls are allowed to stretch/shrink to some physical extent. The model is developed *via* similarity and NS equations and then solved numerically. The results against the parameters that appeared due to physical phenomena are furnished and discussed deeply in the view of physics behind them. It is found that

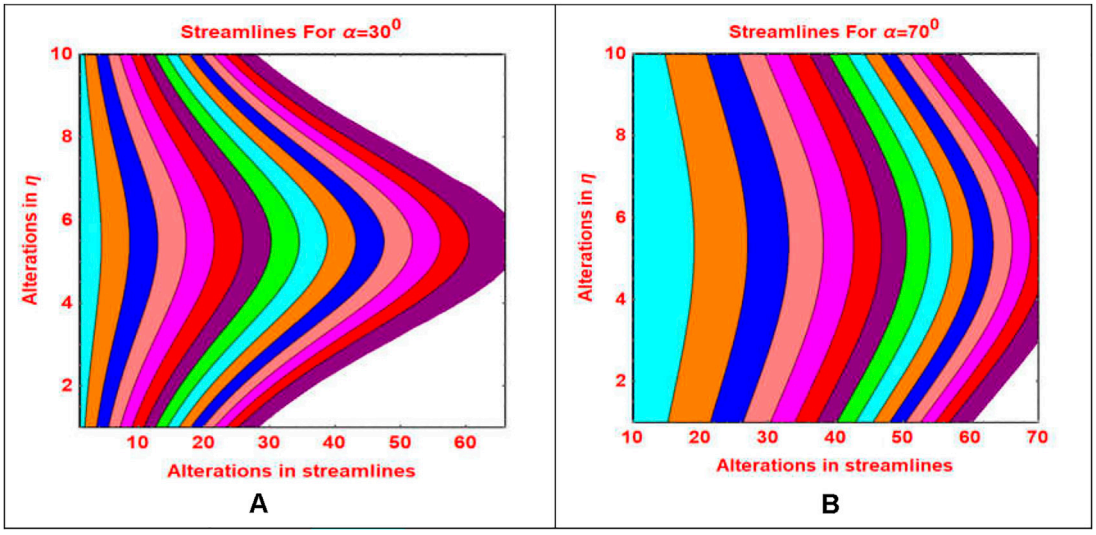


FIGURE 10
Streamlines pattern for different α values **(A)** α = 30° and **(B)** α = 70°.

- High Reynolds number causes backflow phenomena in the locality of channel walls, and maximum fluid motion is pointed out along the central line.
- The energy storage improved by strengthening viscous dissipation effects and reduces for multiple Re in the model.
- Ternary hybrid nanofluid $(Al_2O_3\text{-}CuO\text{-}Cu/H_2O)_{mhnf}$ has outstanding heat transport than conventional hybrid due to the addition of the third particle's volume concentration ($\phi_3$%).
- The optimum thermal behavior in both hybrid and ternary hybrid nanofluids is noticed for shrinking walls, and $(Al_2O_3\text{-}CuO\text{-}Cu/H_2O)_{mhnf}$ is dominant over $(Al_2O_3\text{-}CuO/H_2O)_{hnf}$.
- The local Nusselt number is very high for ternary hybrid nanofluid at various locations inside the channel, and ultra-high thermal conductivity of trihybrid nanoparticles is a key element for this situation.

The presented study revealed that ternary hybrid nanofluid $(Al_2O_3\text{-}CuO\text{-}Cu/H_2O)_{mhnf}$ has a high temperature featuring an under dissipation function and Reynolds number. Therefore, this class would play a vital role rather than normal hybrid and mono nanofluids in various industries to accomplish the products.

## Data availability statement

The raw data supporting the conclusion of this article will be made available by the authors, without undue reservation.

## Author contributions

A and WA formulated the model. A and UK solved the model and plotted the results. A and WA wrote the original draft. KG, ZR, ETE, and AG significantly contributed in revision process.

## Acknowledgments

The authors would like to thank the Deanship of Scientific Research at Umm Al-Qura University for supporting this work by Grant Code: 22UQU4331317DSR46. The author (ZR) extends her appreciation to the Deanship of Scientific Research at King Khalid University, Abha, Saudi Arabia, for funding this work through the Research Group Project Number (RGP.2/334/43).

## Conflict of interest

The authors declare that the research was conducted in the absence of any commercial or financial relationships that could be construed as a potential conflict of interest.

## Publisher's note

All claims expressed in this article are solely those of the authors and do not necessarily represent those of their

affiliated organizations, or those of the publisher, the editors, and the reviewers. Any product that may be evaluated in this article, or claim that may be made by its manufacturer, is not guaranteed or endorsed by the publisher.

## References


Abbasi, A., Al-Khaled, K., Khan, M. I., Khan, S. U., El-Refaey, A. M., Farooq, W., et al. (2021). Optimized analysis and enhanced thermal efficiency of modified hybrid nanofluid ($Al_2O_3$, CuO, Cu) with nonlinear thermal radiation and shape features. *Case Stud. Therm. Eng.* 28, 101425. doi:10.1016/j.csite.2021.101425

Ahmed, N., Adnan, Khan, U., Mohyud-Din, S. T., and Manzoor, R. (2017). Influence of viscous dissipation on a copper oxide nanofluid in an oblique channel: Implementation of the KKL model. *Eur. Phys. J. Plus* 132, 237. doi:10.1140/epjp/i2017-11504-y

Ahmed, N., Adnan, Mohyud-Din, S. T., Khan, U., Nisar, K. S., Baleanu, D., Khan, I., et al. (2020). A novel hybrid model for Cu–$Al_2O_3$/$H_2O$ nanofluid flow and heat transfer in convergent/divergent channels. *Energies* 13, 1686. doi:10.3390/en13071686

Ahmed, N., Mohyud-Din, S. T., Baleanu, D., Nisar, K. S., Khan, I., Sooppy Nisar, K., et al. (2021). Second law analysis of magneto radiative GO-$MoS_2$/$H_2O$–$(CH_2OH)_2$ hybrid nanofluid. *Comput. Mater. Continua* 68 (1), 213–228. doi:10.32604/cmc.2021.014383

Akinshilo, A. T., Ilegbusi, A., Ali, H. M., and Surajo, A. J. (2020). Heat transfer analysis of nanofluid flow with porous medium through Jeffery Hamel diverging/converging channel. *J. Appl. Comput. Mech.* 6 (3), 433–444. doi:10.22055/JACM.2019.29467.1601

Choi, S. U. S. (1995). Enhancing thermal conductivity of fluids with nanoparticles. *ASME* 66, 99–105.

Hamel, G. (1916). Spiralformige bewgungen zaher flussigkeiten. *Jahresber. Dtsch. mathematiker-vereinigung* 25, 34–60.

Jeffery, G. B. (1915). L. *The two-dimensional steady motion of a viscous fluid. Lond. Edinb. Dublin Philosophical Mag. J. Sci.* 629 (172), 455–465. doi:10.1080/14786440408635327

Khan, S. I., Khan, U., Ahmed, N., Mohyud-Din, S. T., Nisar, K. S., et al. (2021). Thermal transport investigation in AA7072 and AA7075 aluminum alloys nanomaterials based radiative nanofluids by considering the multiple physical flow conditions. *Sci. Rep.* 11, 9837. doi:10.1038/s41598-021-87900-w

Kumar, B., Seth, G. S., Singh, M. K., and Chamkha, A. J. (2021). Carbon nanotubes (CNTs)-based flow between two spinning discs with porous medium, Cattaneo–Christov (non-Fourier) model and convective thermal condition. *J. Therm. Anal. Calorim.* 146, 241–252. doi:10.1007/s10973-020-09952-w

Kumar, T. S. (2021). Hybrid nanofluid slip flow and heat transfer over a stretching surface. *Partial Differ. Equations Appl. Math.* 4, 100070. doi:10.1016/j.padiff.2021.100070

Kumbinarasaiah, S., and Raghunatha, K. R. (2022). Numerical solution of the Jeffery–Hamel flow through the wavelet technique. *Heat. Trans.* 51, 1568–1584. doi:10.1002/htj.22364

Mohyud-Din, S. T., Ahmed, N., Khan, U., Khan, I., Abdeljawad, T., Nisar, K. S., et al. (2020). Thermal transport investigation in magneto-radiative GO-$MoS_2$/$H_2O$-$C_2H_6O_2$ hybrid nanofluid subject to cattaneo–christov model. *Molecules* 25, 2592. doi:10.3390/molecules25112592

Patel, H. S., and Meher, R. (2018). Analytical investigation of jeffery–hamel flow by modified adomian decomposition method. *Ain Shams Eng. J.* 9 (4), 599–606. doi:10.1016/j.asej.2016.02.007

Rout, H., Mohapatra, S. S., Shaw, S., Muhammad, T., Nayak, M. K., and Makinde, O. D. (2021). Entropy optimization for Darcy–Forchheimer electro-magneto-hydrodynamic slip flow of ferronanofluid due to stretching/shrinking rotating disk. *Waves Random Complex Media*. doi:10.1080/17455030.2021.1927238

Saeed, A., Jawad, M., Alghamdi, W., Nasir, S., Gul, T., and Kumam, P. (2021). Hybrid nanofluid flow through a spinning Darcy–Forchheimer porous space with thermal radiation. *Sci. Rep.* 11, 16708. doi:10.1038/s41598-021-95989-2

Shanmugapriya, M., Sundareswaran, R., and Kumar, P. S. (2021). Heat and mass transfer enhancement of MHD hybrid nanofluid flow in the presence of activation energy. *Int. J. Chem. Eng.*, 2021, 9473226. doi:10.1155/2021/9473226

Sushila, S. J., and Shishodia, Y. S. (2014). A modified analytical technique for Jeffery–Hamel flow using sumudu transform. *J. Assoc. Arab Univ. Basic Appl. Sci.* 16, 11–15. doi:10.1016/j.jaubas.2013.10.001

Turkyilmazoglu, M. (2014). Nanofluid flow and heat transfer due to a rotating disk. *Comput. Fluids* 94, 139–146. doi:10.1016/j.compfluid.2014.02.009

Zangooee, M. R., Hosseinzadeh, K. H., and Ganji, D. D. (2019). Hydrothermal analysis of MHD nanofluid ($TiO_2$-GO) flow between two radiative stretchable rotating disks using AGM. *Case Stud. Therm. Eng.* 14, 100460. doi:10.1016/j.csite.2019.100460

frontiers | Frontiers in Chemistry

TYPE Original Research
PUBLISHED 02 November 2022
DOI 10.3389/fchem.2022.1061129



OPEN ACCESS

EDITED BY
Jinlin Lu,
Guangzhou Maritime College, China

REVIEWED BY
Yang Li,
Wuhan University of Science and Technology, China
Peng Li,
Soochow University, China

*CORRESPONDENCE
Hui Lu,
luhui@nmu.edu.cn
Shaolin Yang,
slyang@nun.edu.cn

†These authors have contributed equally to this work and share first authorship

SPECIALTY SECTION
This article was submitted to Nanoscience, a section of the journal Frontiers in Chemistry

RECEIVED 04 October 2022
ACCEPTED 24 October 2022
PUBLISHED 02 November 2022

CITATION
Lu H, Sha S, Li T, Wen Q, Yang S, Wu J, Wang K, Sheng Z and Ma J (2022), One-step electrodeposition of ZnO/graphene composites with enhanced capability for photocatalytic degradation of organic dyes. *Front. Chem.* 10:1061129. doi: 10.3389/fchem.2022.1061129



# One-step electrodeposition of ZnO/graphene composites with enhanced capability for photocatalytic degradation of organic dyes

Hui Lu[1,2†*], Simiao Sha[1†], Tong Li[1], Qian Wen[1], Shaolin Yang[1*], Jiandong Wu[1,2], Kang Wang[1], Zhilin Sheng[1] and Jinfu Ma[1]

[1]School of Materials Science and Engineering, North Minzu University, Yinchuan, China, [2]Yinchuan Aini Industrial Technology Development Co., Ltd, Yinchuan, China

Zinc oxide is a popular semiconductor used in catalysts due to its wide bandgap and high exciton binding energy. However, the photocatalytic performance of ZnO was compromised by its insufficient electron-hole separation efficiency and electron transfer rate. Herein, ZnO-reduced graphene oxide (rGO) composite solid catalyst was synthesized by one-step electrodeposition method on FTO substrate using lithium perchlorate ($LiClO_4$) as the supporting electrolyte. Scanning electron microscopy, Raman, Fourier Transform Infrared, and XRD characterizations confirmed the deposition of ZnO and the reduction of graphene oxide Owing to the cooperative effect between rGO and ZnO, the as-prepared ZnO-rGO composites show much enhanced photocatalytic degradation ability compared with pure ZnO nanorods. By optimizing the conditions of electrodeposition of ZnO-rGO composites, the degradation rate of methylene blue can reach 99.1% within 120 min. Thus, the simple preparation and the excellent performance could endow the ZnO-rGO composites with promising application in practical dye-polluted water treatment.

KEYWORDS

**ZnO, graphene oxide, electrodeposition, electrolyte, solid catalyst**

## Introduction

The growing water contamination has become a serious problem with the development of industrialization and urbanization (Liras et al., 2019; Abdel-Karim et al., 2021). As a kind of staining materials, dyes are widely used in pollution-intensive industries such as textile, rubber, papermaking, plastics, and printing (Mansor et al., 2020; Nasir et al., 2021). Untreated dye-containing industrial wastewater produces severe pollution and threatens the ecological environment and human health. In addition, the organic dye pollutants in the wastewater are hard to be decomposed naturally. Among various dye-removal techniques, the degradation of

organic dyes using highly efficient photocatalysts has become the most promising due to its high efficiency, fast reaction, and easy operation (Garg et al., 2020).

Until now, many low-priced, high-performance, and consistent photocatalysts have been produced and used in wastewater treatment, such as, metal oxides ($TiO_2$ and ZnO) (Roshni and Thambidurai, 2022; Umadevi et al., 2022), sulfides (Luan et al., 2020; Ren et al., 2021), and nitrogen oxides (Niu et al., 2012). Among them, ZnO, an n-type semiconductor material of the group II-VI has been widely used in recent years because of its wider bandgap and higher exciton binding energy (Dehghan Nayeri et al., 2013). However, the deficiencies of ZnO including high resistivity, and easy recombination of photogenerated electron-hole pairs seriously hinders the improvement of its photochemical catalysis performance (Anandan et al., 2010). To overcome these shortcomings and improve the photochemical catalysis performance, the ZnO composite materials have been widely investigated (Lonkar et al., 2018). As a two-dimensional carbon nanomaterial with zero bandgap, graphene has the advantages of high electron mobility and excellent conductivity at room temperature, making it a candidate for enhancing the performance of various catalysts (Imran et al., 2021; Kharatzadeh et al., 2021; Moradi et al., 2021). For these reasons, ZnO-rGO composite photocatalysts with better optical and electrical properties were synthesized. The addition of rGO can promote the separation of electron-hole pairs and reduce the recombination rate, and increase the light absorption capacity (Abdelsamad et al., 2018). Therefore, the ZnO-rGO composite can obtain better photocatalytic degradation performance than ZnO. Until now, various techniques for synthesizing ZnO-rGO composites have been exploited. For instance, Azaranga et al. fabricated nanocomposites of ZnO NPs and rGO by sol-gel method, and the ZnO-rGO nanocomposites achieved a degradation efficiency of about 92.5% for methylene blue (MB) within 120 min (Azarang et al., 2015). Tuan et al. prepared ZnO/rGO nanocomposites by hydrothermal method, which can only degrade 60% MB in 60 min (Van Tuan et al., 2020). However, most methods suffer from complex preparation process, high temperature and pressure conditions, difficult recycling and other problems, which limits their practical application.

In this paper, we developed a simple, low-cost, controllable method to synthesize ZnO-rGO composite by one-step electrochemical deposition using GO, zinc nitrate ($Zn(NO_3)_2$) and lithium perchlorate ($LiClO_4$) solution as electrolyte. The use of $LiClO_4$ as supporting electrolyte is conducive to the growth of ZnO and the uniform coverage of rGO nanosheets onto the surface of ZnO nanorods. Since the deposition of ZnO and the reduction of GO were carried out concurrently, the removal of GO with toxic reductants was avoided. Due to the combined effect between rGO and ZnO, the photochemical catalytic activity of ZnO-rGO composites was significantly improved compared with that of pure ZnO nanorods. After optimizing the GO concentration in electrolyte, the photocatalytic degradation rate of MB by ZnO-rGO composites reached 99.1% within 120 min.

# Experimental

## Materials

FTO coated glass (13 ± 1.5 ohm) was purchased from Dalian Qiseguang Solar Technology Development Co., Ltd. Zinc nitrate ($Zn(NO_3)_2$, AR), potassium chloride (KCl, AR) and lithium perchlorate ($LiClO_4$, AR) were purchased from Shanghai Aladdin Biochemical Technology Co., Ltd. The graphene oxide (GO) aqueous solution was provided by Suzhou Carbon Fung Technology Co., Ltd.

## Electrodeposition of ZnO-rGO composite materials

All electrodeposition processes were implemented on a CHI660E electrochemical workstation (Chenhua Instruments, China) using three-electrode system comprised of FTO, Pt wire, and Ag/AgCl as the working electrode, counter electrode, and reference electrode, respectively. The FTO conductive glasses were cleaned with ultrasonic oscillation with the glass cleaning agent, deionized water, and ethanol for 30 min successively. ZnO and ZnO-rGO films were electrochemical deposited on FTO substrates by potentiostatic method at 80 °C with electrodeposition potentials and time of −1.1 V and 600 s, respectively. The electrolyte for ZnO nanomaterials was 10 mM $Zn(NO_3)_2$ and 0.1 M $LiClO_4$ aqueous solution, whereas the ZnO-rGO was deposited with an electrolyte containing 10 mM $Zn(NO_3)_2$, 0.1 M $LiClO_4$, and 5 mg $L^{-1}$ GO. For comparison, ZnO-rGO composite prepared without $LiClO_4$ as supporting electrolytes was named as ZnO-rGO-N. To study the effect of GO concentration on the photochemical degradation of the synthesized ZnO-rGO, the ZnO-rGO composites were prepared with GO concentration of 2, 5, and 8 mg $L^{-1}$, which were named ZnO-2rGO, ZnO-5rGO, and ZnO-8rGO, respectively.

## Characterization

Scanning electron microscopy (SEM) and energy dispersion spectroscopy (EDS) mapping were carried out on a Zeiss Sigma 600 field emission scanning electron microscope. X-ray diffraction (XRD) test was conducted on a Rigaku Dmax-

2500. X-ray photoelectron spectroscopy (XPS) was performed on an ESCALAB Xi + X-ray photoelectron spectrometer. The ultraviolet-visible spectra were measured by using an ultraviolet-visible (UV-vis) spectrophotometer (Beijing Puxi TU-1901). Raman spectra were measured by HORIBA LabRAM micro-Raman microscope irradiated with a 514 nm laser. Fourier Transform Infrared (FTIR) spectra were recorded by Thermo Scientific Nicolet iS5 FTIR Spectrometer.

## Photocatalytic tests

Organic dyes including MB, Rhodamine B (RhB), and Methylene orange (MO) were used as organic pollutants to measure photocatalytic activity, respectively. Three pieces of FTO (1.5 cm × 1.5 cm) coated with ZnO or ZnO-rGO composite materials were immersed into 30 ml organic dyestuff solution with a concentration of 10 mg $L^{-1}$. To achieve the balance of adsorption/desorption, the solution was placed in the dark for 30 min before measurement. Afterwards, the dyestuff solution was irradiated with a mercury lamp (300 W) from a distance of 10 cm for photodegradation. 3 ml of the dye solution was taken to test its absorbance with an UV-vis spectrophotometer every 20 min and returned to the solution after the test. The degradation efficiency was calculated according to the variation of the maximum characteristic absorption peaks. Transient photocurrent tests were performed in a KCl electrolyte with a bias voltage of 0.5 V and 0.1 mol $L^{-1}$1 mmol $L^{-1}$ of BQ, 10 mmol $L^{-1}$ of IPA and 10 mmol $L^{-1}$ of EDTA-2Na were used as trapping agents for $O_2^-$, ·OH and $h^+$, respectively, and the reaction mechanism was tested according to the steps of photocatalytic degradation to analyze the reaction mechanism.

# Results and discussion

In the process of preparing ZnO-rGO composite materials by one-step electrochemical deposition, the choice of supporting electrolytes determines the quality of the deposited film, which is the key to the photocatalytic performance. Figure 1 shows the Chronoamperometry (CA) curves for electrochemical deposition of ZnO and ZnO-rGO nanocomposites using potentiostatic method. These curves have a similar trend: The rapid decrease of current at the initial deposition ascribed to the rapid adsorption of the charge in the electrolyte on the electrode surface, then the increase of current corresponds to the nucleation process, and the subsequent current stabilization stage is the growth of crystal nuclei. The cathode current for depositing ZnO stabilized at -1.4 mA $cm^{-2}$, whereas the stabilized current

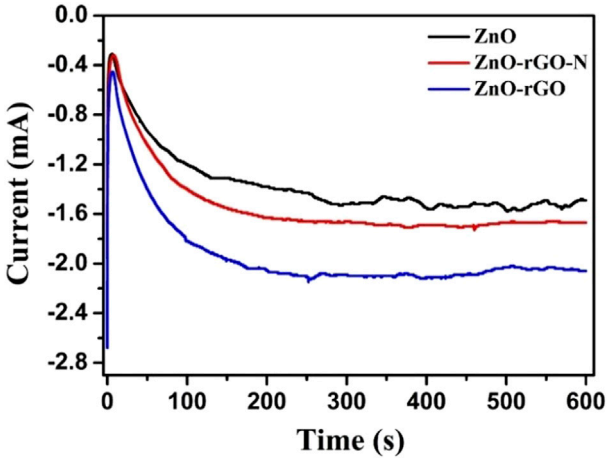


FIGURE 1
CA curves for the electrodeposition of ZnO, ZnO-rGO-N, and ZnO-rGO at a potential of -1.1 V.

was increased to −2.1 mA $cm^{-2}$ with the addition of GO to the electrolyte for preparing ZnO-rGO composite, suggesting that GO promoted the growth rate. It is well-known that GO can be reduced under negative potential (Yang et al., 2014). Thus, the deoxidation of GO and the electrodeposition of ZnO should proceed concurrently. As a comparison, the deposition without adding $LiClO_4$ as the supporting electrolyte, the current was steadied at −1.7 mA $cm^{-2}$. This result suggests that the supporting electrolyte will increase the conductivity of the electrolyte, which is beneficial to the growth of the ZnO-rGO composite.

Figure 2 displays the SEM micrographs of the ZnO, ZnO-rGO-N, and ZnO-rGO deposited on FTO substrates. As seen from Figure 2A, the pure ZnO has a uniform and dense hexagonal rod structure and completely covers the conductive substrate. As for ZnO-rGO-N deposited without supporting electrolyte, the morphology of the electrodeposited ZnO changed to a pencil shape with a larger size (Figure 2B), corresponding to a smaller specific surface area. In addition, rGO sheets were coated on ZnO nanorods due to the addition of GO. With the addition of $LiClO_4$ as a supporting electrolyte, the diameter of ZnO nanorods in the ZnO-rGO composite material becomes smaller in diameter but larger in density (Figure 2C), leading to much larger surface area. The elemental mapping of ZnO-rGO displayed in Figure 2D proves the uniform distribution of C and O on the top of ZnO-rGO, suggesting the uniform coverage of rGO nanosheets on the top of ZnO nanorods.

Figure 3 shows the XRD patterns of ZnO and ZnO-rGO. In the pattern of ZnO, the high crystallinity ZnO with hexagonal wurtzite phase (JCPDS 361–451) was confirmed by the 31.78°, 34.4°, and 36.2° characteristic peaks except the peaks of FTO

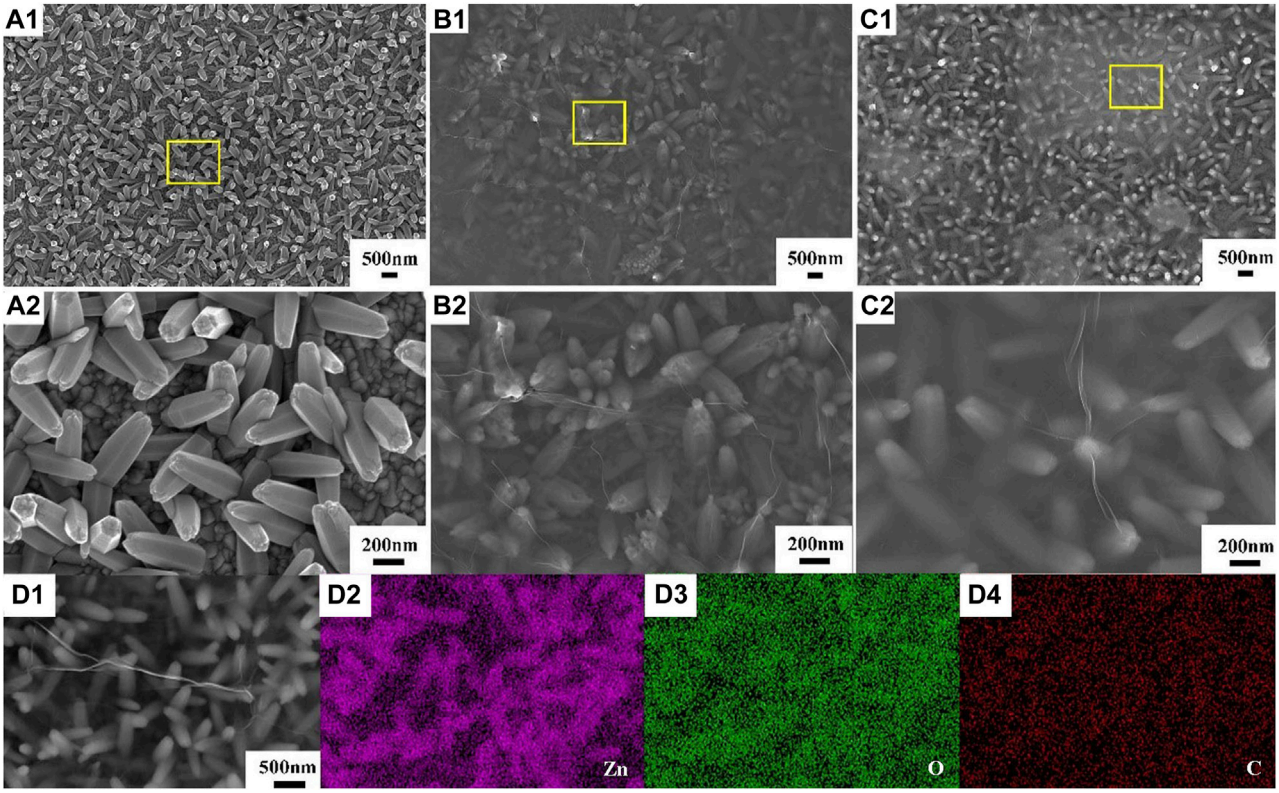


FIGURE 2
SEM micrographs of ZnO **(A)**, ZnO-rGO-N **(B)**, and ZnO-rGO **(C)** deposited on the FTO substrates, EDS elemental mapping of ZnO-rGO composite **(D)**.

corresponding to the planes (100) (002) and (101) respectively. As for ZnO-rGO, the intensities of ZnO peaks decrease due to the coverage of rGO nanosheets. However, the diffraction peaks of rGO cannot be observed, which is probably because that the rGO nanosheets is too thin to be detected by XRD signal.

Figure 3B shows the XPS survey scan spectra of ZnO and ZnO-rGO composite material. The wide range analysis pattern of ZnO-rGO consist of C1s, O1s, and Zn2p. The XPS Zn2p spectra of the ZnO and ZnO-rGO are presented in Figure 3C. The binding energy positions of 1045.1 and 1021.9 eV accord with the two atomic states of Zn2p 1/2 and Zn2p 3/2, confirming the +2 oxidation states of Zn atoms. The binding energy of the two Zn2p peaks shifted slightly, which is due to the hybridization with GO, resulting in the change of the electronic band structure of ZnO. In Figure 3D the C1s scan spectrum of Zn-rGO can be deconvoluted into three peaks centered at the binding energies of 284.3, 286.4 and 288.8 eV, which can be assigned to the carbon atoms of C–C, C–O, and C=O bonds of rGO respectively. Compared with the spectrum of GO Supplementary Figure S1, the intensity of C-O and C=O peaks reduced, indicating that most oxygen-containing groups were removed upon reduction.

The Raman spectra of GO, ZnO and ZnO-rGO composite are shown in Figure 3E. In the spectrum of ZnO-rGO two typical bands corresponding to wurtzite-type ZnO were observed, in consistence with the spectrum of ZnO. The non-polar optical phonon $E_{2H}$ mode can be revealed by a band at 440 $cm^{-1}$, and the band at 580 $cm^{-1}$ is ascribed to the existence of oxygen vacancies, zinc interstitials and defect complexes (Chaudhary et al., 2018; Erdogan et al., 2021). In the higher wavenumber range, the G (1591 $cm^{-1}$) and D peaks (1340 $cm^{-1}$) respectively corresponding to graphitic domains and lattice defects of rGO can be observed (Agarwal and Zetterlund, 2020). Compared with GO, the D to G band intensity ratio of ZnO-rGO increases, suggesting the decrease of average size of the $sp^2$ carbon domains caused by the generation of more vacant lattice sites through the removal of carbon atom accompanied with the oxygenated groups removal.

Figure 3F shows the FTIR spectra of GO, ZnO, and ZnO-rGO composite materials. The wide and high-strength band at 3400 $cm^{-1}$ is attributed to the O-H stretching vibration of water molecules adsorbed on the sample. The peak at 1630 $cm^{-1}$ is ascribed to the C-C/C=C stretching of $sp^2$ carbon domains. The band near 500 $cm^{-1}$ is originated from the vibration absorption

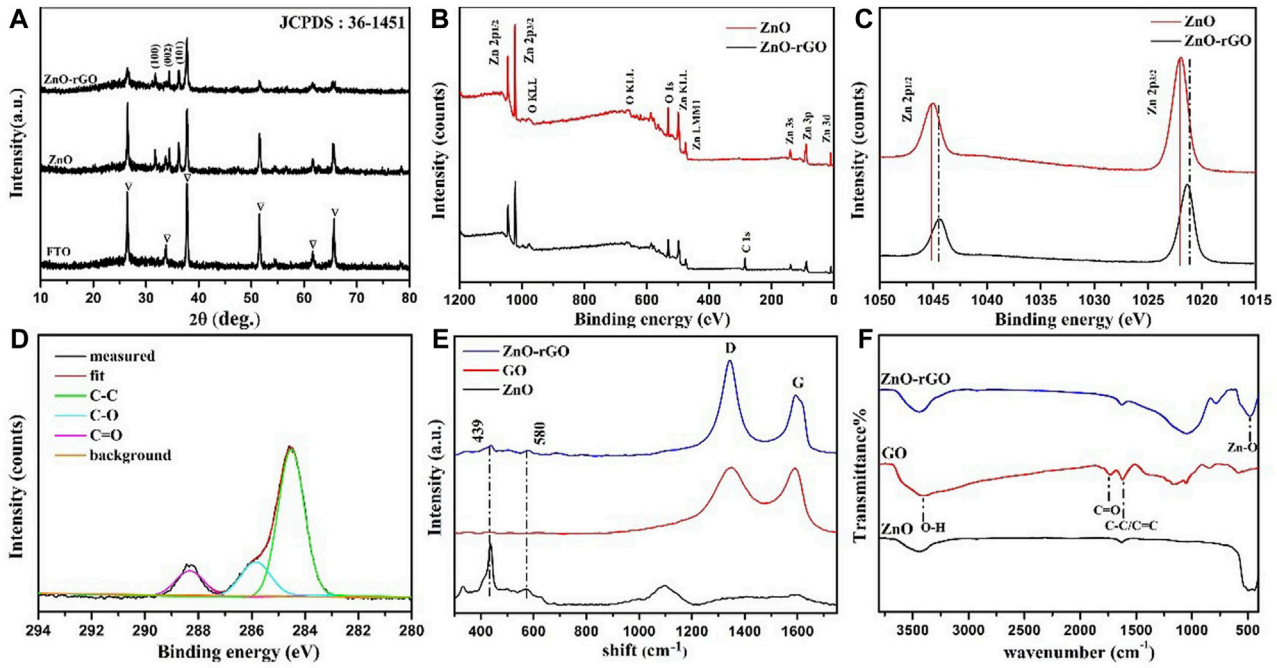


FIGURE 3
XRD patterns of ZnO and ZnO-rGO **(A)**; XPS survey spectra of ZnO and ZnO-rGO photoanodes **(B)**, Zn2p high-resolution spectra of ZnO and ZnO-rGO **(C)**, C1s scan spectrum of ZnO-rGO photoanode **(D)**; Raman spectra of ZnO-rGO and GO composite materials **(E)** and FTIR spectra of GO, ZnO and ZnO-rGO composites **(F)**.

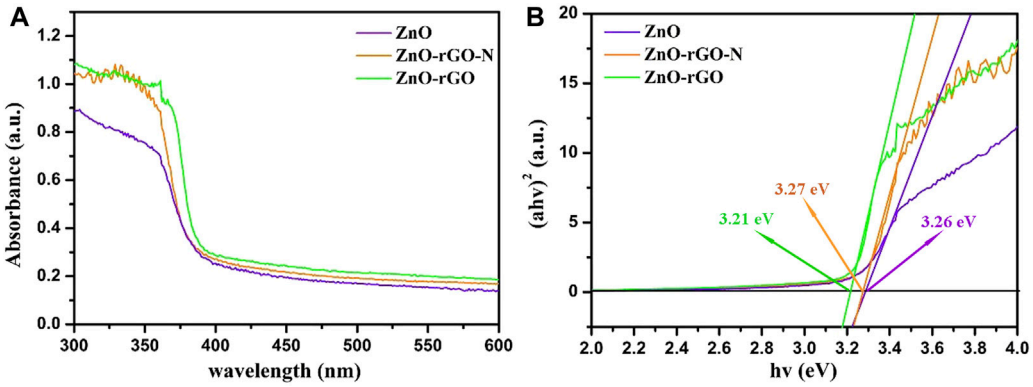


FIGURE 4
UV-vis absorption spectroscopy of ZnO, ZnO-rGO-N and ZnO-rGO composite materials **(A)** and the corresponding curves of $(\alpha hv)^2$ *versus* the *hv* **(B)**.

peak of the Zn-O bond. The stretching vibration absorption peak of the carbonyl group (C=O) in the carboxyl group (-COOH) of GO at 1738 $cm^{-1}$ vanished in ZnO-rGO, proving that GO was reduced in this process (Lu et al., 2021).

The UV-visible absorption spectra of ZnO and ZnO-rGO composite materials are described in Figure 4A. ZnO has obvious absorption in the UV region of 300–400 nm. As for ZnO-rGO-N, the absorbance in UV region increased slightly. In comparison, the absorbance of the ZnO-rGO composite materials enhanced significantly, especially in the area close to visible light (Vanitha et al., 2015). Besides, the absorption edge moves slightly towards the visible light region. The above outcomes indicate that more light can be absorbed for photocatalytic reaction due to the synergistic effect of rGO and ZnO.

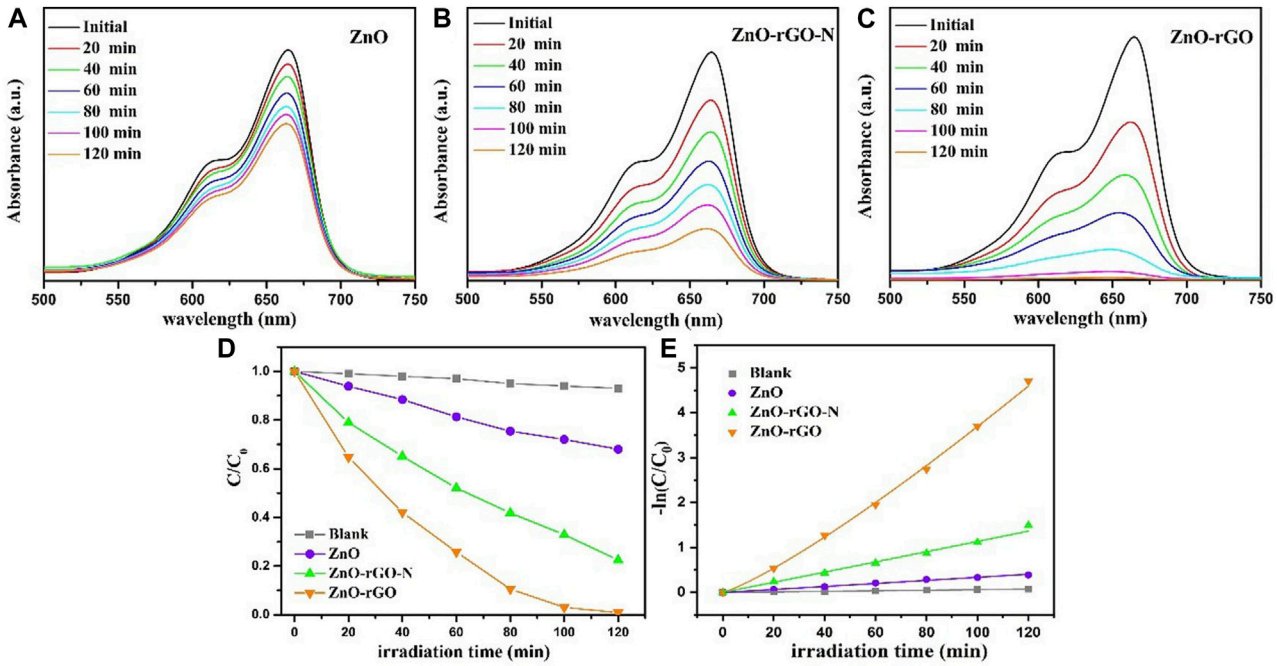


FIGURE 5
The changes of UV-vis spectra of dye degraded by ZnO **(A)**, ZnO-rGO-N **(B)** and ZnO-rGO **(C)** composites as interval illumination times, variation ratios of the concentrations of the MB degraded by different catalysts *versus* irradiation time **(D)**, and the corresponding kinetic curves **(E)**.

According to the plots of $(\alpha h\upsilon)^2$vs $h\upsilon$ displayed in Figure 4B, the bandgap can be calculated by the Kubelka-Munk method:

$$\alpha h\upsilon = A\left(h\upsilon - E_g\right)^{\eta}$$

where $h$, $A$, $\upsilon$, and $E_g$ are Planck constant, absorption constant of direct transition, frequency of light, and the bandgap value, respectively. As we all know, $\eta$ is an index that characterizes the light absorption process, and it is 1/2 for the of ZnO and ZnO-rGO composites with direct bandgap (Lupan et al., 2010). The calculated energy bandgap of ZnO is 3.29 eV. However, the bandgap of ZnO-rGO-N was reduced to 3.27 eV and further decreased to 3.21 eV for ZnO-rGO, which is beneficial to the absorption of photons with lower energy.

To assess the photocatalytic performance, ZnO, ZnO-rGO-N and ZnO-rGO composites were used to degrade methylene blue (MB) under mercury lamp irradiation. Figures 5A–C exhibits the variation of the UV-Vis absorption spectrum of the ZnO, ZnO-rGO-N and ZnO-rGO degraded MB solution with irradiation time. Compared with ZnO and ZnO-rGO-N, the absorption peaks of ZnO-rGO shrank rapidly with the largest extent as the extension of the irradiation time, and the absorption peak almost disappeared in 120 min. Figure 5D shows the variation of the MB concentrations by the degradation of different samples under a mercury lamp. The degradation rate can be calculated by Lambert-Beer law:

$$\text{Degradation rate} = \frac{C_0 - C}{C_0} \times 100\% = \frac{A_0 - A}{A_0} \times 100\%$$

where $C_0$ is the initial concentration of MB, C is the concentration of MB at time t, $A_0$ is the initial absorbance of MB solution, and A is the absorbance of MB solution at time t. As seen from Figure 5D, the MB degradation rate without using photocatalyst was only 7% under irradiation for 120 min, suggesting the MB can hardly be degraded without the aid of photocatalyst. As for ZnO catalyst, it can only degrade 32% of the MB dye within 120 min. After the incorporation of rGO nanosheets, the degradation rates of MB can reach about 77.5%, and 99.1% for MB dye in 120 min by the catalysis of ZnO-rGO-N and ZnO-rGO composites. This result suggests that the photocatalytic performance of ZnO can be significantly improved by the addition of rGO, probably be owing to that the presence of rGO reduced the recombination speed of electron-hole pairs and enhanced the absorption of MB (Kwon et al., 2017). Concurrently, the improvement of photocatalytic degradation efficiency of ZnO-rGO compared with ZnO-rGO-N should be attributed to the finer and more uniform ZnO nanorods (Figure 2), the increase of absorbance in visible region as well as the decrease of band gap width (Figures 4A,B).

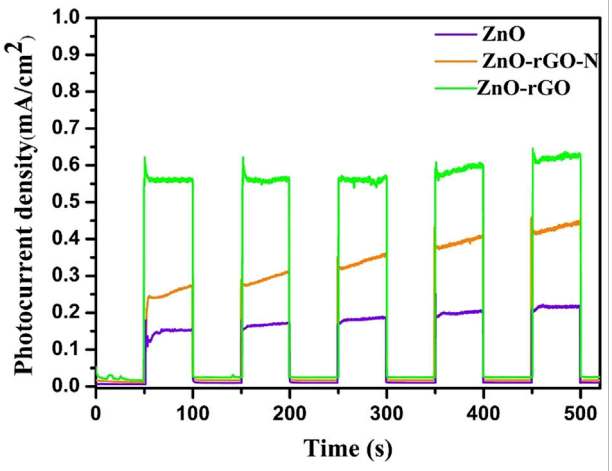


FIGURE 6
Transient photocurrent curves of ZnO, ZnO-rGO-N and ZnO-rGO.

According to the above results, the process of degradation of organic dyestuff by ZnO, ZnO-rGO-N and ZnO-rGO composite materials conformed to the first-order reaction kinetics:

$$-\frac{dC}{dt} = k \times C$$

$$-\ln\left(\frac{C}{C_0}\right) = k \times t$$

$$\ln\left(\frac{C_0}{C}\right) = kt$$

Here, k ($min^{-1}$) represents the first-order rate constant, and t is the irradiation time. Figure 5E shows the first-order kinetic fitting results of these photodegradation, from which it can be distinctly found that the degradation rates follow the sequence: ZnO < ZnO-rGO-N < ZnO-rGO.

The separation of photogenerated carriers during the photocatalytic process was demonstrated by the transient photocurrent curves of the electrochemically tested samples. In transient photocurrent curves, the carrier separation efficiency of the photocatalyst is proportional to the photocurrent corresponding. As can be seen in Figure 6, the photocurrent density of the photocatalyst in the absence of light is located at zero, and the photocurrent density rises rapidly after light exposure and stabilizes at a maximum point with good stability of the cycle within 500 s of discontinuous irradiation. The ZnO-rGO sample shows the maximum photocurrent stability density compared to ZnO and ZnO-rGO-N, which is due to the fact that the addition of rGO can effectively increase the conductivity, improve the electron transfer rate, and promote the separation of photogenerated electron-hole pairs.

The morphologies of the ZnO-rGO composites prepared with electrolytes of different GO concentrations are depicted in Figure 7. In Figure 7A and 7B, the diameter of the ZnO nanorods reduced from 148.49 to 93.3 nm as the GO concentration was raised from 2 to 5 mg $L^{-1}$. When the concentration was further raised to 8 mg $L^{-1}$, the top of the ZnO nanorods was destroyed and the distribution of the nanorods became sparser, leading to the exposure of the substrate (Figure 7C).

Figure 8 exhibits the XRD spectra of pure ZnO and ZnO-rGO composites prepared with various GO concentrations. It can be seen that the characteristic peaks of ZnO and FTO decrease with the increase of GO concentration, which is because of the increased thickness of the rGO nanosheets covering the top of the ZnO nanorods in the ZnO-rGO composite material deposited on the FTO surface, in consistence with the results in Figure 7.

The UV-visible absorption spectra of ZnO-2rGO, ZnO-5rGO and ZnO-8rGO composite materials and corresponding curves of $(\alpha h\nu)^2$ *versus* the hv are described in Figures 9A,B. Compared with ZnO-2rGO, the absorbance of ZnO-5rGO and ZnO-8rGO increased significantly in the visible region, which was conducive to improving the photocatalytic degradation efficiency (Figure 9A). The calculated energy bandgaps of ZnO-2rGO, ZnO-5rGO and ZnO-8rGO from Figure 9B by the Kubelka-Munk formula are 3.29, 3.22, and 3.26 eV respectively.

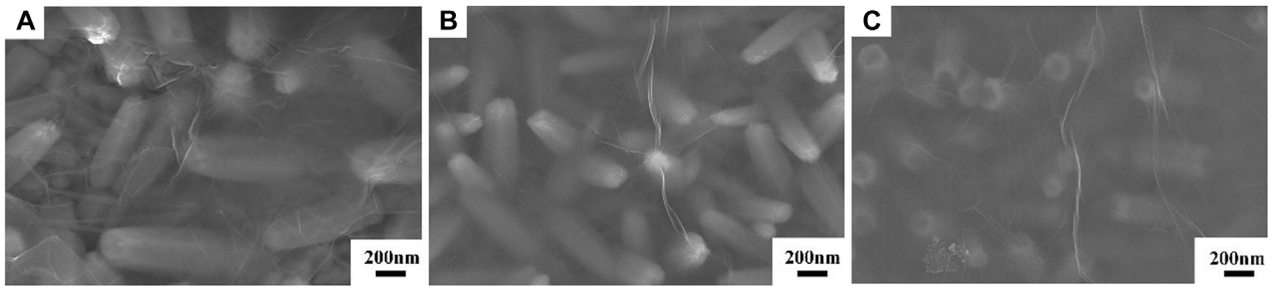


FIGURE 7
SEM micrographs ZnO-2rGO **(A)**, ZnO-5rGO **(B)**, and ZnO-8rGO **(C)**.

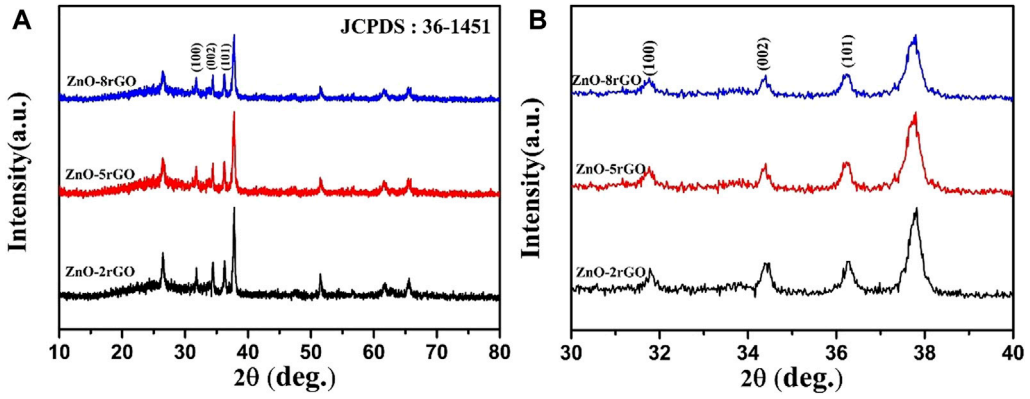


FIGURE 8
XRD spectra of ZnO-rGO composite prepared with different GO concentration **(A)** and partially enlarged pattern **(B)**.

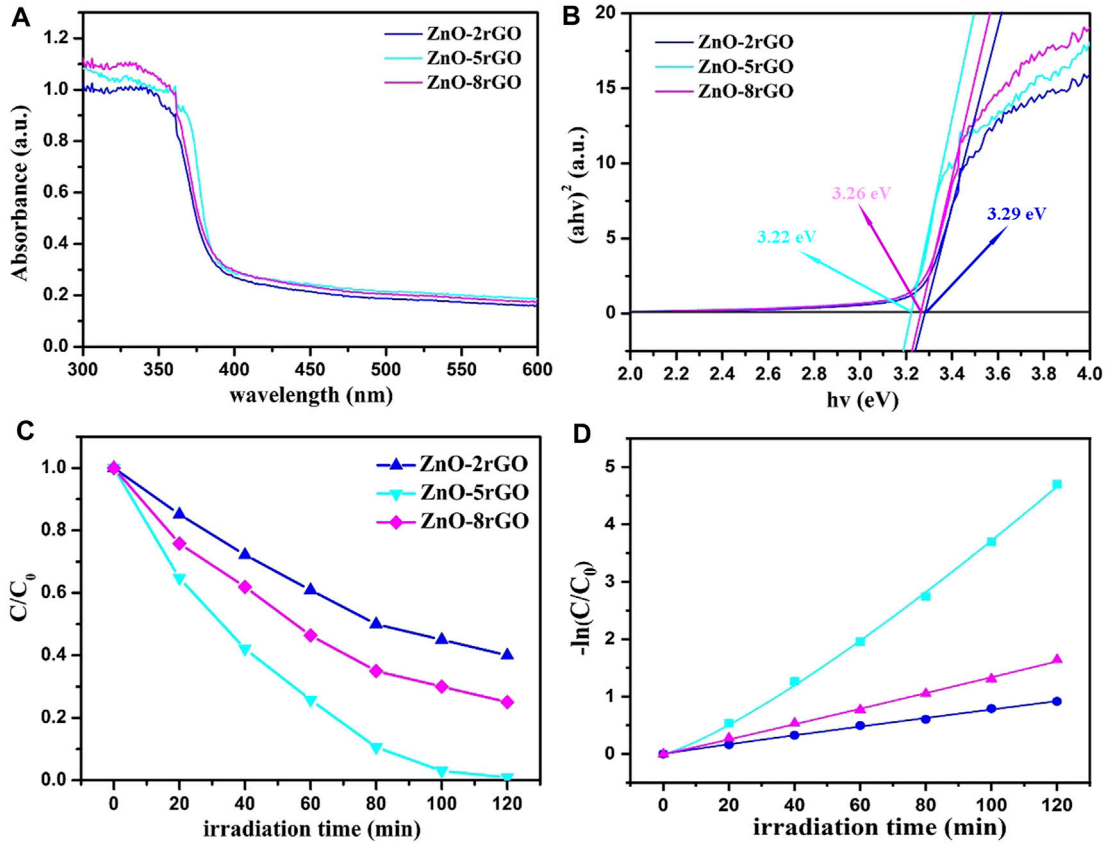


FIGURE 9
UV-vis absorption spectroscopy of ZnO-2rGO, ZnO-5rGO and ZnO-8rGO composite materials **(A)** and the corresponding curves of $(\alpha hv)^2$ *versus* the *hv* **(B)**; variation ratios of the concentrations of the MB degraded by different catalysts *versus* irradiation time **(C)**, and the corresponding kinetic curves **(D)**.

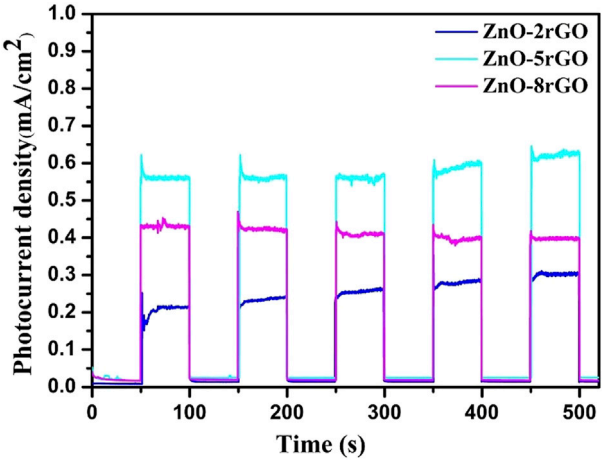


FIGURE 10
Transient photocurrent curves of ZnO-rGO prepared by different concentrations of precursors.

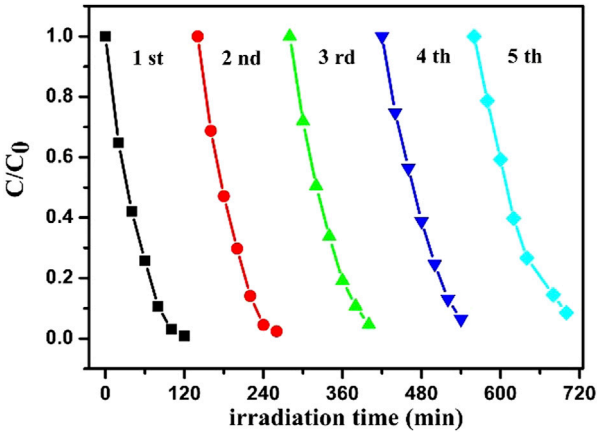


FIGURE 11
The photostability of ZnO-5rGO composite to MB degradation.

Figure 9C shows the variation of the MB concentrations by the degradation of different samples under a mercury lamp, and the absorption spectra are shown in SupplementaryFigure S2. The degradation rates of MB dye by ZnO-2rGO, ZnO-5rGO and ZnO-8rGO composites can reach 60%, 99.1%, and 75% within 120 min. The ZnO-5rGO composites exhibit the best photocatalytic activity, which is ascribable to the largest surface area caused by the dense distribution of the ZnO nanorods with small diameter. The degradation rate of 99.1% for MB in 120 min is larger than previously reported ZnO-rGO composites, such as, ZnO/graphene composite prepared by surfactant-assisted simple hydrothermal method (90% in 130 min) (Zhou et al., 2012), ZnO-rGO composites fabricated by an easy one-step low-temperature chemical etching route (97% in 140 min) (Zhao et al., 2017), and ZnO/GO nanocomposite powder synthesized by novel flame transport approach (60% in 120 min) (Reimer et al., 2014).

The photocurrent test can further illustrate the separation efficiency of photogenerated carriers during the reaction process. Figure 10 shows the transient photocurrent curves with ZnO-2rGO, ZnO-5rGO and ZnO-8rGO as photocatalysts. The degree of photocurrent response of ZnO-2rGO, ZnO-5rGO and ZnO-8rGO was different under 500 s intermittent irradiation. It indicates that the addition of different concentrations of GO in the precursor solution has an effect on the photocatalytic performance of the prepared ZnO-rGO samples, further verifying that the introduction of rGO with higher conductivity and larger specific surface area can be used as the acceptor and emitter of electrons to improve the conductivity and reduce the complexation of photogenerated carriers, resulting in improved photocatalytic performance. The photocurrent intensity of ZnO-5rGO is the largest compared with other samples, indicating that it has the best photocatalytic degradation performance.

For further study the recyclability of ZnO-5rGO as a photocatalytic material, the degradation efficiency of repeatedly used ZnO-5rGO for MB was studied. After each cycle of degradation, the ZnO-5rGO coated FTO was washed with deionized water and then dried. As shown in Figure 11 and S3, the degradation efficiencies of the five cycles for MB are 99.1, 97.6, 95.4, 93.6, and 91.5%, respectively, suggesting the excellent reusability and light stability of the ZnO-rGO composite.

To prove the universal application of ZnO-rGO composite for the degradation of dyestuffs, the degradation of RhB and MO solutions using ZnO-5rGO composites was studied, and the outcomes are presented in Figure 12. It can be observed from Figure 12A and 12B that absorption peaks of both RhB and MO decreased quickly under the irradiation of a mercury lamp. The photocatalytic degradation rate of MO and RhB solutions can be achieved to 90.3% and 93.2% in 120 min, respectively (Figure 12C). Combined with the first-order kinetic fitting results of photodegradation in Figure 12D, it can be concluded that ZnO-rGO composite also has excellent photocatalytic performance for other dyes.

To understand the main active species during the reaction of ZnO-rGO photocatalytic degradation of target degraded organics, the main active species during the photocatalytic reaction of ZnO, ZnO-rGO-N and ZnO-rGO photocatalysts

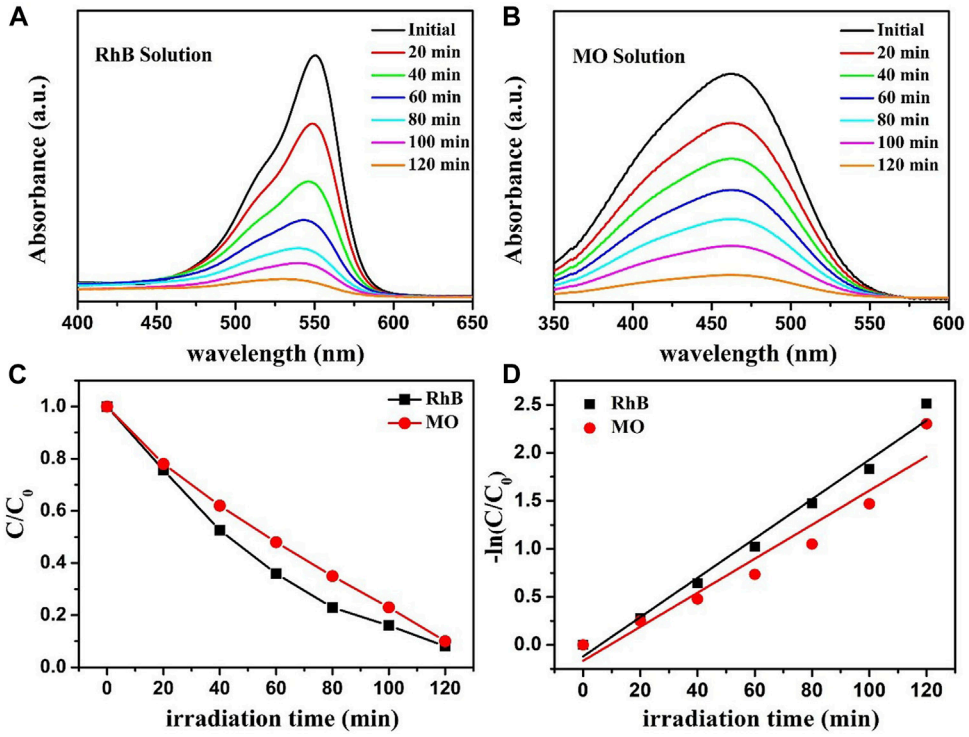


FIGURE 12
The absorption spectra of RhB **(A)** and MO **(B)** solutions that were photocatalytic degraded by ZnO-5rGO composites under mercury lamp irradiation; photocatalytic degradation of RhB and MO by the ZnO-5rGO composites **(C)** and the corresponding kinetic curves **(D)**.

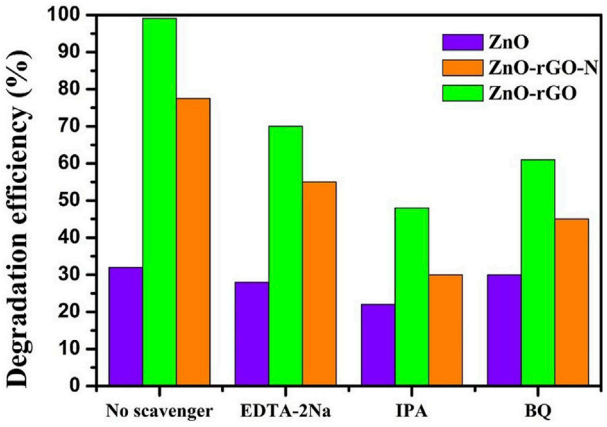


FIGURE 13
Degradation rate of MB degraded by ZnO, ZnO-rGO-N and ZnO-rGO Photocatalysts in the presence of capture agent.

for MB degradation without the addition of active species trapping agents and with EDTA-2Na, IPA and BQ as active species trapping agents are shown in Figure 13. The degradation rate of the target degradants after the addition of active species trapping agents was inversely proportional to the role played by the active species during the reaction. In Figure 13, the degradation rate of ZnO-rGO as a photocatalyst for MB was 99.1% without the addition of active species trapping agent, which changed to 70% with the addition of EDTA-2Na, 48% with the addition of IPA, and 61% with the addition of BQ. The changes in degradation rates after the addition of active species trapping agents indicate that OH is the active species that plays a major role in the photocatalytic degradation of MB.

In this paper, there are many reasons why the photocatalytic degradation rate of ZnO-rGO composite was improved compared with that of ZnO. First, the ZnO nanorods of the synthesized ZnO-rGO composites are lower in diameter but higher in density compared with the pure ZnO, leading to a larger surface area. This will promote the spread and mass transfer of dye and oxygen species in photochemical reactions (Wei et al., 2013). Secondly, as shown in Figure 14, the coverage of rGO nanosheets on the top of ZnO nanorods can receive photo-generated electrons and accelerate charge separation through the charge transfer process. In addition, the generated charge can be quickly transferred, which is beneficial to the degradation of the dye (Kang et al., 2016).

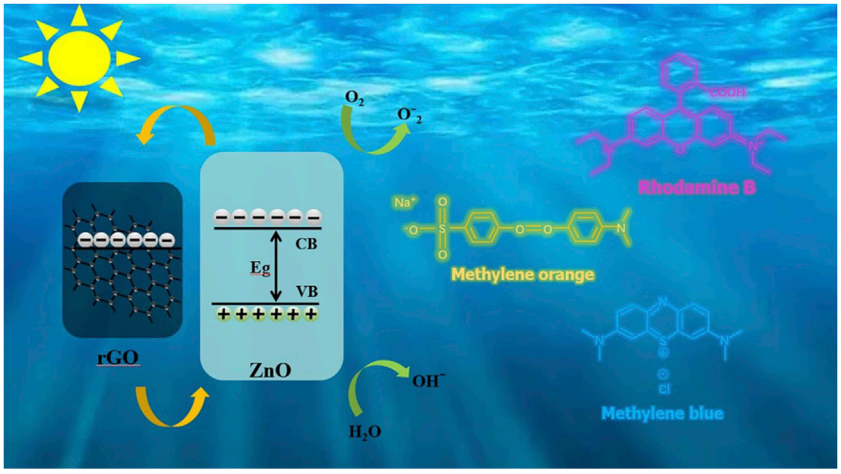


FIGURE 14
Diagram of the photocatalytic degradation mechanism of ZnO-rGO composites.

## Conclusion

The ZnO-rGO photocatalyst was synthesized on the FTO substrate by a one-step electrochemical deposition method. After the incorporation of rGO into ZnO, the photocatalytic performance of the ZnO-rGO was significantly improved. The degradation of MB dye by ZnO-rGO composites synthesized with different concentrations of GO in electrolyte was also studied. The ZnO-rGO prepared with electrolyte containing 5 mg $L^{-1}$ GO achieved the best photodegradation efficiency of 99.1% for degrading MB within 120 min. These outcomes indicate that the ZnO-rGO composites could be an excellent candidate material for photodegradation of organic dyes.

## Data availability statement

The original contributions presented in the study are included in the article/supplementary material, further inquiries can be directed to the corresponding authors.

## Author contributions

Conceptualization and funding acquisition: HL, Methodology: TL and QW; Formal analysis and investigation: JW and KW; Writing – original draft preparation: SS; Writing – review and editing: SY; Resources: JM; Supervision: ZS.

## Funding

This work was supported by the Natural Science Foundation of Ningxia, China (No. 2022AAC03272), and Key Research and Development Project of Ningxia, China (No. 2020BCE01006).

## Conflict of interest

HL, JW was employed by Yinchuan Aini Industrial Technology Development Co., Ltd

The remaining authors declare that the research was conducted in the absence of any commercial or financial relationships that could be construed as a potential conflict of interest.

## Publisher's note

All claims expressed in this article are solely those of the authors and do not necessarily represent those of their affiliated organizations, or those of the publisher, the editors and the reviewers. Any product that may be evaluated in this article, or claim that may be made by its manufacturer, is not guaranteed or endorsed by the publisher.

## Supplementary material

The Supplementary Material for this article can be found online at: https://www.frontiersin.org/articles/10.3389/fchem.2022.1061129/full#supplementary-material

# References

Abdel-Karim, A., El-Naggar, M. E., Radwan, E. K., Mohamed, I. M., Azaam, M., and Kenawy, E. (2021). High-performance mixed-matrix membranes enabled by organically/inorganic modified montmorillonite for the treatment of hazardous textile wastewater. *Chem. Eng. J.* 405, 126964. doi:10.1016/j.cej.2020.126964

Abdelsamad, A. M. A., Gad-Allah, T. A., Mahmoud, F. A., and Badawy, M. I. (2018). Enhanced photocatalytic degradation of textile wastewater using Ag/ZnO thin films. *J. Water Process Eng.* 25, 88–95. doi:10.1016/j.jwpe.2018.07.002

Agarwal, V., and Zetterlund, P. (2020). Strategies for reduction of graphene oxide-a comprehensive review. *Chem. Eng. J.* 405, 127018. doi:10.1016/j.cej.2020.127018

Anandan, S., Ohashi, N., and Miyauchi, M. (2010). ZnO-Based visible-light photocatalyst: Band-gap engineering and multi-electron reduction by co-catalyst. *Appl. Catal. B Environ.* 100, 502–509. doi:10.1016/j.apcatb.2010.08.029

Azarang, M., Shuhaimi, A., Yousefi, R., and Jahromi, S. P. (2015). One-pot sol–gel synthesis of reduced graphene oxide uniformly decorated zinc oxide nanoparticles in starch environment for highly efficient photodegradation of Methylene Blue. *RSC Adv.* 5, 21888–21896. doi:10.1039/c4ra16767h

Chaudhary, D., Simrjit, S., Vankar, V. D., and Khare, N. (2018). ZnO nanoparticles decorated multi-walled carbon nanotubes for enhanced photocatalytic and photoelectrochemical water splitting. *J. Photochem. Photobiol. A Chem.* 351, 154–161. doi:10.1016/j.jphotochem.2017.10.018

Dehghan Nayeri, F., Asl Soleimani, E., and Salehi, F. (2013). Synthesis and characterization of ZnO nanowires grown on different seed layers: The application for dye-sensitized solar cells. *Renew. Energy* 60, 246–255. doi:10.1016/j.renene.2013.05.006

Erdogan, N. H., Kutlu, T., Sedefoglu, N., and Kavak, H. (2021). Effect of Na doping on microstructures, optical and electrical properties of ZnO thin films grown by sol-gel method. *J. Alloys Compd.* 881, 160554. doi:10.1016/j.jallcom.2021.160554

Garg, D., Matai, I., Garg, A., and Sachdev, A. (2020). Tragacanth hydrogel integrated $CeO_2$@rGO nanocomposite as reusable photocatalysts for organic dye degradation. *ChemistrySelect* 5, 10663–10672. doi:10.1002/slct.202002041

Imran, M., Alam, M. M., Hussain, S., Ali, M. A., Shkir, M., Mohammad, A., et al. (2021). Highly photocatalytic active r-GO/$Fe_3O_4$ nanocomposites development for enhanced photocatalysis application: A facile low-cost preparation and characterization. *Ceram. Int.* 47, 31973–31982. doi:10.1016/j.ceramint.2021.08.083

Kang, W., Xu, J., and Wang, X. (2016). The effects of ZnO morphology on photocatalytic efficiency of ZnO/RGO nanocomposites. *Appl. Surf. Sci.* 360, 270–275. doi:10.1016/j.apsusc.2015.10.190

Kharatzadeh, E., Masharian, S. R., and Yousefi, R. (2021). Comparison of the photocatalytic performance of S-SnSe/GO and SnSe/S-GO nanocomposites for dye photodegradation. *Mater. Res. Bull.* 135, 111127. doi:10.1016/j.materresbull.2020.111127

Kwon, Y. T., Kang, S. O., Cheon, J. A., Song, Y., Lee, J. J., and Choa, Y. H. (2017). Fabrication of a Graphene/ZnO based p-n junction device and its ultraviolet photoresponse properties. *Appl. Surf. Sci.* 415, 2–7. doi:10.1016/j.apsusc.2016.10.159

Liras, M., Barawi, M., and de la Peña O'Shea, V. (2019). Hybrid materials based on conjugated polymers and inorganic semiconductors as photocatalysts: From environmental to energy applications. *Chem. Soc. Rev.* 48, 5454–5487. doi:10.1039/c9cs00377k

Lonkar, S., Vijayan Pillai, V., and Alhassan, S. (2018). Facile and scalable production of heterostructured ZnS-ZnO/Graphene nano-photocatalysts for environmental remediation. *Sci. Rep.* 8, 13401. doi:10.1038/s41598-018-31539-7

Lu, H., Sha, S. M., Yang, S. L., Wu, J. D., Sheng, Z. L., Hou, C., et al. (2021). The coating and reduction of graphene oxide on meshes with inverse wettability for continuous water/oil separation. *Appl. Surf. Sci.* 538, 147948. doi:10.1016/j.apsusc.2020.147948

Luan, Q., Chen, Q., Zheng, J., Guan, R., Fang, Y., and Hu, X. (2020). Construction of 2D-ZnS@ZnO Z-scheme heterostructured nanosheets with a highly ordered ZnO core and disordered ZnS shell for enhancing photocatalytic hydrogen evolution. *ChemNanoMat* 6, 470–479. doi:10.1002/cnma.201900630

Lupan, O., Pauporte, T., Chow, L., Viana, B., Pelle, F., Ono, L. K., et al. (2010). Effects of annealing on properties of ZnO thin films prepared by electrochemical deposition in chloride medium. *Appl. Surf. Sci.* 256, 1895–1907. doi:10.1016/j.apsusc.2009.10.032

Mansor, E. S., Ali, H., and Abdel-Karim, A. (2020). Efficient and reusable polyethylene oxide/polyaniline composite membrane for dye adsorption and filtration. *Colloid Interface Sci. Commun.* 39, 100314. doi:10.1016/j.colcom.2020.100314

Moradi, M., Vasseghian, Y., Khataee, A., Harati, M., and Arfaeinia, H. (2021). Ultrasound-assisted synthesis of $FeTiO_3$/GO nanocomposite for photocatalytic degradation of phenol under visible light irradiation. *Sep. Purif. Technol.* 261, 118274. doi:10.1016/j.seppur.2020.118274

Nasir, A. M., Awang, N., Jaafar, J., Ismail, A. F., Othman, M. H. D., Rahman, M. A., et al. (2021). Recent progress on fabrication and application of electrospun nanofibrous photocatalytic membranes for wastewater treatment: A review. *J. Water Process Eng.* 40, 101878. doi:10.1016/j.jwpe.2020.101878

Niu, P., Liu, G., and Cheng, H. M. (2012). Nitrogen vacancy-promoted photocatalytic activity of graphitic carbon nitride. *J. Phys. Chem. C* 116, 11013–11018. doi:10.1021/jp301026y

Reimer, T., Paulowicz, I., Roder, R., Kaps, S., Lupan, O., Chemnitz, S., et al. (2014). Single step integration of ZnO nano- and microneedles in Si trenches by novel flame transport approach: Whispering gallery modes and photocatalytic properties. *ACS Appl. Mat. Interfaces* 6, 7806–7815. doi:10.1021/am5010877

Ren, Z., Li, X., Guo, L., Wu, J. Z., Li, Y., Liu, W., et al. (2021). Facile synthesis of ZnO/ZnS heterojunction nanoarrays for enhanced piezo-photocatalytic performance. *Mat. Lett.* 292, 129635. doi:10.1016/j.matlet.2021.129635

Roshni, A., and Thambidurai, S. (2022). Enhanced photocatalytic and antibacterial activity of ZnO with rice field crab chitosan and plectranthus amboinicus extract. *Mater. Chem. Phys.* 291, 126739. doi:10.1016/j.matchemphys.2022.126739

Umadevi, P., Ramya Devi, K. T., Sridevi, D. V., Suresh, P., and Ramesh, V. (2022). Structural, morphological, optical, photocatalytic activity and bacterial growth inhibition of Nd-doped $TiO_2$ nanoparticles. *Mater. Sci. Eng. B* 286, 116018. doi:10.1016/j.mseb.2022.116018

Van Tuan, P., Phuong, T. T., Tan, V. T., Nguyen, S. X., and Khiem, T. N. (2020). *In-situ* hydrothermal fabrication and photocatalytic behavior of ZnO/reduced graphene oxide nanocomposites with varying graphene oxide concentrations. *Mater. Sci. Semicond. Process.* 115, 105114. doi:10.1016/j.mssp.2020.105114

Vanitha, M., Keerthi, Vadivel S., and Balasubramanian, N. (2015). Visible light photocatalysis of Methylene blue by graphene-based ZnO and Ag/AgCl nanocomposites. *Desalination Water Treat.* 54, 2748–2756. doi:10.1080/19443994.2014.903207

Wei, A., Xiong, L., Sun, L., Liu, Y., Li, W., Lai, W., et al. (2013). One-step electrochemical synthesis of a graphene–ZnO hybrid for improved photocatalytic activity. *Mater. Res. Bull.* 48, 2855–2860. doi:10.1016/j.materresbull.2013.04.012

Yang, S., Deng, B., Ge, R., Zhang, L., Wang, H., Zhang, Z., et al. (2014). Electrodeposition of porous graphene networks on nickel foams as supercapacitor electrodes with high capacitance and remarkable cyclic stability. *Nanoscale Res. Lett.* 9, 672. doi:10.1186/1556-276x-9-672

Zhao, Y., Liu, L., Cui, T., Tong, G., and Wu, W. (2017). Enhanced photocatalytic properties of ZnO/reduced graphene oxide sheets (rGO) composites with controllable morphology and composition. *Appl. Surf. Sci.* 412, 58–68. doi:10.1016/j.apsusc.2017.03.207

Zhou, X., Shi, T., and Zhou, H. (2012). Hydrothermal preparation of ZnO-reduced graphene oxide hybrid with high performance in photocatalytic degradation. *Appl. Surf. Sci.* 258, 6204–6211. doi:10.1016/j.apsusc.2012.02.131

frontiers | Frontiers in Chemistry

TYPE Original Research
PUBLISHED 18 November 2022
DOI 10.3389/fchem.2022.1060523



OPEN ACCESS

EDITED BY
Hailong Wang,
Ningxia University, China

REVIEWED BY
Jian-Fang Wu,
Hunan University, China
Shiliang Mei,
Fudan University, China

*CORRESPONDENCE
Minglei Cao,
cml07114052@163.com

SPECIALTY SECTION
This article was submitted to Nanoscience, a section of the journal Frontiers in Chemistry

RECEIVED 03 October 2022
ACCEPTED 21 October 2022
PUBLISHED 18 November 2022

CITATION
Yin H, Li H, Yu X-x and Cao M (2022), Design of $Sb_2Te_3$ nanoblades serialized by Te nanowires for a low-temperature near-infrared photodetector. *Front. Chem.* 10:1060523. doi: 10.3389/fchem.2022.1060523



# Design of $Sb_2Te_3$ nanoblades serialized by Te nanowires for a low-temperature near-infrared photodetector

Hong Yin[1,2], Huaiyu Li[1], Xiang-xiang Yu[3] and Minglei Cao[4]*

[1]School of Chemistry and Chemical Engineering, Hunan Institute of Science and Technology, Yueyang, China, [2]International Iberian Nanotechnology Laboratory (INL), Braga, Portugal, [3]School of Physics and Optoelectronic Engineering, Yangtze University, Jingzhou, China, [4]School of Mathematics, Physics and Optoelectronic Engineering, Hubei University of Automotive Technology, Shiyan, China

The dangling bond on the surface of bulk materials makes it difficult for a physically contacted heterojunction to form an ideal contact. Thus, periodic epitaxial junctions based on $Sb_2Te_3$ nanoblades serialized by Te nanowires ($Sb_2Te_3$/Te) were fabricated using a one-step hydrothermal epitaxial growth method. X-ray diffraction and electron microscopy reveal that the as-prepared product has a good crystal shape and heterojunction construction, which are beneficial for a fast photoresponse due to the efficient separation of photogenerated carriers. When the $Sb_2Te_3$/Te composite is denoted as a photodetector, it shows superior light response performance. Electrical analysis showed that the photocurrent of the as-fabricated device declined with temperatures rising from 10K to 300K at 980 nm. The responsivity and detectivity were 9.5 × $10^{11}$ μA $W^{-1}$ and 1.22 × $10^{11}$ Jones at 50 K, respectively, which shows better detection performance than those of other Te-based photodetector devices. Results suggest that the as-constructed near-infrared photodetector may exhibit prospective application in low-temperature photodetector devices.

KEYWORDS

**photodetector, responsivity and detectivity, low-temperature, heterojunction, epitaxial growth**

## Introduction

Topological insulators have been experiencing new grading of quantum matter consisting of a bulk gap and Dirac-like surface states (Fu et al., 2007; Xia et al., 2009). These materials were considered using a robust spin-orbit interaction that leads to surface states bridging the bulk band gap. More importantly, the carriers on the surface states of topological insulators have low energy dissipation because of the time-reversal symmetry and spin-orbit coupling (Yu et al., 2018). Moreover, angle-resolved photoemission spectroscopy (ARPES) analysis indicates that the surface states consist of an odd number of helical spin-momentum textured Dirac cones (Pradhan et al., 2017; Sun et al., 2017). Therefore, methods have been developed to synthesize various topological

insulator materials, for example, metal-organic chemical vapor deposition (MOCVD), pulsed-laser deposition (PLD), and physical vapor deposition (PVD) (Jiang et al., 2005; Jin et al., 2005; Matsunaga et al., 2006; Ikeda et al., 2007). Due to unique physical properties and potential applications in more and more fields, such as quantum computing, photodetection, and superconductors, topological insulator materials have been the focus of tremendous recent attention (Duan et al., 2015; Yu et al., 2017). In these devices, photodetectors have gained special attention because of their widespread applications in many areas, such as industrial automatic control, infrared remote sensing, image sensors, and target detection (Yang et al., 2000; Matsunaga et al., 2004; Zhong et al., 2017; Wang et al., 2022). For example, a photoconductor based on topological insulator ($Sb_2Te_3$) film has been prepared, and the device has the ability to detect the 980 nm near-infrared light (Zheng et al., 2015). Zhang et al. reported a polycrystalline $Bi_2Te_3$ film topological insulator for a near-infrared (NIR) photodetector and revealed that the as-prepared device is sensitive to visible and NIR light and the responsivity and gain are $3.3 \times 10^{-5}$ A $W^{-1}$ and $3.85 \times 10^{-5}$, respectively (Wesolowski et al., 2014). In addition, a series of photovoltaic detectors based on topological insulators, such as SnTe/Si and $Sb_2Te_3$/STO, were prepared and exhibited excellent performance (Tominaga et al., 2014; Sun et al., 2017). However, these devices exhibit a large dark current and the very low carrier lifetime of the photoconductor based on one component leads to a slower response speed and little photocurrent.

$Sb_2Te_3$, as a narrow bandgap semiconductor (~0.23 eV), is considered a rhombohedral crystal showing a bulky periodicity along its *c*-axis ($a_{Sb2Te3}$ = 4.26 Å, $c_{Sb2Te3}$ = 30.46 Å). Additionally, Tellurium is a key semiconductor and its bandgap is approximately 0.35 eV (Cheng et al., 2013; Li et al., 2015). Therefore, $Sb_2Te_3$ and Te nanostructures can be epitaxially grown together to form heterojunctions due to the similarity of lattice spacings. Factually, the enhanced concentration of interfaces can strongly boost the formation of the built-in field. The effect is beneficial for separating photon-induced carriers (Lee et al., 2008; Tominaga et al., 2008; Sosso et al., 2009; Dong et al., 2010). Consequently, photodetection performances would be enhanced due to the quantum size effects by forming heterojunctions (Chen et al., 2003; Cozzoli et al., 2006).

Although the synthesis of various $Sb_2Te_3$-Te heterojunctions has been executed and performance has been estimated, the complex and energy-intensive fabrication process of the heterojunction, such as CVD and MBE, seriously restricts their large-scale application. Herein, we settled on a facile one-step hydrothermal method to prepare T-shaped epitaxial $Sb_2Te_3$/Te heterojunctions with feature sizes of hundreds of nanometers. The morphologies and structures of the product were carefully characterized by an electron microscope and X-ray diffraction, respectively. The length of a nanostructure is approximately 10 μm, which is very beneficial in fabricating the photodetector by convenient photolithography processing. The as-fabricated $Sb_2Te_3$/Te photodetector device shows a superior photovoltaic effect because of the superior built-in electric field within the hetero-interface. The responsivity and photoconductivity are estimated as $9.5 \times 10^{11}$ μA $W^{-1}$ and $1.22 \times 10^{11}$ Jones at 50 K, respectively, which is more prior than those previously reported. This study proposes that the T-shaped epitaxial $Sb_2Te_3$/Te heterojunctions show great promise for future optoelectronic device applications.

# Experimental section

## Material synthesis

An eco-friendly hydrothermal method was used to synthesize $Sb_2Te_3$/Te heterostructure nanostrings. In a typical synthesis, 2 mmol L-antimony potassium tartrate ($C_8H_4K_2O_{12}Sb_2$, AR, 99%), 3 mmol sodium selenite (AR, 99%), and 0.3 g polyvinyl pyrrolidone (PVP, 130000, AR, 99%) were dissolved in 40 ml of ethylene glycol (AR, 99%). After vigorous stirring for 10 min, the mixture was put into a 100 ml Teflon-lined stainless-steel autoclave. The autoclave was treated at 180 °C and maintained for 48 h before being cooled in air. The precipitates were isolated by centrifugation, washed with distilled absolute ethanol and water several times to remove possible residues, and dried in a vacuum. Lastly, to improve the degree of crystallinity, the $Sb_2Te_3$/Te composite was placed in a tube and annealed to 300 °C for 2 h in argon.

## Material characterization

Morphological characterizations of the $Sb_2Te_3$/Te nanostrings were performed using scanning electron microscopy (SEM, NOVA 450, FEI) and transmission electron microscopy (TEM, G2 FEI). The crystalline structures of the as-prepared nanofibers were characterized by X-ray diffraction (XRD, Shimadzu XRD-6000). The valence state analysis of the $Sb_2Te_3$/Te nanostrings was performed with an X-ray electron spectrometer (XPS, AXIS-ULTRA DLD-600W).

## Device construction and analysis

The topological insulator $Sb_2Te_3$/Te heteronanostructures are sensitive to acetone, which is usually used to remove the photoresistor during the photolithography process. A focused ion beam (FIB) was employed to define the metal electrode during the fabrication of the NIR photodetector. Briefly, a micro-electrode on $SiO_2$ (300 nm)/Si substrate was fabricated using conventional photolithography, followed by the deposition of

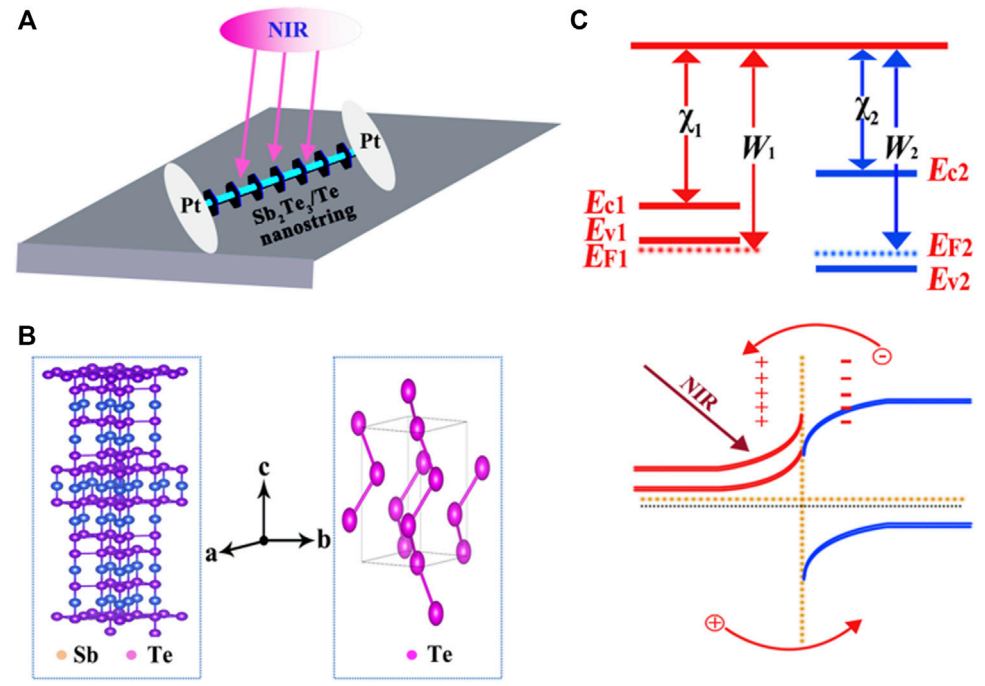


FIGURE 1
**(A)** Schematic illustration of the $Sb_2Te_3$/Te nanostring NIR photodetector. **(B)** Schematic illustration of the crystal structure of the $Sb_2Te_3$ nanosheet and Te nanowire. **(C)** Energy band diagram of the $Sb_2Te_3$/Te nanostring photodetector without and with NIR light illumination.

25 nm titanium and 35 nm gold films by high vacuum electron beam evaporation. Then, the dispersed $Sb_2Te_3$/Te nanostrings were dropped on the micro-electrode and deposited as 50 nm platinum films by FIB. The device characteristics of the topological insulator $Sb_2Te_3$/Te heterostructure are measured using a semiconductor characterization system (Keithley 4200-SCS). The test system was equipped with an automatic cooling system named CCS-350, which was a slow-temperature cycle refrigeration system. For the optoelectronic study, the 980 nm laser (CEL-PF300-T9) is employed as the monochromatic light, which is equipped with an attenuator guided to the NIR device.

## Results and discussion

The proof-of-concept photodetection device (Figure 1A) based on $Sb_2Te_3$/Te nanostrings was fabricated on an $SiO_2$ substrate and the trench width was approximately 5 μm. The Te nanowire is separated by a periodically arranged $Sb_2Te_3$ nanoplate, which formed distinctive p-p heterojunctions. The unique nanostring structure leads to a higher photoelectric conversion efficiency. Figure 1B shows the crystal structure models of $Sb_2Te_3$ and Te. The $Sb_2Te_3$ crystal structure consists of approximately five-atom layers along the *c*-direction, which are known as quintuple layers. Each layer consists of five atoms in order as follows: Te1–Sb–Te2–Sb0–Te10. Furthermore, Te is a hexagonal crystal formed by the accumulation of helical chains through van der Waals interactions. The band structures of $Sb_2Te_3$ and Te are depicted in Figure 1C, respectively. $Sb_2Te_3$ is a p-type topological insulator with a Femi level located in the valance band. The Te is also a p-type semiconductor whose band gap is larger than $Sb_2Te_3$. After combination, a heterojunction can be formed at the interface between $Sb_2Te_3$ and Te. As the work function of $Sb_2Te_3$ is smaller than Te, its electrons will flow into Te and this charge transfer process will form a built-in potential field at the interface. Under infrared light illumination, electron-hole pairs can be generated in $Sb_2Te_3$ and holes will be transferred to Te by built-in potential. These carrier generations and transfers will lead to a detectable photocurrent.

The $Sb_2Te_3$/Te nanostrings are characterized by XRD. Figure 2A (turquoise line) shows the XRD pattern of the $Sb_2Te_3$/Te nanostrings. All peak positions in Figure 2A are indexed to the rhombohedral $Sb_2Te_3$ (JCPDS No. 71-0393) and the hexagonal Te (JCPDS No. 89-4899). The characteristic peaks of $Sb_2Te_3$ and Te are exhibited in Figure 2A such as (015), (110), (205), (101), (012), and (110) planes, which suggest that the as-prepared product is composed of rhombohedral $Sb_2Te_3$ and hexagonal Te. In addition, the diffraction intensities of $Sb_2Te_3$ (006) and (1010) planes are

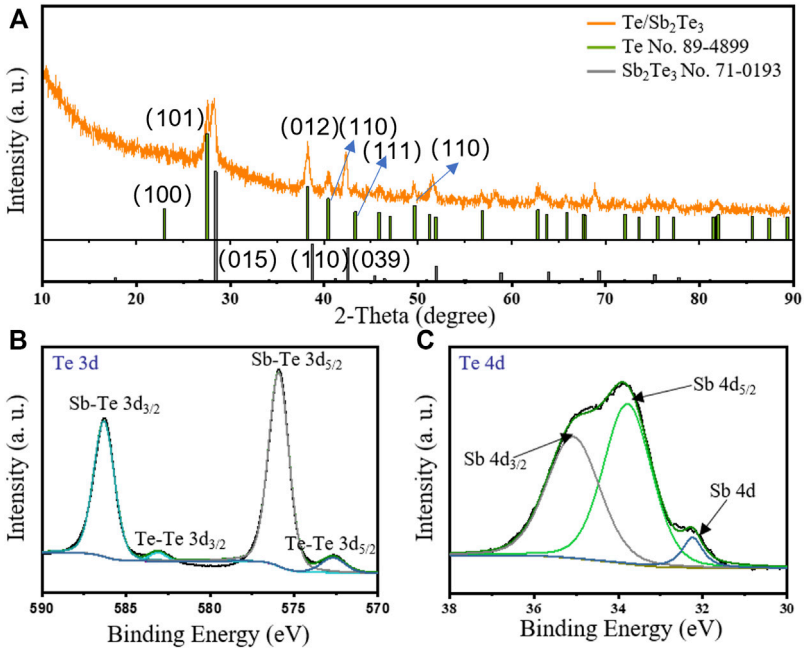


FIGURE 2
**(A)** X-ray diffraction (XRD) pattern of the $Sb_2Te_3$/Te nanostrings. **(B,C)** XPS spectra of Te (3d) and Sb (4d).

extremely sharp; however, those of the (101) and (107) planes are distinctly weak, showing that the (hk0) planes in the $Sb_2Te_3$ nanostructure grew faster than the ($hkl$, $l \neq 0$) planes. Therefore, the $Sb_2Te_3$ crystallization is preferentially grown along with the *a* or *b* axle instead of the *c* axle. As a result, ultrathin $Sb_2Te_3$ nanosheets can be generated in the final products. It is remarkable that the crystallinity is scored as 91.67% after refining (Supplementary Figure S1).

The X-ray photoelectron spectroscopy (XPS) spectra further clarify the structure of $Sb_2Te_3$/Te nanostrings. The sharp peaks of Te (3d) and broad peaks of Sb (3d, 4d) can be clearly separated (Supplementary Figure S2). Figures 2B and C reveal that the electron-binding energies of Te $3d_{3/2}$ and Te $3d_{5/2}$ located at 586.3 eV and at 575.9 eV, respectively, which corresponds to the valence of *Sb-Te*. The binding energies located at 583.0 and 572.6 eV can be ascribed to the $3d_{3/2}$ and $3d_{5/2}$ of *Te-Te* valence. The Raman spectra can also confirm the existence of Te and $Sb_2Te_3$. Two typical characteristic peaks are located at 179 and 235 $cm^{-1}$, which can actually be assigned to Te (Yin et al., 2018) (Supplementary Figure S3). The representative signals of $Sb_2Te_3$ are located at 309 and 343 $cm^{-1}$. All facts confirm that the as-synthesis product exhibits a fine crystallinity with definite constitution and structure.

Figures 3A–C reveal the morphologies of the nanostrings at different magnifications by field-emission scanning electron microscopy (FESEM). The nanostrings are composed of multiple nanosheets that are strung together through the center by Te nanowires. The length of the Te nanostructure is approximately 10 μm (Supplementary Figure S4), which is beneficial for the photodetection device fabrication by conventional photolithography. Figure 3D demonstrates that the $Sb_2Te_3$ nanosheets are embedded in the Te nanowire and the diameter is approximately 300 nm. HRTEM pattern analysis effectively indicates the monocrystalline texture of $Sb_2Te_3$/Te nanostrings (Figures 3E and F). The lattice fringes are noticeable and the d-spacings are 0.2375 and 0.25 nm, which correspond well to the Tellurium (012) and $Sb_2Te_3$ (110) lattice planes, respectively. The selected area electron diffraction (SAED) pattern (Supplementary Figure S5) is well indexed to the hexagonal phase of Tellurium, and corresponding to the diffraction peaks of (012), (101), and (110) planes shown in the XRD pattern. Energy dispersive spectrometer (EDS) spectra confirmed that the nanostrings are composed of Sb and Te elements (Figures 3G–I). Figures 3G–I exhibit the TEM elemental mapping images of the $Sb_2Te_3$/Te nanostring, which further confirms that the as-prepared product is only composed of Te and Sb elements.

The temperature-dependent current-voltage (I-V) curves of the as-fabricated device are studied to disclose its electrical transportation characteristics. Figures 4A and B demonstrate the I-V characteristics from 10 to 300 K in the dark and under 980 nm light illumination (0.5 mW $cm^{-2}$). The dark current increases with falling temperature. This can be attributed to the unique electronic construction, particularly when the Fermi

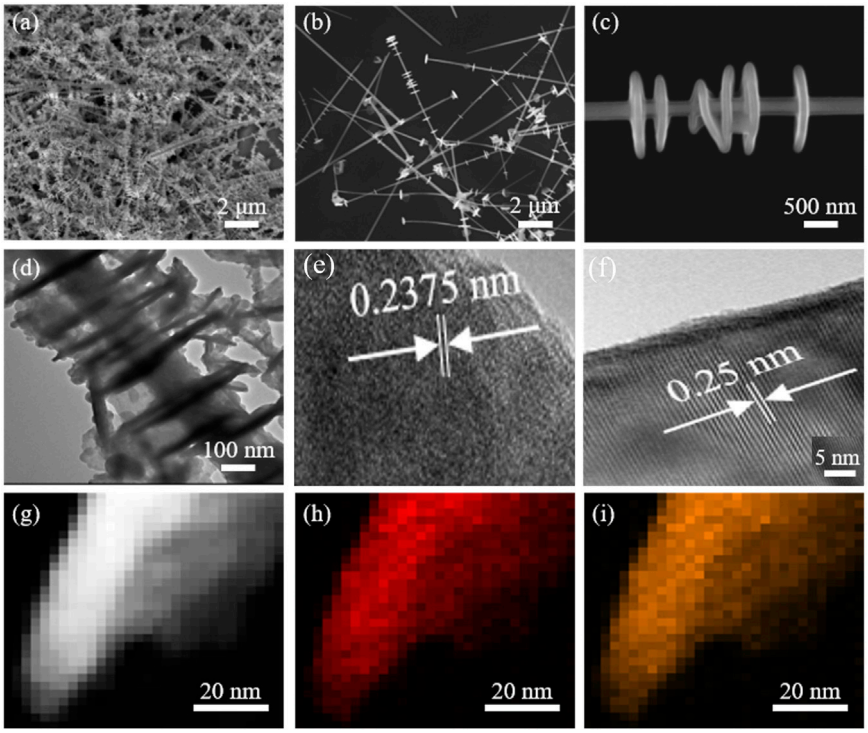


FIGURE 3
**(A–C)** SEM images of the $Sb_2Te_3$/Te nanostrings at different magnifications. **(C)** TEM image of the $Sb_2Te_3$/Te nanostrings. **(D)** TEM image of the $Sb_2Te_3$/Te nanostrings. **(E,F)** HRTEM images of the $Sb_2Te_3$/Te nanostrings **(G–I)** and elemental mapping images of $Sb_2Te_3$/Te nanostrings.

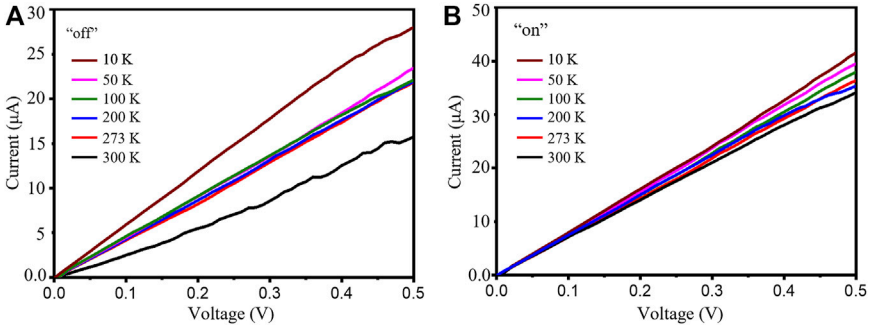


FIGURE 4
I-V curves of the $Sb_2Te_3$/Te nanostrings in the dark **(A)** and under illumination **(B)** at various temperatures from 10 to 300 K.

level is close to the Dirac point. The I-V curves are virtually linear when illuminated by 980 nm light and show that the Te nanowire and Pt-Ti/Au electrode can form a contact form with Ohmic contact.

Considering the temperature-dependent electrical properties of the $Sb_2Te_3$/Te nanostrings, the photoresponse characteristics at different temperatures were studied. Figure 5 shows the temporal photoresponse properties of the device at 10K, 50K, 100K, 200K, 273K, and 300K with periodic irradiation of 980 nm at a bias voltage of 1 V. The figure shows that when the bias voltage is kept unchanged, the change of the current is consistent with the changes of the temperatures. The dark current can decrease to the lowest value of 8.5 μA at 100K and the photocurrent can reach its highest value of 79.5 μA at 10K under the 1 V bias voltage and on/off illumination of

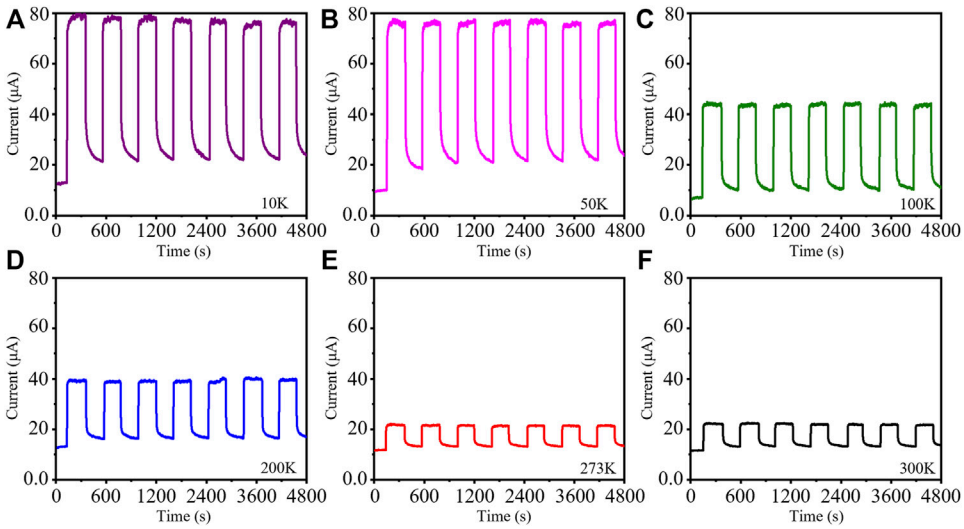


FIGURE 5
Time-resolved photoresponse of the $Sb_2Te_3$/Te nanostring photodetector under different temperatures at 1 V bias voltage: **(A)** 10 K, **(B)** 50 K, **(C)** 100 K, **(D)** 200 K, **(E)** 273 K, and **(F)** 300 K.

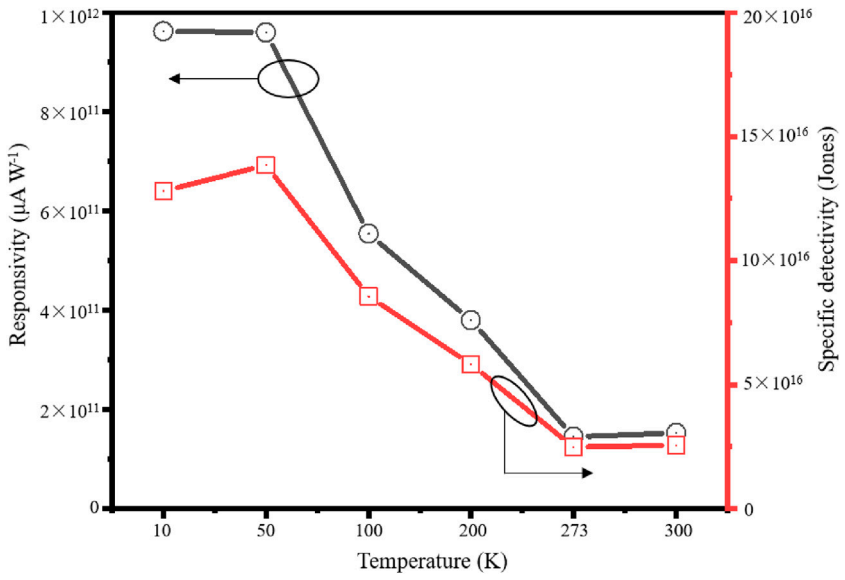


FIGURE 6
Responsivity (*R*) and detectivity (*D**) of a selenium self-supporting film photodetector under different light intensities.

980 nm light. Additionally, the photoresponse characteristics of the as-constructed photodevice are homologous at temperatures of 273 and 300 K due to the temperature effect (Qi et al., 2018). The optical switching behavior of this photodetector is highly reversible with good stability and reproducibility. There is no significant degradation in its switching behavior even after multiple periodic optical switching changes. It is worth noting that different from the conventional photodetectors with a very fast response speed based on semiconductor nanostructures, the as-fabricated device has a moderately (several hundred seconds) slow rising and falling time (Cai et al., 2022). The difference in the response speed is possible due to their distinction of the band structures.

The responsivity ® and detectivity (D*) are also two key index factors of photodetectors. "R" is the photocurrent per unit incident light power on the calculating device, which can reflect the sensitivity of the device to the intensity of incident light. "D*" shows the performance of detecting weak light (Yu et al., 2018). These two key parameters can be derived according to the following equations:

$$R = \frac{I_{ph} - I_d}{PS} \quad (1)$$

$$D^* = \frac{RS^{1/2}}{(2eI_d)^{1/2}} \quad (2)$$

where $I_{ph}$ is the photocurrent, $I_d$ is the dark current, $P$ is the incident light power density (0.5 mW cm$^2$), $S$ is the effective area of the device receiving light (~1.5 × 10$^{-8}$ cm$^2$), and $e$ is the fundamental charge (1.6 × 10$^{-19}$ C) (Xu et al., 2022; Zhang et al., 2022). According to Eqs 1, 2, the "R" and "D*" of the detector under 3 V bias voltage and different illumination intensities are shown in Figure 6. The results show that the detector has a photoresponsive®(R) of approximately 9.5 × 10$^{11}$ μA W$^{-1}$ and a detectable rate (D*) of approximately 1.3×10$^{17}$ Jones under 1 V bias voltage and 50 K with the light irradiation of 980 nm.

## Conclusion

We report a near NIR photodetector based on a topological insulator antimony telluride ($Sb_2Te_3$) and tellurium (Te) heterostructure, which are prepared by controllable hydrothermal and photolithography methods. The elaborately constructed device exhibits topological insulator properties, and the resistance especially decreases with increasing temperature in the range of 10–300 K. Further optoelectronic characterization shows that the as-fabricated photodetector delivers obvious sensitivity to 980 nm light illumination. The performance of responsivity and detectivity are remarkable and are much better than those of other Te-based topological insulator photodetector devices. The research suggests that the as-constructed NIR photodetector may have great potential in low-temperature optoelectronic devices.

## Data availability statement

The datasets presented in this study can be found in online repositories. The names of the repository/repositories and accession number(s) can be found at: https://www.ccdc.cam.ac.uk/structures/- 2211392 and 2211393.

## Author contributions

All authors listed have made a substantial, direct, and intellectual contribution to the work and approved it for publication.

## Funding

This work was financially supported by the National Natural Science Foundation of China (Nos. 52171207, 52271211, 52072120, and 52204311), HORIZON- Marie Skłodowska-Curie Actions-2021-PF (No. 101065098), the Hunan Provincial Natural Science Foundation of China (Nos. 2022JJ40162 and 2022JJ40159), the Scientific Research Fund of Hunan Provincial Education Department, China (Nos. 21B0406 and 21B0591), and the Scientific and Technological Project of Yueyang City.

## Conflict of interest

The authors declare that the research was conducted in the absence of any commercial or financial relationships that could be construed as a potential conflict of interest.

## Publisher's note

All claims expressed in this article are solely those of the authors and do not necessarily represent those of their affiliated organizations or those of the publisher, the editors, and the reviewers. Any product that may be evaluated in this article, or claim that may be made by its manufacturer, is not guaranteed or endorsed by the publisher.

## Supplementary material

The Supplementary Material for this article can be found online at: https://www.frontiersin.org/articles/10.3389/fchem.2022.1060523/full#supplementary-material

## References

Cai, Y., Hou, T.-T., Wang, C.-Y., Tang, Y.-H., Zhang, Z.-Y., Zhang, D., et al. (2022). Fluorescence enhancement of dicyanomethylene-4H-pyran derivatives in solid state for visualization of latent fingerprints. *Front. Chem.* 10, 943925. doi:10.3389/fchem.2022.943925

Chen, G., Dresselhaus, M. S., Dresselhaus, G., Fleurial, J. P., and Caillat, T. (2003). Recent developments in thermoelectric materials. *Int. Mat. Rev.* 48 (1), 45–66. doi:10.1179/095066003225010182

Cheng, L., Chen, Z.-G., Yang, L., Han, G., Xu, H.-Y., Snyder, G. J., et al. (2013). T-shaped $Bi_2Te_3$-Te heteronanojunctions: Epitaxial growth, structural modeling, and thermoelectric properties. *J. Phys. Chem. C* 117 (24), 12458–12464. doi:10.1021/jp4041666

Cozzoli, P. D., Pellegrino, T., and Manna, L. (2006). Synthesis, properties and perspectives of hybrid nanocrystal structures. *Chem. Soc. Rev.* 35 (11), 1195–1208. doi:10.1039/b517790c

Dong, G.-H., Zhu, Y.-J., and Chen, L.-D. (2010). Microwave-assisted rapid synthesis of $Sb_2Te_3$ nanosheets and thermoelectric properties of bulk samples prepared by spark plasma sintering. *J. Mat. Chem.* 20 (10), 1976–1981. doi:10.1039/b915107a

Duan, T., Liao, C., Chen, T., Yu, N., Liu, Y., Yin, H., et al. (2015). Single crystalline nitrogen-doped InP nanowires for low-voltage field-effect transistors and photodetectors on rigid silicon and flexible mica substrates. *Nano Energy* 15, 293–302. doi:10.1016/j.nanoen.2015.05.002

Fu, L., Kane, C. L., and Mele, E. J. (2007). Topological insulators in three dimensions. *Phys. Rev. Lett.* 98 (10), 106803. doi:10.1103/physrevlett.98.106803

Ikeda, T., Collins, L. A., Ravi, V. A., Gascoin, F. S., Haile, S. M., and Snyder, G. J. (2007). Self-assembled nanometer lamellae of thermoelectric PbTe and $Sb_2Te_3$ with epitaxy-like interfaces. *Chem. Mat.* 19 (4), 763–767. doi:10.1021/cm062121p

Jiang, J., Chen, L., Bai, S., Yao, Q., and Wang, Q. (2005). Thermoelectric properties of p-type $(Bi_2Te_3)_x$ $(Sb_2Te_3)_{1-x}$ crystals prepared via zone melting. *J. Cryst. Growth* 277 (1-4), 258–263. doi:10.1016/j.jcrysgro.2004.12.144

Jin, C., Zhang, G., Qian, T., Li, X., and Yao, Z. (2005). Large-area $Sb_2Te_3$ nanowire arrays. *J. Phys. Chem. B* 109 (4), 1430–1432. doi:10.1021/jp046100z

Lee, J. S., Brittman, S., Yu, D., and Park, H. (2008). Vapor-liquid-solid and vapor-solid growth of phase-change $Sb_2Te_3$ nanowires and $Sb_2Te_3$/GeTe nanowire heterostructures. *J. Am. Chem. Soc.* 130 (19), 6252–6258. doi:10.1021/ja711481b

Li, Z., Zheng, S., Zhang, Y., Chen, H., Huang, T., and Lu, G. (2015). High-yield synthesis, controllable evolution, and thermoelectric properties of Te/$Bi_2Te_3$ heterostructure nanostrings. *J. Electron. Mat.* 44 (6), 2061–2067. doi:10.1007/s11664-015-3656-1

Matsunaga, T., Kojima, R., Yamada, N., Kifune, K., Kubota, Y., Tabata, Y., et al. (2006). Single structure widely distributed in a GeTe-$Sb_2Te_3$ pseudobinary system: A rock salt structure is retained by intrinsically containing an enormous number of vacancies within its crystal. *Inorg. Chem.* 45 (5), 2235–2241. doi:10.1021/ic051677w

Matsunaga, T., Yamada, N., and Kubota, Y. (2004). Structures of stable and metastable $Ge_2Sb_2Te_5$, an intermetallic compound in GeTe-$Sb_2Te_3$ pseudobinary systems. *Acta Crystallogr. B* 60 (6), 685–691. doi:10.1107/s0108768104022906

Pradhan, A., Roy, A., Tripathi, S., Som, A., Sarkar, D., Mishra, J. K., et al. (2017). Ultra-high sensitivity infra-red detection and temperature effects in a graphene-tellurium nanowire binary hybrid. *Nanoscale* 9 (27), 9284–9290.

Qi, J., Ma, N., Ma, X., Adelung, R., and Yang, Y. (2018). Enhanced photocurrent in $BiFeO_3$ materials by coupling temperature and thermo-phototronic effects for self-powered ultraviolet photodetector system. *ACS Appl. Mat. Interfaces* 10 (16), 13712–13719. doi:10.1021/acsami.8b02543

Sosso, G., Caravati, S., and Bernasconi, M. (2009). Vibrational properties of crystalline $Sb_2Te_3$ from first principles. *J. Phys. Condens. Matter* 21 (9), 095410. doi:10.1088/0953-8984/21/9/095410

Sun, H., Jiang, T., Zang, Y., Zheng, X., Gong, Y., Yan, Y., et al. (2017). Broadband ultrafast photovoltaic detectors based on large-scale topological insulator $Sb_2Te_3$/STO heterostructures. *Nanoscale* 9 (27), 9325–9332.

Tominaga, J., Fons, P., Kolobov, A., Shima, T., Chong, T. C., Zhao, R., et al. (2008). Role of Ge switch in phase transition: Approach using atomically controlled GeTe/$Sb_2Te_3$ superlattice. *Jpn. J. Appl. Phys. (2008).* 47 (7S1), 5763–5766. doi:10.1143/jjap.47.5763

Tominaga, J., Kolobov, A., Fons, P., Nakano, T., and Murakami, S. (2014). Ferroelectric order control of the Dirac-semimetal phase in GeTe-$Sb_2Te_3$ superlattices. *Adv. Mat. Interfaces* 1 (1), 1300027. doi:10.1002/admi.201300027

Wang, Y.-L., Luo, T., Zhang, J., Fan, C., Li, X., Li, C., et al. (2022). AIE-based fluorescent micro-optical sectioning tomography for automatic 3D mapping of β-amyloid plaques in Tg mouse whole brain. *Chem. Eng. J.* 446, 136840. doi:10.1016/j.cej.2022.136840

Wesolowski, A., Stresman, G., Eagle, N., Stevenson, J., Owaga, C., Marube, E., et al. (2014). Quantifying travel behavior for infectious disease research: A comparison of data from surveys and mobile phones. *Sci. Rep.* 4, 5678. doi:10.1038/srep05678

Xia, Y., Qian, D., Hsieh, D., Wray, L., Pal, A., Lin, H., et al. (2009). Observation of a large-gap topological-insulator class with a single Dirac cone on the surface. *Nat. Phys.* 5 (6), 398–402. doi:10.1038/nphys1274

Xu, T., Yin, H., Yu, P., He, Z., Chen, N., Shen, W., et al. (2022). Ultraviolet photodetectors based on dimetallofullerene $Lu_2$@Cs(6)-$C_{82}$ nanorods. *ACS Appl. Nano Mat.* 5 (1), 1683–1689. doi:10.1021/acsanm.1c04497

Yang, J., Aizawa, T., Yamamoto, A., and Ohta, T. (2000). Thermoelectric properties of p-type $(Bi_2Te_3)_x(Sb_2Te_3)_{1-x}$ prepared via bulk mechanical alloying and hot pressing. *J. Alloys Compd.* 309 (1-2), 225–228. doi:10.1016/s0925-8388(00)01063-x

Yin, H., Yu, X.-X., Yu, Y.-W., Cao, M.-L., Zhao, H., Li, C., et al. (2018). Tellurium nanotubes grown on carbon fiber cloth as cathode for flexible all-solid-state lithium-tellurium batteries. *Electrochim. Acta* 282, 870–876. doi:10.1016/j.electacta.2018.05.190

Yu, X.-X., Yin, H., Li, H.-X., Zhang, W., Zhao, H., Li, C., et al. (2017). Piezo-phototronic effect modulated self-powered UV/visible/near-infrared photodetectors based on CdS:P3HT microwires. *Nano Energy* 34, 155–163. doi:10.1016/j.nanoen.2017.02.033

Yu, X.-X., Yin, H., Li, H.-X., Zhao, H., Li, C., and Zhu, M.-Q. (2018). A novel high-performance self-powered UV-vis-NIR photodetector based on a CdS nanorod array/reduced graphene oxide film heterojunction and its piezo-phototronic regulation. *J. Mat. Chem. C* 6 (3), 630–636.

Zhang, H., li, L., Zheng, D.-s., Xiong, Y., Yu, C., Yin, H., et al. (2022). Broadband photodetector based on vapor-deposited selenium self-supporting films. *Ceram. Int.* 48 (19), 27750–27757. doi:10.1016/j.ceramint.2022.06.075

Zheng, K., Luo, L.-B., Zhang, T.-F., Liu, Y.-H., Yu, Y.-Q., Lu, R., et al. (2015). Optoelectronic characteristics of a near infrared light photodetector based on a topological insulator $Sb_2Te_3$ film. *J. Mat. Chem. C* 3 (35), 9154–9160. doi:10.1039/c5tc01772f

Zhong, B. N., Fei, G. T., Fu, W. B., Gong, X. X., Xu, S. H., Gao, X. D., et al. (2017). Controlled solvothermal synthesis of single-crystal tellurium nanowires, nanotubes and trifold structures and their photoelectrical properties. *CrystEngComm* 19 (20), 2813–2820. doi:10.1039/c7ce00497d

frontiers | Frontiers in Chemistry

TYPE Original Research
PUBLISHED 17 January 2023
DOI 10.3389/fchem.2022.1089080



OPEN ACCESS

EDITED BY
Feng Gu,
Jiangxi University of Science and Technology, China

REVIEWED BY
Shiyong Zhao,
University of Adelaide, Australia
Dongliang Yan,
Guangxi University for Nationalities, China

*CORRESPONDENCE
Kamel Guedri,
kmguedri@uqu.edu.sa

SPECIALTY SECTION
This article was submitted to Physical Chemistry and Chemical Physics, a section of the journal Frontiers in Chemistry

RECEIVED 03 November 2022
ACCEPTED 30 December 2022
PUBLISHED 17 January 2023

CITATION
Fahim T, Laouedj S, Abderrahmane A, Driss Z, Tag-ElDin ESM, Guedri K and Younis O (2023), Numerical study of perforated obstacles effects on the performance of solar parabolic trough collector.
*Front. Chem.* 10:1089080.
doi: 10.3389/fchem.2022.1089080



# Numerical study of perforated obstacles effects on the performance of solar parabolic trough collector

Tayeb Fahim[1], Samir Laouedj[1], Aissa Abderrahmane[2], Zied Driss[3], El Sayed Mohamed Tag-ElDin[4], Kamel Guedri[5]* and Obai Younis[6]

[1]Materials and Reactive Systems Laboratory (LMSR), Djillali Liabes University, Sidi Bel Abbes, Algeria, [2]Laboratoire de Physique Quantique de la Matière et Modélisation Mathématique (LPQ3M), Université Mustapha Stambouli de Mascara, Mascara, Algeria, [3]Laboratory of Electromechanical Systems (LASEM), National School of Engineers of Sfax, University of Sfax, Sfax, Tunisia, [4]Center of Research, Faculty of Engineering, Future University in Egypt, New Cairo, Egypt, [5]Mechanical Engineering Department, College of Engineering and Islamic Architecture, Umm Al-Qura University, Makkah, Saudi Arabia, [6]Department of Mechanical Engineering, College of Engineering in Wadi Addwasir, Prince Sattam Bin Abdulaziz University, Al-kharj, Saudi Arabia

The current work presents and discusses a numerical analysis of improving heat transmission in the receiver of a parabolic trough solar collector by introducing perforated barriers. While the proposed approach to enhance the collector's performance is promising, the use of obstacles results in increased pressure loss. The Computational Fluid Dynamics (CFD) model analysis is conducted based on the renormalization-group (RNG) k-ε turbulent model associated with standard wall function using thermal oil D12 as working fluid The thermo-hydraulic analysis of the receiver tube with perforated obstacles is taken for various configurations and Reynolds number ranging from 18,860 to 81,728. The results are compared with that of the receiver without perforated obstacles. The receiver tube with three holes (PO3) showed better heat transfer characteristics. In addition, the Nusselt number (Nu) increases about 115% with the increase of friction factor 5–6.5 times and the performance evaluation criteria (PEC) changes from 1.22 to 1.24. The temperature of thermal oil fluid attains its maximum value at the exit, and higher temperatures (462.1 K) are found in the absorber tube with perforated obstacles with three holes (PO3). Accordingly, using perforated obstacles receiver for parabolic trough concentrator is highly recommended where significant enhancement of system's performance is achieved.

KEYWORDS

**nanofluid, parabolic trough solar collector, Nusselt number, perforated obstacles, numerical investigation**

## Highlights

- The flow and thermal characteristics of through solar collector was examined.
- The benefits effects of using perforated baffles to enhance heat transfer was analyzed.
- The position and number of perforations was optimized to obtain the best heat transfer.

## Introduction

Growth in global energy demand and the overuse of non-renewable energy sources such as petrol and natural gas have reduced these resources' availability and resulted in harmful severe environmental consequences such as air pollution and global warming (Jamshed et al., 2021; Wu et al., 2021; Zandalinas et al., 2021). Researchers focused on improving technologies involved in renewable energy sources such as solar to address these issues. Solar collectorsuse a heat-exchanging fluid to convert solar power to thermal power. In fact, using the absorber tube absorbs solar light and transfers heat to the absorber fluid. Therefore, the solar collector increases its internal energy, which may be utilized for other purposes (Sayed et al., 2020; Pandey et al., 2021; Shahzad et al., 2021).

Changing traditional working fluids in solar collectors to nanofluids is one of the activities that has gotten a lot of attention in recent years to improve their thermal performance (Aman et al., 2015; Fares et al., 2020; Mourad et al., 2021; Hassan et al., 2022; Khalid et al., 2022). Dehaj et al. (2021) designed and developed an experimental test bench to examine the parabolic trough solar collector (PTSC) efficiency using $NiFe_2O_4$/Water nanofluid as a working fluid. They used a U-shaped absorber tube. Their results show that the PTSC was more effective when the Nickel Ferrite nanofiuid was introduced. In fact, for a volumetric fraction of .05% and a fiow rate of 3 L/min, an efficiency of 51% can be achieved. Farhana et al. (Farhana et al., 2021)investigated the flat plate solar collector efficiency with crystal nano-cellulose (CNC) nanofluid through an experiment. They revealed that the efficiency of the FPSC was enhanced by 2.48% and 8.46% when .5% $Al_2O_3$ and .5% CNC nanofluids were used, respectively.

Hosseini et al. (Hosseini Seyed and Shafiey Dehaj, 2021) calculated the energetic performance of a PTSC working with $Al_2O_3$ and GO nanofiuid with a .2% volume fraction. They found that the thermal efficiency of the PTSC was improved by 63.2% and 32.1% when the GO nanofiuid and the $Al_2O_3$ nanofiuid were used, respectively. Vahidinia et al. (Vahidinia et al., 2021) valued the thermal performance of the PTSC using three types of Syltherm 800 based nanofluids. The first two are $Al_2O_3$ and $SiO_2$, and the third is a hybrid nanofluid merging the above two. They illustrated that the exergy and energy performance of the hybrid nanofluid is always the highest. Vital et al. (Vital Caio. et al., 2021) evaluated the thermo-optical properties of TMN nanofluids such as TiN, ZrN, and HfN in an aqueous medium where the nanofluids were used as working fluids for a direct absorption solar collector (DASC). According to their results, the efficiencies of DASC employing TiN, ZrN, and HfN NF are 6.3%, 5.2%, and 5.6%, respectively. They also stated that these enhancements could be achieved without increasing the demands of pumping power by using a low-concentration regime. Ould-Lahoucine et al. (Ould-Lahoucine et al., 2021) proposed a novel technique to identify the ideal height of the rectangular cooling channel for photovoltaic/thermal (PV/T) collector system employing $TiO_2$-water nanofluid. Before that, they discussed this nanofluid's energy and exergy performances inside the PV/T.

Some researchers focused on nanofluid flow through the absorber tube, which is essentially a channel. Esmaeili et al. (Esmaeili et al., 2019) applied a two-phase model to inspect turbulent flow with both forced and free convection of nanofluid within a 3D rectangular channel (Ajeel Raheem et al, 2022). numerically analyzedthe flow pattern and heat transfer properties of ZnO-water nanofluid within a new channel, where both curved and corrugated profiles for the walls and E-shaped baffles. Berrehal et al. (Berrehal and Sowmya, 2021) analyzed nanofluid flow between two inclined walls using the optimal homotopy asymptotic technique. Ajeel et al. (Ajeel Raheem. et al., 2021) utilized the multi-phase mixture model to evaluate the thermal-hydraulic performance of binary hybrid nanofiuid flowing within a curved-corrugated channel. The results show that using the binary hybrid nanoparticles enhanced the thermal characteristics of the base fluid, thus improving the heat transfer rate in the system. This effect can be furthered by raising the volume fraction or the blockage ratio and reducing the pitch angle.

Recently, a new technique has been employed to enhance nanofluid's heat transport and flow inside channels. It consists of inserting a vortex generator of various shapes and sizes. Their primary purpose is to increase the flow turbulence intensity and eliminate the laminar boundary layer near the walls of the channels. Maadi et al. (Seyed Reza et al., 2021) attempted to enhance the performance of a photovoltaic-thermal system (PV/T) by employing nanofiuid and a wavy-strip insert. The outcomes show that using $Al_2O_3$water-based nanofiuid and wavy-strip inserts improved the PVT system's thermal efficiency by 12.06% compared to typical PVT. Mashayekhi et al. (Ramin et al., 2020) analyzed the impact of two rows of twisted conical strip inserts on the flow of a water-$Al_2O_3$ nanofluid in an oval tube. Their study illustrated that inward Co-Conical inserts provide the highest value of heat transport rate, as it can reach 17% higher than tube without inserts. Hamid et al. (Hamid et al., 2019) performed experiments to study the combined impacts of using $TiO_2$–$SiO_2$ nanofluids and wire coil inserts on a tube's flow and heat transfer. Chadi et al. (Kamel et al., 2021) studied a diamond-water nanofluid's heat transfer and flow through micro-channels fitted with parallelogram ribs and pie-shaped ribs. The outcomes show that the heat transfer rate was highest when the parallelogram ribs were used. Jing et al. (Jing et al., 2020) underlined the significance of the magnetic field and the shape of heating fins on the flow and heat transport in a rectangular enclosure loaded with nanofluid. Azmi et al. (Azmi et al., 2021) scrutinized the performance of $TiO_2$–$SiO_2$/water hybrid nanofluid with various composition ratios flowing inside a tube equipped with wire coil inserts. The outcomes showed that the highest thermal performance factor reached (1.72) with a composition ratio R = .2. In addition, the wire coils can enhance the heat transfer of $TiO_2$–$SiO_2$nanofluids by up to 211.75%. Rathnakumar et al. (Rathnakumar et al., 2014) considered improving heat transport turbulent fiow in a tube by equipping it with helical screw louvered rod inserts and employing (CNT)/water nanofiuids at various volume concentrations. The calculations indicated that the helical louvered rod inserts cause augmentation in heat transfer for a certain Reynolds number compared to a plain tube, whereas the friction factor also increased. Kumar et al. (Kumar et al., 2018) and Sundar et al. (Syam et al., 2020) explored the effect of twisted tape and wire coil with core-rod inserts on the heat transport, the friction factor of $Fe_3O_4$/water nanofiuid fiow inside a double pipe U-bend heat exchanger. Sundar et al. (Syam, Said, Saleh, Singh, Antonio Sousa) calculated the thermal-hydraulic performance of rGO/$Co_3O_4$ hybrid nanofluid in a plain horizontal tube and another one fitted with longitudinal strip inserts. Their findings indicate that the Nusselt number is boosted by 25.65% when the concentration of hybrid nanoparticles in water is .2%. It is further improved by 110.56% when a straight strip is inserted. However, employing linear strip inserts and hybrid nanofluids results in aninsignificantdrawback in fluid friction. Alnaqi et al.

(Abdulwahab et al., 2021)examined the performance of a solar collector fitted with two twisted tape inserts and loaded with MgO-MWCNT thermal oil-based hybrid nanofluid. Mohammed et al. (Hussein et al., 2019) studied numerically the overall thermo-hydraulic performance of nanofiuids in forced convection fiow inside circular tubes fitted with divergent and convergent conical rings inserts. According to their results, the divergent ring inserts produced a 365% enhancement in the performance criteria, making them the best option. Sheikhzadeh et al. (Ghanbar et al., 2019) examined an ethylene-glycol-based hybrid nanofluid's thermodynamic and flow properties in a rectangular channel with turbulators with various wing forms. The result shows that the trapezoidal wings with a volume fraction of .6% provide the best heat transfer performance considering fluid flow.

In recent years, various combinations of nanofluids as well as affecting parameters on the different structures are taken for analysis-oriented with the thermal application such as solar collectors. They have been considered and developed, as a result, effective enhancement of heat transfer achieved by many research works (Rathnakumar et al., 2014; Kumar et al., 2018; Ghanbar et al., 2019; Hamid et al., 2019; Hussein et al., 2019; Jing et al., 2020; Ramin et al., 2020; Syam et al., 2020; Syam, Said, Saleh, Singh, Antonio Sousa; Abdulwahab et al., 2021; Azmi et al., 2021; Kamel et al., 2021; Seyed Reza et al., 2021). To the authors' knowledge, no research has been done on the examination of the position and number of perforations to optimize and to enhance the performance of a photovoltaic-thermal system (PV/T) by employing nanofiuid and a wavy-strip insert. Accordingly, the aim of this study is to improve heat transfer inside parabolic through solar receiver using two different passive methods, perforated obstacles and nanoparticles. This work also investigates the effects of perforated obstacles inserted centrally inside the absorber of a PTC for various cases. Inserts are placed centrally, the diameters of the perforations are large, they are fixed to the top surface of the receiver tube, and their dimensions are much smaller than those found in the literature. In reality, inserting holes in obstacles aids fluid mixing by breaking the thermal boundary layer and aids fluid mixing due to the non-uniform circumferential heat flow profile on the receiver; hence the thermal performance is remarkably improved. The motivated work aims to answer to the following research questions.

- What is the effect of the perforated obstacles on heat transfer in a solar parabolic trough collector using nanofluids?
- What is the impact of the position and number of these perforations on the temperature of thermal oil fluid used?
- What are the benefits effects of using perforated baffles to enhance heat the performance evaluation criteria.
- How friction factor values decrease with the increase in the number of these holes?

# Model description

## Physical model

Figure 1 depicts the solar parabolic system's schematic and the collector's receiver. The parabolic trough collector (PTC) concentrates the direct sunlight on the bottom perimeter of the parabolic trough receiver (PTR). In contrast, the top perimeter of the PTR is exposed to non-concentrated solar irradiation (Figure 1A). Figure 1 shows a cross-section drawing of the PTR (b). A glass cover protects the stainless-steel absorber tube. The space between the metal tube and the glass cover is constantly vacuumed to reduce heat loss. The focused solar energy travels through the glass cover and lands on the metal tube's outer surface. The concentrated solar energy is absorbed and transformed into heat by the metal tube. The heat is conveyed to the heat transfer fluid by conduction and convection modes. The receiver model employed in this study intends to improve the heat transmission performance of PTR by introducing absorber tubes with perforated barriers (Figures 2, 3). Table 1 shows the geometrical characteristics of PTR and perforated barriers. Table 2 also depicts the thermophysical parameters of the working fluid (Thermal oil D12), perforated barriers, and absorber tube.

## Boundary conditions

The boundary conditions are as follows.

- Fluid inlet:

$$V_{x=}V_{in}, \quad V_{y=}V_z = 0 m/s, \tag{1}$$

$$T_f = T_{in} = 400\,K\ (L = 0,\ 00^0 \le \varphi \le 360^\circ \tag{2}$$

- At the walls

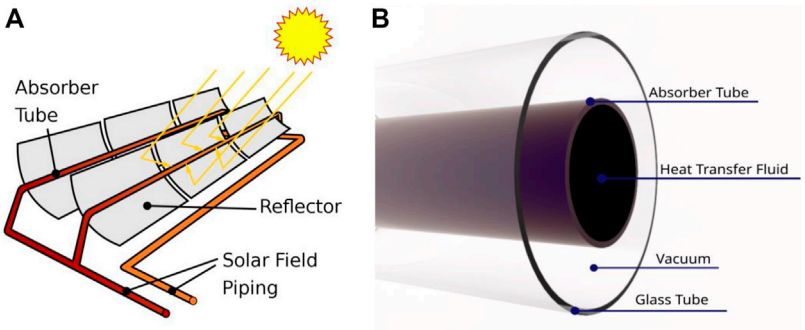


FIGURE 1
**(A)** Parabolic trough collector (PTC). **(B)** Cross-sectional diagram of the parabolic trough receiver (PTR) (Wang et al., 2015).

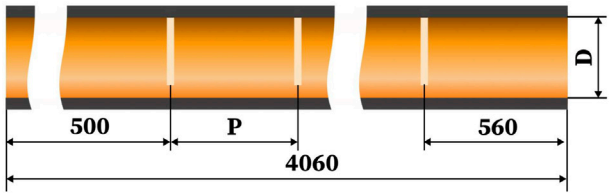


FIGURE 2
The receiver's longitudinal segment with perforated obstruction inserts.

The upper half perimeter of the metal tube is exposed to the uniform heat flux qt, which is calculated as:

$$q_t = DNI \times TGE \times AMT = 1000 \times 0.95 \times 0.96$$
$$= 912 W/m^2 \left(0 \le L \le 4.06 m, 0^o \le \varphi \le 180^o\right) \quad (3)$$

Where DNI, TGE, and AMT are the solar irradiation, the glass envelope transmissivity, and the metal tube absorptivity, respectively. The concentrated solar irradiation qcal was computed by. (Kamel et al., 2021) (Figure 4). The lower half perimeter of the metal tube is subjected to the heat flux qb, which is calculated as:

$$q_b = q_{cal}\ ; \ \left(0 \le L \le 4.06\ m,\ 180^\circ \le \varphi \le 360^\circ\right) \quad (4)$$

- Fully formed conditions are enforced at the fluid outflow.
- In this study, the outer absorber wall is subjected to a non-uniform heat flux estimated using the Monte Carlo Ray Tracing (MCR) method and a DNI of 1000 W/m2. Figure 4 depicts the variation of the heat flux distribution along the bottom-half perimeter of the absorber tube for present and Hachicha et al. (Hachicha et al., 2013) models. Using the current calculation, the heat flux distribution pattern of the absorber tube is plotted in Figure 5.

# Numerical model

## Numerical method

The computational fluid dynamics (CFD) modeling technique was used in this work. The finite volume technique (FVM) is used to discretize the equations. The resulted equations system is solved numerically by employing the commercial package software ANSYS-FLUENT (Release 17.1). The RNG k-ε turbulence model is employed to simulate the turbulent flow of Thermal oil D12 in the solar collector's absorber tube. Second-order UPWIND and QUICK methods are used for discretizing the convective components in momentum and energy equations. For dealing with pressure-velocity coupling, the SIMPLEC method is

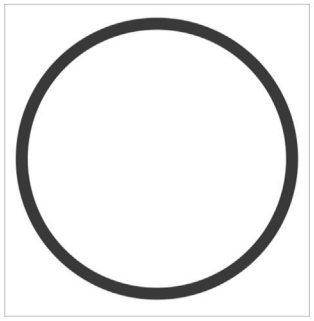

**Case 1:** Smooth absorber.

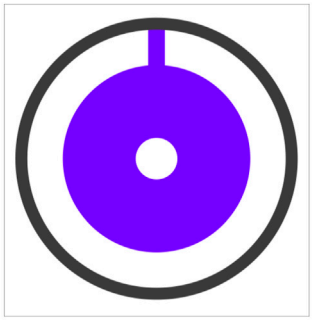

**Case 2:** Perforated obstacles with one hole (PO1).

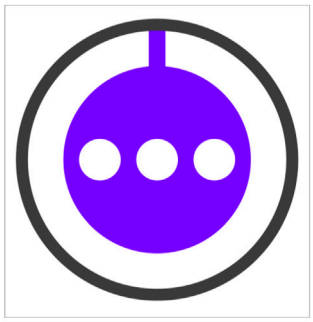

**Case 3:** Perforated obstacles with three holes (PO3).

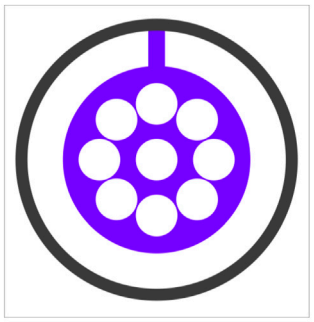

**Case 4:** Perforated obstacles with nine holes (PO9).

FIGURE 3
Cross-section of the receiver tube with perforated obstacles and smooth absorber.

**TABLE 1 The PTR model parameters and perforated obstacles.**

| Parameter | Values | Reference |
|---|---|---|
| Length of the absorber (m) | 4.06 | Wu et al., 2014a, Wu et al., 2014b |
| Internal diameter of the metal tube (m) | .064 | |
| External diameter of the metal tube (m) | .07 | |
| Internal diameter of the Glass cover (m) | .117 | |
| External diameter of the Glass cover (m) | .12 | |
| Glass envelope transmissivity | .95 | |
| Metal tube absorptivity | .96 | |
| Obstacle diameter (mm) | 46 | |
| Perforated obstaclesthickness (mm) | 2 | |
| Diameter of the perforation (mm) | 10 | |
| Distance between two consecutive perforated obstacles (mm) | 128 | |
| Number of perforated obstacles in the absorber tube | 25 | |

utilized. For all equations, the convergence threshold is 10–6. GAMBIT version 2.2 is used to generate and the mesh of the physical model (Figure 6).

## Governing equations

The instantaneous Navier Stokes equation is used to generate the RNG k-turbulent model by using a mathematical approach known as "renormalization group" (RNG) methods (Gnielinski, 1976; Yakhot et al., 1992). The values of k (turbulent kinetic energy) and ε (turbulent dissipation rate) are determined by equations:

$$\rho\left(\frac{\partial k}{\partial t}+\overline{u_j}\frac{\partial k}{\partial x_j}\right)=\frac{\partial}{\partial x_j}\left[\left(\mu+\frac{\mu_t}{\sigma_{k\,(RNG)}}\right)\frac{\partial k}{\partial x_j}\right]+P_k-\rho\varepsilon \tag{5}$$

$$\rho\left(\frac{\partial \varepsilon}{\partial t}+\overline{u_i}\frac{\partial \varepsilon}{\partial x_i}\right)=\frac{\partial}{\partial x_j}\left[\left(\mu+\frac{\mu_t}{\sigma_{\varepsilon\,(RNG)}}\right)\frac{\partial \varepsilon}{\partial x_j}\right]+\frac{\varepsilon}{k}\left(C_{1\varepsilon(RNG)}P_k-C_{2\varepsilon(RNG)}\rho\frac{\varepsilon}{k}\right) \tag{6}$$

Where

$$P_k=-\rho\overline{u_i'u_j'}\frac{\partial \overline{u_i}}{\partial x_j} \tag{7}$$

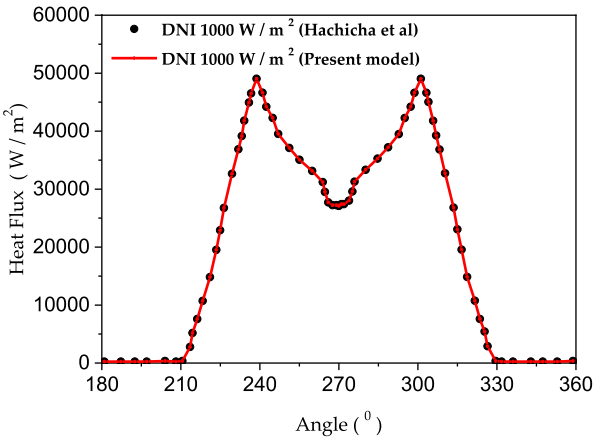


FIGURE 4
Heat flux distribution variation along the bottom half perimeter of the absorber tube.

$$C_{2\varepsilon(RNG)}=\frac{C_{2\varepsilon}+C_\mu\eta^3\left(1-\frac{\eta}{\eta_0}\right)}{1+\beta\eta^3} \tag{8}$$

$$\eta=\frac{k}{\varepsilon}\left(2S_{ij}S_{ij}\right)^{1/2} \tag{9}$$

The turbulent viscosity $\mu_t$ is calcluated as:

$$\mu_t=\rho C_\mu\frac{k^2}{\varepsilon} \tag{10}$$

Where the parameter $\rho$ represents the fluid's density.

$S_{ij}$ denotes the strain tensor rate and is defined as:

$$S_{ij}=\frac{1}{2}\left(\frac{\partial \overline{u_i}}{\partial x_j}+\frac{\partial \overline{u_j}}{\partial x_i}\right) \tag{11}$$

Table 3 summarizes the model constants used.

# Results and discussion

## Grid independency

Numerous calculations were undertaken to determine the total number of grid points required to create an array adequate for measuring flux and thermal field in order to justify the simulation solution's accuracy and consistency. Table 4 illustrates the evolution of the average Nusselt number as a cell number function for Reynolds numbers ranging from $10^4$ to $10^6$.

**TABLE 2 Thermophysical properties of the working fluid, perforated obstacles, and absorber tube.**

| | Working fluid (thermal oil D12) | Perforated obstacles and absorber tube (stainless steel) | Reference |
|---|---|---|---|
| Density (Kg/m3) | 679 | 8,027 | Solutia, (1998) |
| Specific heat (J/Kg.K) | 2,571 | 500 | |
| Thermal conductivity (W/m.K) | .091 | 20 | |
| Viscosity (N.s/m2) | .000346 | — | |

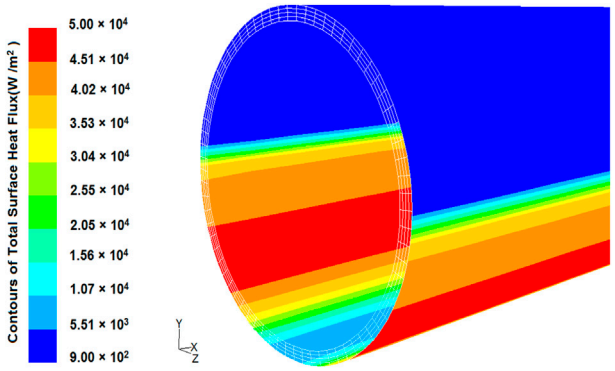


FIGURE 5
Heat flux distribution on the absorber tube surface (current study).

## Code validation

To determine the validity and correctness of the model and numerical solution used in this inquiry, the Nusselt number generated in this study is compared to the Nusselt number computed using the Gnielinski correlation (Petukhov et al., 1970). Gnielinski devised the following equation to get the Nusselt number of a smooth tube:

$$Nu_D = \frac{(f/8)(R_{eD} - 1000)Pr}{1 + 12.7(f/8)^{1/2}(Pr^{2/3} - 1)}; For 3000 \le Re \le 5 \times 10^6 and 0.5 \le Pr \le 2000 \quad (12)$$

Where the Petukhov friction correlation is as used in (Gee and Webb, 1980):

$$f = (0.790 \ln Re_D - 1.64)^{-2}; \ For\ 3000 \le Re \le 5 \times 10^6 \quad (13)$$

By flowing the PTR heat transfer fluid through a metal tube, the heat transfer properties of the fluid are studied. The $Nu_{avg}$, Re, and heat transfer coefficient (h) read are as follows:

$$Nu_{avg} = \frac{h.D}{\lambda} \quad (14)$$

$$Re = \frac{D.v}{\nu} \quad (15)$$

$$h = \frac{q''}{T_{t,a} - T_{f,a}} \quad (16)$$

The Darcy friction factor in turbulent flow regime is as defined in (Amina et al., 2017):

$$f = \frac{2.\Delta P.D}{L.\rho.v^2} \quad (17)$$

Using the relation between the pressure and shear forces, the above expression can be written as:

$$f = \frac{8.\tau_w}{\rho.v^2} \quad (18)$$

To verify the quality of the computational model employed in this study, the Gnielinski and Petukhov correlations for the Nusselt number and friction factor are utilized to evaluate the simulation of heat transfer and flow properties of the thermal oil D12 in the absorber tube. Figure 7 and Figure 8 show the friction factor and Nusselt number comparisons between the numerical results and the correlations for smooth absorber, respectively. The maximum deviation value of the numerical results was found to be around 7.8% and 15%, and the minimum deviation equals 18% and 11% for the Nusselt number and friction factor, respectively. The heat transfer and flow properties are clearly in agreement with the correlations.

## Effect of perforated obstacles on heat transfer

As seen in Figure 9, changes in Reynolds number (Re) generate fluctuations in Nusselt number, which has values of 18860 (v = 15 m/s), 44007 (v = 35 m/s), and 81728 (v = 65 m/s) when using thermal oil D12 as working fluid. The Nusselt number approximately linearly rises in proportion to the Reynolds number; this enhancement is caused by introducing perforated barriers, which improve the heat transfer area. The vortex flow was caused by fluid mixing given by the perforated barriers, and enhanced turbulent intensity at high values of Re leads the thermal boundary layer to be destroyed. The highest gain is seen in absorber tubes with three holes and perforated barriers (PO3). The average Nusselt number improves by 115 percent compared to the standard case with the smooth absorber. Perforated barriers with one hole (PO1) are the second most successful example, with an average Nusselt number enhancement of 108 percent.

In contrast, perforated barriers with nine holes (PO9) have the smallest Nusselt number enhancement, which equals 54 percent. From Figure 10, it can be observed that the smooth case has the

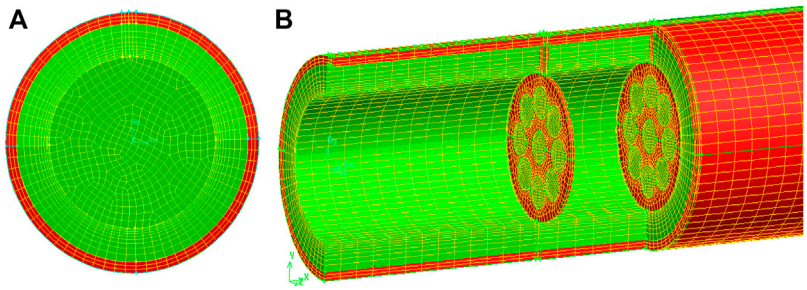


Grids in the cross-section  Grids around the barriers

FIGURE 6
3D mesh of the computational domain.

**TABLE 3** Model constants.

| $C_{\mu}$ | $C_{1\varepsilon(RNG)}$ | $C_{2\varepsilon(RNG)}$ | $\sigma_{k\,(RNG)}$ | $\sigma_{\varepsilon\,(RNG)}$ | $\eta_0$ | $\beta$ |
|---|---|---|---|---|---|---|
| .0845 | 1.42 | 1.68 | .7194 | .7194 | 4.38 | .012 |

**TABLE 4** Mesh effect on the average Nusselt number.

| $N_{cells}$ | | | | | |
|---|---|---|---|---|---|
| | 294600 | 307200 | 330400 | 354400 | |
| Re | Nu | | | | \|δmax\| |
| $10^4$ | 148.123 | 150.021 | 149.613 | 150.461 | 1.57% |
| $10^5$ | 222.104 | 226.371 | 226.719 | 229.004 | 3.10% |
| $10^6$ | 259.121 | 258.223 | 259.942 | 260.781 | .64% |

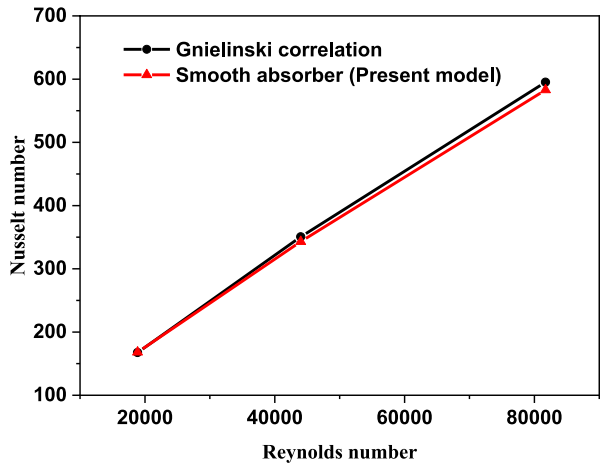


FIGURE 7
Nussle number with Gnielinski correlation.

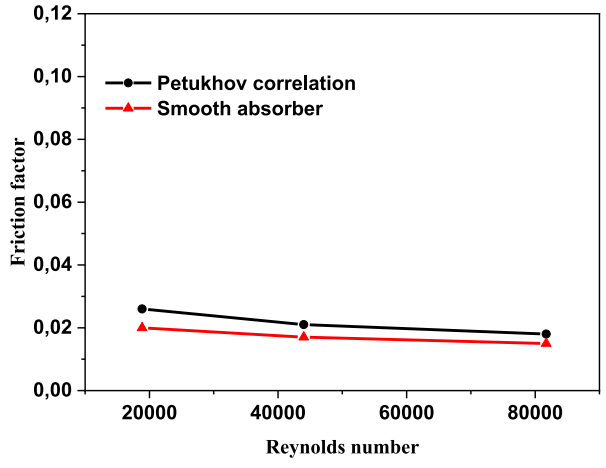


FIGURE 8
Friction factor with Petukhov correlation.

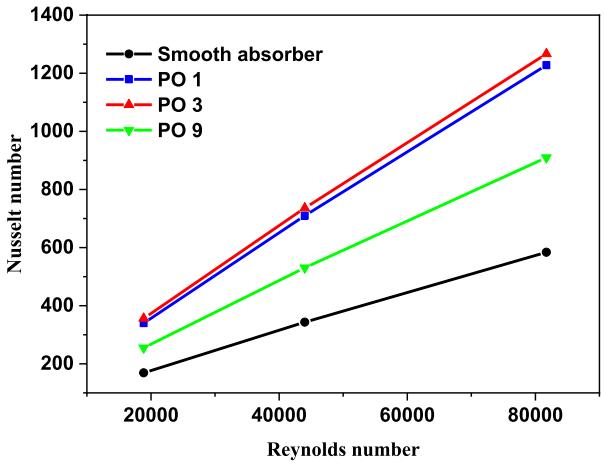


FIGURE 9
Nu variation in the absorber vs. Reynolds number (P/D = 2).

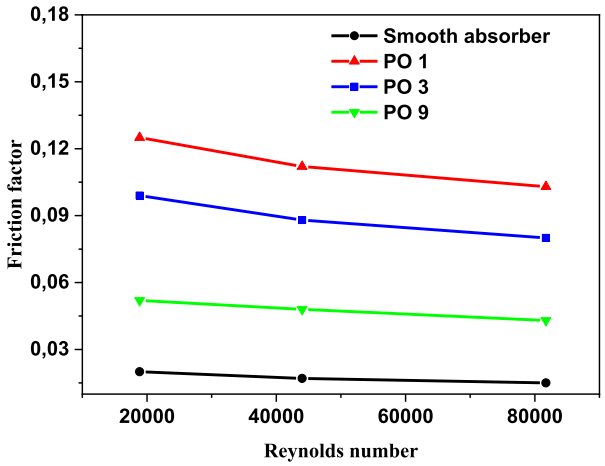


FIGURE 10
Variation in absorber tube's friction factor vs. Reynolds number (P/D = 2).

smallest friction factor of all the cases investigated in this study. The largest friction factor is obtained when perforated barriers with one hole (PO1) are used, followed by perforated barriers with three holes (PO3) and perforated barriers with nine holes (PO9) in the second and third cases, respectively. These higher values are caused by the whirling flow generated by the inserts that function as an obstruction. Figure 11 displays the heat transfer fluid average temperature distribution on sectional planes (y-axis and z-axis) along the entire length of the absorber tube with and without impediments. At the exit, the temperature reaches its peak. Higher temperatures (462.1 K) are achieved in the absorber tube with perforated barriers with three holes (PO3), followed by (461.56 K) for perforated barriers with one hole (PO1), and 454.92 K for perforated barriers with nine holes (PO9). Figure 12 shows the temperature distributions of the PTR absorber tube on two distinct cross-sections with Re = 81728 for various scenarios.

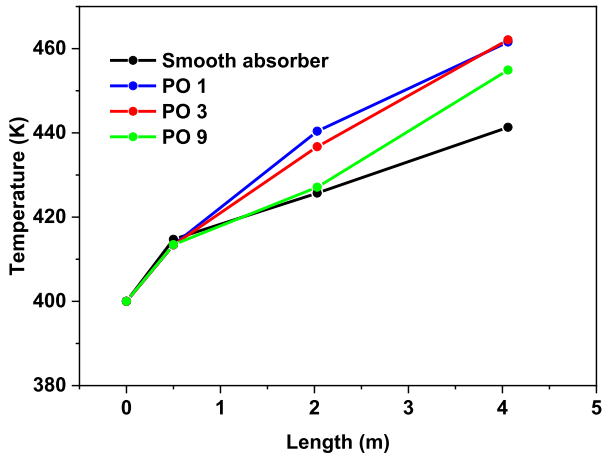


FIGURE 11
Variation in absorber tube's average temperature and without perforated obstacles (Re = 81728, v = .65 m/s).

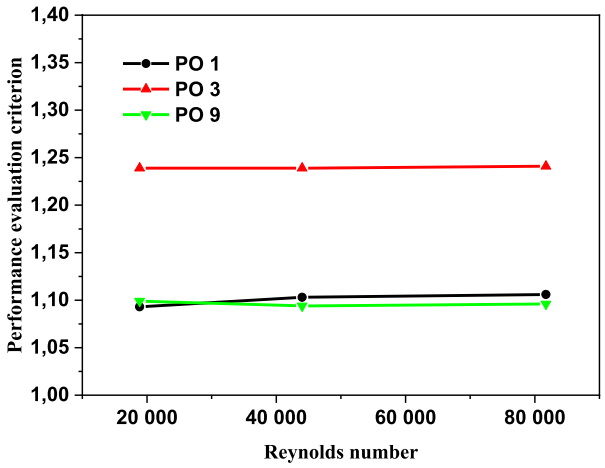


FIGURE 13
Performance evaluation criteria variation vs. Re number.

## Thermal performance analysis

To enhance heat transfer efficiency, it is required to assess both heat transfer and flow resistance concurrently. As a result, as stated below (Xiangtao et al., 2017), the performance evaluation criteria (PEC) are universal assessment tools that reflect a heat transfer unit's overall performance. The thermal performance criterion was calculated as the ratio of the

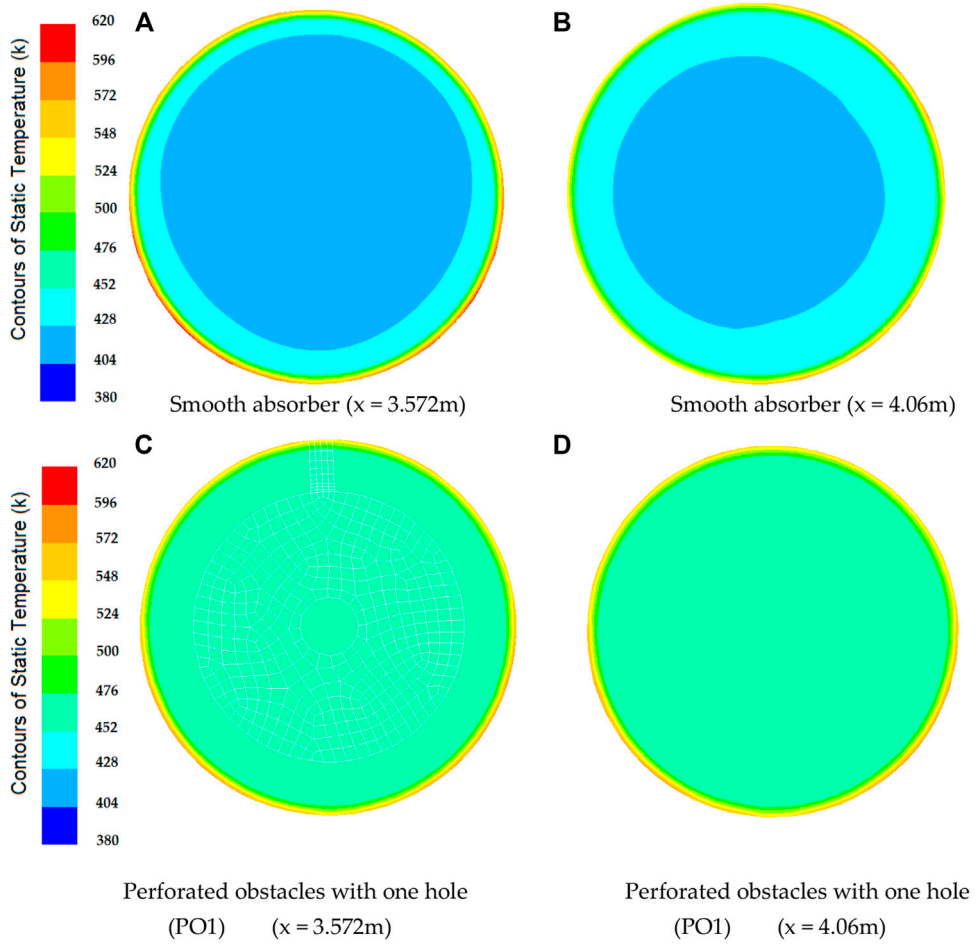


FIGURE 12
Temperature distribution of absorber tube of PTR at cross-sections with Re = 81728.

**TABLE 5** Comparison with literature studies with inserts in the receiver of a parabolic trough solar collector and the present study.

| Cas | Insert type | Increase (%) Nu | PEC | Method | Reference |
|---|---|---|---|---|---|
| **Present study** | Perforated obstacles | 115 | 1,24 | CFD | |
| **Gong Xiangtao** | Pin fin arrays | 9 | 1.12 | CFD | Mwesigye et al. (2016) |
| **Aggrey Mwesigye** | Twisted tape | 58.8 | 1.02 | CFD | Mwesigye et al. (2014) |
| **Aggrey Mwesigye** | Perforated plate | 8–133.5 | .44–1.05 | CFD | |

dimensionless Nusselt number to the dimensionless friction factor.

$$PEC = \frac{Nu/Nu_0}{(f/f_0)^{1/3}} \quad (19)$$

where (Nu0) and (Nu1) represent the smooth absorber case (f0).

Figure 13 illustrates the fluctuation of performance evaluation criteria (PEC); when the PEC values exceed one, it indicates that the inserts have a favorable influence on heat transfer. It is notable that the perforated barriers give a heat transfer boost over the smooth tube. The perforated barriers with three holes had the greatest PEC value (PO3).

Table 5 includes the obtained increase in the Nusselt number (Nu) and in the performance evaluation criteria (PEC). Data has been estimated according to the results of these papers. Moreover, this table shows the method of every study. These studies more specifically, present lower performance evaluation criteria (PEC) compared to the present study. According to the final results, the use of perforated obstacles leads to 1.24% performance evaluation criteria (PEC) enhancement.

## Conclusion

The effect of utilizing varied perforated barriers on the thermal performance of parabolic through the solar receiver is computationally investigated in this work. The following observations could be drawn from this work.

- In comparison to the reference case (smooth absorber), the greatest increase in Nusselt number was 115%, and it was attained by the perforated obstacles with three holes (PO3), followed by 108% for the perforated obstacles with one hole (PO1), while the perforated obstacles with nine holes (PO9) achieved the minimum enhancement of 54%.
- Friction factor values decrease with the increase in the number of holes on obstacles. In the case of the tube without perforated obstacles, friction factor values are less than all the friction factor values with perforated obstacles inserts.
- The perforated barriers in the absorber tube increase the Nusselt number while decreasing the friction factor.
- The highest PEC value was obtained for the perforated obstacles with three holes (PO3).
- The temperature of the heat transfer fluid reaches its maximum value near the exit, while temperatures as high as 462.1 K are obtained in the absorber tube with perforated barriers with three holes (PO3).

## Data availability statement

The original contributions presented in the study are included in the article/Supplementary Material, further inquiries can be directed to the corresponding author.

## Author contributions

All authors listed have made a substantial, direct, and intellectual contribution to the work and approved it for publication. KG, TF, SL, AA: Formal analysis, investigation and writing-original draft. ZD, ET-E, OY: Formal analysis and supervision. MZB-F: Funding acquisition, software and revision. KG, ET-E: Funding acquisition, validation and revision. KG, ET-E: Funding acquisition, resources and revision. TF, SL, AA: Funding acquisition, validation and revision. ZD, ET-E, OY: Conceptualization, editing and revision.

## Funding

The authors extend their appreciation to the Deputyship for Research & Innovation, Ministry of Education in Saudi Arabia for funding this research work through the project number: IFP22UQU4331317DSR174.

## Conflict of interest

The authors declare that the research was conducted in the absence of any commercial or financial relationships that could be construed as a potential conflict of interest.

## Publisher's note

# References


Abdulwahab, A., Alsarraf, J., and Al-Rashed, A. (2021). Hydrothermal effects of using two twisted tape inserts in a parabolic trough solar collector filled with MgO-MWCNT/thermal oil hybrid nanofluid. *Sustain. Energy Technol. Assessments Volume* 47, 101331. doi:10.1016/j.seta.2021.101331

Ajeel Raheem, K., Sopian, K., and Zulkifli, R. (2022). A novel curved-corrugated channel model: Thermal-hydraulic performance and design parameters with nanofluid. *Int. Commun. Heat Mass Transf.*

Ajeel Raheem., K., Zulkifli, R., Sopian, K., Fayyadh, S., Ahmad, F., and Ibrahim, A. (2021). Numerical investigation of binary hybrid nanofluid in new configurations for curved-corrugated channel by thermal-hydraulic performance method. *Powder Technol.* 385, 144–159. doi:10.1016/j.powtec.2021.02.055

Aman, M., Solangi, K., Hossain, M., Badarudin, A., Jasmon, G., Mokhlis, H., et al. (2015). A review of Safety, Health and Environmental (SHE) issues of solar energy system. *Renew. Sustain. Energy Rev.* 41, 1190–1204. doi:10.1016/j.rser.2014.08.086

Amina, B., Abdelylah, B., Samir, L., and Solano, J. P. (2017). Numerical analysis of compound heat transfer enhancement by single and two-phase models in parabolic through the solar receiver. *J. Mech.* 23 (1), 55–61.

Azmi, W. H., Abdul Hamid, K., Ramadhan, A. I., and Shaiful, A. I. M. (2021). Thermal hydraulic performance for hybrid composition ratio of TiO2–SiO2 nanofluids in a tube with wire coil inserts. *Case Stud. Therm. Eng.* 25, 100899. doi:10.1016/j.csite.2021.100899

Berrehal, H., and Sowmya, G. (2021). Heat transfer analysis of nanofluid flow in a channel with non-parallel walls. *J. Mech. Sci. Technol.* 35, 171–177. doi:10.1007/s12206-020-1216-y

Dehaj, M. S., Rezaeian, M., Davoud Mousavi, B., Shamsi, S., and Salarmofrad, M. (2021). Efficiency of the parabolic through solar collector using NiFe2O4/Water nanofluid and U-tube. *J. Taiwan Inst. Chem. Eng.* 120, 136–149. doi:10.1016/j.jtice.2021.02.029

Esmaeili, H., Armaghani, T., Abediniand, A., and Pop, I. (2019). Turbulent combined forced and natural convection of nanofluid in a 3D rectangular channel using two-phase model approach. *J. Therm. analysis Calorim.* 135, 3247–3257. doi:10.1007/s10973-018-7471-9

Fares, R., Abderrahmane, A., Mebarek-Oudina, F., Ahmed, W., Rashad, A. M., Sahnoun, M., et al. (2020). Magneto-free convectiveof hybrid nanofluid inside a non-Darcy porous enclosure containing an adiabatic rotating cylinder. E. *nergy Sources Part A Recovery Util. Environ. Eff.* 136 (4), 1–16.

Farhana, K., Kadirgama, K., Hussein Mohammed, A., Ramasamy, D., Samykano, M., and Saidur, R. (2021). Analysis of efficiency enhancement of flat plate solar collector using crystal nano-cellulose (CNC) nanofluids. *Sustain. Energy Technol. Assessments* 45, 101049. doi:10.1016/j.seta.2021.101049

Gee, D. L., and Webb, R. L. (1980). Forced convection heat transfer in helically rib-roughened tubes. *Int. Heat. Mass Transf.* 23, 1127–1136. doi:10.1016/0017-9310(80)90177-5

Ghanbar, S. A., Faezeh, N. B., Ali Akbar, A. A., and Pourfattah, F. (2019). Wings shape effect on behavior of hybrid nanofluid inside a channel having vortex generator. *Heat Mass Transf.* 55, 1969–1983. doi:10.1007/s00231-018-2489-x

Gnielinski, V. (1976). New equations for heat and masstransfer in turbulent pipe and channel flow. *Int. J. Chem. Eng.* 16, 359–e68.

Hachicha, A. A., Rodriguez, I., Capdevila, R., and Oliva, A. (2013). Heat transfer analysis and numerical simulation of a parabolic trough solar collector. *Appl. Energy* 111, 581–592. doi:10.1016/j.apenergy.2013.04.067

Hamid, A., Azmi, W. H., Mamat, R., and Sharma, K. V. (2019). Heat transfer performance of TiO2–SiO2 nanofluids in a tube with wire coil inserts. *Appl. Therm. Eng.* 152 (4), 275–286. doi:10.1016/j.applthermaleng.2019.02.083

Hassan, M. K., Alqurashi, I. M., Salama, A. E., and Mohamed, A. F. (2022). Correction to: Investigation the performance of PV solar cells in extremely hot environments. *J. Umm Al-Qura Univ. Eng. Archit.* 13, 86. doi:10.1007/s43995-022-00007-9

Hosseini Seyed, M. S., and Shafiey Dehaj, M. (2021). An experimental study on energetic performance evaluation of a parabolic trough solar collector operating with Al2 O3/water and GO/water nanofluids. *nergy* 234, 121317. doi:10.1016/j.energy.2021.121317

Hussein, M., Abuobeida, I. A., Vuthaluru, H., and Liu, S. (2019). Two-phase forced convection of nanofluids flow in circular tubes using convergent and divergent conical rings insertsInternational Communications in Heat and Mass Transfer 101, 10–20.

Jamshed, W., Eid, M. R., Aissa, A., Mourad, A., Nisar, K. S., Shahzad, F., et al. (2021). Partial velocity slip effect on working magneto non-Newtonian nanofluids flow in solar collectors subject to change viscosity and thermal conductivity with temperature. *PLoS ONE* 16, e0259881. doi:10.1371/journal.pone.0259881

Jing, D., Hu, S., Hatami, M., Xiao, Y., and Jia., J. (2020). Thermal analysis on a nanofluid-filled rectangular cavity with heated fins of different geometries under magnetic field effects. *J. Therm. Analysis Calorim.* 139, 3577–3588. doi:10.1007/s10973-019-08758-9

Kamel, C., Belghar, N., Guerira, B., Lachi, M., and Chikhi, M. (2021). Effect of the addition of pie-shaped ribs and parallelogram ribs in micro-channels on thermal performance using diamond-water nanofluid. *SN Appl. Sci.* 3, 316. doi:10.1007/s42452-021-04292-2

Khalid, A. M. A., Obaid, A., Nima, S., Hikmet, Ş. A., Shi, F., Samah, E. A., et al. (2022). Installation of rectangular enclosures filled with phase change nanomaterials on the thrombus walls of a residential building to manage solar radiation in different seasons of the year. *J. Build. Eng.* 57, 104732. doi:10.1016/j.jobe.2022.104732

Kumar, B., Gaurav, P. S., Kumar, M., and Patil, A. K. (2018). A review of heat transfer and fluid flow mechanism in heat exchanger tube with inserts. *Chem. Eng. Process. - Process Intensif.* 123 (1), 126–137. doi:10.1016/j.cep.2017.11.007

Mourad, A., Aissa, A., Mebarek-Oudina, F., Al-Kouz, W., and Sahnoun, M. (2021). Natural convection of nanoliquid from elliptic cylinder in wavy enclosure under the effect of uniform magnetic field: Numerical investigation. *Eur. Phys. J. Plus* 136, 429. doi:10.1140/epjp/s13360-021-01432-w

Mwesigye, A., Bello-Ochende, T., and Meyer, J. P. (2016). Heat transfer and entropy generation in a parabolic trough receiver with wall-detached twisted tape inserts. *Int. J. Therm. Sci.* 99, 238–257. doi:10.1016/j.ijthermalsci.2015.08.015

Mwesigye, A., Bello-Ochende, T., and Meyer, J. P. (2014). Heat transfer and thermodynamic performance of a parabolic trough receiver with centrally placed perforated plate inserts. *Appl. Energy* 136, 989–1003. doi:10.1016/j.apenergy.2014.03.037

Ould-Lahoucine, C., Ramdani, H., and Driss, Z. (2021). Energy and exergy performances of a TiO2-water nanofluid-based hybrid photovoltaic/thermal collector and a proposed new method to determine the optimal height of the rectangular cooling channel. *Sol. Energy* 221, 292–306.

Pandey, A., Kumar, R. R., Kalidasan, B., Laghari, I. A., Samykano, M., Kothari, R., et al. (2021). Utilization of solar energy for wastewater treatment: Challenges and progressive research trends. *J. Environ. Manag.* 297, 113300. doi:10.1016/j.jenvman.2021.113300

Petukhov, B. S., Irvine, T. F., and Hartnett, J. P. (1970). Heat transfer and friction in turbulent pipe flow with variable physical properties. *Adv. Heat. Transf.* 6, 503–564.

Ramin, M., Arasteh, H., Toghraie, D., Motaharpour, H., Keshmiri, A., and Afrand, M. (2020). Heat transfer enhancement of water-Al2O3 nanofluid in an oval channel equipped with two rows of twisted conical strip inserts in various directions: A two-phase approach. *Comput. Math. Appl.* 79 (8), 2203–2215. doi:10.1016/j.camwa.2019.10.024

Rathnakumar, P., Mayilsamy, K., Suresh, S., and Murugesan, P. (2014). Laminar heat transfer and pressure drop in tube fitted with helical louvered rod inserts using CNT/water nanofluids. *J. Bionanoscience* 8 (11), 160–170. Number 3. doi:10.1166/jbns.2014.1225

Sayed, E. T., Wilberforce, T., Elsaid, K., Rabaia, M. K. H., Abdelkareem, M. A., Chae, K.-J., et al. (2020). A critical review on environmental impacts of renewable energy systems and mitigationstrategies: Wind, hydro, biomass and geothermal. *Sci. Total Environ. Sci. Total Environ.* 766, 144505. doi:10.1016/j.scitotenv.2020.144505

Seyed Reza, M., Ali, N., Solomin, E., Hoahn, S., Wongwises, S., and Mahian, O. (2021). Performance improvement of a photovoltaic-thermal system using a wavy-strip insert with and without nanofluid. *Energy Vol.* 234 (1), 121190. doi:10.1016/j.energy.2021.121190

Shahzad, F., Jamshed, W., Sathyanarayanan, S. U. D., Aissa, A., Madheshwaran, P., and Mourad, A. (2021). Thermal analysis on Darcy-Forchheimer swirling Casson hybrid nanofluid flow inside parallel plates in parabolic trough solar collector: An application to solar aircraft. *Int. J. Energy Res.* 45, 20812–20834. doi:10.1002/er.7140

Solutia. Combined heating & cooling highly stable heat transfer fluid. Heat transfer fluids by SOLUTIA. Applied Chemistry, Creative Solution. GROUP PROVOC T.B.S 10-19 (12/98) E. 1998, Available online: http://twt.mpei.ac.ru/TTHB/HEDH/HTF-D12.PDF (12/98.1998).

Syam Sundar, L., Said, Z., Saleh, B., Singh Manoj, K., and Antonio Sousa, C. M. (2020). Combination of Co3O4 deposited rGO hybrid nanofluids and longitudinal strip inserts: Thermal properties, heat transfer, friction factor, and thermal performance evaluations. *Sci. Eng. Prog.* 100695.

Syam, S., Yihun, T. S., Said, Z., Singh, M., and Punnaiah, V. (2020). Energy, efficiency, economic impact, and heat transfer aspects of solar flat plate collector with Al2O3 nanofluids and wire coil with core rod insertsSustainable. *Energy Technol. Assessments* 40, 100772.

Vahidinia, F., Khorasanizadeh, H., and Aghaei, A. (2021). Comparative energy, exergy and CO2 emission evaluations of a LS-2 parabolic trough solar collector using Al2O3/SiO2-Syltherm 800 hybrid nanofluid. *energy Convers. Manag.* 245, 114596. doi:10.1016/j.enconman.2021.114596

Vital Caio ., V. P., Farooq, S., Renato Araujo, E., Rativa, D., and LuisGomez-Malagon, A. (2021). Numerical assessment of transition metal nitrides nanofluids for improved performance of direct absorption solar collectors. *Appl. Therm. Eng.* 190, 116799. doi:10.1016/j.applthermaleng.2021.116799

Wang, F. Q., Tan, J. Y., Ma, L. X., and Wang, C. C. (2015). Effects of glass cover on heat flux distribution for tube receiver with parabolic trough collector system. *Energy Convers. Manag.* 90, 47–52. doi:10.1016/j.enconman.2014.11.004

Wu, X., Deng, H., Li, H., and Guo, Y. (2021). Impact of energy structure adjustment and environmental regulation on air pollution in China: Simulation and measurement research by the dynamic general equilibrium model. *Technol. Forecast. Soc. Change* 172, 121010. doi:10.1016/j.techfore.2021.121010

Wu, Z. Y., Lei, D. Q., Yuan, G. F., Shao, J. J., Zhang, Y. T., and Wang, Z. F. (2014). Structural reliability analysis of parabolic trough receivers. *Appl. Energy**2014*** 123, 232–241. doi:10.1016/j.apenergy.2014.02.068

Wu, Z. Y., Li, S. D., Yuan, G. F., Lei, D. Q., and Wang, Z. F. (2014). Three-dimensional numerical study of heat transfer characteristics of parabolic trough receiver. *Appl. Energy**2014*** 113, 902–911. doi:10.1016/j.apenergy.2013.07.050

Xiangtao, G., Fuqiang, W., Haiyan, W., Tan, J., Lai, Q., and Han, H. (2017). Heat transfer enhancement analysis of tube receiver for parabolic trough solar collector with pin fin arrays inserting. *Sol. Energy* 144, 185–202.

Yakhot, V., Orszag, S. A., Thangam, S., Gatski, T. B., and Speziale, C. G. (1992). Development of turbulence models for shear flows by a double expansion technique. *Phys. Fluids A* 4 (7), pp1510–1520. doi:10.1063/1.858424

Zandalinas, S. I., Fritschi, F. B., Mittler, R., and Global, W. (2021). Global warming, climate change, and environmental pollution: Recipe for a multifactorial stress combination disaster. *Trends Plant Sci.* 26, 588–599. doi:10.1016/j.tplants.2021.02.011

# Frontiers in Chemistry

**Explores all fields of chemical science across the periodic table**

Advances our understanding of how atoms, ions, and molecules come together and come apart. It explores the role of chemistry in our everyday lives - from electronic devices to health and wellbeing.

---

## Discover the latest Research Topics

See more →

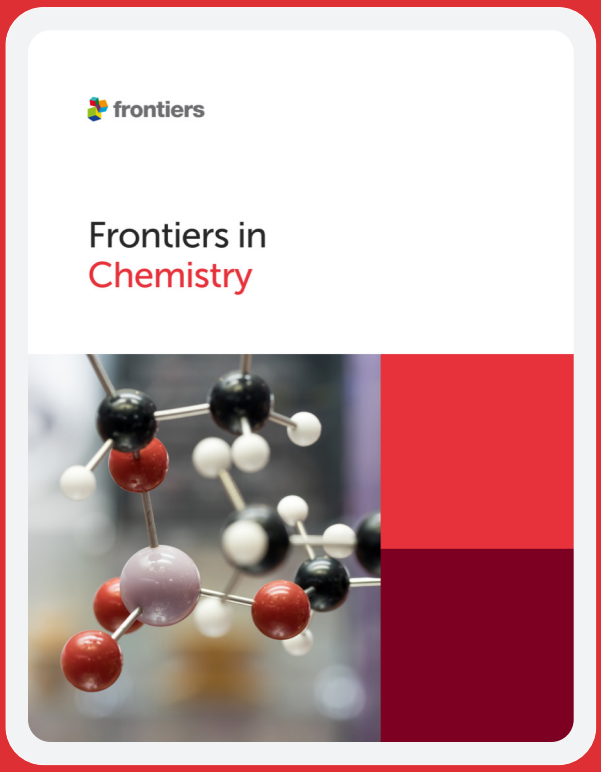


**Frontiers**

Avenue du Tribunal-Fédéral 34
1005 Lausanne, Switzerland
frontiersin.org

**Contact us**

+41 (0)21 510 17 00
frontiersin.org/about/contact